
Search for $t\bar{t}$ resonances in the lepton+jets
channel in proton-proton collisions at
 $\sqrt{s} = 8$ TeV with the ATLAS detector

Dissertation
zur Erlangung des Grades

DOKTOR DER NATURWISSENSCHAFTEN

am Fachbereich Physik, Mathematik und Informatik
der Johannes Gutenberg-Universität Mainz



Dipl.-Phys. Tobias Heck
geboren in Wiesbaden

Mainz, März 2016

1. Berichterstatter : [In der elektronischen Fassung aus Datenschutzgründen entfernt]

2. Berichterstatter : [In der elektronischen Fassung aus Datenschutzgründen entfernt]

Datum der mündlichen Prüfung: 08.11.2016

Dissertation an der Johannes Gutenberg-Universität Mainz (D77)

Kurzfassung

Das *Standardmodell der Teilchenphysik* ist ein bewährtes Modell für das Verständnis der Zusammensetzung und Wechselwirkung gewöhnlicher Materie. Verbleibende offene Fragen geben Hinweise auf Physik jenseits des Standardmodells und motivieren Theorien zur Erweiterung, welche neue schwere Teilchen erwarten. Das top Quark als schwerstes Teilchen im Standardmodell ist ein vielversprechender Kandidat an diese schweren Resonanzen zu koppeln. Das ATLAS Experiment am *Large Hadron Collider* am CERN hat während RUN I im Jahr 2012 Daten bei einer Schwerpunktenenergie von 8 TeV aufgezeichnet, womit eine gesteigerte Sensitivität auf Resonanzen mit einer invarianten Masse von einigen TeV einhergeht. Diese Arbeit präsentiert eine Analyse dieser Daten im Rahmen einer Suche nach neuen schweren Resonanzen, welche in ein anti-/top Paar über den Lepton+Jets Kanal zerfallen. Dieser Zerfallskanal kombiniert gute Unterdrückung von Untergrundprozessen und eine saubere Ereignisrekonstruktion mit einer Signatur von 4 Jets, einem Lepton (Elektron oder Myon) und fehlender Transversalenergie. Die Zerfälle werden sowohl in voll aufgelösten, als auch in geboosteten Ereignistopologien mit kollimierten Zerfallsprodukten analysiert. Dazu werden Topologie spezifische Techniken zur Rekonstruktion und Identifizierung der Zerfallsprodukte verwendet. Die Schwerpunkte dieser Arbeit werden auf die Abschätzung des Untergrundes aus Prozessen der Produktion eines W-bosons mit assoziierten Jets, sowie einer Studie zu Techniken zur Identifizierung von hadronisch zerfallenden top Quarks mit Hilfe von so genannten *top tagging* Algorithmen gelegt. Als finale Diskriminante wird die invariante Masse des kompletten anti-/top Systems rekonstruiert und auf einen Überschuss an Daten gegenüber Erwartungen aus dem Standardmodell untersucht, welche auf eine neue Resonanz hinweisen würden. Da keine signifikanten Abweichungen beobachtet werden, werden obere Grenzen auf den Wirkungsquerschnitt mal Verzweigungsverhältnis auf ausgewählte Modelle jenseits des Standardmodells in der Größenordnung von 2 TeV gesetzt.

Abstract

The *Standard Model of Particle Physics* is a well proven model for the understanding of the constituents and interactions of ordinary matter. Remaining open questions hint at new physics beyond the Standard Model, motivating theories comprising extensions with new heavy particles. The top quark as the heaviest particle of the Standard Model is one of the leading candidates to couple to these new heavy resonances. The ATLAS experiment at the *Large Hadron Collider* at CERN recorded data at a center of mass energy of 8 TeV during RUN I in the data taking period 2012, providing an increased sensitivity for heavy resonances with invariant masses in the TeV scale. This thesis presents an analysis of this data in the context of a search for new heavy resonances decaying to an anti-/top pair in the lepton+jets channel. This decay channel combines good separation power against background processes and clean event reconstruction advantages with a signature of 4 jets, one lepton (electron or muon) and missing transverse energy. The decays are analyzed in resolved, as well as boosted event topologies with collimated decay products. Specific techniques for reconstruction and tagging of the decay products for each topology are applied. Special emphasis is put on the estimation of the contribution of processes with production of W-bosons in association with jets, as well as a study on techniques for identification of hadronically decaying top quarks using so-called *top tagging* algorithms. The mass of the fully reconstructed anti-/top system $m_{t\bar{t}}$ is used as final discriminant, analyzed for excesses between observed data and Standard Model expectations, hinting for new heavy resonances. No significant deviations are observed in these distributions, therefore upper limits on the cross section times branching ratio are set on a selection of beyond the Standard Model theories at the order of 2 TeV.

Contents

1	Introduction	1
2	The Standard Model of Particle Physics	3
2.1	Gauge theories	3
2.2	Fundamental interactions	4
2.3	Fundamental particles	5
2.4	The Higgs mechanism	9
2.5	Top quark physics	10
2.6	Beyond the Standard Model	15
3	The Large Hadron Collider and ATLAS	19
3.1	Particle accelerator parameters	20
3.2	The Large Hadron Collider at CERN	20
3.3	The ATLAS experiment	22
4	Physics object definition and reconstruction	35
4.1	Tracks	35
4.2	Vertices	36
4.3	Electrons	37
4.4	Muons	40
4.5	Jets	41
4.6	Missing transverse energy	47
5	Data and Monte Carlo samples	49
5.1	Dataset	49
5.2	Simulated background samples	52
5.3	Simulated signal samples	55
6	Analysis	59
6.1	Object selection	59
6.2	Event selection	65
6.3	Event reconstruction	68

7	W+Jets background estimation	75
7.1	W+Jets charge asymmetry	76
7.2	W+Jets normalization in resolved topology	77
7.3	W+Jets normalization in boosted topology	81
7.4	Application of W+Jets scale factors	81
7.5	Differences in e +jets and μ +jets channel	84
8	Systematic uncertainties	87
8.1	Luminosity	87
8.2	Physics objects	88
8.3	Backgrounds	89
8.4	Smoothing procedure	96
8.5	Summary	97
9	Comparison of data and Standard Model expectations	99
10	Analysis results	107
10.1	Hypothesis testing	108
10.2	Bayesian method results	110
10.3	CL _S method results	115
10.4	Comparison of CL _S and Bayesian method	117
11	Analysis improvements	119
11.1	Motivation	119
11.2	HEPTOPTAGGER algorithm	120
11.3	Analysis with the HEPTOPTAGGER	124
11.4	Comparison of data and Standard Model expectations	137
11.5	Results	142
12	Summary	145
A	Appendix	147
A.1	Calculation of the longitudinal momentum component of the neutrino $p_{z,\nu}$	147
A.2	Monte Carlo samples	149
A.3	Distributions of systematic uncertainty shifts	152
A.4	Distributions of PDF uncertainty shifts	158
A.5	Limits on cross section times branching ratio	159
A.6	Response and Efficiency of BDT configurations	163
B	List of Figures	164
C	List of Tables	167
D	Bibliography	169

1

Introduction

The idea of indivisible fundamental particles dates back to the ancient Greek, who called those (at that time only hypothetical) basic units *atomos*. These atoms were understood as the most basic components of ordinary matter until the end of the 19th century. Experiments in the beginning of the 20th century proved this belief to be wrong by discovering three subatomic particles (electron, proton and neutron) and thereby heralding the age of modern particle physics. Scientists started constructing particle accelerators to study potential substructures of these subatomic particles, resulting in the discovery that protons and neutrons are composed of even smaller particles, the quarks. Quarks are since then understood as fundamental particles, as well as the electron.

A scientific model to describe these fundamental particles and their interactions has been developed in the 20th century, named the *Standard Model of Particle Physics*, one of the most successful and most accurately tested scientific models ever since. Important milestones of the development of this model were the prediction of the existence and mass of the W -boson, discovered in 1983 at the UA1/UA2 experiments at CERN [1, 2, 3] as well as the top quark, discovered in 1995 at the Tevatron collider by the CDF and DØ experiments [4, 5]. In 2012, the ATLAS and CMS collaborations at CERN announced the discovery of a Higgs-like resonance [6, 7]. All three discoveries were awarded with the Nobel Prize in Physics, reflecting the significant impact on the field of particle physics.

In spite of the big success, there are still several open questions remaining which cannot be answered by the Standard Model, such as the multiplicity of (exactly three) particle families and their observed mass hierarchy, the large number of free parameters (e.g. masses and couplings), the hierarchy of the strength of different forces and value of the mass of the Higgs, the missing link to the gravitational interaction, the source of the observed asymmetry of

matter-antimatter occurrence in our universe or the nature of dark matter and dark energy, representing the major contribution to the total energy in our universe. All these open questions are a hint to physics beyond the Standard Model, which are addressed in various theories suggesting specific extensions of the Standard Model.

These extensions for example predict new heavy particles, which decay into Standard Model particles, like heavy partners of the Z-boson, a Z' resonance, or a heavy partner of the gluon, a so-called Randall-Sundrum Kaluza-Klein gluon g_{KK} , as well as Randall-Sundrum Kaluza-Klein graviton G_{KK} or scalar resonances. The top quark, as the heaviest quark in the Standard Model, is a leading candidate to directly couple to such heavy resonances. Analyzing the decay of $t\bar{t}$ pairs therefore may show an excess in the observed compared to expected distribution of events from Standard Model processes, hinting at the decay of a new heavy resonance to a $t\bar{t}$ pair.

The analysis presented in this thesis is a search for heavy resonances decaying into a $t\bar{t}$ pair, analyzing events with the signature of the decay of $t\bar{t}$ pairs in the lepton+jets channel with $\int \mathcal{L} dt = 21.3 \text{ fb}^{-1}$ of data¹ recorded at the ATLAS experiment during RUN I in 2012 at a center of mass energy² of $\sqrt{s} = 8 \text{ TeV}$. The recorded events are analyzed in resolved and boosted event topologies, using specific kinematic selections and reconstruction algorithms to differentiate between the topologies including top tagging algorithms. The analysis results have been published by the ATLAS Collaboration in [8], while this thesis contains further updates and studies for improvements.

This document starts with a brief introduction to the Standard Model and theoretical discussion of particle physics in chapter 2, followed by a closer look at the concept of particle accelerators, presenting the LHC complex and the ATLAS detector in detail in chapter 3. The definition of physics objects and their reconstruction mechanism at the ATLAS detector is presented in chapter 4. Comparing with the simulated background samples listed in chapter 5, the data recorded at the ATLAS detector is analyzed in chapter 6, presenting the applied object definition and event selection and the reconstruction of $t\bar{t}$ decays in the lepton+jets channel in different topologies. Special emphasis lies on the estimation and treatment of the W+Jets background in chapter 7. The detailed discussion of systematic uncertainties is presented in chapter 8, allowing for a reasonable judgment of the comparison of the distributions of observed data and Standard Model expectations in chapter 9. The final results of the analysis are discussed in chapter 10, including a comparison of two different procedures for limit setting. Further improvements of the presented analysis using additional top tagging techniques are presented in chapter 11, concluded with a summary and outlook on possible future updates given in chapter 12. Additional material is provided in the appendix A.

¹The unit barn [b] is used as an alternative unit for cross sections with $1 \text{ b} = 10^{-24} \text{ cm}^2$.

²The unit of electron volts [eV] is a common unit in high energy particle physics. 1 eV is defined as the amount of energy gained (or lost) by the charge of a single electron moved across an electric potential difference of one volt. Using natural units, setting the elementary charge e , Planck constant \hbar and velocity of light c to $e = \hbar = c = 1$, energy, mass and transverse momentum of a particle can all be given in the same unit [eV]. This convention is used throughout this thesis.

2

The Standard Model of Particle Physics

The *Standard Model of Particle Physics* provides a framework for our understanding of the currently known fundamental particles and their interactions between each other based on gauge theories presented in section 2.1. It has been developed in several steps in the late 20th century, describing the fundamental interactions of the combined electroweak interaction and the strong interaction presented in section 2.2 along with the fundamental particles presented in section 2.3 and incorporating the Higgs mechanism discussed in section 2.4. High luminosity particle accelerators, reaching center of mass energies in the TeV scale, provided the environment for intensive testing of the Standard Model. With the discovery of the Higgs-boson at the Large Hadron Collider (LHC) by the ATLAS and CMS experiments in 2012, the last fundamental component of the Standard Model has been confirmed. Even though no significant deviations have been observed so far, it is not a complete theory, since it can not describe all phenomena observed in nature, as for example gravity, as the most obvious force in daily life. Special emphasis is placed on the discussion of the top quark in section 2.5, which plays an important role for testing theories beyond the Standard Model that predict new particles exemplarily presented in section 2.6 by complementing the well confirmed framework of the Standard Model to answer remaining open questions.

2.1 Gauge theories

The Standard Model is a relativistic quantum field gauge theory. It combines the quantum field gauge theories of Quantum Chromo Dynamics (QCD) and the unified electroweak theory, based on three gauge fields representing the strong interaction (color charge C), the weak interaction (weak isospin L) and the electromagnetic interaction (hypercharge Y).

$$SU(3)_C \otimes SU(2)_L \otimes U(1)_Y$$

Interactions are a consequence of the local gauge invariance under this gauge group, which has been shown to be a renormalizable field theory, ensuring all physical observables to be finite [9]. These fundamental interactions will be discussed in detail in the following section.

2.2 Fundamental interactions

The fundamental interactions are represented by the symmetry groups in the Standard Model. They differ in their coupling quantum number and magnitude of strength. The strong interaction is the strongest force, followed by the electromagnetic and the weak interaction. Gravity as the fourth fundamental force is about 41 orders of magnitude weaker than the strong interaction and thus its impact in high energy particle physics can be neglected.

2.2.1 Electroweak interaction

The electromagnetic interaction is based on the gauge group $U(1)_Y$ and described by Quantum Electro Dynamics (QED). Its mediator is the neutral, massless and non self-interacting photon γ . The interaction range is infinite, providing the basis for technologies like radio or wireless communication of electric devices.

The weak interaction is defined by the $SU(2)_L$ gauge group with massive gauge bosons, two charged W^\pm and one neutral Z^0 , mediating the interaction between particles carrying a weak isospin \vec{I} and a hypercharge Y . Depending on their helicity¹, left-handed fermions carry a total weak isospin of $I = 1/2$ forming a doublet with $I_z = \pm 1/2$, while right-handed fermions with $I = 0$ can only form a singlet with $I_z = 0$. The relation to the electric charge Q is given by the hypercharge Y and the 3rd component of the isospin I_z as $Q = I_z + Y/2$. The weak force plays an important role in β -decays, e.g. during the process of nucleosynthesis in the sun and is only very short ranged, due to the massive bosons. It is the only known force capable of changing quark or lepton flavors². It was observed that coupling within one quark generation is stronger than to other generations, summarized in the Cabibbo-Kobayashi-Maskawa (CKM) matrix V_{CKM} [10, 11] giving the strength of the coupling V_{ij} between two quarks of flavor i and j . Latest results [12] for the matrix elements are shown in equation (2.1), stating couplings and branching ratios³ within one quark generation close to unity, denoted by the diagonal matrix elements, e.g. $\text{BR}(t \rightarrow b + W) \sim |V_{tb}|^2 = 99.9\%$.

¹The helicity h of a particle is defined by the projection of the spin \vec{S} on the direction of movement \hat{p} . Positive values (spin pointing into direction of movement) denote right-handed particles, left-handed otherwise.

²So far this process has only been observed with a W-boson involved, but not mediated by a Z-boson, so-called Flavor Changing Neutral Currents (FCNC).

³The branching ratio (BR) of a decay determines which fraction decays via the given decay mode with respect to the total number of decaying particles.

$$|V_{\text{CKM}}| = \begin{pmatrix} |V_{ud}| & |V_{us}| & |V_{ub}| \\ |V_{cd}| & |V_{cs}| & |V_{cb}| \\ |V_{td}| & |V_{ts}| & |V_{tb}| \end{pmatrix} = \begin{pmatrix} 0.97427(14) & 0.22536(61) & 0.00355(15) \\ 0.22522(61) & 0.97343(15) & 0.04140(120) \\ 0.00886_{-(32)}^{+(33)} & 0.04050_{-(120)}^{+(110)} & 0.99914(5) \end{pmatrix} \quad (2.1)$$

2.2.2 Strong interaction

The strong interaction is defined by the gauge group $SU(3)_C$, described by Quantum Chromo Dynamics (QCD) with the gluon as gauge boson, mediating the interaction between two particles carrying a color charge. The gluon is a massless particle, but carrying a color charge itself, hence it is capable of self-interaction. The color charge was introduced to explain the observation of composite particles with three quarks of the same flavor, which violates the *Pauli Principle*⁴ allowing only two quarks with same flavor, but different spin ($s = \pm 1/2$) in the same state. This quantum number denotes three pseudo colors red (R), blue (B) and green (G) (associated with complementary anti-colors for anti-particles). While quarks carry only one color, gluons carry a color charge as a combination of a color and a different anti-color, leading to an octet of gluons ($3 \otimes \bar{3} = 8 \oplus 1$) and a non-existent color neutral singlet. The coupling strength increases with distance, only allowing for color neutral bound states, which is called *color confinement* and explains the short range character of the strong interaction, despite of the massless gauge boson. Therefore composite particles contain a combination of color and anti-color quarks or form a *white* (R+G+B) state.

2.3 Fundamental particles

The field contents of the Standard Model can be divided into the fermionic, gauge and Higgs sector. The fermionic sector consists of twelve spin-1/2 matter fields, forming the fundamental particles of matter. The gauge sector has another twelve spin-1 vector-like gauge fields in the adjoint representation of the gauge theory, forming the gauge bosons which mediate the interactions as force carriers. The Higgs sector introduces a doublet of Higgs scalar fields, introducing masses to the fermions and intermediate weak bosons via spontaneous electroweak symmetry breaking.

2.3.1 Fermionic sector

The twelve half-integer spin fermions of the Standard Model are the constituents of matter, obeying the *Pauli Principle* and *Fermi Dirac statistic*⁵. They are divided into three generations with the same quantum numbers, except for their masses. Particles of the 2nd and 3rd generation are unstable and decay into 1st generation particles. Therefore ordinary matter

⁴The Pauli Principle prohibits two quanta with exactly the same quantum numbers to occupy the same state.

⁵Fermi-Dirac statistic is part of quantum statistic and describes the macroscopic behavior of a system of identical particles obeying the Pauli principle.

generation	type	name	symbol	mass
1	up	up	u	(2.15 ± 0.15) MeV
	down	down	d	(4.70 ± 0.20) MeV
2	up	charm	c	(1.275 ± 0.025) GeV
	down	strange	s	(93.5 ± 2.5) MeV
3	up	top	t	$(173.29 \pm 0.23 \pm 0.92)$ GeV
	down	bottom	b	(4.18 ± 0.03) GeV

Table 1: Recent mass measurements for the six quarks of the Standard Model, divided into three generations and distinguishing between up- and down-type quarks [14, 15].

only consists of 1st generation particles, while other generations can only be observed in high energy processes. According to their quantum numbers, fermions can be classified as quarks or leptons.

Quarks

Quarks carry a color charge C obeying the strong interaction, as well as an electric charge Q as fraction of the unit charge and an isospin \vec{I} , interacting via the weak and electromagnetic interaction. Each generation contains an up- and a down-type quark. Quarks can change flavor due to the weak interaction via a flavor changing charged current, which is most likely within one generation as denoted by the CKM matrix (cf. equation (2.1)). Quarks are prohibited to exist as free particles (*color confinement*) and therefore form color-neutral composite particles named mesons (2 quarks⁶, anti-/color pair), e.g. charged π^\pm and neutral π^0 pions, or baryons (3 quarks, white (R+G+B) triplet), e.g. protons p or neutrons n .

$$\pi^+ = |u\bar{d}\rangle \quad \pi^- = |d\bar{u}\rangle \quad \pi^0 = \frac{1}{\sqrt{2}} [|u\bar{u}\rangle + |d\bar{d}\rangle] \quad p = |uud\rangle \quad n = |udd\rangle$$

Recent results [13] even state *Pentaquark* particles, consisting of 5 quarks (e.g. $P_c^+ = |u\bar{c}cud\rangle$) following the requirement of color neutrality. The formation of these composite particles is called hadronization with an usual formation time of about $\tau_{\text{hadr}} \approx 3 \cdot 10^{-24}$ s. The top quark is the most massive quark in the Standard Model with a rather short life time of about $\tau_{\text{top}}^{\text{life}} \approx 0.5 \cdot 10^{-24}$ s and therefore has never been observed as part of a composite particle, decaying before hadronization. An overview of the masses of all quarks in the Standard Model as obtained from the latest measurements is listed in table 1.

Leptons

Leptons form the second subgroup of fermions, which do not carry any color charge and do not obey the strong interaction. Leptons with electric charge (electron e , muon μ and tau τ) interact via the electromagnetic and weak interactions, while their neutrino partners (ν_e , ν_μ and ν_τ) do not carry any electric charge and only obey the weak interaction, resulting in a very

⁶The anti-particle partner of a quark q is denoted as \bar{q} . The same convention is applied for neutrinos ν and $\bar{\nu}$.

generation	type	name	symbol	mass [MeV]
1	charged	electron	e	0.511
	neutral	electron-neutrino	ν_e	$< 2 \cdot 10^{-6}$
2	charged	muon	μ	105.66
	neutral	muon-neutrino	ν_μ	< 0.19
3	charged	tau	τ	1776.82 ± 0.16
	neutral	tau-neutrino	ν_τ	< 18.2

Table 2: Recent mass measurements for the six leptons of the Standard Model, divided into three generations and distinguishing electrically charged and neutral types. If no explicit uncertainty on a measurement is given, it is smaller than the given precision [18, 19, 20, 21].

low probability to detect them in nowadays detectors. Neutrinos are treated as massless Dirac fields in the Standard Model, but recent experiments observing neutrino oscillations⁷ [16] hint for neutrinos with non-diminishing masses and also theories treating them as *Majorana*⁸ particles are investigated in neutrino-less double β -decays [17]. Latest measurements of the β -decay spectrum of Tritium performed in Mainz set upper limits on the mass of the electron neutrinos to $m_{\nu_e} < 2.3 \text{ eV}$, listed in table 2 along with masses (or limits) for the other leptons.

Summary of quantum numbers

A summary of the quantum numbers of all fundamental particles, denoting their coupling to the different interactions is given in table 3, including the color charge (strong interaction), the electric charge (electromagnetic interaction) and their isospin, splitting their ground states into singlets or doublets, combined with the hypercharge (weak interaction).

2.3.2 Gauge sector

Bosons are the mediators of the forces in the Standard Model with a full integer spin and obey the *Bose-Einstein statistic*⁹. The Standard Model describes twelve gauge bosons, the photon γ for the electromagnetic, the W^\pm, Z^0 for the weak and eight gluons g for the strong interaction. An overview of the attributes of these gauge bosons can be found in table 4. The Standard Model predicts these gauge bosons to be massless, which is true for the photon and the eight gluons, but the W^\pm and Z^0 bosons are found to have a non-vanishing mass. This problem is solved via the electroweak-symmetry breaking in the Higgs mechanism, described in section 2.4.

⁷Neutrino oscillations describe transformations of the neutrino's lepton flavor.

⁸Majorana particles do not have an anti-particle partner, but represent both identities.

⁹Bose-Einstein statistic is part of quantum statistic and describes the macroscopic behavior of a system of non-interacting indistinguishable particles occupying a set of available energy states.

multiplets (3 generations)			color	I	I_z	Y	Q
Quarks							
$Q_L^i =$	$\begin{pmatrix} u \\ d \end{pmatrix}_L$	$\begin{pmatrix} c \\ s \end{pmatrix}_L$	$\begin{pmatrix} t \\ b \end{pmatrix}_L$	3	1/2	+1/2 -1/2	+2/3 -1/3
$u_R^i =$	u_R	c_R	t_R	3	0	0	+4/3
$d_R^i =$	d_R	s_R	b_R	3	0	0	-2/3
Leptons							
$L_L^i =$	$\begin{pmatrix} \nu_e \\ e \end{pmatrix}_L$	$\begin{pmatrix} \nu_\mu \\ \mu \end{pmatrix}_L$	$\begin{pmatrix} \nu_\tau \\ \tau \end{pmatrix}_L$	0	1/2	+1/2 -1/2	0 -1
$\ell_R^i =$	e_R	μ_R	τ_R	0	0	0	-2
$\nu_R^i =$	ν_{eR}	$\nu_{\mu R}$	$\nu_{\tau R}$	0	0	0	0
Higgs							
$\phi =$	$\begin{pmatrix} \phi^+ \\ \phi^0 \end{pmatrix}$			0	1/2	+1/2 -1/2	+1 0

Table 3: Quantum numbers of the fermionic sector and the Higgs isospin doublet of the Standard Model. The quantum numbers are the isospin I and its 3rd component I_z , the weak hypercharge Y and the electric charge Q . L denotes left-handed fermions forming weak-isospin doublets Q_L^i for quarks and L_L^i for leptons. R denotes right-handed fermions forming singlets for up-type quarks u_R^i and down-type quarks d_R^i or for charged leptons ℓ_R^i and neutrinos ν_R^i .

name	symbol	interaction	mass [GeV]	charge [e]	spin
W	W^\pm	weak	80.385 ± 0.015	± 1	1
Z	Z_0	weak	91.1876 ± 0.0021	0	1
photon	γ	EM	$< 1 \cdot 10^{-18}$	0	1
gluon	$g_{(8\oplus 1)}$	strong	0	0	1

Table 4: Attributes of the twelve gauge bosons of the Standard Model, listing recent mass measurements as well as the charge and spin. Each of them represents the interaction particle of a fundamental force, coupling to a different quantum number of the fermions of the Standard Model [22, 23, 24].

2.3.3 Higgs sector

The Higgs sector of the Standard Model consists of one doublet of Higgs scalar fields in the minimal version of the Standard Model, introduced to give masses to quarks, leptons and intermediate weak bosons via spontaneous breaking of electroweak symmetry.

$$H = \begin{pmatrix} H^+ \\ H^0 \end{pmatrix} \quad (2.2)$$

2.4 The Higgs mechanism

The Lagrangian for the Standard Model does not contain any explicit mass terms for the electroweak gauge bosons (W^\pm, Z^0), which would violate the invariance under local $SU(2)_L$ transformations. An elegant solution to solve this discrepancy due to observation of massive electroweak gauge bosons is the Higgs Mechanism, is to introduce a Higgs potential $V(\phi)$ with field operator H in the Lagrangian.

$$V(\phi) = \mu^2 H^\dagger H + \lambda (H^\dagger H)^2 \quad (2.3)$$

with $\lambda > 0, \mu^2 < 0$, which has a non-vanishing vacuum expectation value

$$\langle H \rangle = \begin{pmatrix} 0 \\ v \end{pmatrix} \quad v = m_H / \sqrt{\lambda} \quad (2.4)$$

with the mass of the Higgs-boson m_H and the coupling λ . This leads to a spontaneous breaking of the electroweak symmetry to

$$SU(3)_C \otimes SU(2)_L \otimes U(1)_Y \quad \Rightarrow \quad SU(3)_C \otimes U(1)_{EM} \quad (2.5)$$

This is commonly referred to as the electroweak symmetry breaking [25, 26, 27]. The masses of the gauge bosons are acquired by their coupling to the Higgs field with the gauge couplings g of $SU(2)_L$ and g' of $U(1)$

$$M_W = \frac{1}{\sqrt{2}} g v \quad M_Z = \frac{1}{\sqrt{2}} \sqrt{g^2 + g'^2} v \quad m_\gamma = 0 \quad (2.6)$$

One remaining degree of freedom predicts another neutral boson, which is the Higgs boson [28, 29]. The mass term of this additional boson $m_h^2 = 2v^2\lambda$ is a free parameter within the Standard Model. The existence of the Higgs boson has been confirmed by the ATLAS [6] and CMS [7] experiments in 2012 at the LHC. Also the matter fields of the Standard Model obtain masses via Yukawa-interactions, generating the quark and lepton masses.

2.5 Top quark physics

A third generation of quarks was already postulated in 1973 by M. Kobayashi and T. Maskawa to explain CP violation observed in Kaon decays. After the discovery of the bottom quark in 1977 it took 18 years until the discovery of the top quark was announced by the CDF [4] and DØ [5] experiments in 1995 at Tevatron, which was the first particle accelerator reaching energies capable of producing anti-/top pairs. Due to the large mass of the top quark ($m_{\text{top}} \sim 173$ GeV) compared to the other fermions in the Standard Model, it can only be produced in high energy processes. This section presents the most important production mechanisms and the different decay channels for anti-/top pairs.

2.5.1 Top quark production

The production of anti-/top pairs in hadron collider experiments is characterized by the strong interaction. At leading order perturbation theory¹⁰ this includes anti-/quark annihilation ($q\bar{q} \rightarrow t\bar{t}$) and gluon-gluon fusion ($gg \rightarrow t\bar{t}$) as denoted by the Feynman diagrams shown in figure 1. Including next-to-leading order (NLO) corrections also allows for quark-gluon initial states. The total $t\bar{t}$ production rate for a pp collider experiment like the LHC is given by the total inclusive cross section $\sigma_{pp \rightarrow t\bar{t}}$, which can be factorized in the partonic cross sections $\hat{\sigma}_{ij \rightarrow t\bar{t}}$ and the parton distribution functions (PDFs). The two energy regimes for hard¹¹ processes at small distance and long-distance effects of partons inside the hadrons are separated by the factorization scale μ_F , typically chosen to be the energy transfer Q of the hard process. Parton distribution functions for these two energy regimes are shown in figure 2. The cross section of a collision of two hadrons A and B denoted by $\sigma(AB \rightarrow t\bar{t})$ is then calculated by the convolution of two PDFs $f_i^A(x_i, Q)$ and $f_j^B(x_j, Q)$, describing the probability density to find a parton of flavor i, j inside the hadron A, B carrying a momentum fraction $x_{i,j}$ as shown in equation (2.7).

$$\sigma_{AB \rightarrow t\bar{t}} = \sum_{i,j \in (q,\bar{q},g)} \int_0^1 \int_0^1 dx_i dx_j f_i^A(x_i, Q) f_j^B(x_j, Q) \hat{\sigma}_{ij \rightarrow t\bar{t}} \quad (2.7)$$

Recent measurements at the LHC with a center of mass energy of $\sqrt{s} = 8$ TeV in the decay of a anti-/top pair via the lepton+jets channel (cf. section 2.5.2) determine a total top quark pair production cross section of $\sigma_{pp \rightarrow t\bar{t}}^{\text{exp}} = 260 \pm 1(\text{stat})_{-23}^{+22}(\text{syst}) \pm 8(\text{lumi}) \pm 4(\text{beam})$ pb compared to a theoretical value of $\sigma_{pp \rightarrow t\bar{t}}^{\text{theo}} = 253_{-15}^{+13}$ pb assuming $m_t = 172.5$ GeV [30].

¹⁰The mathematical description of interaction procedures in particle physics has no exact solutions, but is described by an infinite number of additional terms. The first order perturbation theory describes the most basic and simplest processes while higher orders include additional radiation or loop processes. The simulation of these processes uses mostly LO (leading order) and NLO (next-to LO), sometimes also NNLO (next-to-next-to LO), calculations.

¹¹A hard process or object describes a highly energetic process or object.

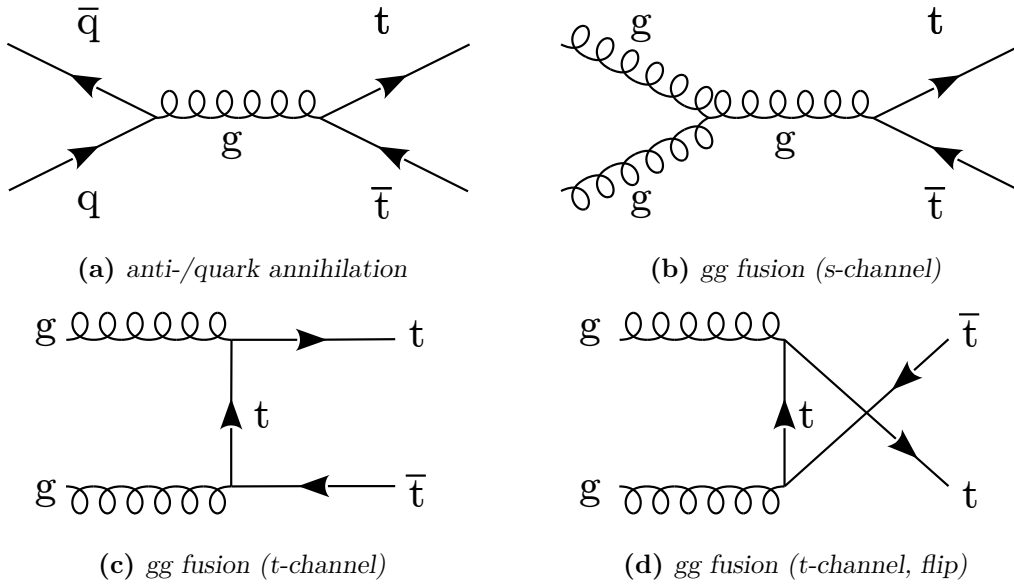


Figure 1: Feynman diagrams of anti-/top pair production at leading order (LO) perturbation theory, distinguishing between (a) anti-/quark annihilation, (b) gluon fusion via the s-channel, (c) exchange of a top quark via the t-channel and (d) its mathematical similar solution due to permutation of the end products.

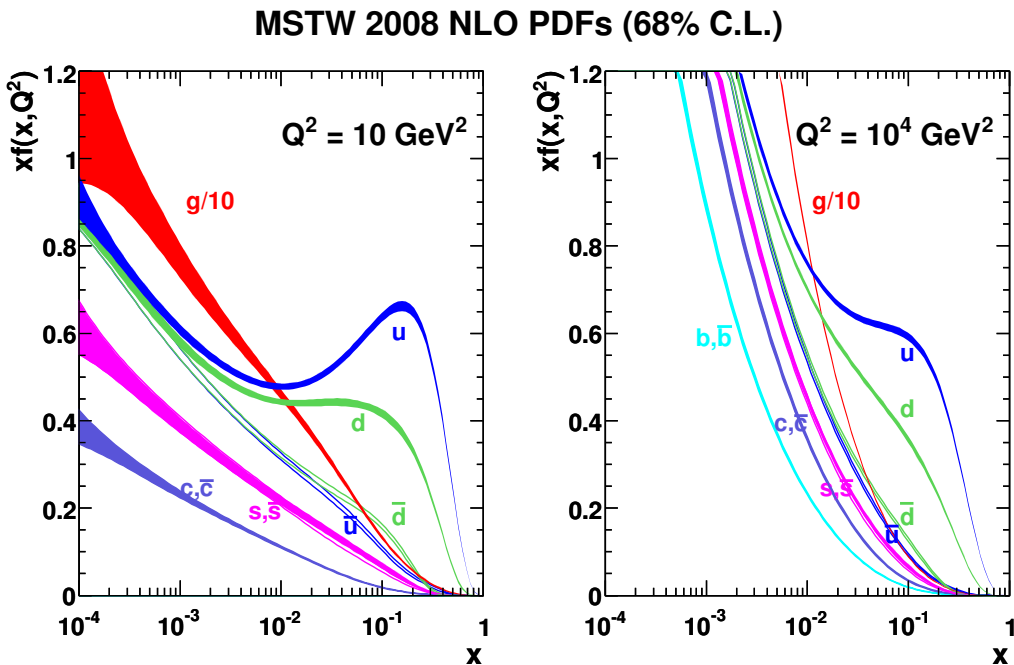


Figure 2: Parton distribution functions (PDFs) xf for quarks and gluons inside a proton as a function of the fraction x of the proton momentum at a given energy scale Q evaluated for low (left) and high (right) energy scales inside the proton [31].

2.5.2 Top quark decay

The top quark decays via the weak interaction into a W-boson and a down-type quark. The decay rates for the different quark flavors are proportional to the square of the CKM matrix elements $|V_{tq}|$, where q can be any down-type quark d, s, b , while the probability for a decay to a bottom quark $|V_{tb}| = 0.99914$ [12] is almost 100%, with a large decay width $\Gamma(t \rightarrow W + b) = 1.35 \text{ GeV}$ (for $m_t = 173.3 \text{ GeV}$) [15]. Implied by this large decay width, the lifetime of a top quark is very short compared to the usual hadronization time scale, thus top quarks decay before they can hadronize and hence no composite particle containing top quarks has been observed so far.

While the b-quark from the top decay hadronizes forming a parton shower, the W-boson decays further via a hadronic or a leptonic decay mode. In the hadronic decay channel, the W-boson decays into an up-type and a down-type quark (with anti-/matter identity). The decay of a W-boson to a top quark and another down-type quark is not possible, because the mass of the top quark is larger than the mass of the W-boson. Due to the six anti-/quark combinations with the relative rates given by the CKM matrix elements and the color factor of 3, the branching ratio for a hadronic W-decay is $\text{BR}(W \rightarrow q\bar{q}') = (67.41 \pm 0.27)\%$ [22]. In the leptonic decay channel, the W-boson decays into a charged lepton ℓ and its neutral neutrino partner ν_ℓ . The branching ratios for the decays into the three different lepton generations are almost equal about 11% as listed in table 5, so the total branching ratio for a leptonic W-decay is about 33%.

The final signature of a $t\bar{t}$ decay depends on the decay modes of the two W-bosons, distinguishing between three different channels. Figure 3 shows a graphical representation of the branching ratios for a $t\bar{t}$ decay and the exact differentiation between the several decay channels, which can be summarized as following with their most recent branching fraction measurements [15].

- **all-hadronic** : $\left[\text{BR}(t\bar{t} \rightarrow Wb + Wb \rightarrow qq\bar{b} + qq\bar{b}) = 45.7\% \right]$

The W-boson of each top decay decays hadronically into a anti-/quark pair, which both hadronize and form a parton shower each. No prompt¹² charged lepton or neutrino is produced from W-bosons from top decays in this channel.

- **lepton+jets** : $\left[\text{BR}(t\bar{t} \rightarrow Wb + Wb \rightarrow qq\bar{b} + \ell\nu_\ell\bar{b}) = 43.8\% \right]$

One of the two W-bosons decays hadronically into a anti-/quark pair forming a parton shower, while the other W-boson decays leptonically to a charged lepton and a neutrino.

- **di-leptonic** : $\left[\text{BR}(t\bar{t} \rightarrow Wb + Wb \rightarrow \ell\nu_\ell\bar{b} + \ell\nu_\ell\bar{b}) = 10.5\% \right]$

The W-boson of each top decay decays leptonically into a charged lepton and a neutrino. No parton showers from prompt quarks from W-bosons from top decays are produced in this channel.

¹²A prompt particle is produced in the main decay in the event, e.g. from a top decay, while a non-prompt particle originates from minor interaction processes in the event.

lepton flavor	process	Branching ratio
electron	$W \rightarrow e + \nu_e$	$(10.71 \pm 0.16)\%$
muon	$W \rightarrow \mu + \nu_\mu$	$(10.63 \pm 0.15)\%$
tau	$W \rightarrow \tau + \nu_\tau$	$(11.38 \pm 0.21)\%$

Table 5: Leptonic decay channels of a W -boson, decaying into a charged lepton ℓ and its neutral neutrino partner ν_ℓ (anti/-matter identities not given explicitly here, which have to be applied depending on the charge of the W -boson) [22].

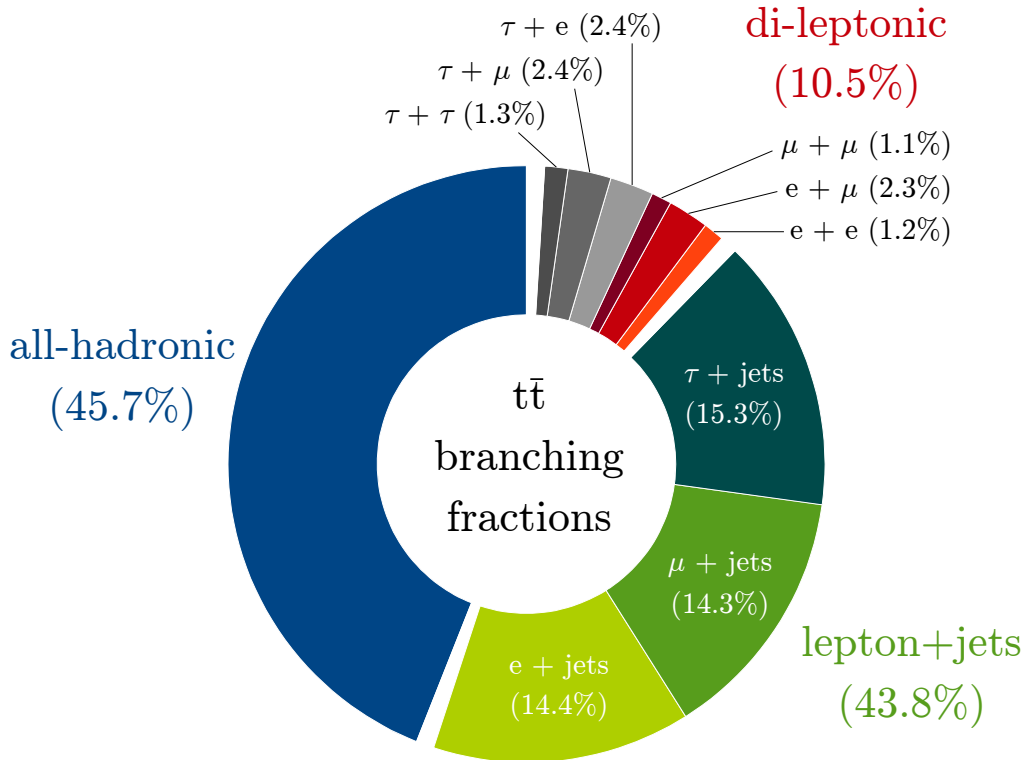


Figure 3: Graphical representation of the branching fractions of the top pair decay distinguishing between all-hadronic, lepton+jets or di-leptonic decay modes depending on the decays of the W -bosons from the top decay using the results listed in [22] and [15].

2.5.3 Lepton+jets channel

The all-hadronic channel is dominated by a large background from multijet processes and a non-trivial challenge of combinatorics to assign the decay products to the two top decays, but does not involve neutrinos leaving the detector without interaction. The di-leptonic channel on the other hand does not suffer from large multijet background, but involves two neutrinos, which have to be reconstructed by finding a reasonable way to split the missing transverse energy information.

The lepton+jets channel combines advantages of both channels with reduced multijet background and combinatorics compared to the all-hadronic channel and allows for a cleaner event reconstruction of missing transverse energy (since only one neutrino is involved) along with a larger branching fraction compared to the di-leptonic channel. To profit from these significant advantages, the lepton+jets channel is chosen as the analysis channel in this thesis. The Feynman diagram for the decay of a $t\bar{t}$ pair in the lepton+jets channel is shown in figure 4 with a signature of 4 jets (arising from the hadronization of the quarks $q\bar{q}'b\bar{b}$, cf. section 4.5), a single charged¹³ lepton ℓ and missing transverse energy (reconstructed from the transverse energy balance in the detector, cf. section 4.6) carried away by the neutral neutrino ν_ℓ .

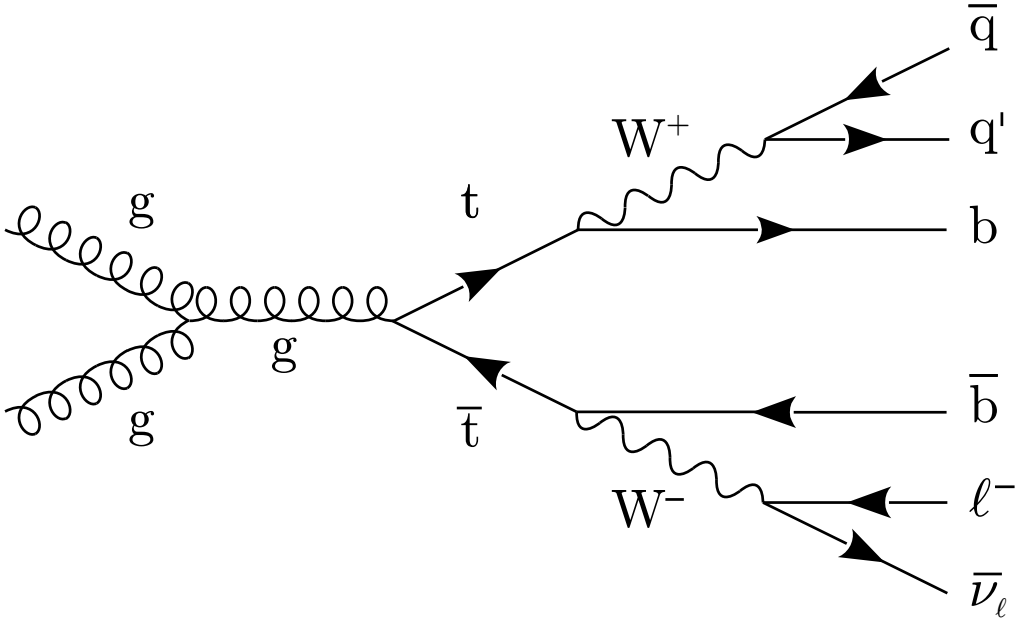


Figure 4: Feynman diagram of the decay of a anti-/top pair, produced in gluon-gluon fusion, decaying via the lepton+jets channel with one hadronically and one leptonically decaying W -boson. (Note : The shown hadronic and leptonic decay modes assigned to the t and \bar{t} are only exemplary and can be swapped, i.e. the lepton charge is not taken as a constraint on the event selection.)

¹³Charged leptons will be referred to as $\ell \in [e, \mu, \tau]$ and neutrinos as ν_ℓ in the following

2.5.4 Recent top measurements

First measurements of the top quark mass during its discovery in the di-lepton and lepton+jets channels performed by the CDF and DØ experiments at Tevatron in 1995 ranged from 176 to 199 GeV with uncertainties of more than 10% [4, 5]. Latest measurements of the top quark mass, combining results of the CMS and ATLAS experiments at the LHC and Tevatron stating $m_t = 173.3 \pm 0.8$ GeV with a much higher precision, along with recent results of the determination of the $t\bar{t}$ cross section are shown in figure 5.

2.6 Beyond the Standard Model

Several open questions in the Standard Model motivate theories for physics Beyond the Standard Model (BSM), which predict new heavy particles coupling to the known particles of the Standard Model leading to an increased total production cross section for these particles due to the additional production channels. Several of these predicted heavy resonances strongly couple to top quarks due to its large mass. These models can be classified according to the spin, color and parity of the new heavy resonances and their resonance width.

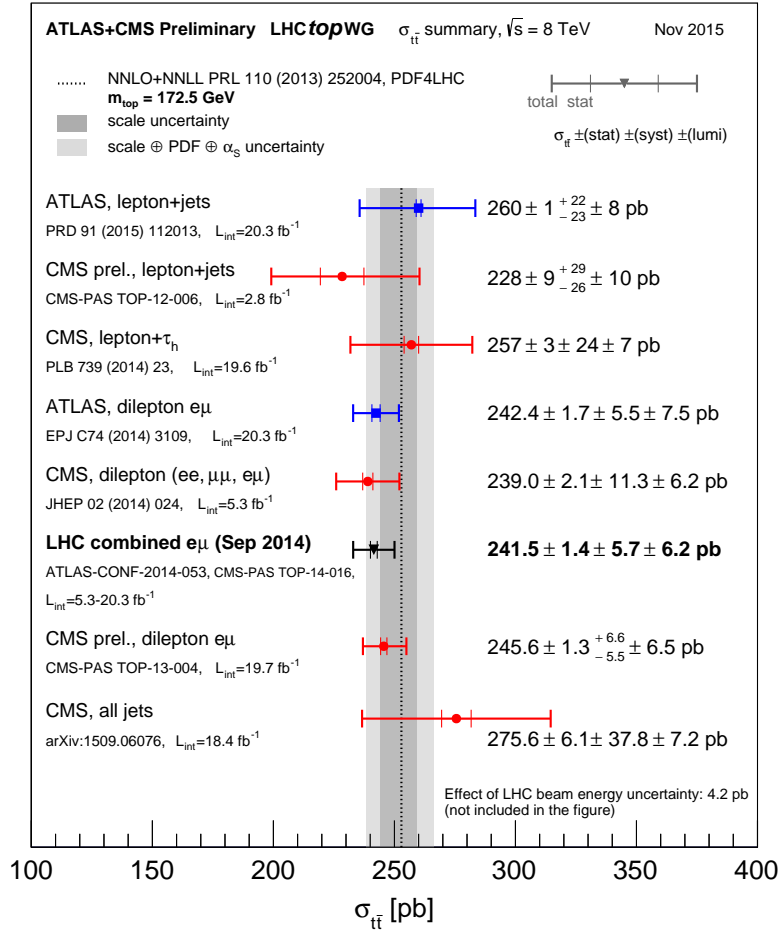
The analysis in this thesis is model independent in order to compare with several different models in parallel. Specific models will be used as benchmark models to test for compensations of possible deficits or excesses in the spectrum of the final discriminant to quantify the sensitivity of the analysis. These selected models will be presented in more detail, but only represent a small selection of many more models available, covering different resonance spins and widths. A summary of the reach of recent ATLAS analyses testing a variety of BSM models is shown in figure 6.

2.6.1 Topcolor

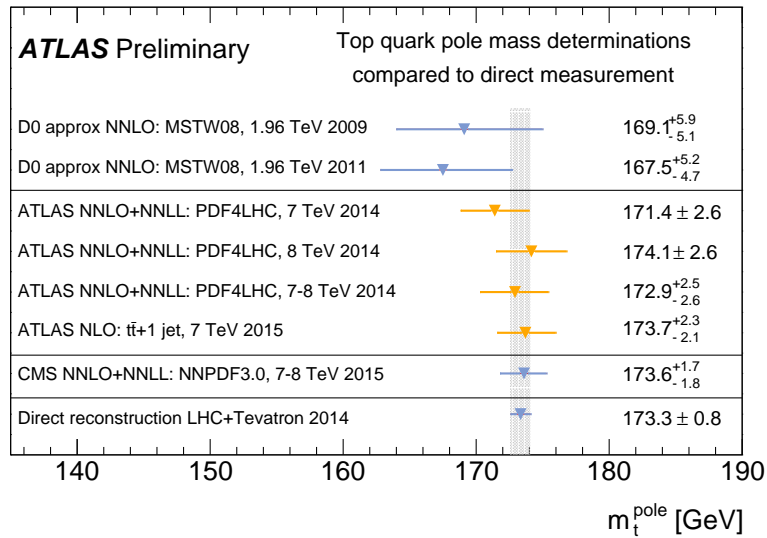
Topcolor models provide solutions for the questions of the large top quark mass and electroweak symmetry breaking through top quark condensation associated with symmetry breaking of a new strong force. A specific model considered in this analysis is a leptophobic topcolor Z' , spin-1 color singlet, with couplings only to first and third generation quarks and is tuned for a strong coupling to $t\bar{t}$ pairs as described in model IV in [33, 34]. The parameters used for the generation of a resonance with a narrow width of $\Gamma/m = 1.2\%$ was originally used in searches for $t\bar{t}$ resonances by the DØ [35] and CDF [36] collaborations, while this width is smaller than the mass resolution of $\sim 10\%$ at the ATLAS detector. Earlier iterations of this analysis also used the same model to set constraints excluding Z' with masses less than 1.74 TeV with $\int \mathcal{L} dt = 4.7 \text{ fb}^{-1}$ data at $\sqrt{s} = 7$ TeV [37].

2.6.2 Randall-Sundrum

The Randall-Sundrum (RS) models propose extra dimensions with warped geometry, predicting excitations of Standard Model particles and providing a missing link to the weak nature



(a) Recent $t\bar{t}$ cross section measurement



(b) Recent top pole mass measurement

Figure 5: Recent measurements of the (a) $t\bar{t}$ cross section combining LHC (ATLAS and CMS) results and (b) top pole mass combining LHC (ATLAS and CMS) and Tevatron (D0) results [32].

of gravity. Limiting the model to one extra dimension leads to a broad width $\Gamma/m = 15.3\%$ spin-1 color octet excitation of the gluon, a so-called RS Kaluza-Klein gluon g_{KK} [38]. Earlier iterations of this analysis excluded g_{KK} masses less than 2.5 TeV with $\int \mathcal{L} dt = 4.7 \text{ fb}^{-1}$ data at $\sqrt{s} = 7 \text{ TeV}$ [37]. Since other models use different widths parameters, this analysis also tests a width scan from 10% to 40% for this resonance.

Allowing for more than one extra dimension with the Standard Model fields in the warped bulk and appropriately localized fermions explaining the flavor structure of the Standard Model leads to an excitation of the graviton, a so-called RS Kaluza-Klein graviton G_{KK} [39], commonly referred to as *Bulk* RS graviton. The model depends on the curvature of the warped extra dimension chosen such that decays to light fermions are suppressed and also photon branching ratios are negligible. This spin-2 color singlet has a width of 3-6% and a branching ratio of $\sim 68\%$ to $t\bar{t}$ pairs above 1 TeV resonance mass. This model has not been tested so far in $t\bar{t}$ resonances analyses in the lepton+jets channel.

2.6.3 Scalar

Another class of new resonances are scalar (spin-0) color singlets, produced via gluon fusion and decaying to $t\bar{t}$. These narrow scalar resonances are generated with a neglected interference with Standard Model $t\bar{t}$ production. It is mainly used to evaluate experimental sensitivities and set upper limits on the production cross sections, since no particular BSM model predicts resonances with this specifications, i.e. the interference tuning.

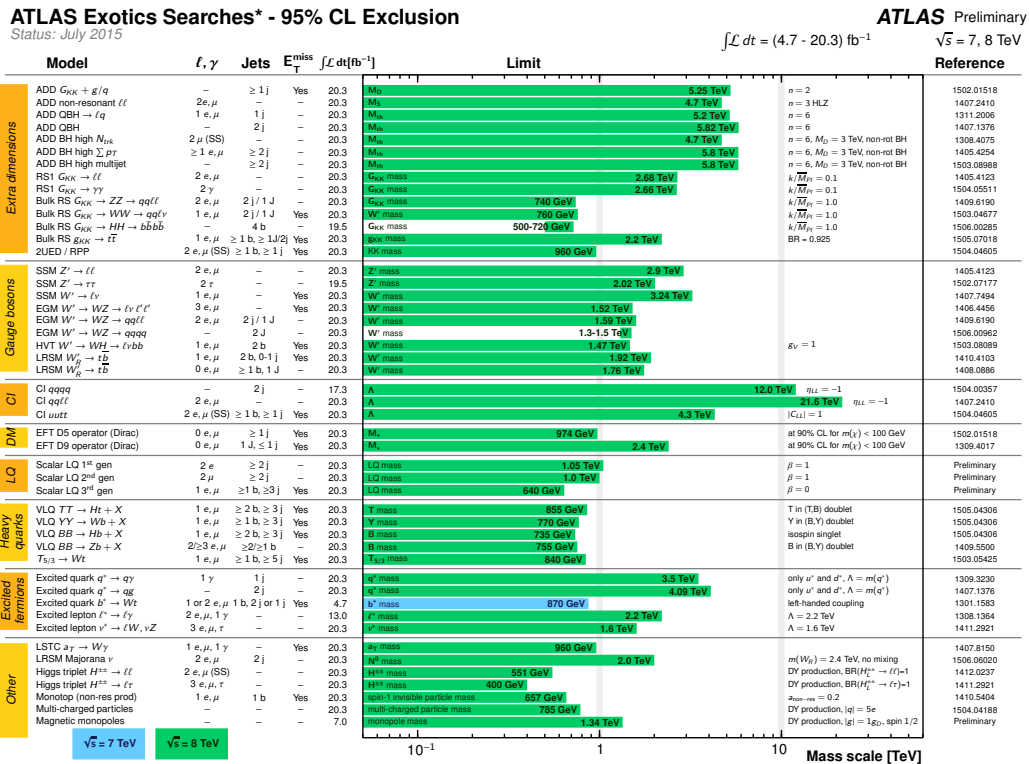


Figure 6: Current reach of ATLAS searches for new phenomena. Only a representative selection of searches setting exclusion limits on the masses of new heavy resonances using $\sqrt{s} = 7 \text{ TeV}$ and $\sqrt{s} = 8 \text{ TeV}$ data results is shown [40].

3

The Large Hadron Collider and ATLAS

The high energy regime in the GeV-TeV region can be studied very efficiently with particle accelerators, ramping up particle beams made of e.g. electrons or protons up to velocities close to the speed of light. Collimating these beams and colliding them at specific interaction points allows to study the most complex processes in particle physics and simulate the conditions right after the *Big Bang*¹. In the 20th century, physicists constructed first generations of particle accelerators as linear colliders, like the *Stanford Linear Accelerator Center* (SLAC) in Stanford (USA) in 1966, colliding electron and positron beams at a central interaction point. The next generation of accelerators was designed as circular colliders, facing the problem of synchrotron radiation², as the *Large Electron Positron Collider* (LEP) at the CERN in Geneva (Switzerland) starting beams in 1989. The first hadron collider was built in 1983 at the *Fermi National Accelerator Laboratory* (Fermilab) in Illinois (USA), colliding anti-/proton beams at the Tevatron collider. The LEP was replaced in 2008 by the *Large Hadron Collider* (LHC), which uses proton-proton beams, reducing³ the energy loss due to synchrotron radiation. Although protons as composite particles only provide a fraction of the energy for the actual interaction particles.

A general overview of important particle accelerator parameters is given in section 3.1, followed by an overview of the CERN accelerator complex and the Large Hadron Collider in section 3.2. Special emphasis is put on the detailed discussion of the ATLAS detector in section 3.3.

¹The Big Bang currently is the most accepted theory for creation of our universe, that all particles evolved from a very dense singularity "exploding" in a Big Bang about 13 billion years ago.

²A charged particle forced on a circular track suffers a certain energy loss per circuit, due to radiation of electromagnetic waves, described by $\Delta E \sim \frac{1}{R m^4}$ (accelerator radius R , particle mass m).

³The reduced energy loss is explained by the difference in proton and electron mass $m_{\text{proton}} \approx 1839 \cdot m_{\text{electron}}$

3.1 Particle accelerator parameters

Two important design parameters for particle accelerators are the *center of mass energy* \sqrt{s} and the *Luminosity* \mathcal{L} . Analyzing the collisions in the center of mass system, the sum of all momenta is zero. The definition of the squared center of mass energy denoted by the variable⁴ s with the momentum of two beams $p_{\text{beam}1,2}$ and the momenta of the outgoing particles $p_{i,\text{out}}$ is shown in equation (3.1).

$$s = \left(|p_{\text{beam}1}| + |p_{\text{beam}2}| \right)^2 = \left(\sum_{i=1}^n p_{i,\text{out}} \right)^2 \quad \text{center of mass energy } \sqrt{s} \quad (3.1)$$

The instantaneous luminosity \mathcal{L} shown in equation (3.2) describes the intensity of the particle beams, depending on different beam parameters, such as the revolution frequency f describing the frequency of beams circuiting in a circular accelerator, the number of bunches n_b per particle beam and the number of particles per bunch N_i . Assuming a Gaussian shape for the beams, the transverse width of each beam is described by σ_x and σ_y , while the x-y-plane is orthogonal to the beam axis. With knowledge of the luminosity one can calculate the reaction rate R for a specific process with cross section σ as shown in equation (3.3) and also the number of expected events N for a given period of data taking, with the integrated luminosity over time \mathcal{L}_{int} , denoted in equation (3.4).

$$\text{luminosity :} \quad \mathcal{L} = \frac{n_b f N_1 N_2}{4 \pi \sigma_x \sigma_y} \quad [\text{cm}^{-2} \text{s}^{-1}] \quad (3.2)$$

$$\text{reaction rate :} \quad R = \sigma \cdot \mathcal{L} \quad (3.3)$$

$$\text{number of events :} \quad N = \sigma \cdot \int \mathcal{L} dt = \sigma \cdot \mathcal{L}_{\text{int}} \quad (3.4)$$

A larger instantaneous luminosity allows for a quicker collection of necessary statistic. Therefore, one important goal for particle accelerators is to increase the instantaneous luminosity. The LHC for example is designed for a center of mass energy of up to $\sqrt{s} = 14$ TeV and an instantaneous luminosity of up to $\int \mathcal{L} dt = 10^{34} \text{ cm}^{-2} \text{ s}^{-1}$ [41].

3.2 The Large Hadron Collider at CERN

CERN is an international organization for particle physics research, established in 1954 by 20 contributing European countries and has been a leading center for particle physics ever since. its name is derived from the French expression *Conseil Européen pour la Recherche Nucléaire*, although today it is known as *European Organization for Nuclear Research*. It provides several facilities and a large scientist community for different kinds of experiments.

⁴The name evolved from the so-called Mandelstam variables, used to describe two particle scattering.

Earlier generations of accelerators at CERN are used as pre-accelerators for the LHC today. The linear accelerator LINAC2 provides protons with energies of up to 50 MeV. These low energy protons are injected into the *Proton-Synchrotron Booster* increasing their energy to about 1.4 GeV. The protons are then further accelerated in the *Proton-Synchrotron* (PS) with a peak energy of 28 GeV. This was the first major accelerator at CERN, starting operation in 1959 and providing particle beams for several experiments. The last pre-acceleration stage for the proton beam is the *Super Proton Synchrotron* (SPS), boosting the protons to energies of up to 450 GeV. Earlier accelerating electrons and positrons as input for the LEP, the protons from the SPS are finally injected into the LHC, which increases the energy up to 7 TeV per beam. Many other experiments are also provided with the proton beams of these pre-accelerators, and the structure can also be used to provide heavy ion beams for designated experiments. An overview of the accelerators and some of the largest experiments at CERN is shown in figure 7.

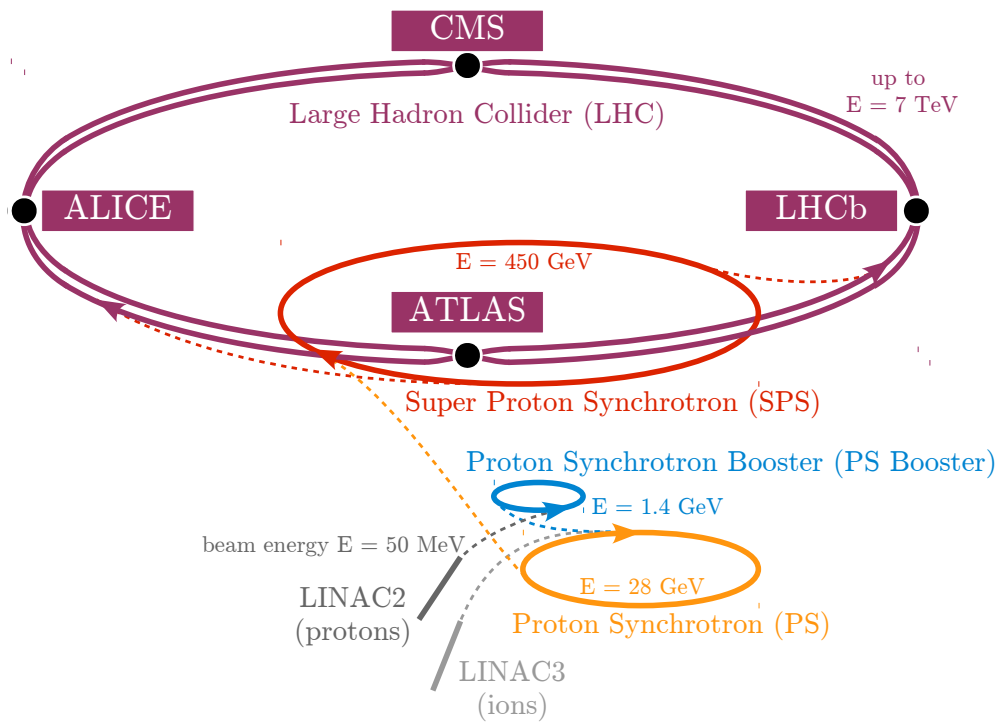


Figure 7: Overview of the CERN collider complex, showing the pre-accelerators providing proton beams with step-by-step increasing beam energy up to 7 TeV in the Large Hadron Collider for the four largest experiments (simplified version based on [42]).

The LHC is the largest human built particle accelerator. With a total circumference of 27 km located in a tunnel on average about 100 m below ground level at the swiss-french border in the Geneva area, it consists of approximately 8000 di-, quadru-, sextu- and octupole magnets focusing, stabilizing and bending the beam on a circular orbit. The strong magnetic fields necessary to bend the high energy proton beams can only be achieved by superconducting magnets, cooled to a temperature of 1.9 K with liquid Helium. Eight Long Straight Sections (LSS) contain instrumentation for collimation or beam extraction, while four of them are

used as crossing points of the two proton beams with big caverns hosting the four main experiments at the LHC, named ALICE, LHCb, CMS, briefly discussed in the following, and ATLAS, discussed in detail in section 3.3.

ALICE (A Large Ion Collider Experiment)

This experiment is dedicated to study the physics of strongly interacting matter and quark-gluon plasma in nucleus-nucleus interactions in heavy ion collisions, but also analyses proton-proton collisions [43].

LHCb (Large Hadron Collider Beauty)

The study of the decays of hadrons containing bottom (also-called beauty quark, giving the detector its name) or charm quarks, as also looking for evidences for new physics via the Charge-Parity-Violation (CP-Violation) is the main purpose of the LHCb experiment. [44].

CMS (Compact Muon Solenoid)

As one of the two largest multi-purpose experiments at the LHC, the main purposes of CMS is the search for new physics beyond the Standard Model and precision measurements of Higgs-boson properties. Its purpose and general structure is similar to the ATLAS detector, but its assembling and technologies used are different [45].

3.3 The ATLAS experiment

The ATLAS (A Toroidal LHC Apparatus) detector is one of the two multi-purpose experiments at the LHC covering a broad spectrum of particle physics with a total size of 46 x 26 x 26 m. The high luminosity and center of mass energy reached at the LHC allows for improved precision measurements and offers a good discovery potential for new physics beyond the Standard Model in the TeV energy regime. The major challenge in order to observe these rare events is to distinguish them from other processes and particles produced during the proton-proton interaction. Figure 8 shows an overview of the ATLAS layout, consisting of the inner detector for tracking and vertexing, electromagnetic and hadronic calorimeters for particle energy measurements and the muon spectrometer, specially designed to detect muons traversing the detector. The inner detector contains a superconducting solenoid magnet providing magnetic fields of up to 2 T, bending the tracks of charged particles to allow for precise momentum measurements. Superconducting air-core magnets surrounding the calorimeters provide another toroidal magnetic field to allow for muon momentum measurements. The detector components are described in more detail in the following subsections using the technical design reports for ATLAS [46, 47].

3.3.1 Geometry

The ATLAS detector has a cylindrical geometry and is composed of a barrel, covering the central region of the detector around the interaction point of the two beams, and two end

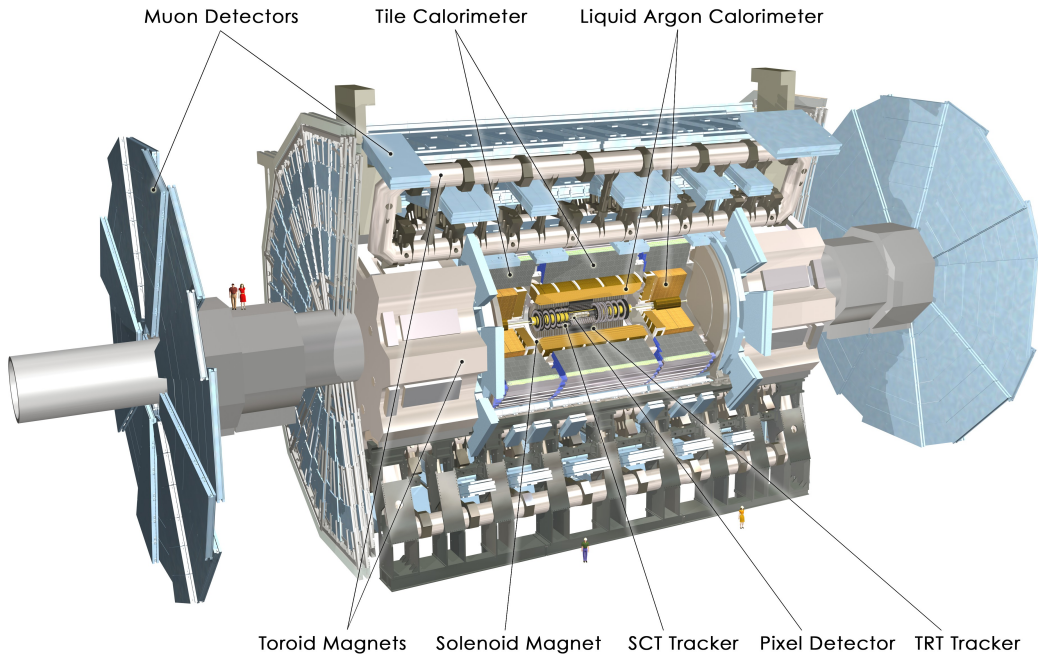


Figure 8: Overview of the ATLAS detector, showing the main detector components: the Inner Detector with the Pixel detector, the Semi-Conductor (SCT) and Transition Radiation Tracker (TRT), the Solenoid and Toroid Magnets, the Liquid Argon and Tile Calorimeters and the outer part with the Muon Detector [48].

caps, covering the forward and backward region of the detector at the end of the central barrel. In Cartesian coordinates, the beamline is aligned with the z -axis by definition, the y -axis is vertical and the x -axis horizontal to ground level. The part of the detector described by the positive z -axis is called *A-side*, the other one (negative z -axis) is called *C-side* and the x - y -plane at $z=0$ is called *B-side*.

The trajectories of charged particles in the detector can be described by five specific helix parameters, while three of them are defined in the x - y -plane:

- $1/p_T$: The reciprocal of the transverse momentum with respect to the beam-axis, used to determine the curvature of the track of a particle.
- ϕ : The azimuth angle with $\tan(\phi) = p_y/p_x$ and $\phi \in [-\pi, +\pi]$
- d_0 : The transverse impact parameter, defined as the transverse distance to the beam axis at the point of closest approach. The sign is defined according to the reconstructed angular momentum of the track about the axis.

Two additional parameters are defined in the R - z -plane:

- $\cot(\theta)$: The cotangent of the polar angle with $\cot(\theta) = p_z/p_T$ and $\theta \in [0, \pi]$.
- z_0 : The longitudinal impact parameter, defined as the distance of the track at the point of closest approach to the beam in z -direction to the interaction point.

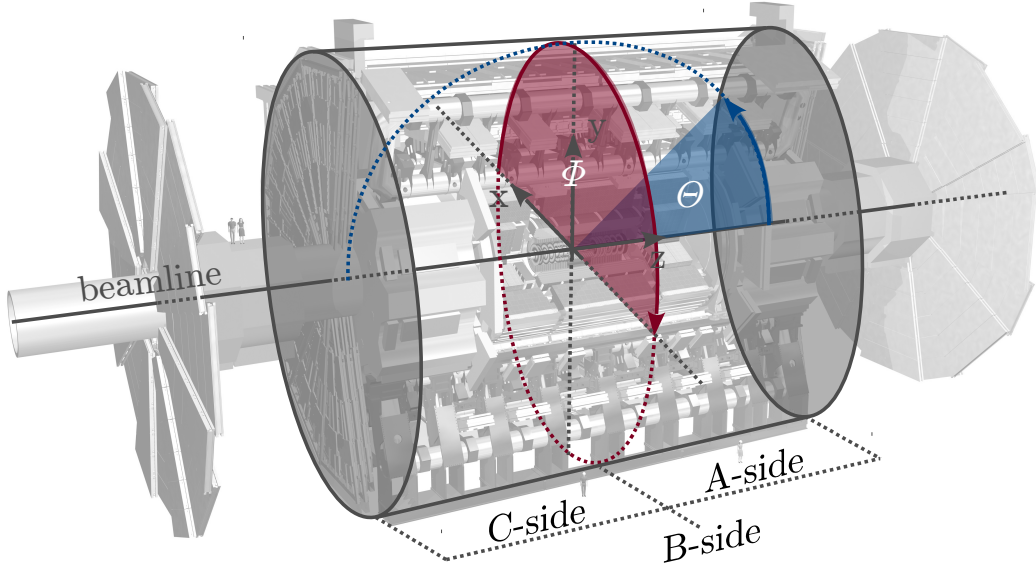


Figure 9: Geometry of the ATLAS detector showing the orientation of the Cartesian coordination system with coordinates x , y and z . Particle tracks are described by the polar coordinates with the azimuth angle ϕ defined in the x - y -plane and the polar angle θ defined in the R - z -plane (based on [48]).

The orientation of the coordinate system, the azimuth angle ϕ defined in the x - y -plane and the polar angle θ defined in the R - z -plane are shown in figure 9.

In high energy physics, the particles move at a velocity close to the speed of light, so that relativistic effects have to be considered. Instead of the polar angle θ one uses the pseudorapidity η defined in equation (3.5). The rapidity y is a Lorentz invariant expression to describe the velocity of relativistic particles and the pseudorapidity η corresponds to the rapidity for particles with velocities close to the speed of light and hence negligible masses compared to their momentum $m \ll p$. Therefore these particles can be treated as massless in terms of their pseudo rapidity.

$$\eta = -\ln \left[\tan \left(\frac{\theta}{2} \right) \right] \quad (3.5)$$

Figure 10 shows a sketch for the interpretation of the pseudorapidity η depending on the polar angle θ of the particle four momentum axis in the geometry of the detector.

By definition, the pseudorapidity is positive in the forward region (defined by the positive z -axis from the interaction point), and negative in the backward region. From a particle transverse to the beam axis $\eta(\theta = 90^\circ) = 0$ the pseudorapidity diverges to infinity for particles close to the beam axis $\eta(\theta = 0^\circ) \rightarrow \infty$ and $\eta(\theta = 180^\circ) \rightarrow -\infty$. Particles exceeding the detector region of $|\eta| > 4.5$ can not be considered for analysis, because the calorimeters do not cover areas exceeding this maximum pseudorapidity (i.e. no physical detector material

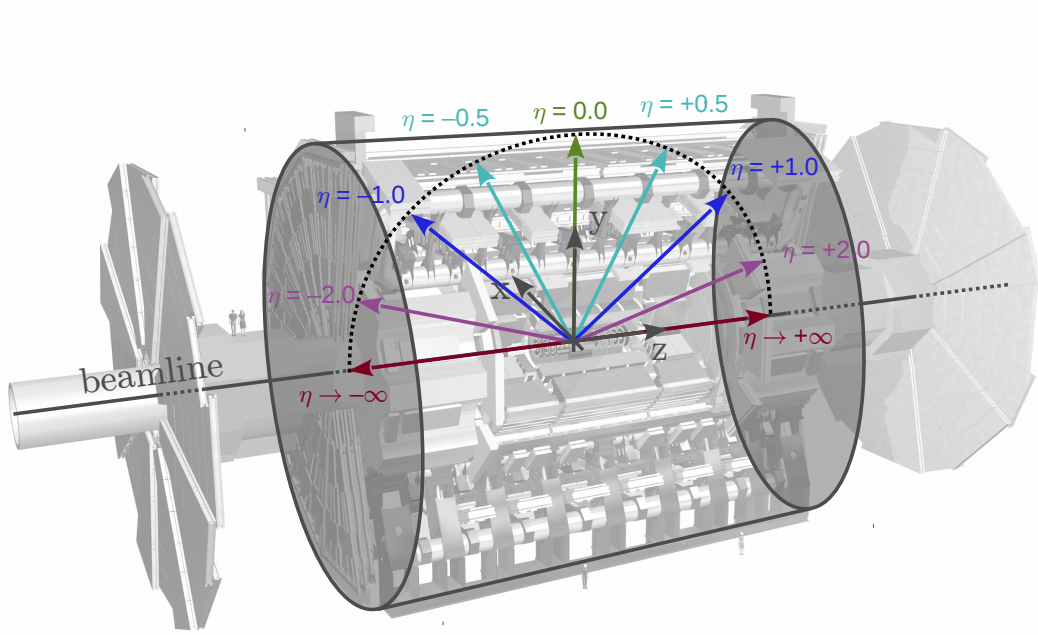


Figure 10: Definition of the pseudorapidity η at the ATLAS detector depending on the polar angle θ . The pseudorapidity is defined to be positive in the forward region, and negative in the backward region. Close to the beamline, it diverges to infinity (based on [48]).

is available in this region so close to the beam axis). The detectors used to reconstruct the tracks of particles close to the interaction point actually only cover a region up to $|\eta| < 2.5$. Another important quantity is the distance between two objects i and j . Using the polar angle ϕ and the pseudorapidity η , one can calculate a defined distance ΔR_{ij} between these two objects via equation (3.6), which is used for isolation criteria of physics objects or for the clustering of energy deposits to form jet objects, as described in section 4.5.

$$\Delta R_{ij} = \sqrt{(\eta_i - \eta_j)^2 + (\phi_i - \phi_j)^2} = \sqrt{(\Delta\eta)^2 + (\Delta\phi)^2} \quad (3.6)$$

3.3.2 Inner Detector

The inner detector consists of three subsystems, the Pixel detector, the Semi-Conductor Tracker (SCT) and the Transition Radiation Tracker (TRT) optimized for tracking and vertexing of transitioning particles crucial for shower reconstruction and identification of primary and secondary vertices and is surrounded by a superconducting solenoid magnet. A detailed view of the arrangement of the subsystems in the central detector and endcap region is shown in figure 11.

The *Pixel detector* is divided into three concentrically arranged pixel module layers around the beampipe in the central detector region and three additional discs in the forward/backward region in the endcaps of the detector limited to pseudorapidities of $|\eta| < 2.5$. The modules

consist of silicon sensors and readout electronics providing a high granularity crucial for the spatial resolution necessary for vertex and track reconstruction in the high pileup (multiple interactions per beam crossing) environment in pp collisions at the LHC. Since the Pixel detector is the closest element to the beamline, it also has to provide sufficient radiation hardness over the long runtime of the LHC at high instantaneous luminosity.

The *Semi-Conductor Tracker* (SCT), surrounding the Pixel Detector, is arranged in four double-layers of silicon microstrip detectors and additional discs in the forward/backward region in the endcaps of the detector limited to pseudorapidities of $|\eta| < 2.5$.

The *Transition Radiation Tracker* (TRT) combines tracking and identification of particles limited to pseudorapidities of $|\eta| < 2.0$. It consists of densely packed straw tubes filled with Xenon gas with a central wire electrode and is enclosed in polypropylene fibers. Highly relativistic particles transitioning these materials with different dielectric constants emit transition radiation photons depending on the relativistic⁵ velocity p/m with a threshold around $\beta\gamma > 1 \cdot 10^3$ resulting in high energy depositions in the gas filled straws. These hits can be well distinguished from low energy track ionization hits allowing for electron identification apart from the tracking information.

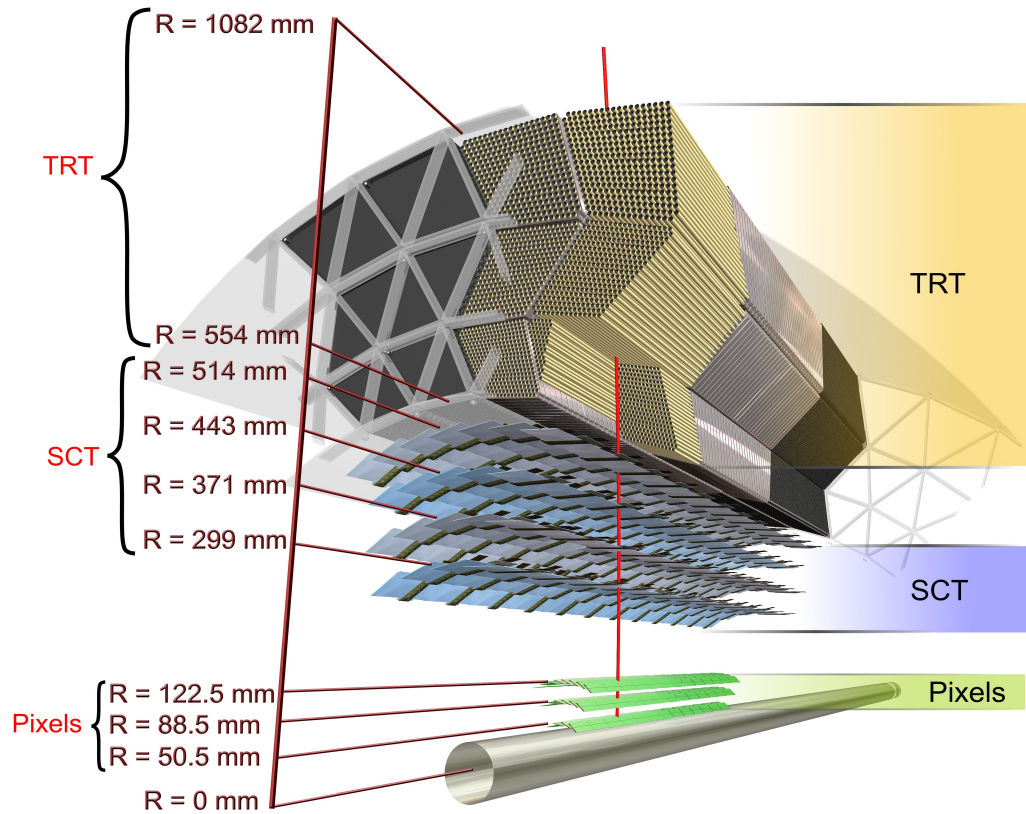
The combination of the hit information of charged particles along their trajectory through the subsystems of the Inner Detector provides high precision track and vertex reconstruction (cf. section 4.1 and 4.2) and the magnetic field provided by the solenoid magnet additionally allows for momentum and charge determination measuring the track curvature.

3.3.3 Calorimeter systems

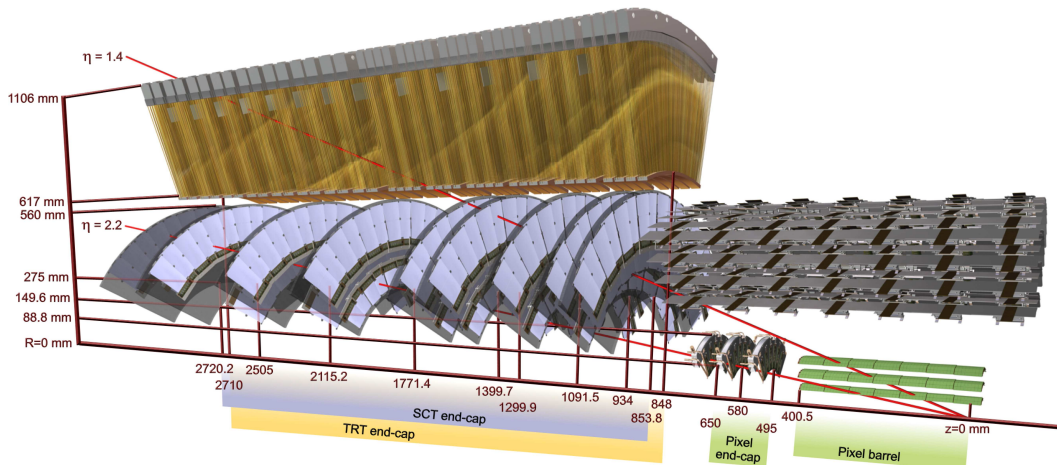
The calorimeter systems of the ATLAS detector are optimized to measure the energies of the particles produced in the pp collisions at the LHC. The calorimeter is divided into two different types, the electromagnetic (EMCal) and hadronic (HCal) calorimeters, optimized for different particle types as typical sampling calorimeters. A detailed view of the ATLAS calorimeter system is shown in figure 12.

The *Electromagnetic Calorimeter* (EMCal), surrounding the Pixel detector and the solenoid magnet, is designed to measure energies of particles like electrons and photons interacting mainly via the electromagnetic interaction, producing characteristic electromagnetic showers. The absorber consists of multiple layers of lead with Liquid Argon (LAr) as active sampling material, providing a homogeneous response allowing for determination of the energy of the transitioning particle. The EMCal is divided into a central barrel, endcap calorimeter (EMEC) in the backward region and a forward calorimeter (FCal) in the forward region, covering pseudorapidities of up to $|\eta| < 4.9$ and up to 26 radiation lengths. Three different layers with different granularities in $\Delta\eta$ and $\Delta\phi$ allow for good separation power of two photons or electrons (cf. section 4.3).

⁵Relativistic factor defined as $\gamma = (1 - \beta^2)^{-0.5}$ with $\beta = v/c$, velocity v of a particle and speed of light c .



(a) Inner Detector central barrel region



(b) Inner Detector endcap region

Figure 11: Sensors and structural elements of the ATLAS Inner Detector, with the Pixel Detector, Semi-Conductor Tracker (SCT) and the Transition Radiation Tracker (TRT) for the (a) barrel part with the red line denoting the transition of a charged particle with a pseudorapidity of $\eta = 0.3$ [49] and the (b) endcap region with the red lines denoting the transition of two charged particles with a pseudorapidity of $\eta = 1.4$ and $\eta = 2.2$ [50].

The *Hadronic Calorimeter* (HCal) is optimized to measure energies of neutral and charged hadrons and is installed around the EMCal, covering up to 10 nuclear interaction lengths. The hadronization of quarks and gluons due to the strong interaction produces hadronic parton showers in the HCal. The absorber of the HCal is made out of steel with plastic scintillator tiles as active sampling material in the central region. Due to higher radiation levels in the forward/backward regions of the detector, these parts of the HCal use copper or tungsten and Liquid Argon as passive and active material respectively. The granularity is not as fine as for the EMCal, since single hadrons in the hadronic parton shower are not reconstructed explicitly (cf. section 4.5).

The energy resolution $\frac{\sigma_E}{E}$ of a sampling calorimeter can generally be described by the noise term of electrons and pileup (N), mainly for low energies, the sampling due to stochastic energy measurement fluctuations (S) for intermediate energies and the energy loss in the sampling material (C), which is scaling with the energy, as denoted by equation (3.7).

$$\frac{\sigma_E}{E} = \frac{N}{E} + \frac{S}{\sqrt{E}} + C \quad (3.7)$$

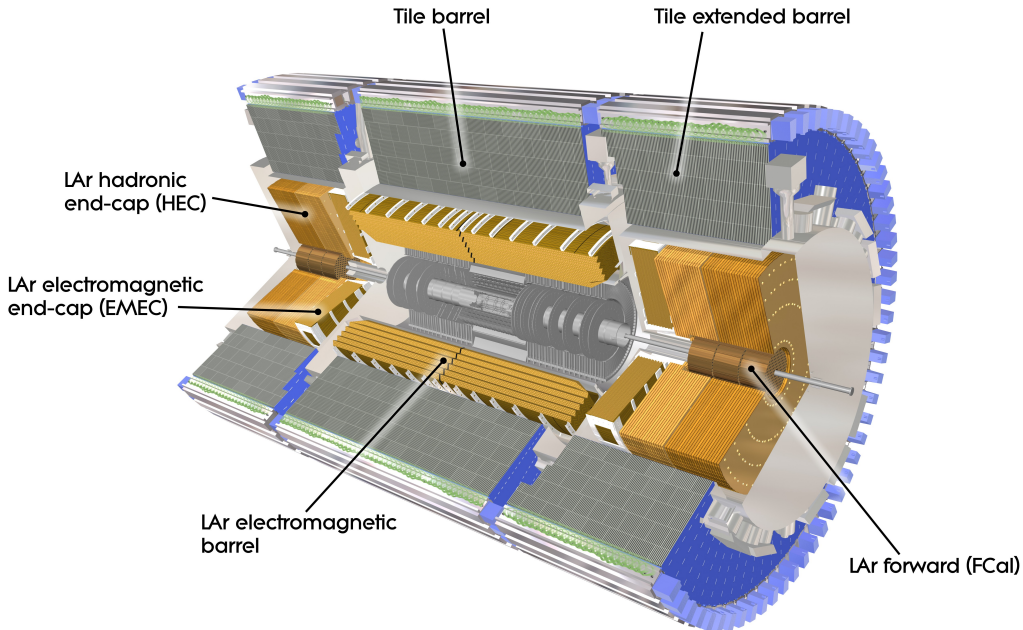


Figure 12: Cut-away view of the ATLAS calorimeter system. It is composed by an electromagnetic barrel with liquid argon (LAr) as sampling medium, a tile barrel and tile extended barrel in the barrel region. The end-cap region consists of a hadronic (HEC) and electromagnetic (EMEC) calorimeter and a forward (FCal) calorimeter in the forward region [51].

3.3.4 Muon system

While other charged particles deposit all or most of their energy in the calorimeters, muons pass these detector components almost without any energy deposition, since they are minimum ionizing particles⁶. Thus the most outer part of the ATLAS detector is a large muon spectrometer identifying muons and reconstructing their momenta measuring their curvature in the toroidal magnetic field induced by the air-core toroid magnets of about 0.5 T. Monitored Drift Tubes (MDT) arranged in three cylindrical shells are used as tracking chambers in the central region, while Cathode Strip Chambers (CSC) are installed for the forward/backward regions. Bunch crossing identification⁷ for fast muon triggering is achieved by installing Resistive Plate Chambers (RPC) in the barrel and Thin Gap Chambers (TGC) in the forward/backward region. A detailed view of the muon system is shown in figure 13. Combination of the information from the muon system and the Inner Detector allows for efficient muon reconstruction (cf. section 4.4).

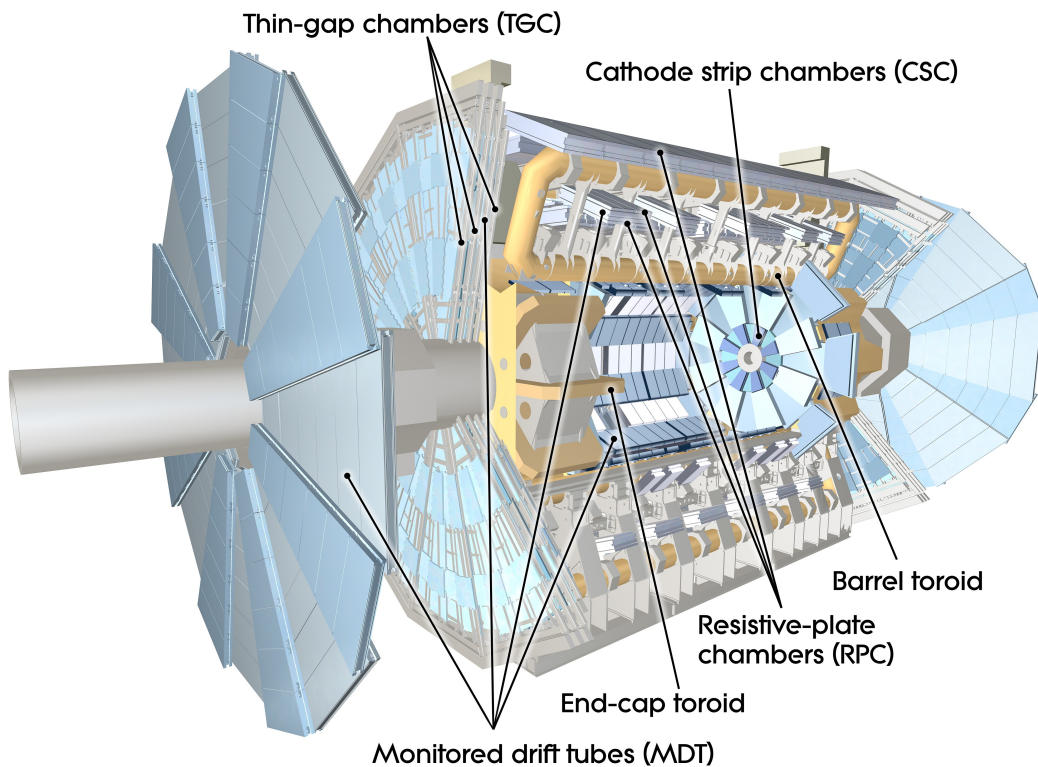


Figure 13: View of the muon spectrometer, showing the different spectrometer components: the barrel and end-cap toroid creating the magnetic field, Monitored Drift Tubes (MDT) and Cathode Strip Chambers (CSC) providing tracking information for the barrel and end-cap region respectively, gaseous Resistive Plate Chambers (RPC) and multi-wire Thin Gap Chambers (TGC) for bunch crossing identification [52].

⁶The energy loss per transition depth of minimum ionizing particles is described by the Bethe-Bloch formula, estimating the energy deposition per flight distance within a given material.

⁷Bunch crossing identification is a technique for differentiation between successive beam interactions.

3.3.5 Luminosity detectors

A very important challenge at colliders like the LHC and detectors like ATLAS is to achieve a precise determination of the instantaneous and the integrated luminosity delivered. The absolute luminosity delivered by the LHC is determined using so-called *Van der Meer* scans [53], shifting the two beams relative to each other step by step and measuring the reaction rate in order to gain information about the beam dimensions $\sigma_{x,y}$. The relative luminosity recorded at the ATLAS detector is determined using dedicated forward detectors, with LUCID and BCM being the most important ones. The *Luminosity Cherenkov Integrating Detector* (LUCID) [54] is a Cherenkov detector with 20 optically reflecting gas tubes installed in the forward region of the ATLAS detector ($5.6 < |\eta| < 5.9$) around the beam pipe, detecting the Cherenkov radiation emitted during the interaction of charged particles in the gas tubes in order to calculate the number of interactions per bunch crossing in the detector. The *ATLAS Beam Conditions Monitor* (BCM) [55] is a radiation-hard diamond sensor located around the beampipe at both sides of the ATLAS detector. Besides measuring the number of collisions in the detector, its main purpose is to monitor the beam quality in real time. If any anomalies in the beam quality occur, the BCM triggers a beam dump to protect the ATLAS detector from radiation damage due to beam losses.

3.3.6 Trigger system

With the design value of one interaction per bunch crossing every 25 ns, the event rate in the ATLAS detector is 40 MHz. Processing about 160 million readout channels at this high rate exceeds current possibilities of data processing and storage. Therefore the event rates are significantly reduced in three steps in real time, using a dedicated trigger system [56] to identify events with interesting but rare processes and rejecting ordinary QCD events. The first level trigger (LVL1) is purely hardware-based, reducing the event rate down to about 75 kHz with a decision time per event of less than $2.5 \mu\text{s}$, performing fast scans of calorimeter and muon system regions for interesting information, providing so-called Regions of Interest (ROIs). Only information for events passing the LVL1 trigger is fully read out from all components of the detector and stored in buffers. The event rate is further reduced down to about 4 kHz by the software-based second level trigger (LVL2) with dedicated selection algorithms processing the ROIs provided by the LVL1 trigger, already with a decision time of about 40 ms due to the reduced event rate. The last trigger stage is the software-based event filter (EF), which analyzes the full event information with a time window of a few seconds and decreases the event rate to a final 300 Hz, suitable for permanent storage. This trigger chain allows to filter interesting events and also deal with the large number of interactions per bunch crossing, causing overlaying signals in the detector, called pileup. The physical data rate is reduced from initial $\sim 58 \text{ TB/s}$ down to about 450 MB/s. Peak values measured during RUN I in 2012 even exceeded these design values, shown in a full overview of all components, data flow, event rates and decision times of the ATLAS trigger and Data Acquisition (DAQ) system in figure 14 [57].

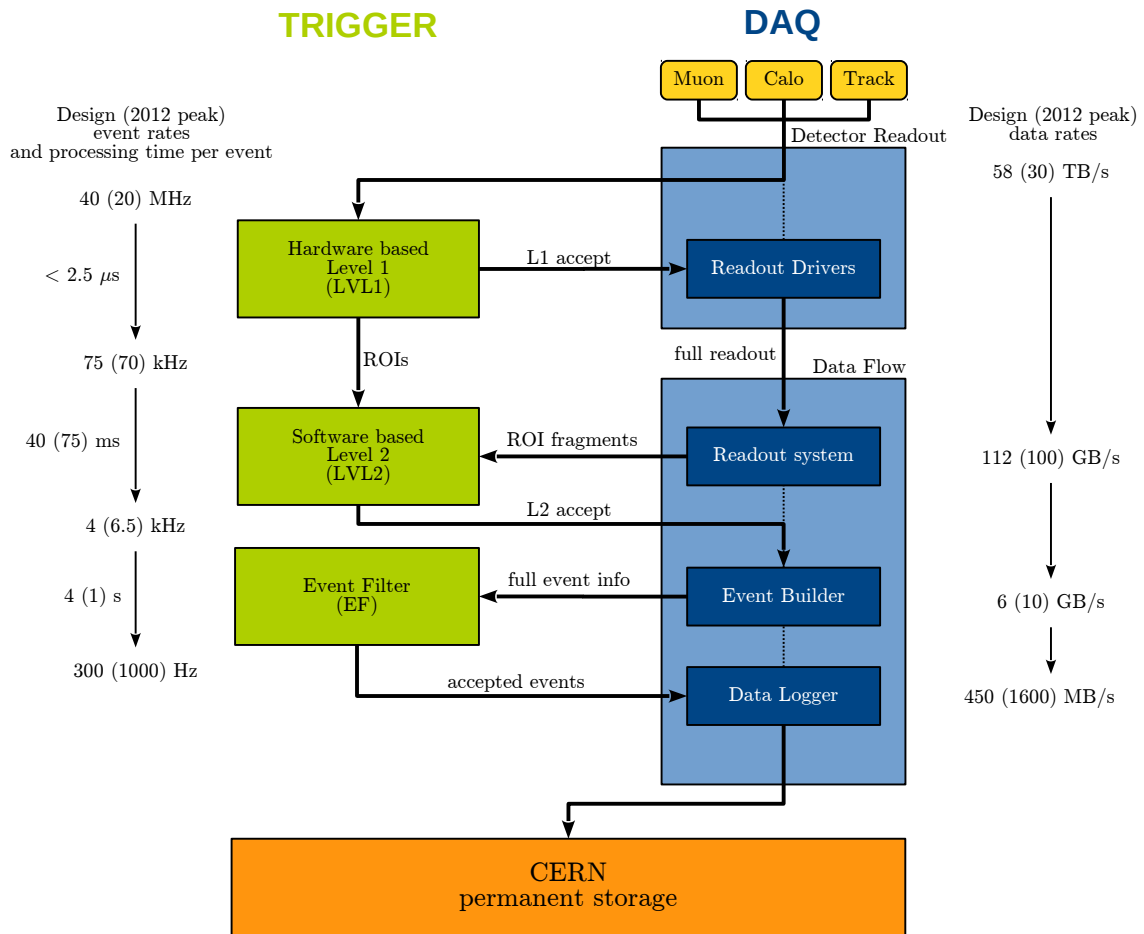


Figure 14: The ATLAS trigger and Data Acquisition (DAQ) system, reducing the initial event rate of 40 MHz down to about 300 Hz in three steps by the hardware based LVL1 and software based LVL2 triggers and the event filter (EF), and decreasing the data rate from initial 58 TB/s down to about 450 MB/s (simplified version based on [57]).

3.3.7 Data acquisition and computing

If an event passes the trigger system of the ATLAS detector, it is recorded by the Data Acquisition (DAQ) system and fully reconstructed at a computer cluster at CERN. This cluster is the first level of the ATLAS computing hierarchy [58] forming the worldwide LHC Computing Grid (LCG) [59]. Starting from CERN (Tier-0), the data is distributed to a small number of large computing centers (Tier-1), serving smaller centers (Tier-2). Additional local centers (Tier-3) at universities only keep a small amount of replica, transferred from other tiers for the end user. This grid provides a decentral layout guaranteeing parallel accessibility of the data for many scientists all around the world.

3.3.8 LHC and ATLAS performance

The first beams have been successfully circulated in the LHC ring in summer 2008. On September 19th 2008, an electrical fault occurred in sector 3-4 of the LHC during powering tests of the main dipole circuit. The resulting electrical arc led to mechanical and electrical damage and displacement of some dipole magnets, release of helium from the magnet cold mass and contamination of the insulation and beam vacuum enclosures [60]. The LHC was shut down for about 14 months for reparation, installation and intense testing of further protection systems [61].

First beams after the forced shutdown were circulated in 2009, starting with collisions in November 2009 with a reduced energy of 450 GeV per beam, which was increased to 3.5 TeV per beam in March 2010. In the original operation schedule, it was foreseen to have a 2 year long shutdown (LS1) starting 2012 after about 2 years of operation to allow for reparation and upgrades. Due to the delay in 2008, it was decided to postpone LS1 to the beginning of 2013 and to increase the beam energy to 4 TeV per beam for the run in 2012, due to the very successful operation of the LHC in 2011 with promising physics outlook. Beginning of 2013, the last beams were circulated after a very successful first data taking period (RUN I, 2010-2012), followed by LS1 in 2013 and 2014 [62].

Beginning of June 2015 [63], the LHC started the second data taking period (RUN II) with an increased energy of 6.5 TeV per beam [64]. A second long shutdown (LS2) is foreseen for 2018 for further upgrades [65] and the upgrade to the *High Luminosity LHC* with an instantaneous luminosity above $10^{35} \text{ cm}^{-2} \text{ s}^{-1}$ in 2021 is prepared [66]. An overview of the run parameters for the different run periods and the design values is shown in table 6.

The ATLAS detector and its single components have already been tested even before start of first collisions using cosmic particles passing the detector. It has delivered an excellent data taking efficiency in RUN I with a good performance of all components. Figure 15(a) shows the luminosity weighted relative fraction of good quality data delivery by the various ATLAS subsystems during LHC fills with stable beams in pp collisions at $\sqrt{s} = 8 \text{ TeV}$, and after switching the tracking detectors on. Runs between April 4th and December 6th 2012,

run	year	\sqrt{s} [TeV]	$\langle\mu\rangle$	N_b	s_b [ns]	$\mathcal{L}_{\text{peak}}$ [$\text{cm}^{-2}\text{s}^{-1}$]	\mathcal{L}_{int} [fb^{-1}]
	2010	7	2.0	368	50	$2.07 \cdot 10^{32}$	0.045
RUN I	2011	7	9.1	1380	50	$3.65 \cdot 10^{33}$	5.08
	2012	8	20.7	1380	50	$7.73 \cdot 10^{33}$	21.3
RUN II	2015	13	13.5	2808	25	$5.00 \cdot 10^{33}$	3.9
Design		14	23	2808	25	$\mathcal{O}(10^{34})$	-

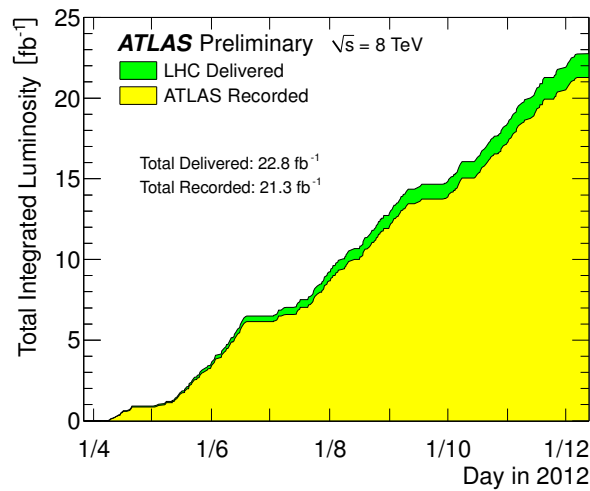
Table 6: The LHC run parameters for RUN I [67, 68] and RUN II [64, 69] and comparison with the design values [41], listing the center of mass energy \sqrt{s} , the average number of interactions per bunch crossing at the ATLAS detector $\langle\mu\rangle$, the number of bunches (proton packets) in the beam N_b , the time spacing between two bunches in the beam s_b , the peak instantaneous luminosity recorded at the ATLAS detector $\mathcal{L}_{\text{peak}}$ and the total integrated luminosity \mathcal{L}_{int} recorded at the ATLAS detector.

corresponding to a recorded integrated luminosity of $\int \mathcal{L} dt = 21.3 \text{ fb}^{-1}$, are accounted. Data taken up to November 10th were reprocessed with improved conditions. When the stable beam flag is raised, the tracking detectors undergo a so-called warm start, which includes a ramp of the high-voltage and, for the Pixel System, turning on the pre-amplifiers. At the beginning of 2012 this applied to the SCT and Pixel Detector, but from June 1st 2012 the configuration was changed to only include the pixel detector in the warm start and account for any longer ramp-up time by the SCT in the DQ efficiency. The inefficiency due to this warm start, as well as the DAQ inefficiency, are not included in the table above, but accounted for in the ATLAS data taking efficiency.

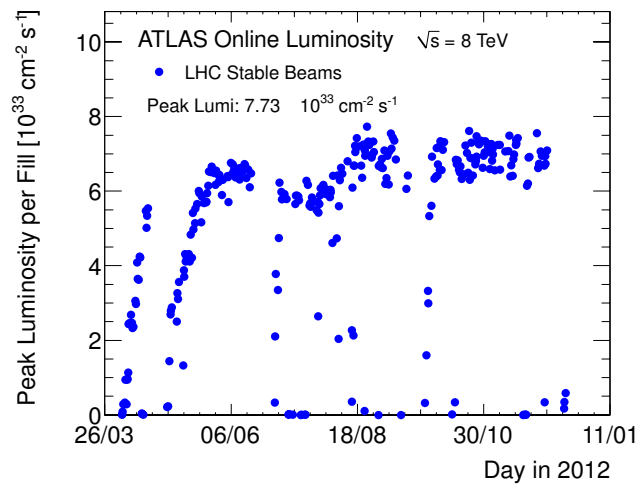
Figure 15(b) shows the cumulative luminosity (green) of $\int \mathcal{L} dt = 22.8 \text{ fb}^{-1}$ versus time delivered by the LHC and $\int \mathcal{L} dt = 21.3 \text{ fb}^{-1}$ recorded by ATLAS (yellow) during stable beams and for pp collisions at $\sqrt{s} = 8 \text{ TeV}$ center of mass energy in 2012. The delivered luminosity accounts for the luminosity delivered from the start of stable beams until the LHC requests ATLAS to put the detector in a safe standby mode to allow a beam dump or beam studies. The reduced recorded compared to the delivered luminosity reflects the DAQ inefficiency, as well as the inefficiency of the so-called warm start. Figure 15(c) shows the maximum instantaneous luminosity versus day delivered to ATLAS while only the peak luminosity during stable beam periods is shown.

ATLAS p-p run: April-December 2012										
Inner Tracker			Calorimeters		Muon Spectrometer				Magnets	
Pixel	SCT	TRT	LAr	Tile	MDT	RPC	CSC	TGC	Solenoid	Toroid
99.9	99.1	99.8	99.1	99.6	99.6	99.8	100.	99.6	99.8	99.5
All good for physics: 95.5%										
Luminosity weighted relative detector uptime and good quality data delivery during 2012 stable beams in pp collisions at $\sqrt{s}=8$ TeV between April 4 th and December 6 th (in %) – corresponding to 21.3 fb ⁻¹ of recorded data.										

(a) Overall ATLAS performance in RUN I



(b) Integrated luminosity



(c) Instantaneous luminosity

Figure 15: Performance of the ATLAS detector in RUN I with the (a) luminosity weighted relative fraction of good quality data delivery by the various ATLAS subsystems during LHC fills with stable beams in pp collisions at $\sqrt{s} = 8$ TeV, and after switching the tracking detectors on [70] and a (b) total integrated luminosity of $\int \mathcal{L} dt = 21.3 \text{ fb}^{-1}$ with a (c) peak instantaneous luminosity of $\mathcal{L}_{\text{peak}} = 7.73 \cdot 10^{33} \text{ cm}^{-2} \text{ s}^{-1}$ [68].

4

Physics object definition and reconstruction

The identification and reconstruction of particles produced in the ATLAS detector during the proton-proton interactions is crucial for a proper reconstruction of the full event. The information provided by the several sub-components of the ATLAS detector (cf. chapter 3) is used to reconstruct the paths and energies of leptons and parton showers in the detector. An overview of the definition and reconstruction of objects relevant for this analysis is shown in the following sections, starting with raw tracks in section 4.1 originating from vertices described in section 4.2. The lepton selection is restricted to electrons in section 4.3 and muons in section 4.4. Parton showers are combined to non-physical but very important objects called jets, discussed in section 4.5. Neutrinos traversing the detector only contribute to the missing transverse energy as discussed in section 4.6.

4.1 Tracks

The trajectories (tracks) of charged particles traversing the ATLAS detector are reconstructed using the information from the Pixel, SCT and TRT detector components, where these particles deposit a small fraction of their total energy (referred to as a hit). Several different algorithms process these hit points to reconstruct outgoing tracks starting from seeds close to the interaction point (inside-out) and extrapolate them to the TRT. Another algorithm starts with seeds in the TRT and reconstructs the tracks backwards towards the inner parts of the detector. Both reconstructed tracks are combined to increase the track reconstruction efficiency [71]. Figure 16 shows the reconstruction efficiency as a function of the transverse momentum p_T and pseudo rapidity η of the tracks for 2012 data at $\sqrt{s} = 8$ TeV.

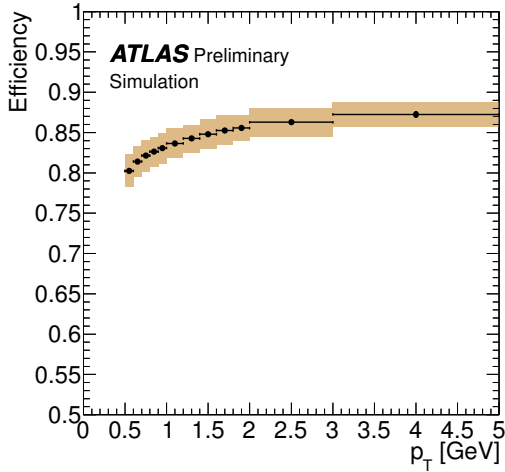
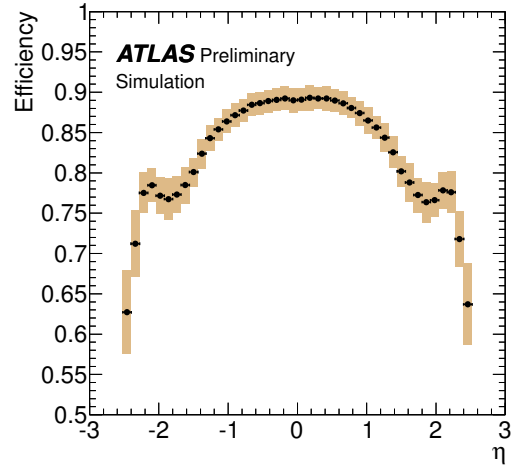

 (a) Reconstruction efficiency vs. p_T

 (b) Reconstruction efficiency vs. η

Figure 16: Inner Detector tracking efficiency defined as number of matched tracks compared to number of generated charged particles versus (a) track p_T and (b) track η for 2012 $\sqrt{s} = 8$ TeV data [72].

4.2 Vertices

A vertex in particle physics describes a point of interaction between at least two particles with two or more tracks originating from this point. The vertex with the largest sum of $|p_{T,i}^2|$ of associated tracks i reconstructed in the Inner Detector (cf. section 4.1) is referred to as the *primary vertex*. Depending on the average number of interactions per event μ , multiple interaction points can be reconstructed in one event, which is called pileup. Figure 17 shows the average number of vertices $\langle n_{\text{vtx}} \rangle$ versus the average number of interactions μ at the ATLAS detector for simulation and 2012 data at $\sqrt{s} = 8$ TeV. The identification of secondary vertices, which are caused by the decay of B-hadrons, and the associated jets is crucial for the technique of b-tagging (cf. section 4.5.6). Details on the expected vertexing performance can be found in [71].

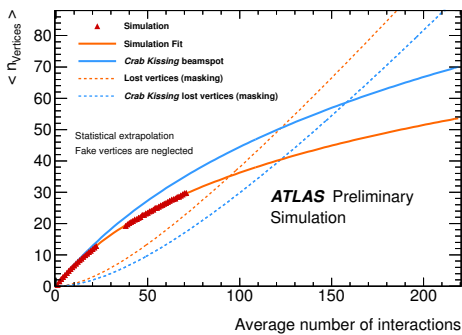
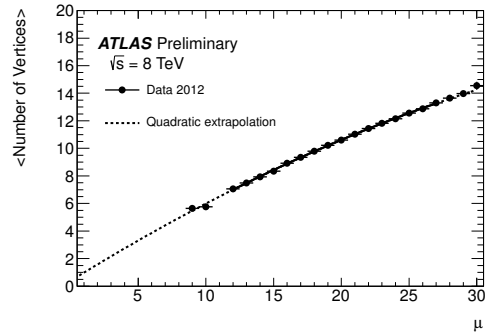

 (a) $\langle n_{\text{vtx}} \rangle$ vs μ , simulation

 (b) $\langle n_{\text{vtx}} \rangle$ vs μ , data

Figure 17: Average number of vertices $\langle n_{\text{vtx}} \rangle$ vs. the average number of interactions μ for (a) simulation and (b) data for 2012 $\sqrt{s} = 8$ TeV data [73].

4.3 Electrons

Electrons traversing the ATLAS detector are identified using the track information provided by the Inner Detector and are reconstructed from energy depositions in the electromagnetic (EM) calorimeter. The reconstruction is limited to the central detector region of $|\eta| < 2.47$. A brief overview over the different steps for electron reconstruction and identification is given in the following, more details can be found in [71, 74].

4.3.1 Electron reconstruction

Charged particles like electrons deposit fractions of their energy in multiple EM calorimeter cells. The $\eta - \phi$ space of the EM calorimeter is divided into towers of energy corresponding to the granularity of the EM calorimeter middle layer combined with the pre-sampler detector. A sliding-window algorithm [75] searches for clusters of towers with $E_T > 2.5$ GeV, which are used as seed-clusters for the electron-track candidate reconstruction. The reconstructed tracks from the Inner Detector are loosely matched to these seed-clusters to form electron-candidates. The energy of these electron candidates is taken from the combined cluster energy from the calorimeter layers as well as the pre-sampler, while the momentum information is taken from the track, if a sufficient amount of hits in the Pixel and SCT components can be found. Figure 18 shows the electron reconstruction efficiency as a function of the transverse energy p_T and pseudo rapidity η of the electrons for 2012 data at $\sqrt{s} = 8$ TeV.

4.3.2 Electron identification

Information about the shape of the electromagnetic shower and quality of reconstructed tracks associated to the electrons provides various discriminants for electron identification. Three different sets corresponding to a different selection efficiency for real electrons and rejection of fake backgrounds are provided, denoted as *loose*, *medium* and *tight*. The discriminating variables used in the definitions are listed in table 7. In order to provide an identification efficiency independent of the p_T and η of the electrons, these cut requirements are varied as a function of p_T and η . The transition region between the barrel and endcap calorimeter (denoted by the region $1.37 < |\eta| < 1.52$) suffers from a significantly reduced efficiency and resolution and is usually excluded in analysis. An updated set of definitions with slightly tighter cuts on the given variables are denoted as "++" definitions (e.g. *medium++*). Figure 19 shows the combined electron identification and reconstruction performance as a function of the transverse energy p_T and pseudo rapidity η of the electrons for 2012 data at $\sqrt{s} = 8$ TeV.

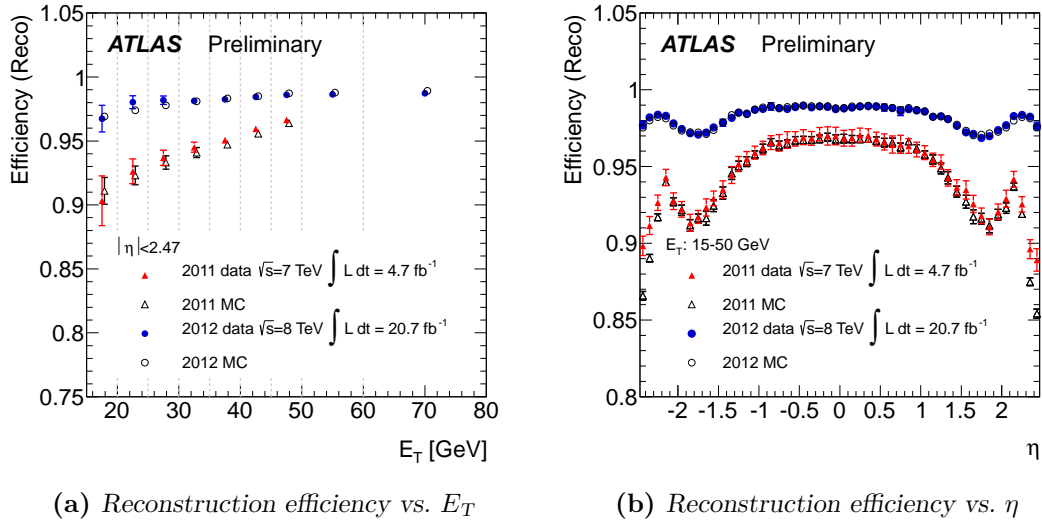


Figure 18: Electron reconstruction efficiency as a function of (a) electron E_T and (b) electron η comparing between 2011 data at $\sqrt{s} = 7$ TeV and 2012 data at $\sqrt{s} = 8$ TeV [74].

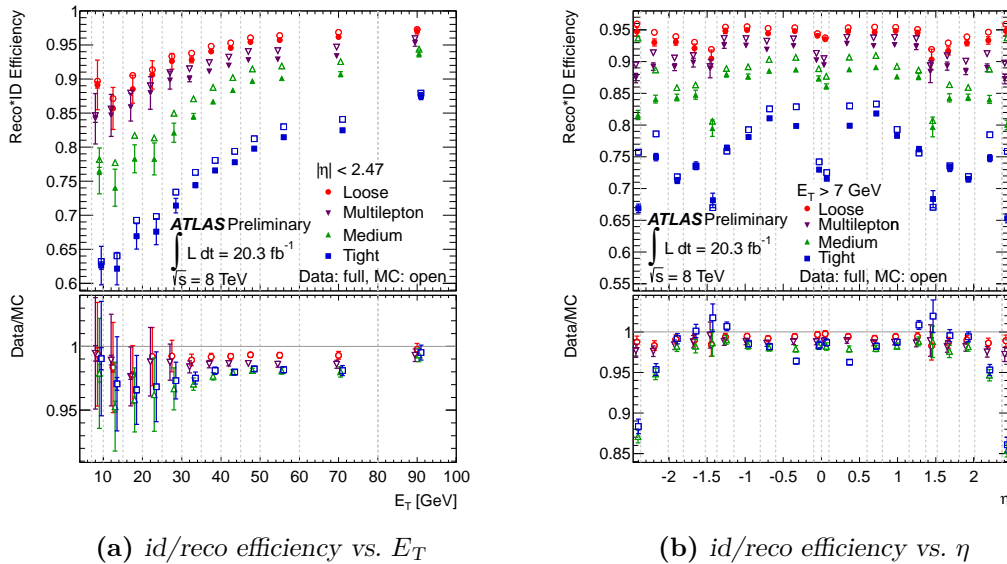


Figure 19: Combined electron identification and reconstruction efficiency as a function of (a) electron E_T and (b) electron η for 2012 data at $\sqrt{s} = 8$ TeV [74].

Name	Description	Variable
Loose selection		
Hadronic leakage	Ratio of E_T in the first layer of the hadronic calorimeter to E_T of the EM cluster (used over the range $ \eta < 0.8$ or $ \eta > 1.37$)	R_{Had1}
	Ratio of E_T in the hadronic calorimeter to E_T of the EM cluster (used over the range $ \eta < 0.8$ or $ \eta > 1.37$)	R_{Had}
Middle layer of EM calorimeter	Lateral shower width, $W_{\eta 2} = \sqrt{(\sum E_i \eta_i^2) / (\sum E_i) - ((\sum E_i \eta_i) / (\sum E_i))^2}$ where E_i is the energy and η_i is the pseudorapidity of cell i and the sum is calculated within a window of 3×5 cells	$W_{\eta 2}$
	Ratio of the energy in 3×7 cells over the energy in 7×7 cells centered at the electron cluster position	R_{η}
Strip layer of EM calorimeter	Shower width, $w_{\text{stot}} = \sqrt{(\sum E_i (i - i_{\text{max}})^2) / (\sum E_i)}$ where i runs over all strips in a window of $\Delta\eta \times \Delta\phi \approx 0.0625 \times 0.2$, corresponding typically to 20 strips in η , and i_{max} is the index of the highest energy strip	w_{stot}
	Ratio of the energy difference between the largest and second largest energy deposits in the cluster over the sum of these energies	E_{ratio}
Track quality	Number of hits in the pixel detector	nPixel
	Number of total hits in the pixel and SCT detectors	nSi
Track-cluster matching	$\Delta\eta$ between the cluster position in the strip layer and the extrapolated track	$\Delta\eta_1$
Medium selection (including loose criteria)		
Back layer of EM calorimeter	Ratio of the energy in the back layer to the total energy in the EM accordion calorimeter	f_3
Track quality	Number of hits in the B-layer (discriminates against photon conversions)	nBlayer
	Transverse impact parameter	d_0
TRT	Total number of hits in the TRT	nTRT
	Ratio of the number of high-threshold hits to the total number of hits in the TRT	F_{HT}
Tight selection (including loose and medium criteria)		
Track-cluster	$\Delta\phi$ between the cluster position in the middle layer and the extrapolated matching track	$\Delta\phi_2$
	Ratio of the cluster energy to the track momentum	E/p
Conversions	Veto electron candidates matched to reconstructed photon conversions	isConv

Table 7: Definition of discriminating variables applied for loose, medium and tight electron identification provided for an electron selection with specific purity [74].

4.4 Muons

The reconstruction of muons is mainly based on the hit and track information from the muon spectrometer in combination with the tracks reconstructed in the Inner Detector, but also hit information from the calorimeters is taken into account. The muon identification is performed with different muon types, depending on the reconstruction criteria and available information in the Inner Detector (ID), Muon Spectrometer (MS) and calorimeters.

- **Standalone** : Muons are reconstructed only from the MS information and extrapolated to the interaction point taking into account the estimated energy loss of the muon in the calorimeters.
- **Combined (CB)** : The reconstruction is performed separately using information from the ID and MS and afterwards combined to one track using STATistical COmbination (STACO). This type of muons is commonly used in analysis.
- **Segment-tagged (ST)** : A track reconstructed from ID information is extrapolated to the MS and has to be associated with at least one local track segment in the MS.
- **Calorimeter-tagged (CaloTag)** : A track reconstructed from ID information is extrapolated to the calorimeter and has to be associated to an energy deposit in the calorimeter compatible with a minimum ionizing particle.

Figure 20 shows the muon reconstruction performance as a function of the transverse momentum p_T and pseudo rapidity η of the muon for 2012 data at $\sqrt{s} = 8$ TeV for the different muon types. More details on muon reconstruction and identification can be found in [71, 76].

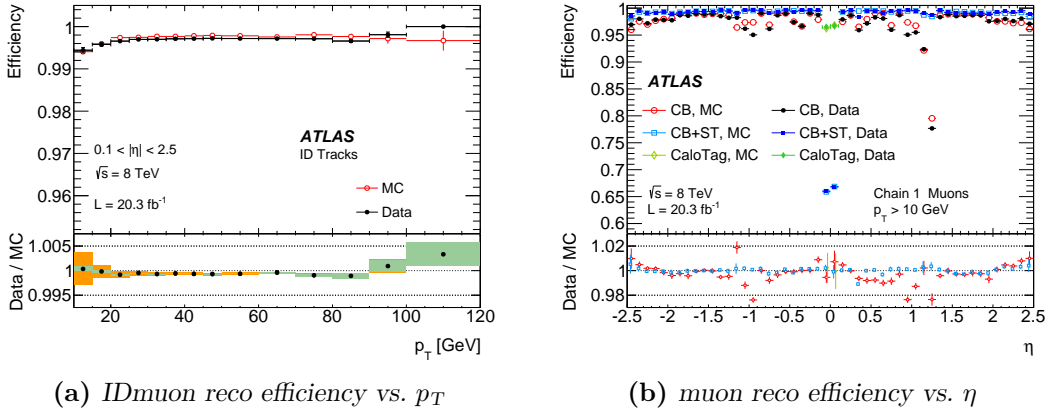


Figure 20: Muon reconstruction efficiency measured in $Z \rightarrow \mu\mu$ events for muons with $p_T > 10$ GeV (a) as a function of p_T for ID muons and (b) as a function of η for different muon reconstruction types for 2012 data at $\sqrt{s} = 8$ TeV [76].

4.5 Jets

A parton shower consists of several secondary particles produced during the process of hadronization of quarks and gluons depositing their energy in the calorimeters. Most of the energy of these showers is deposited in the hadronic calorimeter but is usually also accompanied by hits in the electromagnetic calorimeter and Inner Detector due to the presence of charged particles in the parton shower. These hits form clusters of energy, which are grouped to so-called topoclusters. To avoid dealing with too many distinct energy signatures, these groups are combined to a so-called *jet*, which is usually defined by a given radius, denoting the characteristic conical shape of parton showers. These objects have to be calibrated and can be further analyzed for substructure and identifying the flavor of the initial partons. These procedures will be discussed in detail in the following.

4.5.1 Topoclusters

The energy depositions of traversing particles in calorimeter cells are summed to form clusters, which are locally calibrated to account for energy deposited outside the cluster and in dead material. Beside the sliding window algorithm e.g. used for electron reconstruction (cf. section 4.3), the jet reconstruction uses so-called topoclusters as input. Starting with a seed cell above a large energy threshold t_{seed} , neighboring cells of the same cluster exceeding a given low energy threshold t_{cell} defined by a function of the expected noise are added, resulting in a topocluster with a variable number of associated cells compared to the fixed-size clusters produced by the sliding-window algorithm. A neighboring cell can serve as an additional seed if it exceeds a medium energy threshold t_{neighbor} . The low threshold t_{cell} ensures that tails of showers are not discarded, while the higher thresholds for seeds t_{seed} and neighbors t_{neighbor} effectively suppress both electronics and pileup noise, which designates them also for reconstruction of missing transverse energy (cf. section 4.6).

4.5.2 Jet reconstruction

The reconstruction and i.e. determination of the momentum of jets as a non-physical object is a non-trivial calculation. A proper jet definition should be independent of non-perturbative effects like underlying events due to multiple interactions per bunch crossing or hadronization and should be infrared safe (independent of soft radiations) as well as collinear safe (independent of collinear splitting). Available reconstruction algorithms can basically be divided into cone and cluster algorithms. Cone algorithms are based on the maximization of the energy within a geometric cone, starting with a certain *seed* and combining all jet-candidates within a given radius to this seed to form a jet cone. Cluster algorithms are based on the pair-wise combination of objects into final jets. This thesis focuses on cluster algorithms, which are based on the calculation of the distance d_{ij} between two jet-candidates i and j . This distance is calculated using equation (4.1) with the transverse energy $E_{T,i} = |\vec{p}_T|$ of a cluster i and calculates all possible combinations for d_{ij} .

$$d_{ij} = \min\left(E_{T,i}^{2m}, E_{T,j}^{2m}\right) \frac{(\Delta R_{ij})^2}{R} \quad d_{iB} = E_{T,i}^{2m} \quad (4.1)$$

The variable d_{iB} defines the distance of the jet-candidate i to the beam line and $(\Delta R_{ij})^2$ the radial distance between two jet-candidates in the $(\eta - \phi)$ -plane (cf. equation (3.6)). If the distance of a jet-candidate to the beam is smaller than to any other jet-candidate, it is considered as a final jet and not taken into account in further calculations anymore. Otherwise two jet-candidates with the closest distance d_{ij} are combined to a new jet-candidate. Using the R variable, one can define a radius for the jets, determining the distance at which a jet is resolved from another jet compared to the beamline. A differentiation between three jet reconstruction algorithms is provided by altering the exponent parameter m of the calculation of the minimum transverse energy in equation (4.1).

k_t jet reconstruction algorithm

The k_t algorithm [77, 78] allows for a reverse parton shower with $m = +1$, which leads to a preferred combination of low p_T jet-candidates first. This algorithm allows for detailed studies of jet substructure variables. The specific calculation of the distance d_{ij} for the k_t algorithm results in equation (4.2).

$$d_{ij}^{k_t} = \min\left(E_{T,i}^2, E_{T,j}^2\right) \frac{(\Delta R_{ij})^2}{R} \quad (4.2)$$

anti- k_t reconstruction jet algorithm

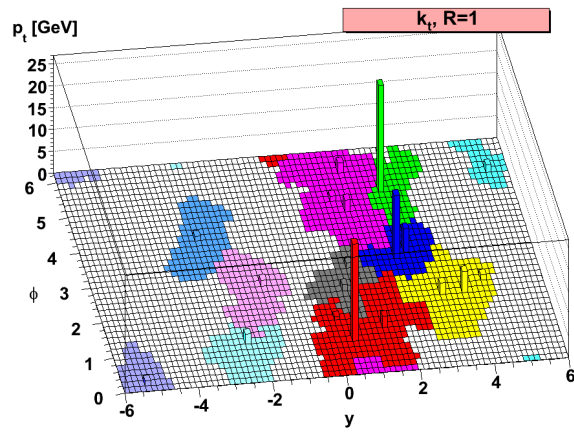
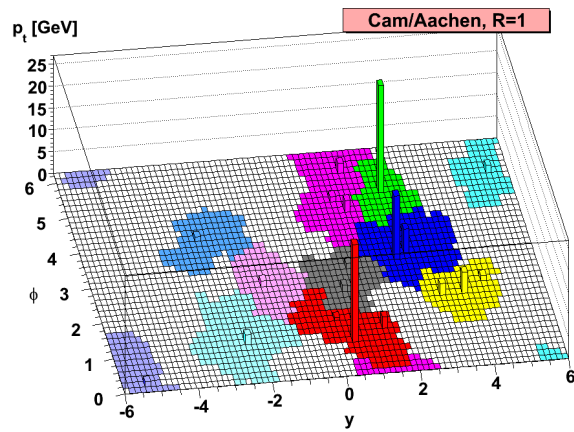
The anti- k_t jet algorithm [79] with $m = -1$ combines high p_T jet-candidates first and clusters lower p_T jet-candidates to it afterwards. This leads to a conical jet shape centered around the highest p_T clusters and allows for a fair share between two overlapping hard jets, while the assignment depends on the relative p_T and their distance. Equation (4.3) shows the specific calculation of the distance d_{ij} for the anti- k_t algorithm.

$$d_{ij}^{\text{anti-}k_t} = \min\left(E_{T,i}^{-2}, E_{T,j}^{-2}\right) \frac{(\Delta R_{ij})^2}{R} \quad (4.3)$$

Cambridge/Aachen jet reconstruction algorithm

The Cambridge/Aachen (C/A) jet algorithm [80, 81] describes a more simple reconstruction algorithm. While the k_t and anti- k_t algorithms consider the transverse energy p_T of the different jet-candidates, the C/A algorithm ignores this information and simply combines objects with the smallest distances to each other, by setting the exponent parameter to $m = 0$, as shown in equation (4.4). This algorithm can improve the single-jet mass resolution, removing small and peripheral subjects.

$$d_{ij}^{\text{C/A}} = \frac{(\Delta R_{ij})^2}{R} \quad (4.4)$$

(a) k_t jet reconstruction algorithm

(b) Cambridge/Aachen jet reconstruction algorithm

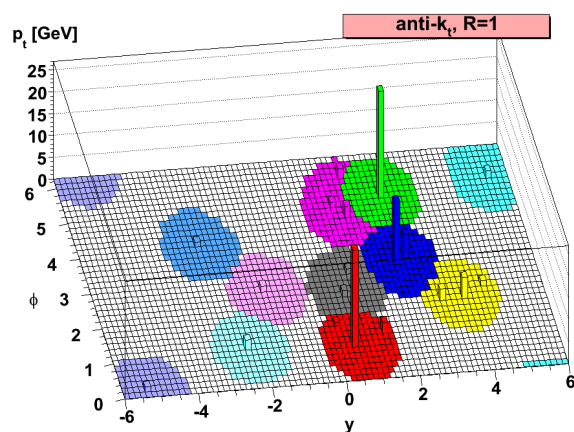
(c) $anti-k_t$ jet reconstruction algorithm

Figure 21: A comparison of the resulting jet-shape of the most common jet reconstruction algorithms used at ATLAS, showing an event reconstructed with a jet cone radius of $R = 1.0$ for the (a) k_t , (b) Cambridge/Aachen and (c) $anti-k_t$ jet reconstruction algorithm in the $(y - \phi)$ -plane [79].

Comparison of the jet algorithms

A comparison of the jet reconstruction for one specific event on parton-level together with many random soft objects, so-called ghosts, projected on the $y-\phi$ plane and using a jet radius parameter of $R = 1.0$, is shown in figure 21, illustrating the active catchment areas of the resulting hard jets for each reconstruction algorithm. The plot for the k_t algorithm in figure 21(a) shows non-conical shapes and that the highest p_T cluster is not always the center of the reconstructed jet. The Cambridge/Aachen algorithm shown in figure 21(b) also denotes non-conical shapes, but the reconstructed jets are build around the highest p_T cluster. For both of these algorithms, the jet shape is defined by the added ghosts. The most intuitive behavior is achieved by the anti- k_t algorithm shown in figure 21(c) with conical shapes and centered high p_T clusters of the reconstructed jets and also energy entries of overlapping jets are properly assigned to the highest p_T jet close-by.

4.5.3 Jet calibration

The reconstructed jets are calibrated to account for additional effects in the detector components, affecting the jet kinematics. A pileup correction derived from MC simulations is applied as a function of the number of the reconstructed primary vertices per event N_{PV} (actual collisions in a given event) and expected average number of interactions μ , which accounts for in-time pileup (multiple interactions within one event) and out-of-time pileup (effects from preceding/subsequent interactions). Also an origin correction is applied, changing the jet axis such that it is pointing back to the primary vertex instead of the nominal center of the ATLAS detector as well as a correction of energy and pseudorapidity derived from comparisons with truth¹ jets from MC simulation. To account for differences in MC and data, the last step is a residual in-situ correction² applied to jets reconstructed from real data events [82].

4.5.4 Jet trimming

Ideally a jet only consists of the particles from a hard scattering event. In reality the incoming states already radiate before scattering, so-called initial state radiation (ISR), or interact multiple times (MI) and also effects from pileup have a degrading impact on the reconstruction of jets. Especially boosted topologies are affected, where large radius jets with $R \geq 1.0$ are used to collect all the collimated decay products from e.g. top quark decays. In order to reduce the contamination from ISR, MI or pileup in such large radius jets, the technique of trimming provides a powerful suppression. Therefore the initial large radius jets are declustered into subjets with a smaller jet radius R_{sub} , rejecting soft contributions with a transverse momentum smaller than a given fraction f_{cut} of the original jet and rebuilding the initial jet from the remaining subjets. This procedure has proven to achieve significant improvement in event reconstruction [83].

¹Truth information is provided in MC samples, documenting the exact identities and decay chains of particles.

²Residual in-situ corrections are based on real data (in-situ), correcting/calibrating the remaining issues (residual) not accounted for by the preceding corrections/calibrations.

4.5.5 Jet vertex fraction

The Jet Vertex Fraction (JVF) variable is an important estimate of the pileup contribution in a reconstructed jet object, i.e. for small radius jets. The jet reconstruction algorithms do not apply any pileup suppression techniques, while the JVF measures the probability of a jet to originate from a specific primary vertex, which provides a separation power between jets from hard scatter and those originating from additional interactions. Figure 22 shows the discrimination power of the JVF variable and the jet selection efficiency as a function of the jet p_T for different JVF cut values for 2012 data at $\sqrt{s} = 8$ TeV. Further information can be found in [84].

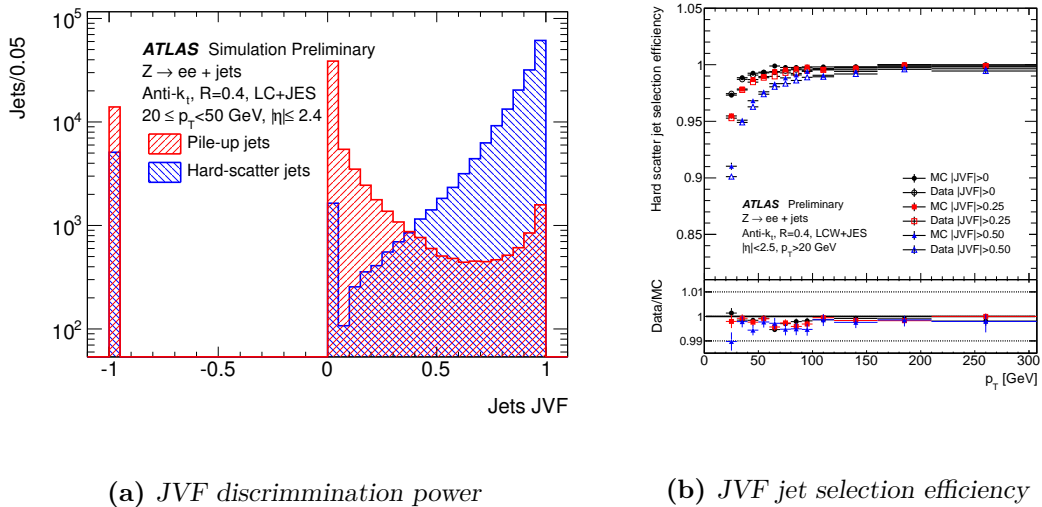


Figure 22: Jet Vertex Fraction (JVF) variable (a) discrimination power and (b) jet selection efficiency as function of the jet p_T to differentiate between hard scatter jets from the main interaction point and pileup jets from other interactions [84].

4.5.6 B-tagging

B-quarks originating from the decay of particles produced during the proton-proton collision (e.g. top quarks) hadronize and form B-hadrons. These composite particles have a lifetime of the order of a few picoseconds, allowing them to traverse a distance of the order of a few millimeters before decaying into other particles. This decay results in a secondary vertex, which can be clearly separated from the primary vertex of the hard proton-proton interaction, allowing for an efficient identification of jets originating from b-quarks. The most common algorithm for b-tagging is the *MV1* tagger, which represents a neural network based on the discriminating variables of impact parameter (*IP3D*), secondary vertex (*SV1*) and more refined (*JetFitter*) b-tagging algorithms. The resulting *MV1* tag weight is interpreted as probability for a jet to originate from a b-quark. Using the distribution of tag weights, one can choose a working point for the analysis with a specific efficiency and background rejection. Figure 23 shows the b-tagging performance as a function of the transverse jet momentum p_T and the light-jet rejection vs. b-jet efficiency for 2012 data at $\sqrt{s} = 8$ TeV [85].

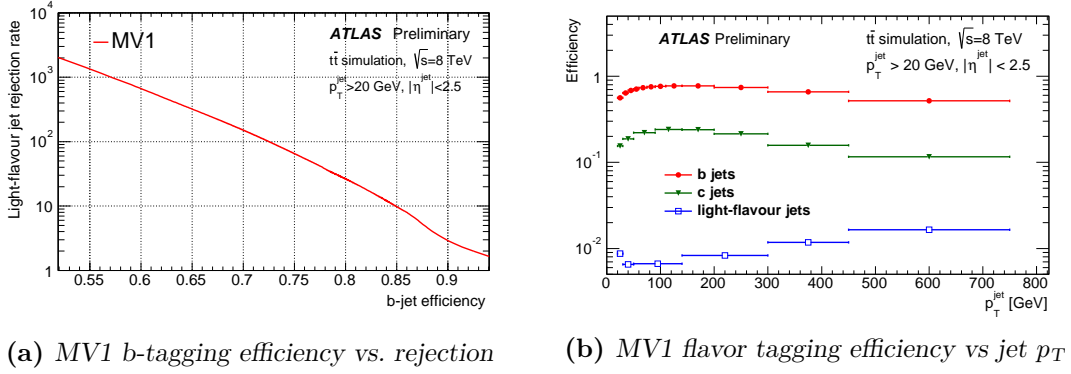


Figure 23: Tagging efficiencies for the MV1 tagger (a) for b-jet vs light jet rejection and (b) for b-, c- and light-flavor jets vs. jet p_T [85].

4.5.7 Top tagging

The identification of jets containing all decay products of a hadronic top decay is a big challenge especially in boosted topologies. While the decay products, i.e. jets, are usually well separated in resolved topologies and can be reconstructed independently, they are strongly collimated in boosted topologies resulting in overlapping, indistinguishable objects. Therefore these hadronic top decays in boosted topologies are usually reconstructed with large radius jets. Large radius jets originating from top decays have a higher mass and p_T compared to jets from QCD processes, taken as a first simple requirement for a tagging decision for top jets. For a more significant identification of these objects as top jets, one can analyze their substructure. The most common algorithms for top tagging analyze jets clustered with the C/A or k_t jet reconstruction algorithm, since these algorithms combine hardest objects last and allow for a proper declustering, a reversed clustering procedure (cf. section 4.5.2). A basic substructure information is provided by the splitting distance $\sqrt{d_{ij}}$ between two jets i and j , i.e. for the first two subjets $\sqrt{d_{12}}$ obtained from the first declustering step of the large jet, which is a measure for the momentum fraction of the two hardest subjets within the large jet (i.e. for the k_t declustering compare with equation (4.2)). These rather simple cuts are e.g. used by the ATLAS tagger also used in the analysis in this thesis. Another variable is the so-called N -subjettiness τ_N and ratios $\tau_{ij} = \frac{\tau_i}{\tau_j}$, which describes how well jets can be described as containing N or fewer subjets [86].

$$\tau_N = \frac{1}{d_0} \sum_k p_{T,k} \cdot \min(\Delta R_{1k}, \Delta R_{2k}, \dots, \Delta R_{Nk}) \quad d_0 = \sum_k p_{T,k} \cdot R \quad (4.5)$$

A more detailed analysis of jet substructure is performed e.g. by the HEPTOPTAGGER [87, 88], which analyzes triplets of subjets (due to the three decay products $t \rightarrow Wb \rightarrow q\bar{q}'b$). Masses of the subjet combinations m_{ij} and m_{ijk} allow for a more precise identification of the subjet components and constraints, since for e.g. the mass of a combination of two subjets should add up to the mass of a W-boson. A more detailed discussion of the top tagging technique with the HEPTOPTAGGER is given in context of a top tagging study in the lepton+jets $t\bar{t}$ environment presented in chapter 11.

4.6 Missing transverse energy

Particles obeying only the weak interaction, like neutrinos, traverse the ATLAS detector while depositing hardly any energy in the detector material. While these particles can not be detected directly (i.e. their energy can not be measured from explicit energy depositions in the detector), they can be analyzed indirectly. The vectorial sum of the transverse momenta of all decay products of the proton-proton interaction in the center of mass system of the pp pair must cancel out, while these weakly interacting particles leaving the detector cause an imbalance in the momentum sum in the transverse plane, referred to as missing transverse energy E_T^{miss} . It is estimated calculating the vector sum of all reconstructed particles detected in the ATLAS detector and also taking non assigned calorimeter cells and proper energy scales into account. An important challenge is the treatment of pileup, which is accounted for by applying a soft term vertex fraction (STVF), including contributions from low $p_T < 20$ GeV jets and tracks not associated to physical objects, similar to the technique applied for the jet vertex fraction (JVF) (cf. section 4.5.5). Figure 24 shows the E_x^{miss} and E_y^{miss} resolution vs. the scalar sum of transverse energy in the event with and without pileup suppression via STVF for 2012 data at $\sqrt{s} = 8$ TeV. Further information can be found in [89].

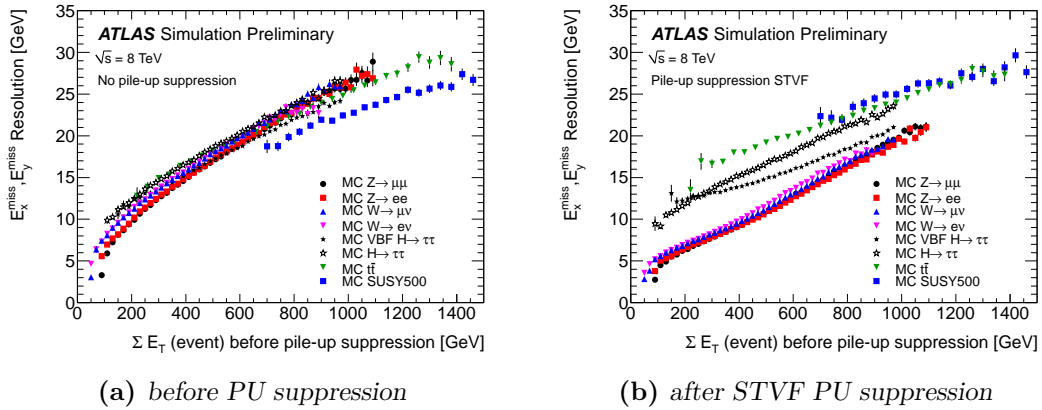


Figure 24: E_x^{miss} and E_y^{miss} resolution comparing all MC samples (a) before pileup suppression and (b) with pileup suppression via STVF [89].

The information of missing transverse energy is not sufficient for the full reconstruction of a neutrino leaving the detector, since the longitudinal component is missing. This issue is usually handled by a constraint on the combined system of the lepton and reconstructed neutrino from the W-decay, as discussed in section 6.3.1 for the analysis in this thesis.

5

Data and Monte Carlo samples

The strategy of the analysis presented in this thesis is to compare spectra produced from real recorded data with Standard Model predictions from simulations. Therefore both data types are processed through the same reconstruction algorithms for the ATLAS detector. Signal and background processes producing jets and prompt leptons are simulated using Monte Carlo (MC) generators. These simulations are processed through the full ATLAS detector simulation [90], based on GEANT4 [91] or a fast simulation using parametrized showers in the calorimeters [92]. Additional simulated proton-proton collisions generated using Pythia v8.1 [93] are overlaid to simulate the effects of additional collisions from the same and nearby bunch crossings. All simulated events have to fulfill the same quality requirements and the full analysis chain and reconstruction as for data, while the simulated trigger and selection efficiency is corrected to match the performance observed in data.

Details on the used dataset are presented in section 5.1, while Monte Carlo samples for background estimation are discussed in section 5.2. Simulation of benchmark signal models are described in section 5.3. A list of the exact dataset names of the considered Monte Carlo samples can be found in the appendix in A.2.

5.1 Dataset

The analysis is based on the full dataset recorded in RUN I during the 2012 data taking period of proton-proton collisions at a center of mass energy of $\sqrt{s} = 8$ TeV with the ATLAS experiment, providing a total integrated luminosity of $\int \mathcal{L} dt = 21.3 \text{ fb}^{-1}$ with a peak instantaneous luminosity of $\mathcal{L}_{\text{peak}} = 7.73 \cdot 10^{33} \text{ cm}^{-2} \text{ s}^{-1}$ and an average of $\langle \mu \rangle = 20.7$ interactions per bunch crossing (cf. section 3.3.8). After applying data-quality requirements

for good running conditions for both LHC and ATLAS machines in all parts, a *Good for Physics* dataset is selected with remaining $\int \mathcal{L} dt = 20.3 \text{ fb}^{-1}$ considered in the analysis. The evolution of the amount of data in RUN I during the 2012 data taking period delivered by LHC, recorded by ATLAS and tagged as Good for Physics is shown in figure 25.

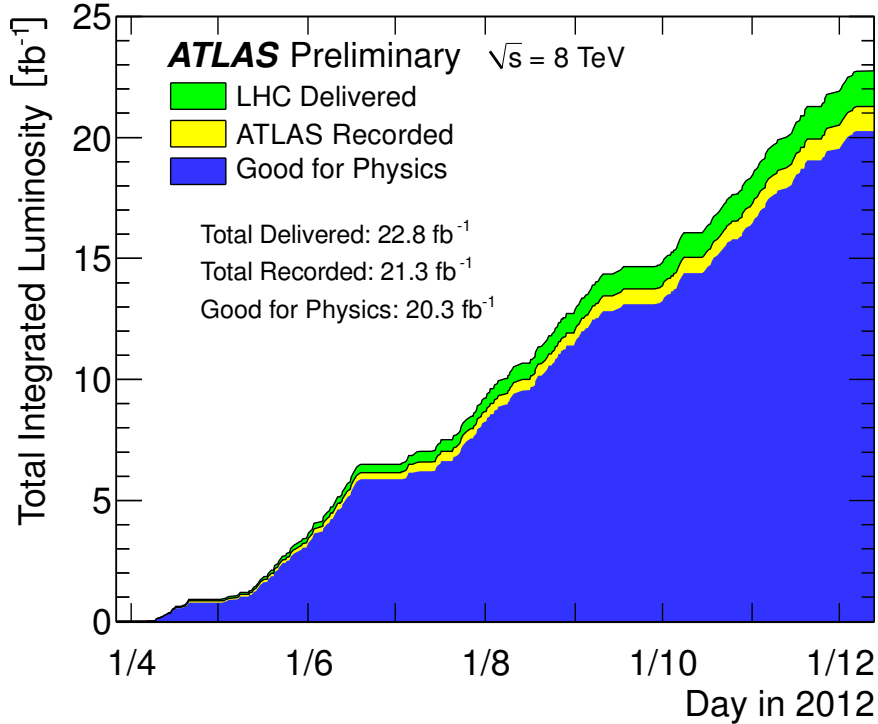


Figure 25: *Good for physics 2012 ATLAS dataset integrated luminosity of $\int \mathcal{L} dt = 20.3 \text{ fb}^{-1}$ after applying good run conditions for all LHC and ATLAS machine components [68].*

Events are selected with a single lepton trigger, i.e. `EF_e24vhi_medium1 OR EF_e60_medium` for the *Egamma stream* and `EF_mu24i_tight OR EF_mu36_tight` for the *Muon stream*. These are EventFilter (EF) triggers (triggered at level 1 and confirmed at the high level trigger) for electrons (e) or muons (mu) with a given cut on the lepton p_T , applying isolation (i) and specific identification criteria (medium, tight, cf. section 4.3.2 for electrons and section 4.4 for muons). The `EF_e24vhi_medium` trigger additionally uses a varied η threshold (v) as coarse dead material correction and a hadronic core isolation (h). These triggers are available for the full dataset and all run periods.

A fraction of the recorded data during the 2012 data taking was not reconstructed directly, but stored for later reconstruction, since the computing bottleneck for dealing with the huge amounts of data is not storage, but processing CPU power. This so-called *Delayed stream* uses a low p_T large radius jet trigger `EF_j220_a10tcem_delayed` (central $|\eta| < 3.2$ (j), $p_T > 220$ GeV, full-scan¹ anti- k_t $R = 1.0$ (a10) reconstructed jet, reconstructed from topoclusters (tc) calibrated on electromagnetic (em) scale). The trigger is emulated from the level 1 `L1_J75`

¹The reconstruction can either use only specific regions of interest (ROI) or a full-scan of the calorimeter information.

(central $|\eta| < 3.2$ (j), $p_T > 75$ GeV) jet trigger and the level 2 L2_j165_c4cchad (central $|\eta| < 3.2$ (j), $p_T > 75$ GeV, ROI with $R = 0.4$ (c4) reconstructed jet using calorimeter cells (cc) and calibrated on EM+JES (had) scale) jet trigger.

While the benefit of adding events from the Delayed stream for the e +jets channel was found to be marginal and therefore is not taken into account in this analysis, the Delayed stream can be used to recover an intrinsic muon trigger inefficiency due to a lack of geometric coverage of the muon chambers. Figure 26 shows the efficiency of the muon triggers in the central and forward region, stating a plateau efficiency of about 80%. The acceptance of the μ +jets channel is significantly increased by the addition of the Delayed stream, e.g. by about 20-25% for a Z' resonance at 3000 GeV in the context of the analysis in this thesis as denoted in figure 27, comparing the selection efficiency with and without addition of the Delayed stream. To avoid double counting with the muon selection, only events failing the muon triggers mentioned before are considered. Since recording of events for the Delayed stream was only activated starting in period B, the Delayed stream corresponds to a reduced total integrated luminosity of $\int \mathcal{L} dt = 17.4 \text{ fb}^{-1}$ and its simulation is normalized accordingly.

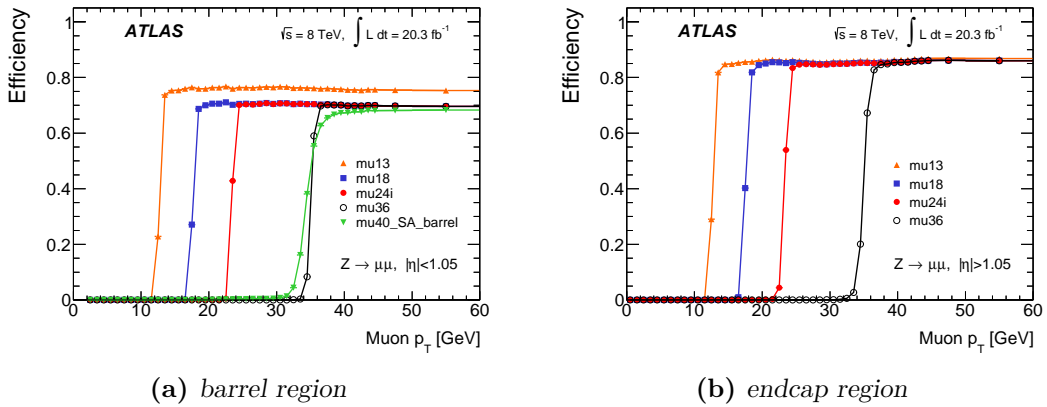


Figure 26: Muon trigger efficiency for the mu24i, mu36 and other triggers for the (a) barrel region and (b) endcap region [94].

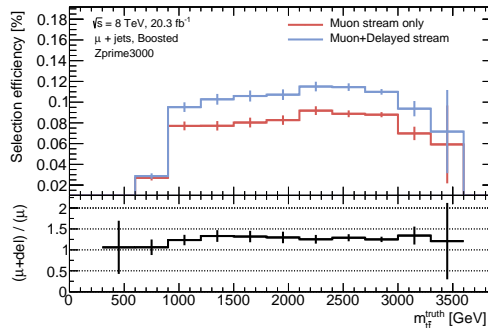


Figure 27: Selection efficiency vs. the true invariant $t\bar{t}$ mass $m_{t\bar{t}}^{\text{truth}}$ for a Z' resonance with a mass of 3000 GeV with and without addition of the Delayed stream in the μ +jets channel in a selection for a boosted topology. The bottom panel shows the direct comparison between the two cases in a ratio plot.

5.2 Simulated background samples

Since the characteristic signature of the decay of a $t\bar{t}$ pair via the lepton+jets channel can also result from other background processes, these contributions have to be estimated for the analysis for a reasonable comparison to the recorded data. This section describes the Monte Carlo simulation samples used for background estimation. All standard background MC samples are generated using the CTEQ6L1 NLO PDF set. Specific samples for estimation of systematic uncertainties use different PDF sets, as stated in detail in section 8.3. Details on the generators and tunes can be found in [8].

5.2.1 $t\bar{t}$

The dominant but also irreducible background for this analysis are Standard Model $t\bar{t}$ processes. These processes are simulated with the POWHEG+PYTHIA generators. The POWHEG event generation is tuned with the `hdamp` parameter², set to a reference top mass of 172.5 GeV in order to achieve good agreement with the differential cross section measurements. To achieve better statistic in regions of large invariant $t\bar{t}$ masses $m_{t\bar{t}}$, specific mass slices are used for masses above $m_{t\bar{t}} > 1$ TeV and combined with the standard sample, while ensuring orthogonality. Events from all $t\bar{t}$ samples are re-weighted to account for interference with diagrams of electroweak processes (more details in [95]). The Feynman diagram for this process decaying in the lepton+jets channel is given in figure 4.

Alternative $t\bar{t}$ samples are used to evaluate systematic uncertainties, such as using different event generators, variation of the reference top mass or modified tunes for initial and final state radiation (cf. section 8.3.1). Another set of samples using the alternative CT10NLO PDF set is used for estimation of the PDF uncertainty (cf. section 8.3.5).

5.2.2 V+Jets

The major background in this analysis originates from single W -boson production in association with jets (W +Jets). These processes are simulated with the ALPGEN+PYTHIA generators including samples with exactly 0-4 (exclusive) and 5 or more (inclusive) additional³ light jets (from u, d, s quarks) for $W \rightarrow \ell + \nu_\ell$ processes and also from 0-2 exclusive and 3 inclusive heavy quarks (single c , and $c\bar{c}$ or $b\bar{b}$ pairs), taking into account the masses of these heavy quarks. Special samples filtered for a truth-level ungroomed⁴ jet with $p_T > 250$ GeV are added orthogonally for improved statistic in boosted topologies. The normalization and heavy flavor composition of the W +Jets background is corrected for inaccuracies using a data-driven procedure, as described in more detail in chapter 7.

Standard Model processes with single Z -boson production in association with jets (Z +Jets) are simulated with the ALPGEN+PYTHIA generators using a similar configuration as for

²The `hdamp` variable is a control parameter for high p_T radiation which was set to infinity in earlier samples, leading to a downward trend in data/MC comparisons.

³A general reference to W +Jets in the following also includes samples with no additional jet.

⁴An ungroomed jet has no pileup correction (filtering, pruning, trimming) applied.

the W +Jets samples with different jet multiplicities for soft ($Z \rightarrow \ell\ell$ +light jets) and hard ($Z \rightarrow \ell\ell$ +hard jets, i.e. $c\bar{c}$ or $b\bar{b}$ pairs) processes. These processes contribute to a single lepton signature if e.g. a produced lepton is rejected or misidentified, or, in the case of a hadronically decaying Z -boson, if a lepton from another process or shower is falsely selected. Exemplary Feynman diagrams for W +Jets and Z +Jets processes are given in figure 28.

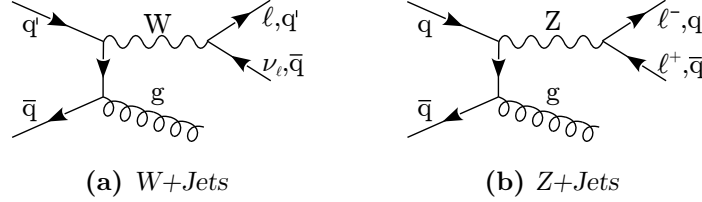


Figure 28: Feynman diagrams for V +Jets background processes for (a) W +Jets and (b) Z +Jets production (only main production channels, charge conjugations can be applied). Additional jets may result from initial and final state radiation.

5.2.3 $t\bar{t}+V$

Production of a $t\bar{t}$ pair in association with a single vector boson is simulated using the MADGRAPH+PYTHIA generators for W - or Z -bosons and also with additional jet production. Exemplary Feynman diagrams for $t\bar{t}+V$ processes are given in figure 29.

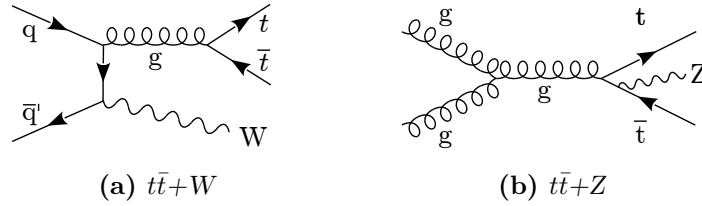


Figure 29: Feynman diagrams for $t\bar{t}+V$ background processes, differentiating between (a) $t\bar{t}+W$ and (b) $t\bar{t}+Z$ production (only main production channels, charge conjugations can be applied). Additional jets may result from initial and final state radiation.

5.2.4 Diboson

The SHERPA generator is used for estimation of the diboson background for production of two W - or Z -bosons and also events with mixed vector boson identities in different decay modes are considered. Exemplary Feynman diagrams for diboson processes are given in figure 30.

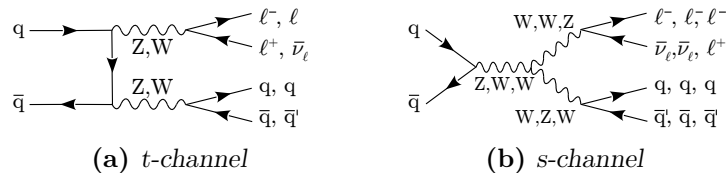


Figure 30: Feynman diagrams for diboson background processes, differentiating between the (a) t - and (b) s -channel (only main production channels, charge conjugations can be applied).

5.2.5 Single top

Also the production of single top quarks is considered using the POWHEG+PYTHIA generators in the s- and Wt-channel as well as in the t-channel specifically generated for top and anti-top identities. Alternative single top samples are used for estimation of the PDF uncertainty using the alternative CT10NLO PDF set (cf. section 8.3.5). Exemplary Feynman diagrams for single top processes are given in figure 31.

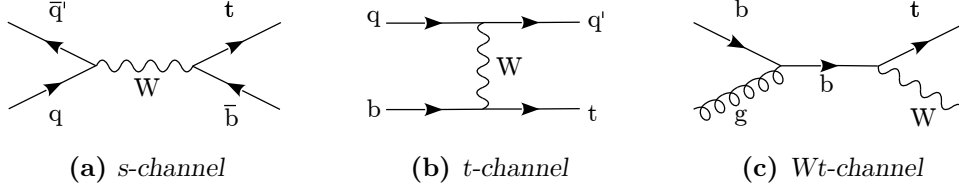


Figure 31: Feynman diagrams for single top background processes, differentiating between the (a) s-, (c) t- and (b) Wt-channel (only main production channels, charge conjugations can be applied).

5.2.6 Multijet (Data-driven)

Background from sources of non-prompt leptons, which is mainly due to QCD multijet production, suffers from large systematic and statistical uncertainties for simulation and hence is estimated from data. Since the lepton selection used in the analysis is too tight for a statistically significant study of this background, a looser quality requirement is applied as lepton selection to investigate the phase space regions dominated by QCD multijet events. All other event topology and kinematic criteria are kept identically to the signal region selection, in order to avoid additional systematic uncertainties.

The background is estimated using the so-called *matrix method*, which disentangles the mixture of prompt leptons originating from W/Z bosons and the multijet background with non-prompt leptons. Two variables are defined, reflecting the probability that a loose lepton from each of these two categories also passes the tighter signal selection, the efficiency ε for prompt leptons and the false-identification rate f for non-prompt leptons. These parameters are derived from data.

The total number of events with loose leptons passing the full signal selection, except for using the loose lepton definition, is defined as

$$N_{\text{loose}} = N_{\text{prompt}} + N_{\text{QCD}} \quad (5.1)$$

While the fraction of events with leptons also passing the tight selection can be written as

$$N_{\text{tight}} = \varepsilon \cdot N_{\text{prompt}} + f \cdot N_{\text{QCD}} \quad (5.2)$$

given the efficiency ε and the false-identification rate f as defined above. Defining similarly

anti-tight events with loose leptons failing the tight selection $N_{\text{anti-tight}}$ as

$$N_{\text{anti-tight}} = (1 - \varepsilon) \cdot N_{\text{prompt}} + (1 - f) \cdot N_{\text{QCD}} \quad (5.3)$$

one can estimate the QCD contribution in the signal region as

$$f \cdot N_{\text{QCD}} = \frac{(\varepsilon - 1) \cdot f}{(\varepsilon - f)} N_{\text{tight}} + \frac{\varepsilon \cdot f}{(\varepsilon - f)} N_{\text{anti-tight}} \quad (5.4)$$

Beside this overall QCD yield estimation, also kinematic distributions can be provided for the multijet background, calculating a weight for each event with the described pre-selection based on equation (5.4) with $(N_{\text{tight}}, N_{\text{anti-tight}}) = (0, 1)$ or $(1, 0)$. For the calculation of the W+Jets scale factors (cf. chapter 7), this procedure is also performed for pre-tagged (no b-tagging applied) events (cf. section 6.2).

5.3 Simulated signal samples

Monte-Carlo simulations for specific Beyond the Standard Model theories (cf. section 2.6) are generated to test for compensations of potential deficits/excesses in the comparison of data with the predictions from background processes.

5.3.1 Leptophobic topcolor Z'

A narrow leptophobic topcolor Z' resonance is simulated with default PYTHIA8 SSM Z' generator settings and the MSTW2008LO PDF set, corresponding to a width of about $\sim 3\%$ for masses from 400 up to 3000 GeV. The cross sections are calculated at leading order (LO) in QCD using QTEQ6L1 PDFs and multiplied by a k-factor⁵ of 1.3 to account for LO \rightarrow NLO corrections. The predicted cross sections for specific masses for a Z' resonance are given in table 8, ranging from 45.66 pb^{-1} for a mass of 400 GeV down to 1.47 nb^{-1} for 3000 GeV. The branching ratio to $t\bar{t}$ for the given model for a width of 1.2% is $\text{BR}(Z' \rightarrow t\bar{t}) = 33\%$ for resonance masses above 1 TeV [95].

5.3.2 Randall-Sundrum Kaluza-Klein graviton G_{KK}

A narrow RS Kaluza-Klein graviton G_{KK} resonance is simulated with MADGRAPH5 event generator and interfaced with Pythia8 using the CTEQ6L1 PDF set. The width for this resonance varies from about 2.8% for a mass of 400 GeV up to 6.2% for a mass of 2500 GeV. No LO \rightarrow NLO correction is applied. The predicted cross sections for specific masses for a RS Kaluza-Klein graviton G_{KK} resonance are given in table 9, ranging from 1.943 pb^{-1} for a mass of 400 GeV down to $23.45 \mu\text{b}^{-1}$ for 2500 GeV. The branching ratio to $t\bar{t}$ for the given model is $\text{BR}(G_{KK} \rightarrow t\bar{t}) = 65\%$ up to 68% for resonance masses of 1 to 2.5 TeV [95].

⁵If only leading order contributions are considered for a given sample, the impact of higher orders can be estimated without performing a specific calculation, but providing a global so-called *k-factor*, which is used to scale the contribution of the given sample accordingly.

$m_{Z'}$ [GeV]	$\Gamma_{Z'}$ [%]	$\sigma_{\text{LO}}(Z') \times \text{BR} \times 1.3$ [pb]	DS ID
400	2.86	45.66	110899
500	2.94	24.63	110901
750	3.05	5.65	110902
1000	3.10	1.66	110903
1250	3.12	0.566	110904
1500	3.14	0.213	110905
1750	3.15	0.0853	110906
2000	3.16	0.0357	110907
2500	3.17	0.00687	110909
3000	3.17	0.00147	110910

Table 8: Mass points used for Monte Carlo samples for resonant Z' signal processes $Z' \rightarrow t\bar{t}$, listing the cross section times branching ratio $\sigma \times \text{BR}$ (taken from the TC2 model [96]) corrected with a k-factor of 1.3 and resonance width Γ (chosen as in the $t\bar{t}$ Pythia8 SSM Z' production) for a given resonance mass and the unique dataset ID [95].

$m_{G_{KK}}$ [GeV]	$\Gamma_{G_{KK}}$ [%]	$\sigma \times \text{BR}$ [pb]	DS ID
400	2.810	1.943	182865
500	3.674	1.342	182866
600	4.337	0.622	182867
700	4.799	0.2859	182868
800	5.125	0.1368	182869
900	5.361	0.06838	182870
1000	5.535	0.03569	182871
1200	5.769	0.01077	182872
1400	5.915	0.003578	182873
1600	6.011	0.001288	182874
1800	6.078	0.0004936	182874
2000	6.125	0.0001978	182876
2500	6.199	0.00002345	182877

Table 9: Mass points used for Monte Carlo samples for resonant RS Kaluza-Klein graviton $G_{KK} \rightarrow t\bar{t}$ processes, listing the cross section times branching ratio $\sigma \times \text{BR}$ and resonance width Γ for given resonance masses and the dataset ID [95].

5.3.3 Randall-Sundrum Kaluza-Klein gluon g_{KK}

A broad RS Kaluza-Klein gluon g_{KK} resonance is simulated with MADGRAPH5 event generator and interfaced with Pythia8 using the MSTW2008LO PDF set. Denoting the usually large width of these resonances as well as for consistency with earlier results, a width of 15.6% has been chosen for this model for a mass range of 400 to 3000 GeV. Since there is no consensus in the literature as to the validity of various calculations for this model, no k-factor for LO→NLO corrections is applied. The predicted cross sections for specific masses for a RS Kaluza-Klein gluon g_{KK} resonance are given in table 10(a), ranging from 112.2 pb⁻¹ for a mass of 400 GeV down to 0.012 pb⁻¹ for 3000 GeV. For resonance masses of 1, 2 and 3 TeV, a scan of the resonance width from 10% to 40% with the predicted cross sections listed in table 10(b) is performed to test for the impact of the arbitrary chosen resonance width on the results.

5.3.4 Scalar resonances

To account for spin-0 scalar resonances decaying to $t\bar{t}$, the Higgs Effective Couplings FormFact model implemented in MADGRAPH using the CTEQ6L1 PDF set has been simulated with a negligible resonance width of 0.66% for a mass range from 400 to 3000 GeV. No cross section for the scalar model are quoted at the moment, as agreed with the ATLAS Higgs group.

m [GeV]	$\sigma \times \text{BR}$ [pb]	DS ID	m [GeV]	Γ [%]	$\sigma \times \text{BR}$ [pb]	DS ID
400	112.2	182764		10	3.61	145583
500	81.9	115550		15	5.37	158765
600	45.0	115551		20	7.08	145584
700	25.2	115552	1000	25	8.72	145585
800	14.6	115553		30	10.30	145586
900	8.81	119318		35	11.70	158766
1000	5.47	115554		40	13.10	158767
1150	2.82	119319		10	0.080	158770
1300	1.52	115555		15	0.133	158771
1600	0.500	115556		20	0.193	158772
1800	0.255	115799	2000	25	0.257	158773
2000	0.137	119582		30	0.324	158774
2250	0.067	158768		35	0.393	158775
2500	0.0351	158769		40	0.461	158776
2750	0.0196	180575		10	0.0057	180384
3000	0.0120	180576		15	0.0113	180385
(a) constant resonance width $\Gamma = 15.3\%$				20	0.0184	180386
			3000	25	0.0268	180387
				30	0.0361	180388
				35	0.0462	180389
				40	0.0568	180390
(b) variable resonance width						

Table 10: Mass points used for Monte Carlo samples for resonant RS Kaluza-Klein gluon $g_{KK} \rightarrow t\bar{t}$ processes, listing the cross section times branching ratio $\sigma \times \text{BR}$ and resonance width Γ for given resonance masses for (a) constant and (b) variable resonance width and the unique dataset ID [95].

6

Analysis

With the detector setup described in section 3 and the object definitions and reconstruction techniques presented in section 4, a search for new heavy resonances introduced by theories beyond the Standard Model (cf. section 2.6) decaying into a $t\bar{t}$ pair via the lepton+jets channel (cf. section 2.5.3) is presented in the following section. Selection criteria applied to objects considered for the analysis are summarized in section 6.1, followed by requirements on the general properties of the analyzed event in section 6.2. The full reconstruction of the $t\bar{t}$ system in the analyzed event is discussed in section 6.3.

This analysis has been published in [8] with additional material available in [95]. The full analysis presented has been processed within the context of this thesis, including updates and improvements in further studies compared to the published version.

6.1 Object selection

After reconstruction and identification of physics objects (cf. section 4), object specific quality requirements are applied in order to select electrons, muons, jets and missing transverse energy suitable for the reconstruction of the full $t\bar{t}$ system. The detailed requirements for each individual object type are listed in the following sections and mostly follow the prescriptions of the ATLAS *TopReconstructionGroup* [97]. The common prescriptions are used among a variety of analysis involving $t\bar{t}$ decays to allow for a common standard and reasonable comparison.

6.1.1 Electrons

The quality requirements applied to the electron collection are listed in table 11 with a brief explanation of the specific requirements. Beside a general selection, applying algorithm and acceptance cuts, as well as an association to the collision vertex by a requirement on the longitudinal impact parameter z_0 , a medium and a tight selection are defined. While the medium selection (only used for multijet QCD estimates) requires a simple quality check on summarized hit information in the detector components, the tight selection (used for the main analysis) requires an explicit p_T -dependent isolation criterion. The variable `MI10_max40_ptsum` (mini-isolation¹) is defined as the sum of the transverse momenta of all tracks within a cone of radius $R < (10 \text{ GeV} / E_T)$ centered on the electron cluster and is required to be dominated by the electron momentum with more than 95% in order to tag the electron as *isolated*. This requirement reduces backgrounds from non-prompt sources and hadrons with high electromagnetic energy fraction in the calorimeter during the showering process and is specifically useful for boosted top quark decays. Compared to the standard isolation requirement, this procedure shows a more stable efficiency vs. background rejection performance at high values of transverse energies E_T as shown in a previous iteration of the analysis [37]. Electrons passing these criteria will be referred to as *selected electrons* in the following.

6.1.2 Muons

The quality requirements applied to the muon collection are listed in table 12 with a brief explanation of the specific requirements. The general selection requires a combined (CB) muon within acceptance ranges and specific requirements on the number of hits in the Pixel/SCT/TRT detector modules compared to the number of dead modules crossed to ensure good quality of the hit information used for reconstruction. The association to the collision vertex is achieved by a requirement on the longitudinal impact parameter z_0 (similar to the procedure used for electrons), as well as an additional requirement on the significance of the transverse impact parameter relative to the primary vertex d_0/σ_{d_0} , allowing for an improved multijet background rejection. Tight muons also have to fulfill the p_T -dependent isolation requirement similar to the electron selection. Muons passing these criteria will be referred to as *selected muons* in the following.

6.1.3 Jets

This analysis uses two different jet collections depending on the kinematic topology of the event. For resolved event topologies with separately reconstructable top decay products, a collection of small-radius jets with a radius parameter of $R = 0.4$ is used. For boosted event topologies facing overlapping top decay products, an additional collection of large radius jets with a radius parameter of $R = 1.0$ is used to collect the collimated particles of the hadronic top decay in one large jet. Both collections are reconstructed with the inclusive

¹The mini-isolation technique is used in this analysis deviant to the common prescriptions.

Name	Requirement	Description
General selection		
Reconstruction algorithm	author 1 or 3	1 : calorimeter-based 2 : track-based 3 : 1 and 2 combined
Transverse energy	$E_T > 25 \text{ GeV}$	Hard electrons (using $E_T = E_{\text{cluster}} / \cosh(\eta_{\text{track}})$)
Pseudo rapidity	$ \eta_{\text{cluster}} < 2.47$ (excluding calorimeter transition region $1.37 < \eta_{\text{cluster}} < 1.52$)	Central detector region with sufficient tracking detector coverage
Dead pixels	$OQ\&1146 == 0$	Bitwise comparison with OQ (object quality) map to reject electrons with known dead pixel modules involved
Impact parameter	$z_0 < 2.0 \text{ mm}$	Longitudinal impact parameter relative to the collision vertex
Medium selection		
Identification	<i>mediumPP</i>	Identification requirement (cf. Section 4.3)
Hit requirements	<i>isEM & 0x2</i>	Bitwise comparison for summarized hit quality requirements
Tight selection		
Identification	<i>tightPP</i>	Identification requirement (cf. Section 4.3)
Isolation	$\text{ptSum}/p_T < 0.05$	Isolated electron without non-prompt sources close-by, using <i>MI10-max40-ptsum</i>

Table 11: Electron quality requirements applied to the electron collection to select electrons suitable for the analysis, divided into a medium and tight selection for QCD/Multijet estimates and the analysis respectively.

Name	Requirement	Description
General selection		
Reconstruction algorithm	author 12	combined muons within tight category (cf. Section 4.4)
Transverse momentum	$p_T > 25$ GeV	Hard muons
Pseudo rapidity	$ \eta < 2.5$	Central detector region with sufficient tracking detector coverage
Hit requirements	Pixel hits, SCT hits, Pixel/SCT holes, TRT hits/outliers	Fraction of hits compared to dead modules crossed must satisfy minimum threshold
Impact parameter	$z_0 < 2.0$ mm (longitudinal) $ d_0/\sigma_{d_0} < 3$ (transverse)	Impact parameter relative to the collision vertex
Identification	<i>tight</i>	Identification requirement (cf. Section 4.4)
Tight selection		
Isolation	$ptSum/p_T < 0.05$	Isolated muon without non-prompt sources close-by, using <i>MI10_max40_ptsum</i>

Table 12: Muon quality requirements applied to the muon collection to select muons suitable for the analysis, divided into a medium and tight selection for QCD/Multijet estimates and the analysis respectively.

anti- k_t jet clustering algorithm (cf. section 4.5) using the *E-scheme* recombination scheme² as implemented in FASTJET [98]. The setup and acceptance cuts applied for the two collections, such as a minimum p_T requirement and central detector region, are listed in table 13. A requirement on the jet vertex fraction is defined for the small radius collection only, while the large radius collection has trimming applied additionally. The trimming procedure reduces contributions from pileup, which has a stronger impact on the large radius than on the small radius jet collection. The tighter requirement on the pseudo rapidity of $|\eta_{1.0}| < 2.0$ compared to $|\eta_{0.4}| < 2.5$ ensures the whole jet to be contained in the central part of the detector.

Additional isolation criteria and a removal of overlaps with other physics objects like electrons and muons are described in section 6.1.4. Jets passing these criteria will be referred to as *selected jets* in the following.

B-tagging is applied to the small radius jet collection only using the MV1 tagger (cf. section 4.5.6) at a working point of 70% tagging efficiency, corresponding to a b-tagging weight of $w_{MV1} > 0.7892$. Jets have to fulfill $p_T > 25$ GeV and pass the JVF requirement in order to be considered for b-tagging. A positive b-tag is not required for all small radius jets, but is an additional flag to check for a minimum number of b-tags per event to reject background contributions which have a b-tag available less likely. Scaling factors are applied to jets in MC found inside and outside large radius jets separately to correct for differences between the b-tagging efficiency in simulated events and observed data.

6.1.4 Overlap removal

Since the reconstruction of objects like jets (cf. section 4.5), electrons (cf. section 4.3) and muons (cf. section 4.4) is based on their energy deposits in the calorimeters and associated tracks in the inner detector and is performed separately for each object type, these objects have a certain possibility of overlaps. Especially each electron is also reconstructed as a jet since the clusters of the EM calorimeter are included in the jet reconstruction, forming a duplicate of the same physical object resulting in a double-counting of energy depositions. In order to clean the event, an overlap removal depending on the radial distance of the specific objects is applied, applying an electron-jet duplicate removal, as well as an overlap removal between jets and electrons and between jets and muons.

Electron duplicate/overlap removal

The standard procedure to prevent overlap between jets and electrons is to remove jets within $\Delta R(j, e) < 0.2$ to an electron (electron duplicate removal), and afterwards removing electrons within $\Delta R(j, e) < 0.4$ to the remaining jets (electron isolation). This simple procedure leads to a significantly increased event rejection for events with a boosted topology. These events face a more collimated b-jet and electron from the leptonically decaying top³ and hence fulfill the removal criteria more often compared to resolved topologies with well

²The E-scheme is a simple recombination scheme, adding up the four-vectors of the considered objects.

³The decay $t \rightarrow Wb \rightarrow \ell\nu b$ will be referred to as *leptonically decaying top*, although it contains a b-quark.

Name	Requirement	Description
Small radius jets		
Clustering algorithm	anti- k_t , E-Scheme, topocluster	Common jet reclustering algorithm setup (cf. Section 4.5.2)
Jet radius	$R = 0.4$	Small radius jets used for resolved and boosted event topologies
Transverse momentum	$p_T > 25$ GeV	Select hard jets with minimum p_T
Pseudo rapidity	$ \eta < 2.5$	Central detector region to ensure good detector material coverage
Jet vertex fraction	$ \text{JVF} > 0.5$	Ensure association of jet to primary vertex (cf. Section 4.5.5) (only applied for jets fulfilling $ \eta < 2.4$ and $p_T < 50$ GeV)
Large radius jets		
Clustering algorithm	anti- k_t , E-Scheme, topocluster	Common jet reclustering algorithm setup (cf. Section 4.5.2)
Jet radius	$R = 1.0$	Large radius jets only used for boosted event topologies
Transverse momentum	$p_T > 25$ GeV	Select hard jets with minimum p_T
Pseudo rapidity	$ \eta < 2.0$	Central detector region to ensure sufficient tracking detector coverage
Trimming	$R_{\text{sub}} = 0.3,$ $f_{\text{cut}} = 0.05$	Reduce contributions from pileup (cf. Section 4.5.4)

Table 13: Jet quality requirements applied to the jet collection to select jets suitable for the final analysis, divided into a selection for small and large radius jets used for different event topologies.

separated objects. In order to recover this efficiency loss, an *electron-in-jet overlap removal* procedure has been developed within the ATLAS $t\bar{t}$ resonances group for this analysis [99]. This procedure subtracts the four-vector of a selected electron from a corresponding jet found within $\Delta R(j, e) < 0.4$ and recalculates the jet vertex fraction value of this jet if any of the electron's tracks were included in the calculation. For the altered jet collection, all selected electrons that are still within $\Delta R(j, e) < 0.2$ to a jet are removed from the electron collection and jets that were affected by this electron in the previous step are restored to their original properties. This adapted procedure improves the efficiency by about 33% (52%) for a 2.5 (3.0) TeV Z' resonance compared to the standard procedure [95].

Muon overlap removal

The overlap removal between jets and muons is performed with a p_T -dependent cone around the muon with $\Delta R(j, \mu) < 0.04 + 10 \text{ GeV}/p_T^\mu$. If a jet is found within this cone, the muon is removed from the collection. This p_T -dependent ΔR cut, i.e. a shrinking cone with increasing muon momentum, is used to preserve muons originating from highly boosted top quark decays, exploiting the anti-correlation between the muon p_T and its radial distance from the b-quark. If a muon is close to a jet and is removed, it is most likely from non-prompt sources and hence not suitable for this analysis.

After these two procedures, the jet quality requirements presented in section 6.1.3 are re-applied to the resulting jet collection, since some kinematics, i.e. the JVF and p_T values, might have changed due to the electron-in-jet overlap removal.

The procedures explained above are only applied to the small-radius jet collection. For the large radius jet collection, a simple electron-jet duplicate removal is applied, removing jets closer than $\Delta R(e, j) < 0.5$ to the electron. This jet collection is used in the boosted topology reconstruction only, where the t and \bar{t} decays are rather back to back with a large distance of the large radius top jet for the hadronically decaying top quark to the lepton on the side of the leptonically decaying top quark. Hence this more simple ΔR cut is justified, since real electron duplicates will be removed more likely, instead of the most interesting large radius jet containing the information of the hadronically decaying top.

6.2 Event selection

All events are analyzed for specific quality criteria. General selection criteria listed in section 6.2.1 select events with good run conditions of the ATLAS detector during recording, as well as applying lepton criteria to ensure a lepton+jets environment and minimum E_T^{miss} criteria to reject other background processes as e.g. W+Jets or multijet QCD. Topology specific criteria are applied afterwards for the boosted topology (referred to as *boosted selection* in the following) in section 6.2.2 and for the resolved topology (referred to as *resolved selection* in the following) in section 6.2.3 in parallel, while ensuring orthogonality. The final yields are then further divided into b-tagging categories listed in section 6.2.4.

6.2.1 General selection

The following criteria are applied to all events, pre-selecting the lepton+jets $t\bar{t}$ environment.

Event quality

Each event has to fulfill specific event criteria rejecting events with incomplete information, liquid argon noise bursts or corrupted tile calorimeter data. A centrally provided Good Runs List⁴ has to flag the event as "good for physics" and also the primary vertex has to fulfill quality criteria, e.g. with at least 4 tracks associated.

Single lepton+jets signature

In order to select the correct signature resulting from a top quark pair decay, the event has to fulfill the lepton trigger requirement presented in section 5.1. A tighter criterion is the presence of exactly one selected electron (muon) and explicitly no selected muon (electron) fulfilling the quality criteria listed section 6.1 in in the electron (muon) channel. Additionally this selected single lepton has to match the appropriate lepton stream trigger decision (apart from the Delayed stream, since here only a large jet trigger is used). Contributions with tau-leptons are not considered explicitly, but taken into account in the e +jets and μ +jets channels, since taus decay to an electron or muon and the corresponding neutrino with a $\text{BR}(\tau \rightarrow \ell + \nu_\ell) \sim 18\%$ each. The additional neutrino in the event leads to a mis-reconstruction of the primary neutrino from the leptonic W-decay, which represents an acceptable bias as a soft contribution close to the primary neutrino. Hadronic decays of taus, mainly to pions and more rarely to kaons, are not considered in this analysis, since the reconstruction complexity increases drastically at a negligible gain of acceptance.

Event cleaning and background rejection

Additional cleaning of the event is achieved by rejecting all events containing a bad flagged jet, which is triggered by spikes and large noise in different detector modules and hints for a generally bad event quality. To reduce contributions from multijet QCD background, which usually does not involve any primary neutrinos and hence does not provide a large contribution of missing transverse energy, a cut on the missing transverse energy of $E_T^{\text{miss}} > 20$ GeV is applied, as well as a minimum criterion of $(E_T^{\text{miss}} + m_{T,W}) > 60$ GeV while the transverse mass $m_{T,W}$ of the W is defined in equation (6.1), with the p_T of the lepton ℓ and the neutrino ν (represented by the missing transverse energy E_T^{miss}) and the angle $\phi_{\ell,\nu}$ between these two objects.

$$m_{T,W} = \sqrt{2 \cdot p_{T,\ell} \cdot p_{T,\nu} \left(1 - \cos(\Delta\phi_{\ell,\nu})\right)} \quad (6.1)$$

⁴GRL : data12_8TeV.periodAllYear_DetStatus-v58-pro14-01_DQDefects-00-00-33_PHYS_StandardGRL_All_Good.xml

6.2.2 Boosted selection

The following criteria are applied after the general selection, selecting for a boosted topology.

Leptonic b-jet

A small-radius jet has to be associated to the leptonically decaying top quark by requiring a jet within $\Delta R(\ell, j) < 1.5$ to the lepton, selecting the highest p_T jet if there is more than one jet fulfilling this criterion. This identified jet will be referred to as *leptonic b-jet*⁵ or j_{lep} in the following.

Hadronic top jet

A large radius jet has to be identified as the full top jet of the hadronically decaying top. A jet is chosen if it satisfies a significant boost denoted by a minimum transverse momentum of $p_T > 300(380)$ GeV (Delayed stream) and a mass of at least $m_{\text{jet}} > 100$ GeV. The first k_t splitting scale (cf. section 4.5.7) denoting a suitable substructure of the large jet has to satisfy $\sqrt{d_{12}} > 40$ GeV (ATLAS tagger). The isolation from the leptonically decaying top is ensured by a cut on the radial distance to the leptonic b-jet by $\Delta R(j, j_{\text{lep}}) > 1.5$ as well as an angular isolation from the lepton by $\Delta\phi(j, \ell) > 2.3$. Also here the highest p_T jet is selected if more than one jet satisfies all these criteria. This identified jet will be referred to as *hadronic top jet* or j_{top} in the following.

Mainly to reject W+Jets background, the leptonic b-jet or at least one small-radius jet close to the hadronic top jet within $\Delta R(j_{R=0.4}, j_{\text{top}}) < 1.0$ has to be b-tagged.

6.2.3 Resolved selection

The following criteria are applied after the general selection, selecting for a resolved topology.

The resolved selection needs at least 4 small-radius jets of which at least one has to satisfy the b-tagging conditions, to be associated to the top decay products. This association is performed with a χ^2 algorithm, which will be presented in more detail in the context of event reconstruction in section 6.3.3. The quality of this fit has to satisfy $\text{Log}_{10}(\chi^2) < 0.9$ ($\chi^2 < 7.94$) in order to be accepted for the resolved selection. Orthogonality to the previously presented boosted selection is guaranteed by rejecting events which already passed the boosted selection criteria.

6.2.4 B-tagging categories

The final events passing all boosted or resolved topology quality requirements are divided into three categories for each selection, depending on the specific b-tagging results. In the boosted selection, the leptonic top candidate t_ℓ has a b-jet matched if the jet matched to the leptonic side is b-tagged and the hadronic top candidate t_h has a b-jet matched, if another b-tagged small radius jet is found within $\Delta R(j, j_{\text{top}}) < 1.0$ to the large radius jet top candidate

⁵Although this jet is referred to as a *b-jet*, it is not explicitly required to fulfill the b-tagging conditions.

j_{top} . In the resolved selection, the matching is assigned by the χ^2 algorithm, checking for b-tags associated to the specific jets assigned to the leptonic and hadronic top decays (cf. section 6.3.3).

Depending on this matching, the following categories are defined

1. DoubleTag : Both hadronic top t_h and leptonic top t_ℓ candidates have b-jets matched.
2. LepTag : Only the leptonic top t_ℓ candidate has a b-jet matched
3. HadTag : Only the hadronic top t_h candidate has a b-jet matched

This categorization results in twelve final signal regions which are considered in this analysis: Resolved and boosted selection, each for the e +jets and μ +jets lepton selection, split into three b-tagging categories.

6.2.5 Selection efficiency

The selection efficiency for the boosted topology suffers losses from the large radius jet and b-tagging requirements. The contribution of the resolved selection is negligible for resonance masses above 1.5 TeV due to the overlap with the boosted selection. The overall selection efficiency times acceptance is larger for isolated muons than isolated electrons above the same resonance mass point as shown in figure 32. This results from inefficiencies of the electron identification and overlap removal in the boosted environment.

6.3 Event reconstruction

Increased event yields due to the contribution of a new heavy resonance decaying to a $t\bar{t}$ pair should appear in the spectrum of the reconstructed $t\bar{t}$ mass $m_{t\bar{t}}$ as an excess of events above the Standard Model expectation. All events passing the pre-selections presented in section 6.2 are assumed to be a final state of a $t\bar{t}$ decay, although of course background contributions from non- $t\bar{t}$ processes remain, and are treated like that, i.e. fully reconstructed as a $t\bar{t}$ pair. The reconstruction techniques for the different topologies are presented in the following sections.

6.3.1 Neutrino Reconstruction

Neutrinos are not detected directly in the ATLAS detector, since they are very unlikely to interact with the detector material. Nevertheless their energy and momentum can be estimated by the missing transverse energy (cf. section 4.6). This information can be assigned to the p_x and p_y momenta of the neutrino, while the longitudinal component p_z is unknown, since only transverse energy is considered. This is not suitable for a decent reconstruction of the leptonically decaying top quark ($t \rightarrow Wb \rightarrow \ell\nu_\ell b$), since the neutrino represents a significant contribution of this decay.

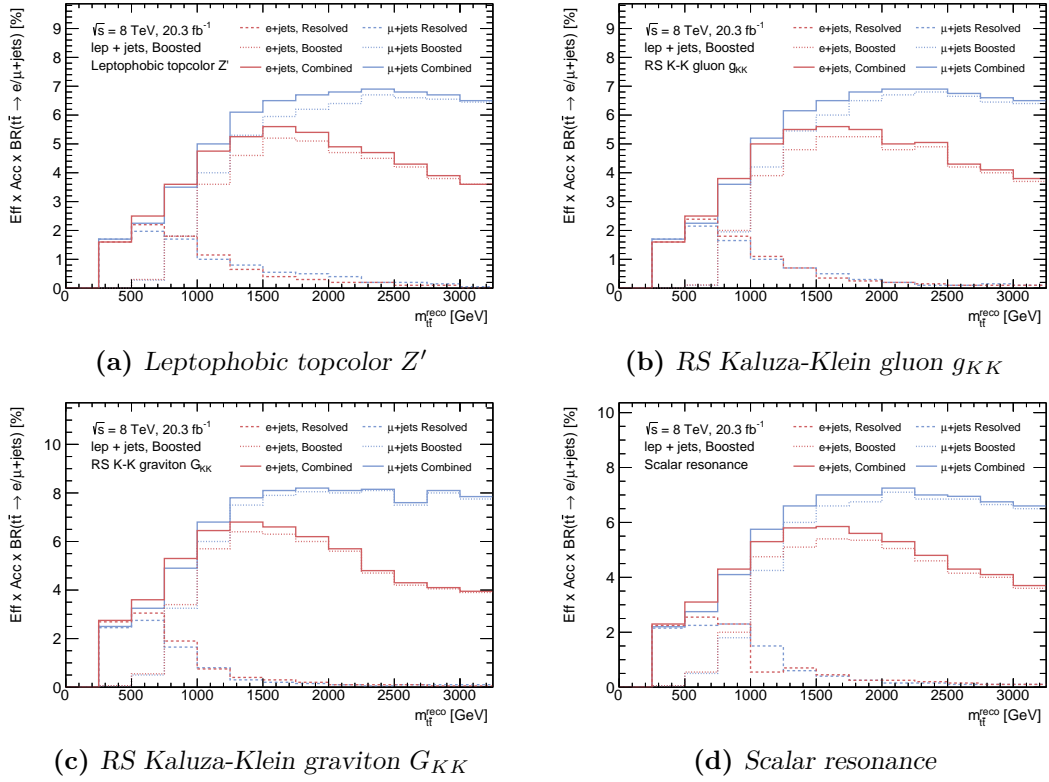


Figure 32: Selection efficiency times acceptance times branching ratio as a function of the true $m_{t\bar{t}}$ for selected benchmark signal models: (a) leptophobic topcolor Z' , (b) RS Kaluza-Klein gluon g_{KK} , (c) RS Kaluza-Klein graviton G_{KK} and (d) scalar resonance. The dashed and dotted lines show the Resolved and Boosted selection respectively, as well as the combination with the straight line.

Since the W-boson decays into a lepton and a neutrino, the sum of the four-momenta of the lepton p_ℓ and the neutrino p_ν has to add up to the four-momentum of the W-boson p_W , i.e. one is able to reconstruct the correct W mass. Using an on-shell constraint on the W mass with a reference mass $M_W = 80.4$ GeV, one can compute the longitudinal momentum component $p_{z,\nu}$ of the neutrino, assuming that the majority of the missing transverse momentum actually stems from the neutrino. Analyzing this system (cf. section A.1) one retrieves a quadratic equation in $p_{z,\nu}$ which can be solved for two possible solutions shown in equation (6.2) with the abbreviation $\xi = \frac{M_W^2}{2} + p_{T,\ell} p_{T,\nu} \cos(\Delta\phi_{\ell,\nu})$, the energy of the lepton E_ℓ and the momentum components p_i of the lepton and neutrino.

$$(p_{z,\nu})_{1,2} = \frac{\xi p_{z,\ell}}{p_{T,\ell}^2} \pm \sqrt{\left(\frac{\xi p_{z,\ell}}{p_{T,\ell}^2}\right)^2 - \frac{E_\ell^2 p_{T,\ell}^2 - \xi^2}{p_{T,\ell}^2}} \quad (6.2)$$

If two real solutions exist for $p_{z,\nu}$, the solution is chosen depending on the topology selection (cf. section 6.3.2 and section 6.3.3). If no real solution can be found by the algorithm, the four-momentum of the E_T^{miss} is rescaled and rotated, applying a minimum variation to $p_{x,\nu}$ and $p_{y,\nu}$ necessary to find exactly one real solution for $p_{z,\nu}$ [100]. A justification for this procedure is given by the fact, that a mismeasurement of the missing transverse momentum is the most likely explanation for a lack of a real solution.

6.3.2 Boosted reconstruction

After the general event selection presented in section 6.2.1 and the boosted specific event selection presented in section 6.2.2, the selected objects for the boosted topology are the following:

- One reconstructed neutrino ν (using the solution with smaller $p_{z,\nu}$ if more than one available (cf. section 6.3.1))
- One selected charged lepton (electron or muon)
- One selected small-radius anti- k_t $R = 0.4$ jet associated to the leptonic top decay j_{lep}
- One selected large radius anti- k_t $R = 1.0$ jet j_{top} with significant boost

While the large radius jet j_{top} is considered as the hadronically decaying top candidate t_h , the four-vectors of the reconstructed neutrino, selected lepton and leptonic b-jet j_{lep} are combined to form the leptonically decaying top candidate t_ℓ . Both top candidates are combined to form the full $t\bar{t}$ system, providing the invariant mass $m_{t\bar{t}}$. The reconstructed invariant mass for different signal models and resonance masses in the boosted topology is shown in figure 33.

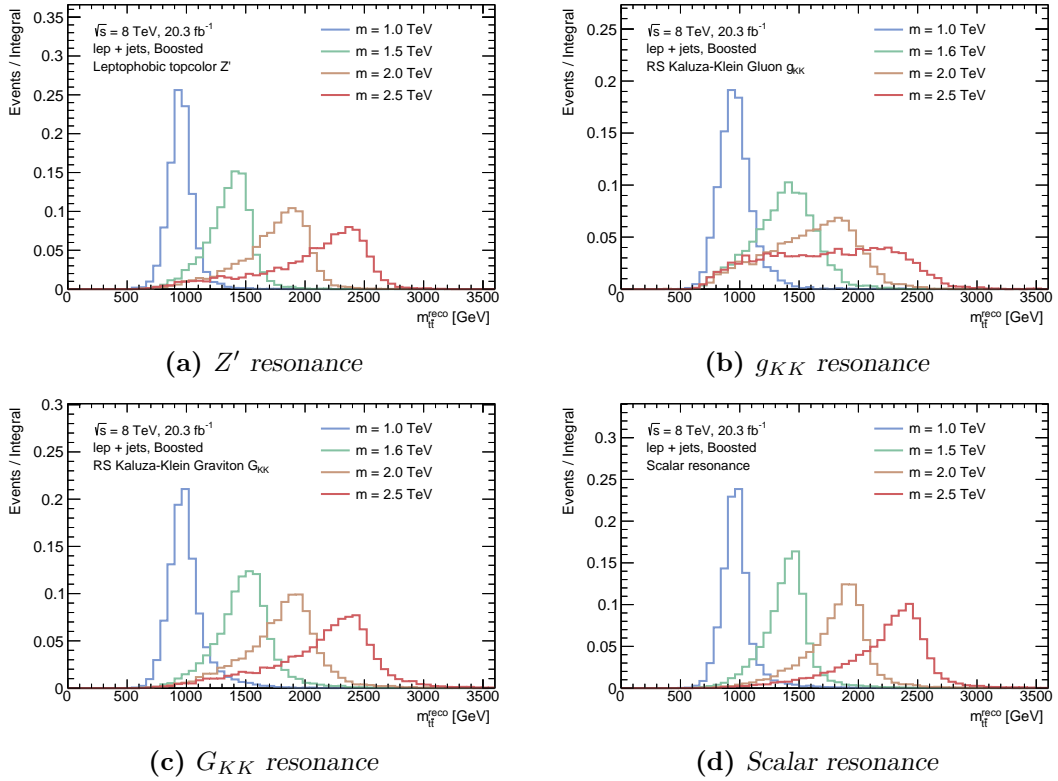


Figure 33: Reconstructed invariant mass of the $t\bar{t}$ system $m_{t\bar{t}}$ for selected benchmark model, a (a) leptophobic topcolor Z' , (b) RS Kaluza-Klein gluon g_{KK} , (c) RS Kaluza-Klein graviton G_{KK} and (d) scalar resonance for events satisfying the boosted selection and using the boosted-topology reconstruction. Each histogram is normalized to its integral.

6.3.3 Resolved reconstruction

The reconstruction of the final $t\bar{t}$ system in the resolved selection is performed using a χ^2 algorithm, searching for the best assignment of the objects selected in the general pre-selection presented in section 6.2.1 and the resolved specific event selection presented in section 6.2.3. Since there are at least four selected jets, the association of these jets to the top quark decay products is a combinatoric problem. Therefore the used algorithm searches for the minimum of the χ^2 formula defined in equation (6.3) for all possible permutations of jet assignments to the top decay products, to find the best combination.

$$\chi^2 = \underbrace{\left[\frac{m_{jj} - m_W}{\sigma_W} \right]^2}_{W_h} + \underbrace{\left[\frac{m_{jjb} - m_{jj} - m_{(t_h-W)}}{\sigma_{(t_h-W)}} \right]^2}_{t_h} + \underbrace{\left[\frac{m_{j\ell\nu} - m_{t_\ell}}{\sigma_{t_\ell}} \right]^2}_{t_\ell} + \underbrace{\left[\frac{(p_{T,jjb} - p_{T,j\ell\nu}) - (p_{T,t_h} - p_{T,t_\ell})}{\sigma_{\Delta p_T}} \right]^2}_{\Delta p_T} \quad (6.3)$$

This formula uses constraints on specific variables, while the first term is a constraint on the mass m_W of the hadronically decaying W-boson W_h , reconstructed by the combination of two small radius jets m_{jj} . The second term is a constraint on the mass m_{t_h} of the hadronically decaying top quark t_h , reconstructed by the combination of the hadronically decaying W-boson and a third small radius jet m_{jjb} . Since the mass of the top quark m_{t_h} and the W-boson m_W are highly correlated, the mass difference $m_{jjb} - m_{jj}$ of these terms is analyzed to decouple the constraint from the first term. The third term constrains the mass m_{t_ℓ} of the leptonically decaying top quark t_ℓ , reconstructed by the combination of the reconstructed neutrino, the selected lepton and a small radius jet $m_{j\ell\nu}$. The last term arises as a constraint on the expected transverse momentum balance between the two decaying top quarks p_{T,t_h} and p_{T,t_ℓ} .

The parameter values for the constraints are determined from reconstructed MC events in which the right combination is identified from the MC truth information optimized for Z' samples with masses ranging from 0.5 to 2 TeV. The resulting values are listed in table 14.

$m_W = 82.4$ GeV	$m_{(t_h-W)} = 89.0$ GeV
$m_{t_\ell} = 166.0$ GeV	$\sigma_{(t_h-W)} = 15.7$ GeV
$\sigma_W = 9.6$ GeV	$\sigma_{t_\ell} = 17.5$ GeV
$p_{T,t_h} - p_{T,t_\ell} = 0.43$ GeV	$\sigma_{\Delta p_T} = 46.1$ GeV

Table 14: Parameters for the χ^2 algorithm used for the resolved reconstruction [95].

The reconstructed invariant mass for different signal models and resonance masses in the resolved topology before and after the veto for events already passing the boosted topology reconstruction is shown in figure 34. The low mass tails visible in the $m_{t\bar{t}}$ distributions for both resolved and boosted topologies arise from two main effects. Radiation of the objects used in the final reconstruction is not taken into account and shifts the reconstructed mass towards lower values, particularly affecting high-mass resonances. Additionally the steep falling parton luminosity with increasing partonic center of mass energy causes a tail at lower masses in the Breit-Wigner signal shape, which has a large effect on broad resonances. The experimental resolution for the invariant mass of the $t\bar{t}$ system, extracted from a Gaussian fit of the relative difference of the truth and reconstructed mass, is 8% for the resolved selection at a resonance mass of 400 GeV improving to 6% for 1 TeV, and 6% in the boosted selection independent of the mass of the resonance.

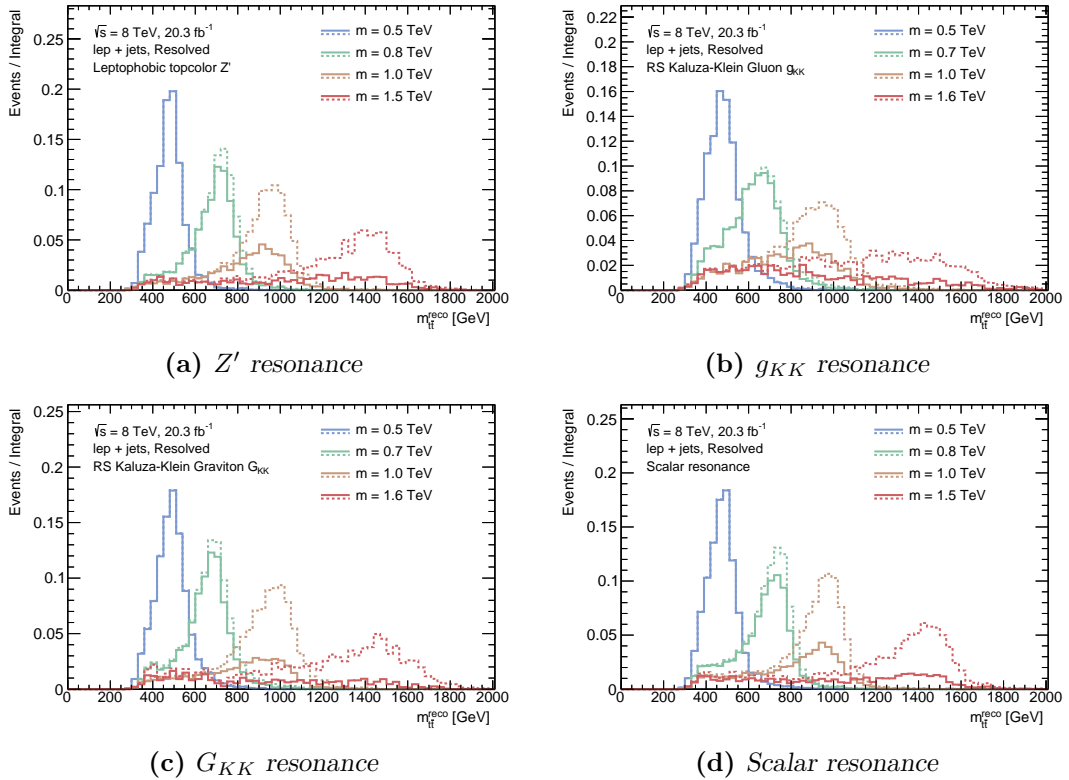


Figure 34: Reconstructed invariant mass of the $t\bar{t}$ system $m_{t\bar{t}}$ for selected benchmark models, (a) leptophobic topcolor Z' , (b) RS Kaluza-Klein gluon g_{KK} , (c) RS Kaluza-Klein graviton G_{KK} and (d) scalar resonance for events satisfying the resolved selection and using the resolved-topology reconstruction, before (dashed lines) and after (straight lines) applying the veto for events passing the boosted selection. Each pair of histograms is normalized to the integral of the histogram before applying the veto.

6.3.4 Event display

Figure 35 shows the event display of an exemplary event recorded at the ATLAS detector and fully reconstructed in the boosted selection of the μ +jets channel. The upper, left pad shows a cut-away view along the x-y plane of the ATLAS detector with the electromagnetic (green ring) and hadronic (red ring) calorimeter, surrounded by the muon chamber (blue rings). The bottom pad shows a cut-away view along the x-z plane and the right pads show the $\eta - \phi$ plane. Energy depositions in the detector are illustrated by yellow blocks/towers. The green and red cones/circles represent reconstructed small ($R = 0.4$) and large radius ($R = 1.0$) jets respectively (as used in the analysis), while the white straight line denotes a muon and the missing transverse energy (originating from a non-interacting neutrino) is betoken by the straight red line (dashed circle).

The event display shows a clear separation between the leptonic and hadronic top decays and the overlap of the reconstructed decay products for the hadronic top candidate. This event represents a highly energetic $t\bar{t}$ decay with a final reconstructed invariant $t\bar{t}$ mass of $m_{t\bar{t}} = 2.5$ TeV.

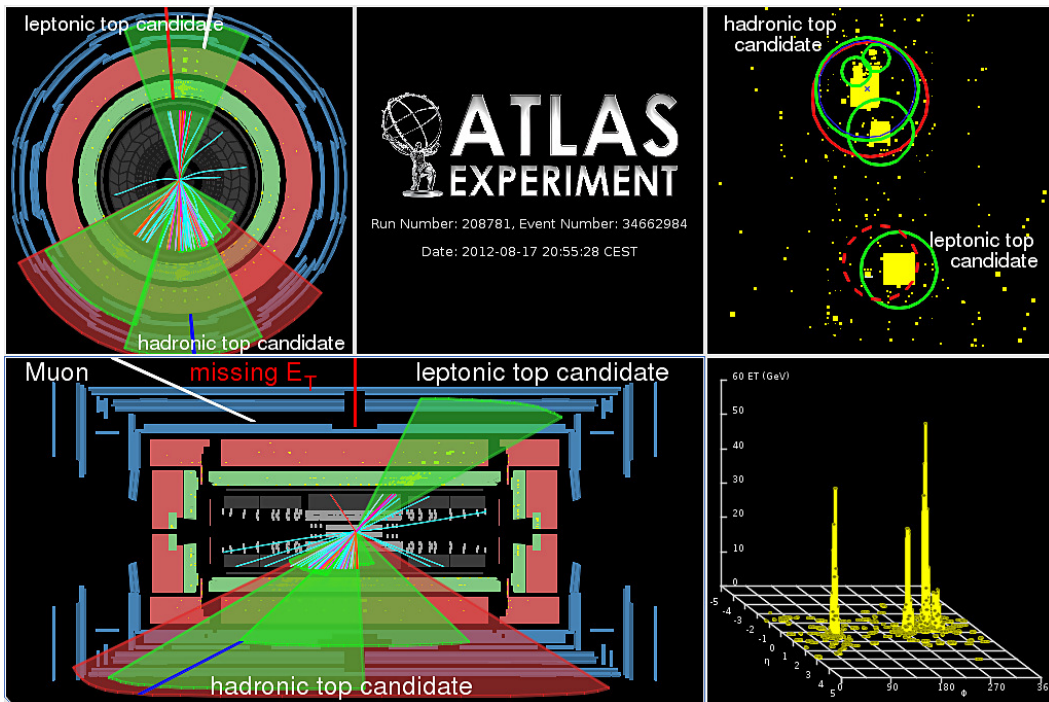


Figure 35: Event display of a boosted $t\bar{t}$ decay recorded at the ATLAS detector during RUN I in 2012 at $\sqrt{s} = 8$ TeV (RunNr. #208781, EventNr. #34662984), showing an event fully reconstructed in the boosted selection of the μ +jets channel with an invariant mass of $m_{t\bar{t}} = 2.5$ TeV [101].

7

W+Jets background estimation

Production of a W-boson with associated jets (W+Jets) is the largest background in this analysis and is simulated for different heavy and light flavor final states (cf. section 5.2.2). Since the overall normalization and the heavy flavor (HF) composition is not accurately known in MC, a data driven approach is used to derive scale factors (SFs) to correct the W+Jets HF composition and to apply a normalization. This approach was first described in [102] and is adapted and improved for this analysis. The resulting SFs are also used in a recent $t\bar{t}$ differential cross section measurement analysis [103]. This study represents the major contribution to the published analysis in the context of this thesis.

Asymmetrical cross sections for positively and negatively charged leptons originating from W-decays are used to derive a normalization for the W+Jets background. The source of charge asymmetry in W-decays is discussed in detail in section 7.1 and the normalization procedure for the resolved selection in section 7.2, which combines a charge asymmetry normalization in section 7.2.1 and a method to extract flavor specific SFs in section 7.2.2. The treatment of the W+Jets background in the boosted selection is based on the resolved topology and discussed in detail in section 7.3. The factors for charge asymmetry normalization and HF composition are derived simultaneously and applied to each individual event, depending on the charge of the selected lepton, the small radius anti- k_t $R = 0.4$ jet multiplicity bin and the flavors of the W-decay products as described in section 7.4. A further investigation on the large differences in flavor SFs observed for the e +jets and μ +jets channel is discussed in section 7.5.

7.1 W+Jets charge asymmetry

The production of vector bosons like the W-boson at the LHC requires $q\bar{q}$ fusion. A positively charged W-boson W^+ can be produced from processes like $u\bar{d} \rightarrow W^+$ or $c\bar{s} \rightarrow W^+$, depending on the corresponding parton distribution functions (PDF) products $u(x_1)\bar{d}(x_2)$ with relative momentum fractions x_i . A negatively charged W-boson however is produced from charge conjugated processes, i.e. $\bar{u}d \rightarrow W^-$ or $\bar{c}s \rightarrow W^-$, with PDF products $\bar{u}(x_1)d(x_2)$.

The LHC accelerates and collides proton-proton beams, while a proton is composed of 2 up- and one down-quark. Hence it is more likely to have an up-quark of the proton's valence¹ quarks participating in an interaction producing a W^+ boson than a down quark for W^- production [104]. These relative differences in the anti-/quark PDFs lead to an overall charge asymmetry in the production of W-bosons (with and without associated jets). The ratio of the cross sections for W^\pm production at the LHC $r = \frac{\sigma(pp \rightarrow W^+)}{\sigma(pp \rightarrow W^-)}$ is well understood and predicted with a higher precision than the total W cross section for W-boson production in association with three or more jets [31]. Therefore one can extract a W+Jets normalization using the theoretical prediction for this ratio r as presented in section 7.2.1.

A next-to-next-to leading order (NNLO) correction is applied to this ratio by comparing the ratio A of W+Jets yields for positively and negatively charged W-bosons without any selection applied for the standard analysis samples (ALPGEN+PYTHIA, cf. section 5.2.2) to the result C of a W^\pm process simulation using a Drell-Yan sample including NNLO corrections (which is not used in the analysis itself), also without any selection applied, shown in equation (7.1).

$$A = \left. \frac{N_{W^+}}{N_{W^-}} \right|_{\text{no selection}}^{\text{NNLO}} = 1.408 \quad C = \left. \frac{N_{W^+}}{N_{W^-}} \right|_{\text{no selection}}^{\text{NLO}} = 1.447 \quad (7.1)$$

The correction $\frac{A}{C}$ is applied to the NLO yields as given in equation (7.2), while the normalization of total W+Jets yields has to remain constant.

$$\frac{N_{W^+}^{\text{NNLO}}}{N_{W^-}^{\text{NNLO}}} = \frac{N_{W^+}^{\text{NLO}}}{N_{W^-}^{\text{NLO}}} \cdot \frac{A}{C} \quad N_{W^+}^{\text{NNLO}} + N_{W^-}^{\text{NNLO}} \stackrel{!}{=} N_{W^+}^{\text{NLO}} + N_{W^-}^{\text{NLO}} \quad (7.2)$$

Solving these equations for the corrected yields $N_{W^\pm}^{\text{NNLO}}$ one can define NLO→NNLO correction factors s_{NNLO}^\pm for positive and negative W charge categories separately as given in equation (7.3) using the ratio $R = \left. \frac{N_{W^+}}{N_{W^-}} \right|_{\text{pre-selection}}^{\text{NLO}}$ of W+Jets yields at NLO level and after applying a pre-selection at analysis level.

$$s_{\text{NNLO}}^- = \frac{(1+R)}{\left(1+R \cdot \left(\frac{A}{C}\right)\right)} \quad s_{\text{NNLO}}^+ = \left(\frac{A}{C}\right) \cdot s_{\text{NNLO}}^- \quad (7.3)$$

¹A proton is composed of 3 (uud) *valence quarks*, determining the quantum numbers of the proton, and an indefinite number of virtual anti-/quark pairs, so-called *sea quarks*, arising from vacuum fluctuations due to QCD interactions with gluons coupling between the valence quarks. These virtual quarks carry a much smaller momentum fraction of the proton than valence quarks.

7.2 W+Jets normalization in resolved topology

The input yields for the derivation of a W+Jets normalization are extracted at pre-tag level after applying all general selection cuts (cf. section 6.2.1), i.e. before applying any topology specific selection, and split by the charge of the selected lepton (± 1).

For the flavor normalization presented in section 7.2.2, these yields are also provided at tag level, checking for at least one b-tagged small radius anti- k_t $R = 0.4$ jet in the event, split in jet multiplicity and for W+Jets samples additionally divided into decay flavors (heavy flavors W_{cc} , W_c and W_{bb} and a combination of all light flavors W_{ll} , but independent of the lepton flavor $W_{e\nu_e}$, $W_{\mu\nu_\mu}$ or $W_{\tau\nu_\tau}$). Apart from the 4 inclusive jet multiplicity bin SF applied in this analysis (since the analysis requires at least 4 small radius jets), these SFs are also provided for other jet multiplicities suitable for other analysis as from 1-4 exclusive (ex) and 3-5 inclusive (in) jet multiplicities. An overview of the input yields in the different categories for all combined W+Jets background samples in the e +jets channel is shown in figure 36.

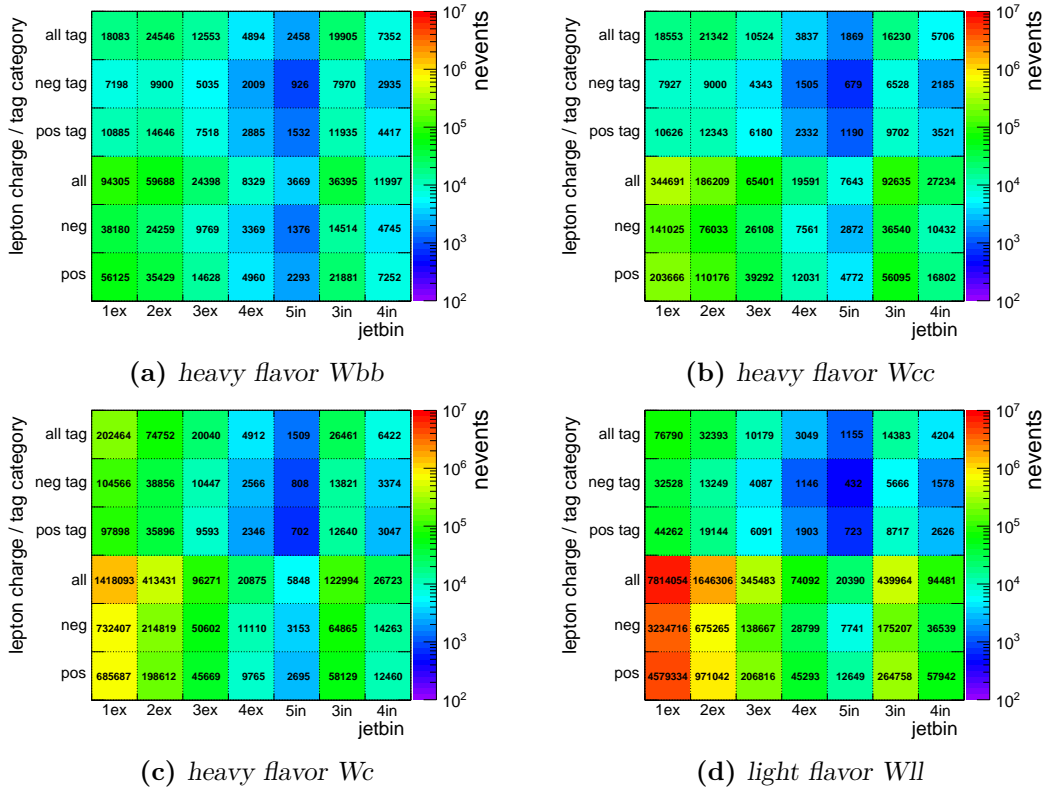


Figure 36: Event yields for all combined W+Jets samples in the e +jets channel split by W-decay heavy flavors (a) W_{bb} , (b) W_{cc} and (c) W_c and combined light flavors (d) W_{ll} . The yields are provided in categories of lepton charge (positive, negative, all) and jet multiplicities at tag/pre-tag level and are used as input for the derivation of W+Jets normalization scale factors in different jet multiplicities.

7.2.1 Charge asymmetry normalization

The estimation of the total W+Jets event yield at pre-tag level in data $N_{\text{data},W}^{\text{pre-tag}}$ is given by equation (7.4)

$$N_{\text{data},W}^{\text{pre-tag}} = N_{\text{data},W^+}^{\text{pre-tag}} + N_{\text{data},W^-}^{\text{pre-tag}} = \left(\frac{r_{\text{MC}} + 1}{r_{\text{MC}} - 1} \right) (D_{\text{asym},+}^{\text{pre-tag}} - D_{\text{asym},-}^{\text{pre-tag}}) \quad (7.4)$$

$$r_{\text{MC}} = \frac{N_{\text{MC},W^+}^{\text{pre-tag}}}{N_{\text{MC},W^-}^{\text{pre-tag}}} = \frac{\sigma(pp \rightarrow W^+)}{\sigma(pp \rightarrow W^-)} \quad (7.5)$$

while the ratio r_{MC} in equation (7.5) is evaluated for the signal region kinematic cuts using yields from Monte Carlo simulation and $D_{\text{asym},\pm}^{\text{pre-tag}}$ is the estimation of charge-asymmetric events with a positive (negative) charged lepton in data originating from W+Jets processes. These yields are estimated by subtracting other charge asymmetric contributions in MC ($t\bar{t}+V$, single top) from the data yields. Other non-W+Jets contributions in MC ($t\bar{t}$, diboson, Z+Jets, multijets) are treated as charge symmetric and cancel out in the $(D_{\text{asym},+}^{\text{pre-tag}} - D_{\text{asym},-}^{\text{pre-tag}})$ term. Figure 37 shows an overview of the asymmetries in lepton charge observed for the different background samples at pre-tag level, while samples with an asymmetry within $\pm 3\%$ are considered as symmetric. A smaller tolerance has not shown any significant changes in the final SFs. The charge asymmetry normalization n_{CA} is obtained by comparing the yields of W+Jets events in MC and data $n_{\text{CA}} = \frac{N_{\text{data},W}^{\text{pre-tag}}}{N_{\text{MC},W}^{\text{pre-tag}}}$.

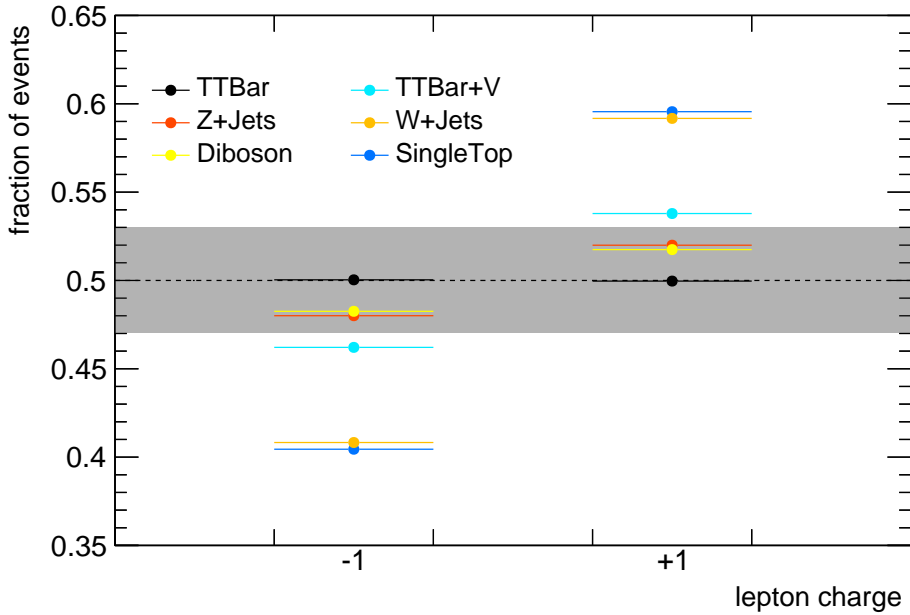


Figure 37: Charge asymmetry for MC background samples at pre-tag level, showing the difference in fraction of events with negative or positive lepton charge. Samples with an asymmetry within $\pm 3\%$ are considered as symmetric.

7.2.2 Flavor normalization

Three unknown SFs $K_{bb,cc}$, K_c and K_{ll} , are obtained from a linear equation system with three independent equations shown in equation (7.6). The bb and cc flavor components are treated jointly since they arise from very similar processes and allows to solve an equation system of three linear equations.

$$\begin{pmatrix} n_{CA} \cdot (N_{MC,W^-}^{bb} + N_{MC,W^-}^{cc}) & n_{CA} \cdot N_{MC,W^-}^c & n_{CA} \cdot N_{MC,W^-}^{ll} \\ (f_{bb} + f_{cc}) & f_c & f_{ll} \\ n_{CA} \cdot (N_{MC,W^+}^{bb} + N_{MC,W^+}^{cc}) & n_{CA} \cdot N_{MC,W^+}^c & n_{CA} \cdot N_{MC,W^+}^{ll} \end{pmatrix} \cdot \begin{pmatrix} K_{bb,cc} \\ K_c \\ K_{ll} \end{pmatrix} = \begin{pmatrix} D_{W^-} \\ 1.0 \\ D_{W^+} \end{pmatrix} \quad (7.6)$$

These equations contain the event yields N_{MC,W^\pm}^i for a given W-boson charge W^\pm and flavor $i \in [bb, cc, c, ll]$ in simulation at tag level and the number of tagged W+Jets events in data D_{W^\pm} , obtained by subtracting all non-W+Jets MC contributions from the data yields at tag level as in equation (7.7).

$$D_{W^\pm} = N_{\text{data}}^\pm - N_{MC}^\pm \quad (7.7)$$

The factors f_i represent the fraction of W+Jets events for a given flavor at pre-tag level as defined in equation (7.8).

$$f_i = \frac{N_{MC,W^+}^{i,\text{pre-tag}} + N_{MC,W^-}^{i,\text{pre-tag}}}{\sum_j (N_{MC,W^+}^{j,\text{pre-tag}} + N_{MC,W^-}^{j,\text{pre-tag}})} = \frac{N_{MC,W}^{i,\text{pre-tag}}}{N_{MC,W}^{\text{pre-tag}}} \quad \text{for } i, j \in [bb, cc, c, ll] \quad (7.8)$$

Hence the second row of the linear equation system in equation (7.6) denotes the intuitive requirement, that the total sum of all flavor fractions after applying the SFs has to remain constant, see equation (7.9).

$$(f_{bb} + f_{cc}) \cdot K_{bb,cc} + f_c \cdot K_c + f_{ll} \cdot K_{ll} = 1.0 \quad (7.9)$$

An extrapolation factor $k_{bbtocc} = \frac{f_{cc}}{f_{bb}}$ is calculated from the initial fractions and f_{cc} in equation (7.9) can be replaced by $f_{cc} = f_{bb} \cdot k_{bbtocc}$.

The first and third line of the linear equation system in equation (7.6) represent the adaption of the MC yields to the data yields at tag level by applying the SFs K_i for each flavor i and the charge asymmetry normalization, as expanded in equation (7.10).

$$n_{CA} \cdot \left((N_{MC,W^\pm}^{bb} + N_{MC,W^\pm}^{cc}) \cdot K_{bb,cc} + N_{MC,W^\pm}^c \cdot K_c + N_{MC,W^\pm}^{ll} \cdot K_{ll} \right) = D_{W^\pm} \quad (7.10)$$

The linear equation system is solved for the vector $(K_{bb,cc}, K_{cc}, K_c)^T$ in an iterative process for the 2 exclusive jet multiplicity bin, applying the SFs to the pre-tag yields after each

iteration and recalculating the charge asymmetry normalization n_{CA} . The flavor fractions f_i are not altered within the iterative process. This procedure converges to suitable precision after already about 10 iterations. The 2 exclusive jet multiplicity bin has been chosen for this procedure, since it shows the most stable behavior with the smallest systematic uncertainty mainly arising from b-tagging/light tagging efficiency and heavy flavor components of the W+Jets background as well as suitable statistic dominated by the W+Jets background [102].

Starting with default values $K_i = 1.0$, the iterative process loops over the following steps

1. Apply scale factors K_i to MC pre-tag yields used for calculation of n_{CA} , i.e.

$$N_{MC,W^\pm}^{\text{pre-tag}} = \sum_i N_{MC,W^\pm}^{j,\text{pre-tag}} \cdot K_i \quad \text{for } i \in [bb, cc, c, ll]$$
2. Calculate charge asymmetry normalization n_{CA} (cf. section 7.2.1)
3. Build linear equation system $M_{3 \times 3} \cdot \vec{K} = \vec{D}$
4. Solve equation system for scale factors $\vec{K} = M_{3 \times 3}^{-1} \cdot \vec{D}$
5. Go back to step 1.

After this iterative process, also the flavor fractions f_i are altered by applying the final SFs K_i , while keeping the ratio of f_{cc} and f_{bb} constant, as stated before.

$$f_i^{2\text{ex, final}} = f_i^{2\text{ex}} \cdot K_i^{2\text{ex}} \quad \text{for } i \in [bb, cc, c, ll] \quad (7.11)$$

Afterwards the SFs are extrapolated to the other jet multiplicity bins j by applying the changes of the flavor fraction of the 2 exclusive jet bin to each flavor i , calculating the final SF K_i^j . Note that the resulting sum of flavor fractions has to be normalized within each jet multiplicity bin.

$$f_i^{j,\text{final}} = f_i^j \frac{f_i^{2\text{ex, final}}}{f_i^{2\text{ex}}} \quad K_i^j = \frac{f_i^{j,\text{final}}}{f_i^j} \quad (7.12)$$

The SFs obtained for the resolved selection in the e +jets and μ +jets channel are listed in table 15 including statistical uncertainties.

A more quantitative understanding is given by the actual distributions of jet multiplicities for all lepton charges combined shown in figure 38 before and after the iterative procedure at pre-tag and tag level for the e +jets and μ +jets channel. The top panel shows the number of events in the given jet multiplicity bin, showing the contribution of each background sample and explicitly split into flavor contributions for the W+Jets background, overlaid by the number of observed data events. The bottom panel shows a ratio of observed data and Standard Model expectations as a qualitative comparison. The iterative procedure fixes the data/MC ratio for the 2 exclusive bin at tag level to 1.0 as shown in figure 38(f) and figure 38(h), denoting a by construction perfect agreement between data and background. Also other jet multiplicity bins show an improved data/MC ratio after applying the resulting SFs.

Earlier iterations of this analysis used one single set of SFs applied in the main analysis with a corresponding systematic uncertainty applied. Since the W+Jets contributions as major background in this analysis affects many other systematic uncertainties, this resulted in a double counting of the impact of some systematic uncertainties. This issue is studied intensively within the context of this thesis by providing a single set of W+Jets SFs for each major systematic uncertainty in this analysis. Therefore the input yields are recalculated for each major systematic uncertainty, plugged into the presented procedure and a final set of scale factors is retrieved. This new procedure has an overall diminishing effect on several systematic uncertainties, reducing the impact of the W+Jets background and avoiding double counting (cf. section 8.3.2).

7.3 W+Jets normalization in boosted topology

The heavy flavor SFs derived for the resolved selection in section 7.2.2 are used for the boosted selection as well. The charge asymmetry normalization though is recalculated for the different kinematic regime in the boosted selection. Since the final signal region selection event yield after the boosted selection is too small for a reliable evaluation of the appropriate SFs, a specific boosted W+Jets control region selection is used. Therefore the selection (cf. section 6.2.2) is loosened by dropping the b-tagging requirement and the jet mass and $\sqrt{d_{12}}$ cuts as well as the $\Delta\phi(j, \ell)$ requirement for the hadronic top-jet selection to enhance the event acceptance.

Analyzing the events in this boosted W+Jets control region and applying the W+Jets SFs derived for the resolved topology without applying the charge asymmetry normalization, the obtained yields for positive/negative charged leptons are used to recalculate the charge asymmetry normalization n_{CA} following the procedure presented in section 7.2.1. Only one overall charge asymmetry normalization is calculated for all jet multiplicity bins as listed in table 16.

7.4 Application of W+Jets scale factors

The W+Jets SFs are applied to each individual event. To ease the application for all analyzers, a tool has been developed and added to the `ttResoSingleLepton` common analysis code package. This tool takes the lepton channel, W+Jets flavor and the jet multiplicity bin as input and returns an event weight for this given setup.

The W+Jets yields at pre-tag level used during the derivation of the SFs are shipped with the tool and used as starting point. These yields $N_i^{j,\text{in}}$ for a given W+Jets flavor i and jet multiplicity bin j are altered with the corresponding SF K_i^j for the given setup.

$$N_i^{j,\text{out}} = N_i^{j,\text{in}} \cdot K_i^j \quad (7.13)$$

Bin	K_{bb}	K_{cc}	K_c	K_u	n_{CA}
1ex	1.444 ± 0.078	1.444 ± 0.078	0.759 ± 0.031	1.019 ± 0.005	1.046 ± 0.011
2ex	1.419 ± 0.077	1.419 ± 0.077	0.746 ± 0.030	1.001 ± 0.005	1.051 ± 0.011
3ex	1.384 ± 0.075	1.384 ± 0.075	0.728 ± 0.030	0.976 ± 0.005	1.003 ± 0.011
4ex	1.348 ± 0.073	1.348 ± 0.073	0.709 ± 0.029	0.951 ± 0.005	1.017 ± 0.011
5in	1.305 ± 0.070	1.305 ± 0.070	0.686 ± 0.028	0.921 ± 0.004	1.045 ± 0.011
3in	1.373 ± 0.074	1.373 ± 0.074	0.722 ± 0.029	0.969 ± 0.005	1.007 ± 0.011
4in	1.338 ± 0.072	1.338 ± 0.072	0.703 ± 0.029	0.944 ± 0.005	1.023 ± 0.011

(a) e +jets channel

Bin	K_{bb}	K_{cc}	K_c	K_u	n_{CA}
1ex	1.745 ± 0.060	1.745 ± 0.060	0.739 ± 0.025	1.004 ± 0.004	1.042 ± 0.006
2ex	1.683 ± 0.058	1.683 ± 0.058	0.713 ± 0.024	0.968 ± 0.004	1.065 ± 0.006
3ex	1.612 ± 0.055	1.612 ± 0.055	0.683 ± 0.023	0.927 ± 0.003	1.015 ± 0.006
4ex	1.539 ± 0.053	1.539 ± 0.053	0.652 ± 0.022	0.885 ± 0.003	0.977 ± 0.006
5in	1.468 ± 0.050	1.468 ± 0.050	0.622 ± 0.021	0.844 ± 0.003	0.972 ± 0.006
3in	1.590 ± 0.054	1.590 ± 0.054	0.673 ± 0.023	0.914 ± 0.003	1.003 ± 0.006
4in	1.522 ± 0.052	1.522 ± 0.052	0.645 ± 0.022	0.875 ± 0.003	0.975 ± 0.006

(b) μ +jets channel

Table 15: W +Jets scale factors for each W +Jets flavor and the charge asymmetry normalization in different jet multiplicity bins for the (a) e +jets and (b) μ +jets channel. This analysis uses the 4 inclusive (4in) jet bin in the resolved and 2 exclusive (2ex) jet bin in the boosted selection, other jet bins are provided for other analysis.

channel	n_{CA}
e +jets	0.807 ± 0.010
μ +jets	0.730 ± 0.005

Table 16: The charge asymmetry normalization for the boosted topology for the e +jets and μ +jets channel.

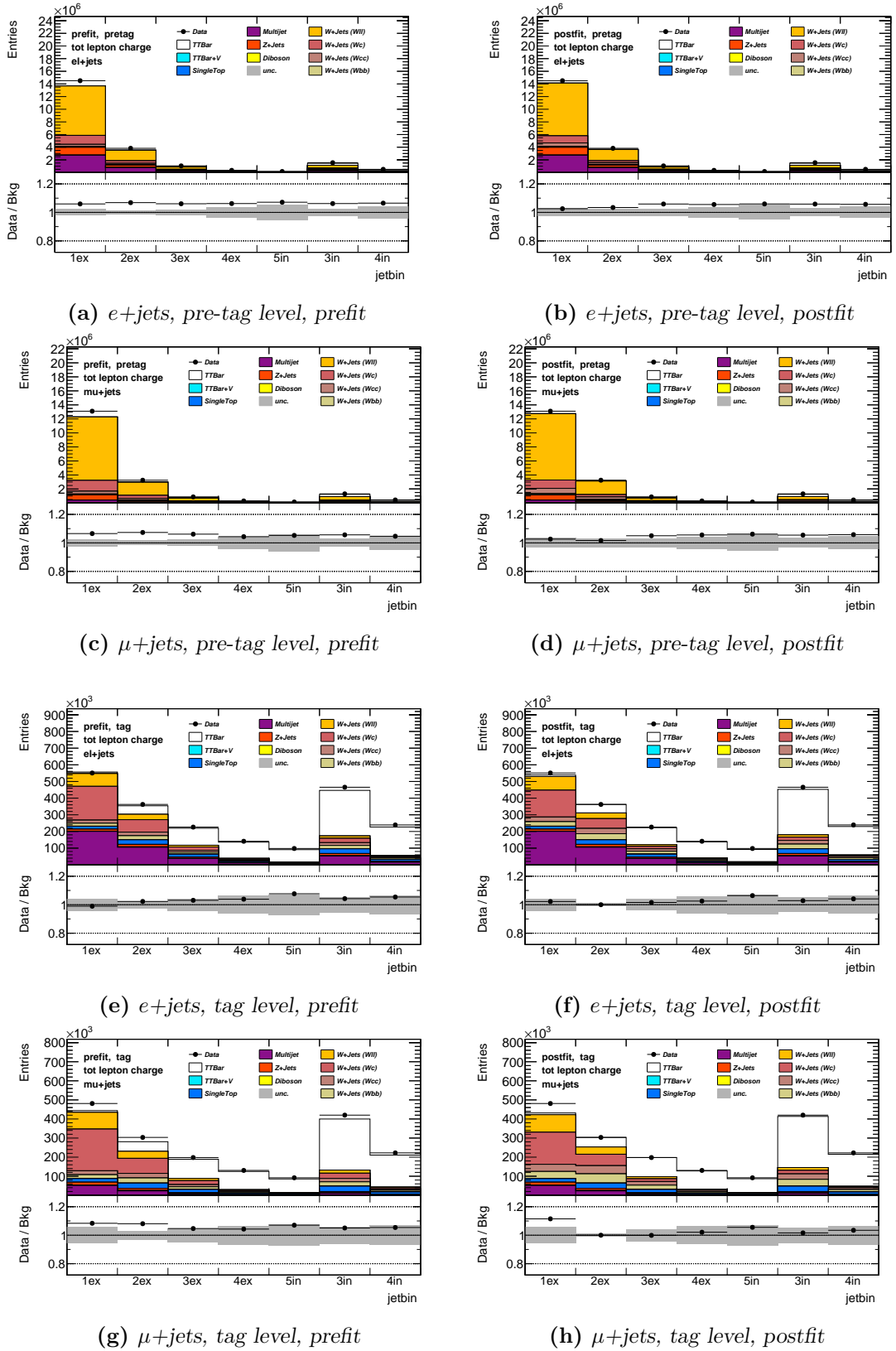


Figure 38: Jet multiplicities for W+Jets normalization for all lepton charges combined, at pre-tag level (a),(c) before and (b),(d) after the iterative procedure and at tag level (e),(g) before and (f),(h) after the iterative procedure for $e+jets$ and $\mu+jets$ channel respectively, applying statistical variation on the flavor fractions as gray uncertainty band.

Since the heavy flavor SFs are only used to correct the composition of flavors, but must not have an effect on the overall normalization of the yields, the sum of output yields is normalized to the sum of input yields. The normalization of the W+Jets background is treated afterwards applying the charge asymmetry normalization $n_{CA,j}$.

The final event weight w for the given jet multiplicity bin j is calculated as in equation (7.14).

$$w = N_i^{j,\text{out}}/N_i^{j,\text{in}} \cdot n_{CA,j} \quad (7.14)$$

7.5 Differences in e +jets and μ +jets channel

Table 15 states a difference in single SFs of up to 13% between the e +jets and μ +jets channel. To confirm the reliability of the derived SFs, this difference is investigated in more detail.

The difference cannot be observed if only heavy flavor factors are applied to the corresponding samples, but not applying charge asymmetry normalization at tag level. Figure 40(a) shows a good agreement between e +jets and μ +jets channel, while the remaining differences are mostly covered within QCD uncertainty. Hence the main difference must be caused by the charge asymmetry factors, which differ by about $\sim 5\%$ between e +jets and μ +jets channel. Comparing the values of the r_{MC} ratio introduced in equation (7.5) for light flavor only ($W + e\nu$ and $W + \mu\nu$) and all (including heavy flavor) W+Jets samples shows the same difference in e +jets and μ +jets channel. Therefore the flavor composition itself is not the main cause of the difference in charge asymmetry.

Since the evolution of the r_{MC} ratio with the cuts applied in the analysis at pre-tag level does not show any significant effect, the detector acceptance for leptons in different η regions is analyzed. The ratio is expected to be strongly dependent on the detector region in lepton η with larger values for r_{MC} in the forward/backward region of the detector compared to the central region, since positively charged W-bosons are more likely to be produced in the non-central region due to their connection to valence quarks carrying a larger momentum fraction of the proton as discussed in section 7.1. This behavior is shown in figure 39(a), but one can also observe an independence of the lepton flavor, since the same acceptance is observed for e +jets and μ +jets channel. The difference in integrated r_{MC} values is caused by a different geometrical acceptance for electrons and muons in specific detector regions due to an individual trigger efficiency, so that muons are more likely to be selected in the forward/backward detector region, while electrons are more often selected in the central detector region, as shown in figure 39(b). This indicates an intrinsic preference of larger r_{MC} values for the μ +jets channel. While a symmetrization of the isolation criteria for electron/muons does not show a significant change, applying a p_T/η re-weighting to the truth leptons reduces the difference between the r_{MC} values in e +jets and μ +jets channel from $\sim 5\%$ to $\sim 2\%$.

Different phase spaces for the e +jets and μ +jets and hence channel specific PDF descriptions result in a distinction within the PDF uncertainty for the two channels. The difference in

e +jets and μ +jets channel due to the charge asymmetry is mostly covered within this PDF uncertainty, as shown in figure 40(b) at pre-tag level.

Hence it is understood, that the difference in the e +jets and μ +jets channel scale factors is mainly caused by different phase spaces for the e +jets and μ +jets channel and by detector acceptance for electrons/muons in central and forward/backward η regions and the scale factors are considered reliable. This study has also been discussed in [95].

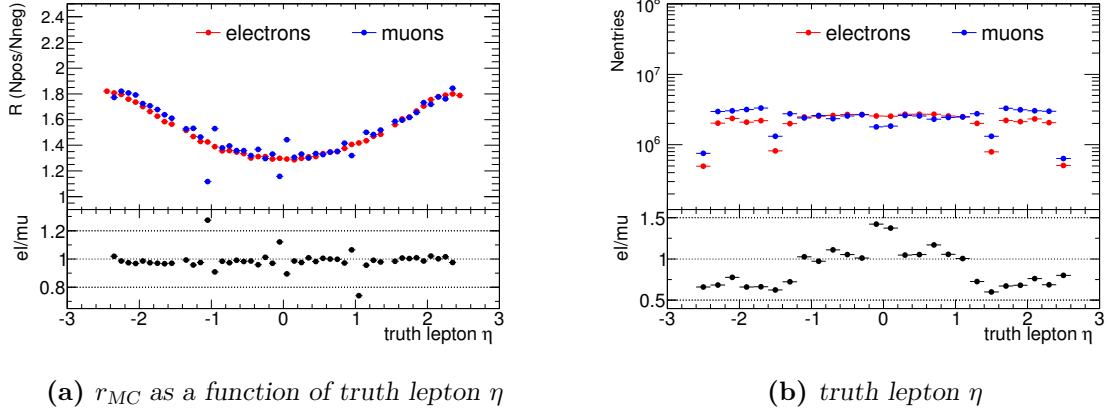


Figure 39: Detector acceptance for the (a) r_{MC} ratio and (b) truth leptons as a function of the truth lepton η at pre-tag level. (Large spikes in (a) for muons indicates the transition region of the muon chamber sub parts, where muons are bent into/out of the muon chamber by the magnetic field.)

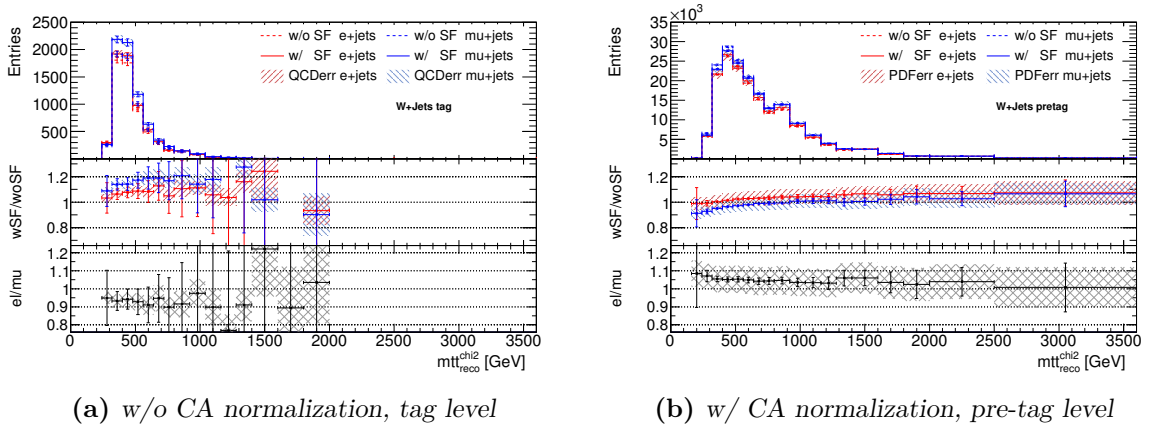


Figure 40: Effect of the W+Jets scale factors on the $m_{t\bar{t}}$ spectrum. Figure (a) does not apply charge asymmetry normalization (only flavor fraction correction) and compares with QCD uncertainty at tag level, figure (b) additionally applies charge asymmetry normalization and compares with PDF uncertainty at pre-tag level. Both figures also show a double ratio of the e +jets and μ +jets channel scale factor effect.

8

Systematic uncertainties

A good understanding of the impact of experimental and theoretical systematic uncertainties on the predictions for the signal and background processes is crucial for a reasonable interpretation of the final results. This section presents the systematic uncertainties taken into account in this analysis and the procedures used to estimate their impact. Beside a general uncertainty on the measured luminosity at the LHC described in section 8.1, systematic uncertainties can be divided into those affecting reconstructed objects like jets and leptons discussed in section 8.2 or those affecting the modeling of background or signal processes as presented in section 8.3. A smoothing is applied to the final systematic shift spectra introduced in section 8.4 and a summary of the impact of all systematic uncertainties is given in section 8.5.

8.1 Luminosity

The uncertainty on the integrated luminosity is 2.8%. It is derived, following the same methodology as that detailed in [105], from a preliminary calibration of the luminosity scale derived from beam separation scans performed in November 2012. This uncertainty is applied to all signal and background samples except multijet and W+Jets, since those are estimated from data.

8.2 Physics objects

Uncertainties on the identification and reconstruction of physics objects have a large impact on the final results of the analysis and are discussed in the following. A more detailed discussion can be found in [8] and [95].

8.2.1 Leptons

The lepton identification and reconstruction is affected by isolation efficiency as well as trigger and reconstruction efficiency of the single-lepton triggers, which are estimated from $Z \rightarrow ee$ and $Z \rightarrow \mu\mu$ events. To account for the different event topologies of Z and $t\bar{t}$ events, these uncertainties are corrected using studies of high jet multiplicity $Z \rightarrow \ell\ell$ events. A smaller impact is observed for uncertainties on the energy scale and reconstruction for leptons.

8.2.2 Small radius jets

The small radius anti- k_t jet collection is studied for uncertainties on the jet energy scale (JES) and jet energy resolution (JER), as well as uncertainties on the jet vertex fraction (JVF). The JES uncertainty is broken down into specific sub-components, while most of them are found to have a minor impact and are added in quadrature for one combined component, some major impact components are treated explicitly. The overall JES uncertainty is one of the systematic uncertainties with the biggest impact in the resolved selection.

8.2.3 Large radius jets

The large radius anti- k_t jet collection is similarly studied for JES and JER uncertainties, also here with a breakdown of JES components analyzed for major impact components. Since special cuts on jet masses are applied for this collection in the boosted selection, also uncertainties on the jet mass resolution (JMR) and jet mass scale (JMS) as well as dependence on the k_t splitting scale are taken into account. Especially the scale uncertainties have a big impact on the boosted selection, while the impact of large radius jet uncertainties is of minor importance for the resolved selection, since it is only affected passively due to veto on events passing the boosted selection.

8.2.4 B-tagging

Simultaneous variations of the uncertainties on the b-tagging efficiency and rejection provide an estimate for the b-tagging uncertainty. The uncertainties on c- and light-jets tagging (mis-tag rates) are of minor impact and hence used as a combined uncertainty each instead of component breakdown. The identification of b-jets on the contrary was studied in eigenvector variation breakdown, considering the most relevant ones. To account for uncertainties on the modeling of the track reconstruction in high- p_T environments, an additional b-tagging uncertainty for high-momentum jets above $p_T > 300$ GeV is applied with a strong impact on large resonance masses.

8.3 Backgrounds

The following subsections describe uncertainties affecting specific processes such as the $t\bar{t}$ decay and W-boson production in association with jets as the main backgrounds as well as an estimation of multijet processes and other minor backgrounds.

8.3.1 TTBar

Since the contribution from Standard Model $t\bar{t}$ processes is the dominant and irreducible background in this analysis, the estimation of systematic uncertainties affecting $t\bar{t}$ processes is an essential task, studied explicitly for different sources as presented in the following.

Overall normalisation

The overall normalization uncertainty on the total background is dominated by the $t\bar{t}$ cross section uncertainty. It's calculated in QCD at NNLO level including re-summation of next-to-next-to-leading logarithmic (NNLL) soft gluon terms, resulting in an uncertainty of 6.5%.

Generator uncertainties

Several generators are available for MC sample production. Even though the one describing the background best (in comparison to data) is chosen, the choice of NLO $t\bar{t}$ can affect the result, as well as the choice of generators used for parton showering and fragmentation. To account for these systematic uncertainties the nominal POWHEG+PYTHIA spectra are compared to generator setups POWHEG+HERWIG (at ATLAS Fast Simulation (AFII) level) and MC@NLO+HERWIG (at Full Simulation (FS) level). With the event yield per bin i for the given generator setup y_{setup}^i the variation Δ^i is applied symmetrically.

The generator uncertainty (MCGen) is derived via equation (8.1).

$$\Delta_{\text{MCGen}}^i = \left(y_{\text{FS, POWHEG+PYTHIA}}^i - y_{\text{FS, MC@NLO+HERWIG}}^i \right) \quad (8.1)$$

The parton shower uncertainty (PS) is corrected with a factor accounting for differences for the full simulation in the nominal samples and the ATLAS Fast Simulation, derived via equation (8.2).

$$\Delta_{\text{PS}}^i = \left(y_{\text{AFII, POWHEG+PYTHIA}}^i - y_{\text{AFII, POWHEG+HERWIG}}^i \right) \cdot \frac{y_{\text{nominal}}^i}{y_{\text{AFII, POWHEG+PYTHIA}}^i} \quad (8.2)$$

Top mass uncertainty

The nominal $t\bar{t}$ MC sample is produced with a reference top mass of $m_t = 172.5$ GeV. The uncertainty on the shape of the $m_{t\bar{t}}$ distributions from this choice is evaluated by comparing the shapes with two POWHEG+PYTHIA MC samples produced with reference top masses of $m_t^{\text{up}} = 175.0$ GeV and $m_t^{\text{down}} = 170.0$ GeV. To approximate a 1.0 GeV uncertainty on the top quark mass, reflecting uncertainties on recent top mass measurements (cf. section 2.5.4),

the difference to the nominal sample is scaled by a factor of 0.4 and the cross sections used for the different samples are adapted to the nominal sample to avoid double counting in the normalization uncertainty, which is treated separately. With the event yield per bin i for the nominal sample y_{nominal}^i and the up/down variation for the systematic samples $y_{\text{up/down}}^i$, the uncertainty $\Delta_{\text{topmass,up/down}}^i$ is derived as

$$\Delta_{\text{topmass,up/down}}^i = 0.4 \cdot \left(y_{\text{up/down}}^i - y_{\text{nominal}}^i \right) \quad (8.3)$$

QCD ISR/FSR

The uncertainty due to initial- and final state QCD radiation (ISR/FSR) is estimated from ACERMC+PYTHIA Monte Carlo samples generated with up and down variations of the PYTHIA ISR and FSR parameters. Comparing the up/down variation event yields $y_{\text{up/down}}^i$ for bin i with the nominal event yield y_{nominal}^i obtained from a MC@NLO sample, the 1σ variation $\Delta_{\text{ISR/FSR}}^i$ is applied symmetrically to the MC@NLO sample after computing

$$\Delta_{\text{ISR/FSR}}^i = \frac{\left| y_{\text{up}}^i - y_{\text{down}}^i \right|}{\left(y_{\text{up}}^i + y_{\text{down}}^i \right)} \cdot y_{\text{nominal}}^i \quad (8.4)$$

8.3.2 W+Jets

Uncertainties on W+Jets are mainly driven by scale and parton matching uncertainties as well as the composition of heavy flavor contributions and corresponding normalization.

Scale and parton matching uncertainties

W+Jets MC modeling provides a number of tunable parameters with the default values chosen to best reproduce data samples. Uncertainties on shape-changing effects can be estimated by shifting these parameters and re-scaling events accordingly, e.g. using the p_T of the leading jet per event as reference. Two parameter variations have turned out to have the most significant impact on the final observables and are considered in this analysis

- iqopt3 : functional form of the factorization and re-normalization scale tuning
- ptjmin10 : minimum $p_T > 10$ GeV threshold for partons considered in showering (setup for default samples is $p_T > 15$ GeV)

The systematic impact of these parameters is considered by applying a re-weighting on event-basis, depending on the leading jet p_T per event. To avoid double counting of the W+Jets normalization uncertainty, which is treated separately in the context of the W+Jets SF procedure (cf. chapter 7), the varied spectra are normalized to the nominal yields.

The fit functions for the ptjmin10 uncertainty applied as a scale function were derived for a precedent analysis, not considering high p_T regions explicitly (due to the lower center of mass energy used in this analysis), resulting in a non-reasonable divergent behavior of the scale functions for high p_T regions. For the increased center of mass energy data used in this

analysis, these high p_T regions are crucial for the boosted topology reconstruction. Hence this uncertainty was re-derived for a higher threshold of $p_T > 25$ GeV (ptjmin25) providing new functions to estimate this uncertainty as shown in figure 41 using the example of the 4 inclusive and all jet bins combined. Figure 42 shows the impact of the ptjmin systematic uncertainty on the final $m_{t\bar{t}}$ discriminant spectrum for the two p_T threshold setups. The bottom panels show the ratio between the up/down variation due to the ptjmin systematic compared to the nominal spectrum, denoting the divergent character of the ptjmin10 uncertainty in figure 42(a), while the re-derived ptjmin25 uncertainty in figure 42(b) shows a much more stable behavior in high p_T regions. Consequently the ptjmin10 uncertainty is replaced by the re-derived ptjmin25 uncertainty in this thesis.

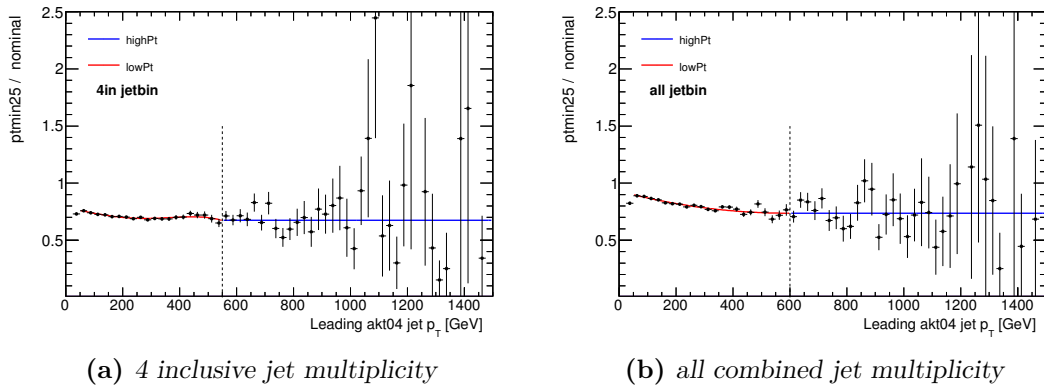


Figure 41: Fits of the comparison for ALPGEN showering with nominal ($p_T > 10$ GeV) and altered minimum p_T threshold for partons for derivation of $ptjmin25$ ($p_T > 25$ GeV) $W+Jets$ uncertainty weights depending on the leading jet p_T per event in different jet multiplicity bins, here shown using the example of the (a) 4 inclusive and (b) all combined jet multiplicity bin.

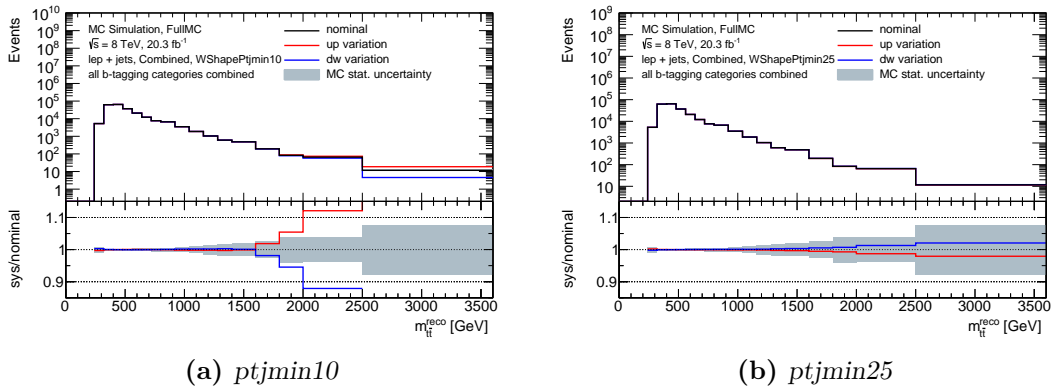


Figure 42: Comparison of the impact of the (a) $ptjmin10$ and (b) $ptjmin25$ systematic uncertainties on the final $m_{t\bar{t}}$ distributions. The upper panel shows the $m_{t\bar{t}}$ distribution for the nominal spectrum and the up/down variation due to the applied systematic. The bottom panel shows the ratio of the variation compared to the nominal spectrum.

Heavy flavor and normalization scaling

Uncertainties on the composition of the W+Jets background from different heavy flavor contributions and normalization scale factors are taken into account by applying a specific data-driven scale factor for each major systematic uncertainty used in this analysis (cf. chapter 7). These scale factors are applied in the evaluation of the corresponding systematic variation spectra with a generally diminishing effect on the systematic variation as shown in figure 43 using the example of two systematic uncertainties.

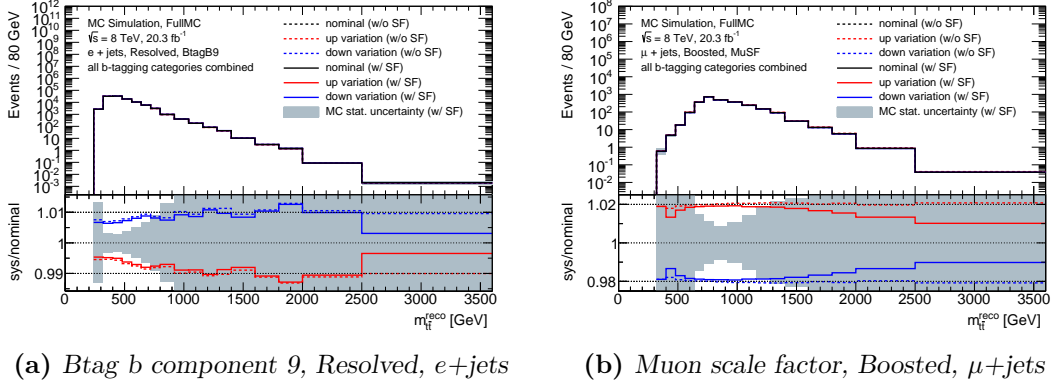


Figure 43: Effect of W+Jets scale factors on the impact of different systematic uncertainties, shown here using the example of the (a) *btag b component 9 (BtagB9) in the resolved selection, e+jets channel* and the (b) *Muon scale factor (MuSF) in the boosted selection, μ +jets channel*.

8.3.3 Multijet

Systematic uncertainties on multijet processes are evaluated using several different definitions of multijet control regions that result in slightly different estimations of the false-identification rate f (cf. section 5.2.6). Systematic uncertainties associated with object reconstruction and MC simulation are also considered, resulting in a total normalization uncertainty of 20%.

8.3.4 Other backgrounds

Other minor backgrounds are assigned with a normalization uncertainty, as of 7.7% for single top and 48% for Z+Jets processes. For diboson processes a combination of the NLO PDF and scale uncertainties as well as additional uncertainties from the requirements on the jet multiplicity is used, resulting in a final normalization uncertainty of 34%. More details on these uncertainties can be found in [95].

8.3.5 PDF uncertainties

The procedure used to derive the PDF uncertainties follows the *TopPdfUncertainty* [106] prescriptions considering three different PDFsets, provided¹ by the LHAPDF group [107].

¹Version 6.0.5 from <http://lhapdf.hepforge.org/>

- CT10 : CT10n1o (central + 52 error sets) [108, 109]
- MSTW : MSTW2008n1o68c1 (central + 40 error sets) [31, 110]
- NNPDF : NNPDF23_n1o_as_0118 (central + ensemble of 100 PDFs) [111]

Each of these PDFsets provides a central PDF value X_0 and a certain number N of error set variations $X_{1..N}$, varying around the central value. Each PDFset is combined to a PDFset specific overall uncertainty for up ΔX_0^{up} and down ΔX_0^{down} variation using the Intra-PDF procedure and these are afterwards combined to an overall Inter-PDF uncertainty envelope. A unique set of W+Jets SFs (cf. chapter 7) is derived for each individual PDF set variation.

CT10

The CT10 PDFset provides a central ($n = 0$) variation and $N_{\text{CT10}} = 52$ error set variations, while each even variation ($2n$) is an up-variation and each uneven variation ($2n - 1$) is the corresponding down-variation. The Intra-PDF procedure used for this PDFset is the symmetric Hessian, checking the difference for each variation pair, not taking the central value into account as shown in equation (8.5). This uncertainty is applied symmetrically for up/down uncertainty, i.e. $X_0^{\text{up}} = X_0 + \Delta X_0$ and $X_0^{\text{down}} = X_0 - \Delta X_0$. In order to correspond to 68% confidence level errors, a reduction by a factor of 1.645 is applied.

$$\Delta X_0 = \frac{1}{2} \cdot \sqrt{\frac{1}{1.645} \cdot \sum_{n=1}^{N/2} (X_n - X_{(n+1)})^2} \quad (8.5)$$

MSTW

The MSTW PDFset provides a central ($n = 0$) variation and $N_{\text{MSTW}} = 40$ error set variations, while each even variation ($2n$) is an up-variation and each odd variation ($2n - 1$) is the corresponding down variation. The Intra-PDF procedure for this PDFset is the asymmetric Hessian, checking for the direction of each pair of variations and adding them correspondingly to the up/down uncertainty combination, i.e. $X_0^{\text{up}} = X_0 + \Delta X_0^{\text{up}}$ and $X_0^{\text{down}} = X_0 - \Delta X_0^{\text{down}}$. If both lead into the same direction, the larger one is applied to both combinations as shown in equation (8.6) and (8.7).

$$\Delta X_0^{\text{up}} = \sqrt{\sum_{n=1}^{N/2} \left(\max[0, (X_{2n} - X_0), (X_{2n-1} - X_0)] \right)^2} \quad (8.6)$$

$$\Delta X_0^{\text{down}} = \sqrt{\sum_{n=1}^{N/2} \left(\max[0, (X_0 - X_{2n}), (X_0 - X_{2n-1})] \right)^2} \quad (8.7)$$

NNPDF

The NNPDF PDFset does not provide a set of explicit up/down variation PDFs, but a mean value ($n = 0$) and other PDFs ($n > 0$) with parameters varied to provide a full ensemble of $N_{\text{NNPDF}} = 100$ PDFs instead. In that way the best value is the mean of all the ensembles (already provided as PDF $n = 0$), shown in equation (8.8) and the intra-PDF uncertainty is the standard deviation (on a sample ensemble, which requires $N-1$ in the denominator) as shown in equation (8.9). This uncertainty is applied symmetrically for up/down uncertainty, i.e. $X_0^{\text{up}} = X_0 + \Delta X_0$ and $X_0^{\text{down}} = X_0 - \Delta X_0$.

$$X_0 = \frac{1}{N} \cdot \sum_{n=1}^{N/2} X_n \quad (8.8)$$

$$\Delta X_0 = \sqrt{\frac{1}{N-1} \cdot \sum_{n=1}^{N/2} (X_n - X_0)^2} \quad (8.9)$$

PDF Combination

The Inter-PDF uncertainty is calculated by creating an envelope of the uncertainties of all three PDF sets. Therefore the PDF sets are combined in a linear way, taking the mean of central values of each PDF set i as combined central value as shown in equation (8.10) and the extremum (min and max) of the variations of each PDF set i is taken and the half of the interval is used as uncertainty, as shown in equation (8.11).

$$X_0^{\text{mean}} = \frac{1}{3} \cdot \sum_i X_0^i \quad \text{for each PDFset } i \in [\text{CT10}, \text{MSTW}, \text{NNPDF}] \quad (8.10)$$

$$\Delta X_0^{\text{mean}} = \frac{1}{2} \cdot \left| \max[X_0^i + \Delta X_0^{i,\text{up}}] - \min[X_0^i - \Delta X_0^{i,\text{down}}] \right| \quad (8.11)$$

The PDF set used for each sample in first order is ignored and the uncertainty is calculated on these three PDFsets instead. Hence a shifted central value is not applied in the analysis, but the uncertainty envelope is applied to the nominal value for each sample. Figure 44 shows the combined InterPDF uncertainties. More plots of the IntraPDF uncertainties can be found in the appendix A.4.

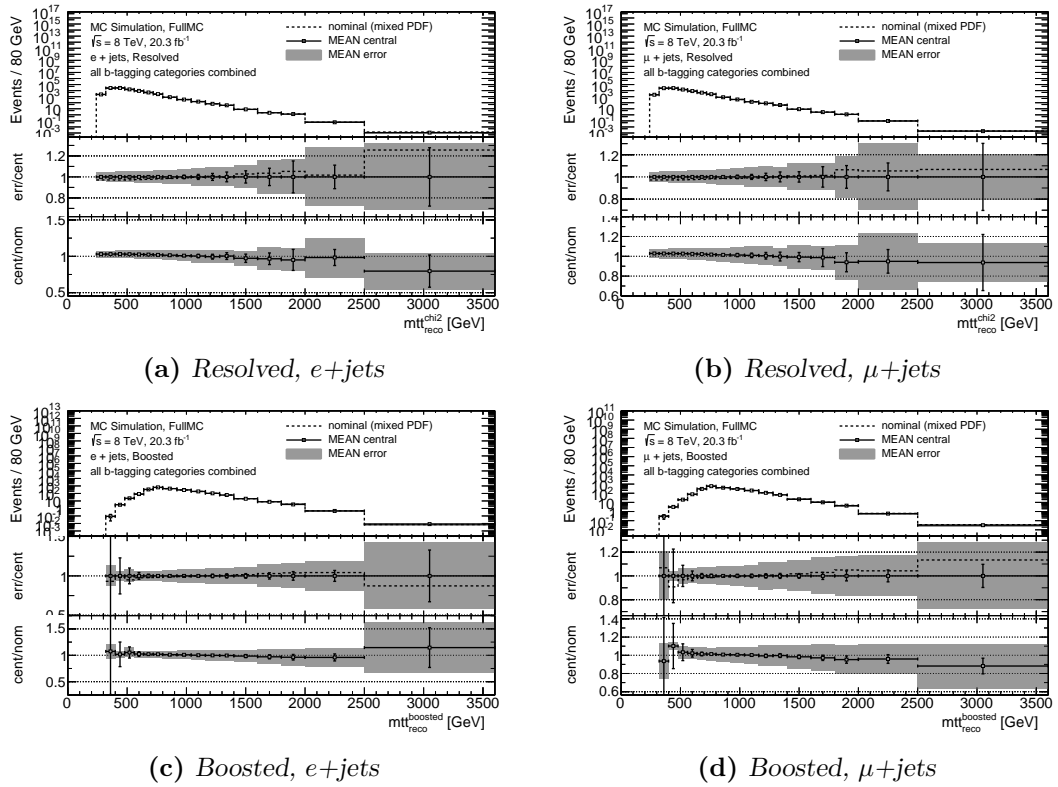


Figure 44: Combined InterPDF uncertainties on the $m_{t\bar{t}}$ spectrum for the Resolved selection in (a) $e+jets$ and (b) $\mu+jets$ channel and for the Boosted selection in (c) $e+jets$ and (d) $\mu+jets$ channel. The grey band shows the final PDF variation, illustrated in a ratio compared to the central variation and to the nominal spectrum.

8.4 Smoothing procedure

Small impact systematic uncertainties often suffer from statistical fluctuations, leading to an overestimation in single bins. A smoothing procedure is applied to prevent this non-trivial effect, which, beside the large number of systematic uncertainties, may lead to problems in profiling and/or over-constraints of nuisance parameters or even failure of fitting convergence when searching for excesses in the final spectra. This procedure is applied to all systematic uncertainties involving differences in event selections, this includes e.g. energy correction or MC comparison uncertainties, while uncertainties defined by altered scale-factors are not considered for smoothing, since they do not suffer from statistical fluctuations.

The smoothing procedure searches for bins with statistically insignificant systematic variations and merges them, averaging their impact as a more reliable estimation. For each bin i the relative statistical uncertainty Δ_{stat}^i as defined in equation (8.12) with the statistical error of the nominal histogram e_{nom}^i and the systematic variation e_{var}^i and the nominal yield n_{nom}^i is calculated.

$$\Delta_{\text{stat}}^i = \frac{\sqrt{(e_{\text{nom}}^i)^2 + (e_{\text{var}}^i)^2}}{n_{\text{nom}}^i} \quad (8.12)$$

Looping over the bins sorted in descending order of their statistical variation, if the systematic variation in the considered bin i with defined as $\Delta_{\text{syst}}^i = |n_{\text{var}}^i - n_{\text{nom}}^i|$ is smaller than twice the statistical uncertainty as defined in equation (8.13), this bin is considered to be merged with one of its neighbors to improve the statistical significance.

$$\frac{\Delta_{\text{syst}}^i}{\Delta_{\text{stat}}^i} \stackrel{!}{\leq} 2.0 \quad (8.13)$$

Merging with a neighbor bin j is considered appropriate only, if the neighbor bin also satisfies the threshold defined in equation (8.13) or the relative systematic uncertainty after merging doesn't exceed twice the statistical uncertainty of the current bin, cf. equation (8.14).

$$\frac{|\Delta_{\text{syst}}^i + \Delta_{\text{syst}}^j|}{\Delta_{\text{stat}}^i} \cdot \frac{n_{\text{nom}}^i}{n_{\text{nom}}^i + n_{\text{nom}}^j} \stackrel{!}{\leq} 2.0 \quad (8.14)$$

If both the left and right adjacent bins fulfill one of these conditions, and hence are both considered appropriate for merging, the bin with the larger relative statistical uncertainty is chosen for merging, see equation (8.15).

$$\text{bin considered for merging : } \max \left(\frac{\Delta_{\text{stat}}^{\text{left}}}{n_{\text{nom}}^{\text{left}}}, \frac{\Delta_{\text{stat}}^{\text{right}}}{n_{\text{nom}}^{\text{right}}} \right) \quad (8.15)$$

If the current bin is not considered for merging, the bin with the next largest relative statistical uncertainty Δ_{stat}^i is checked. If the current bin is merged, the bin loop starts from the beginning considering the reduced number of bins. If no bin is considered for merging or the histograms has only one bin left, the iterative procedure ends.

After this procedure, the original binning is restored, but adapting the systematic variation for merged bins. The effect of the procedure on the spectra is shown in figure 45 using the example of the small radius jet energy resolution (JER) and large radius jet mass resolution (JMRBOOST) systematics (more plots can be found in the appendix A.3). These systematic uncertainties show large variations in high $m_{t\bar{t}}$ mass regions, all well within the statistical uncertainty. The smoothing procedure removes these fluctuations, complying with the bins with rather low statistical uncertainties around 500 (800) GeV in figure 45(a) (45(b)).

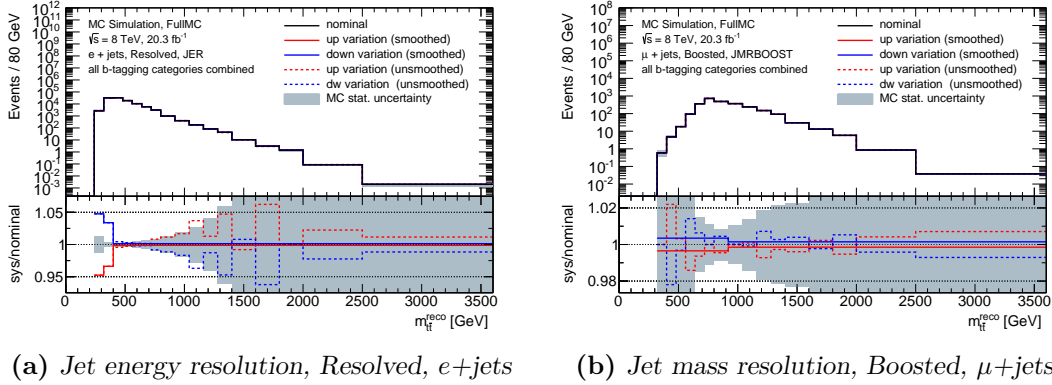


Figure 45: Effect of systematic smoothing exemplarily shown for (a) small radius jet energy resolution (JER) in the resolved selection, $e+jets$ channel and (b) large radius jet mass resolution (JMR) in boosted selection, $\mu+jets$ channel.

8.5 Summary

A summary of the dominant uncertainties in this analysis is given in table 17, stating the average relative impact on the total yield of summed background processes and a benchmark model Z' resonance with a mass of 1.75 TeV. Only the impact on the overall normalization is given while some systematic uncertainties have a significant effect on specific processes or a dependence on the reconstructed invariant $t\bar{t}$ mass $m_{t\bar{t}}$, fully taken into account in the analysis for all uncertainties. The strongest effects arise from the small radius jet energy scale (JES), parton distribution functions (PDF) and b-jet identification, but also $t\bar{t}$ normalization as well as parton shower and fragmentation has a larger uncertainty. The reconstruction in boosted topologies as for the Z' with a resonance mass of 1.75 TeV is especially affected by the b-tagging b-jet efficiency, dominated by the high- p_T b-tagging uncertainty.

The impact of each uncertainty on the reconstructed $m_{t\bar{t}}$ discriminant in the resolved and boosted selections in the $e+jets$ and $\mu+jets$ channel separately is shown in the appendix in section A.3.

Systematic uncertainties	Resolved		Boosted	
	impact [%]		impact [%]	
	Bkg.	Z'	Bkg.	Z'
Luminosity	2.5	2.8	2.6	2.8
Parton Distribution Function (PDF)	5.3	9.4	8.6	9.2
Initial (ISR) / Final state radiation (FSR)	4.2	-	4.0	-
$t\bar{t}$ parton shower and fragmentation	6.0	-	5.5	-
$t\bar{t}$ normalization	5.6	-	5.8	-
$t\bar{t}$ electro-weak virtual correction	0.2	-	0.3	-
$t\bar{t}$ generator	2.0	-	0.4	-
$t\bar{t}$ top quark mass	1.0	-	2.9	-
W+Jets generator	< 0.1	-	< 0.1	-
Multi-jet normalization e +jets	0.2	-	< 0.1	-
Multi-jet normalization μ +jets	0.1	-	< 0.1	-
Large-R jet energy (JES) / mass scale (JMS)	< 0.1	< 0.1	11.5	3.1
Large-R jet energy (JER) / mass resolution (JMR)	< 0.1	< 0.1	1.2	< 0.1
Small-R jet energy scale (JES)	5.7	3.0	0.4	1.6
Small-R jet energy resolution (JER)	1.0	4.2	0.9	0.9
Jet vertex fraction	2.7	2.3	0.3	0.1
b-tagging b-jet efficiency	1.0	2.0	2.8	17.1
b-tagging c-jet efficiency	0.1	0.7	0.1	2.1
b-tagging light-jet efficiency	< 0.1	< 0.1	0.1	0.2
Electron efficiency	0.3	0.6	0.6	1.3
Muon efficiency	0.9	1.0	0.9	1.1
MC statistical uncertainty	0.1	3.3	0.2	1.0
All systematic uncertainties	12.9	12.0	17.6	20.2

Table 17: Average impact of the dominant systematic uncertainties on the total background yield and on the estimated yield for a Z' resonance with a mass of 1.75 TeV for combined e +jets and μ +jets channel in resolved and boosted selection. Shifts are given in percent of the nominal yield. Uncertainties not applicable (e.g. uncertainties on $t\bar{t}$ modeling) for a Z' resonance are denoted with a bar (-) in the table.

9

Comparison of data and Standard Model expectations

After applying all event selection criteria, a total selected event yield of 224 105 and 8 209 remains in observed data, while a total of 214901 ± 27722 and 9232 ± 1625 are expected from simulation of Standard Model processes for the resolved and boosted selection respectively. Both yields agree within their uncertainties. The detailed expected yields for each background source are listed in table 18 including associated systematic uncertainties.

The following figures present a comparison between observed data and Standard Model expectations for the distributions of specific kinematic variables. Each figure is split into two panels. The top panel shows the Standard Model expectations in a stacked histogram, including $t\bar{t}$ (white), W+Jets (yellow) and all remaining (merged, blue) background processes. The statistical and total systematic uncertainty are plotted as gray and shaded uncertainty bands respectively. The figure is overlaid with the distributions for observed data, denoted by the black bullets. The bottom panel of each figure shows a ratio of the observed data compared to the total Standard Model expectations, providing a more quantitative estimate of the general agreement.

Figure 46 shows the reconstructed hadronically and leptonically decaying top candidates as well as the hadronically decaying W-candidate for the resolved selection. Equivalent distributions for the two top candidates and the leading jet transverse momentum for the boosted selection are shown in figure 47.

The distributions of the invariant $t\bar{t}$ mass $m_{t\bar{t}}$ are shown in the twelve distinguishable analysis channels in figure 48 and figure 49 for the resolved and boosted selection respectively, separated by the lepton channel and by b-tagging category of the reconstructed events. A

combination of the lepton channels and b-tagging categories for each topology selection as well as a full combination of all twelve channels is presented in figure 50.

The distributions for observed data and Standard Model expectations agree within their uncertainties, showing some slight shape differences seen especially in high mass regions in the boosted selection.

Source	$e+\text{jets}$	$\mu+\text{jets}$	total
$t\bar{t}$	$4\,111 \pm 687$	$4\,070 \pm 680$	$8\,181 \pm 1\,366$
Singletop	137 ± 20	154 ± 22	291 ± 42
$t\bar{t}+V$	37 ± 4	38 ± 4	75 ± 8
Multijet	91 ± 18	9 ± 2	100 ± 20
W+Jets	235 ± 21	258 ± 23	493 ± 45
Z+Jets	34 ± 6	17 ± 3	51 ± 9
Diboson	21 ± 4	20 ± 4	41 ± 8
Total	$4\,666 \pm 821$	$4\,566 \pm 804$	$9\,232 \pm 1\,625$
Data	4 151	4 058	8 209

(a) *Boosted selection*

Source	$e+\text{jets}$	$\mu+\text{jets}$	total
$t\bar{t}$	$92\,609 \pm 12\,317$	$91\,552 \pm 12\,176$	$184\,161 \pm 24\,493$
Singletop	$3\,840 \pm 442$	$3\,783 \pm 435$	$7\,623 \pm 877$
$t\bar{t}+V$	274 ± 14	268 ± 14	542 ± 28
Multijet	$5\,284 \pm 999$	$1\,050 \pm 198$	$6\,334 \pm 1\,197$
W+Jets	$6\,470 \pm 718$	$7\,145 \pm 793$	$13\,615 \pm 1\,511$
Z+Jets	$1\,370 \pm 452$	632 ± 209	$2\,002 \pm 661$
Diboson	319 ± 56	305 ± 54	624 ± 110
Total	$110\,166 \pm 14\,211$	$104\,735 \pm 13\,511$	$214\,901 \pm 27\,722$
Data	114 780	109 325	224 105

(b) *Resolved selection*

Table 18: Event yields for data and Standard Model expectations after applying the full (a) boosted and (b) resolved selection and reconstruction, including the impact of the sum in quadrature of all systematic uncertainties on the Standard Model expectations as uncertainty.

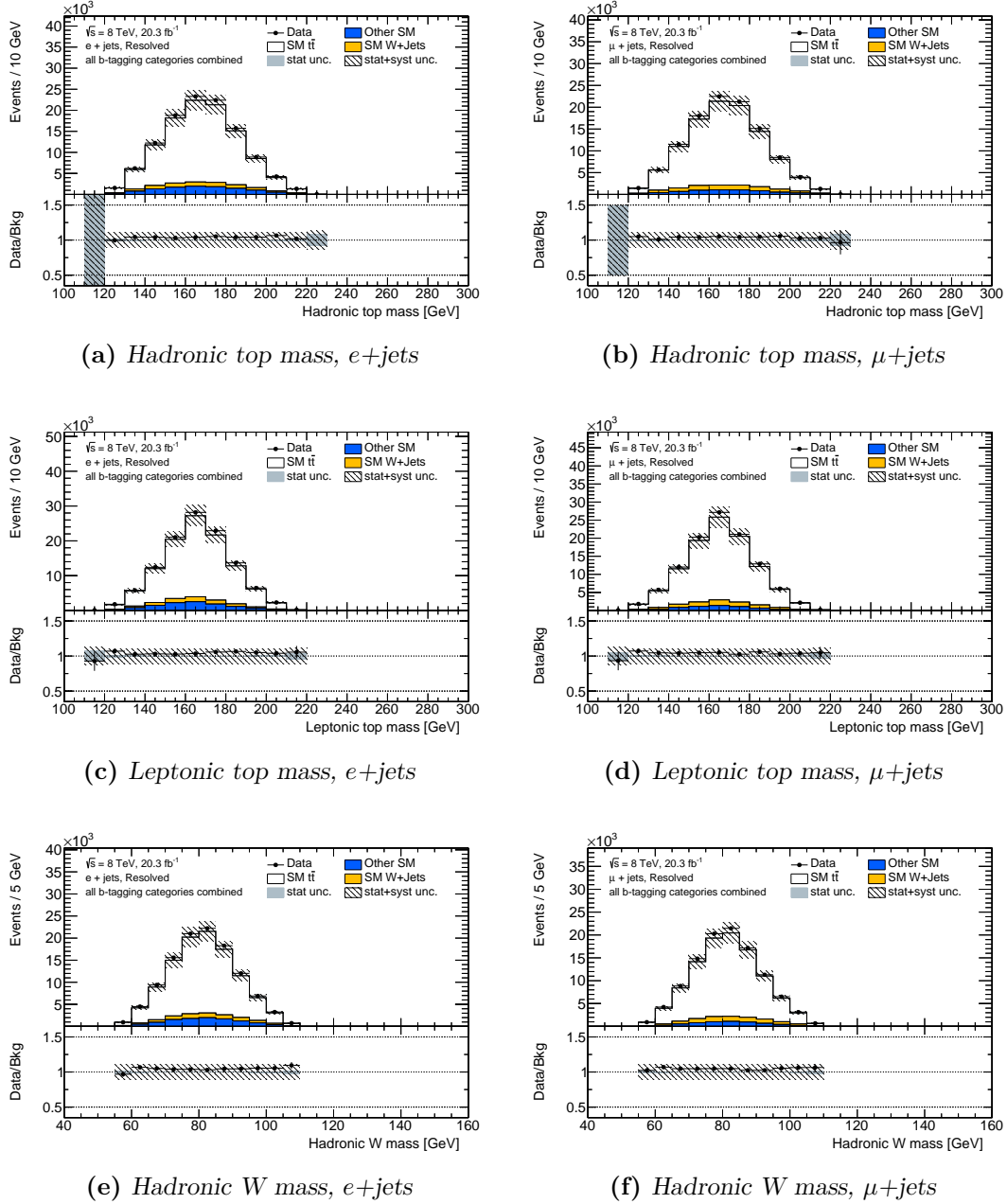


Figure 46: Comparison of data and Standard Model expectations for specific variables of the resolved selection: Reconstructed mass of the (a),(b) hadronically decaying top candidate, the (c),(d) leptonically decaying top candidate and the (e),(f) hadronically decaying W -boson candidate in the $e+jets$ and $\mu+jets$ channel separately after the reconstruction in the resolved topology. The Standard Model background is shown in a stacked histogram, including $t\bar{t}$, $W+Jets$ and all remaining (merged) background processes. The bottom panel shows the data/MC agreement with the gray and shaded area indicating the statistical and the total systematic uncertainty respectively.

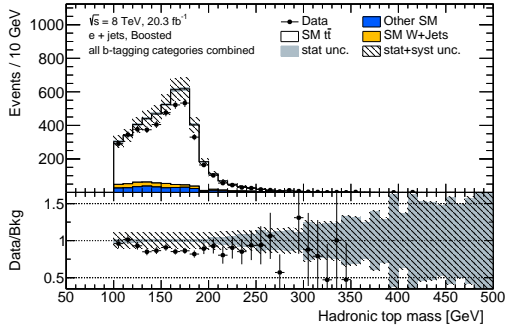
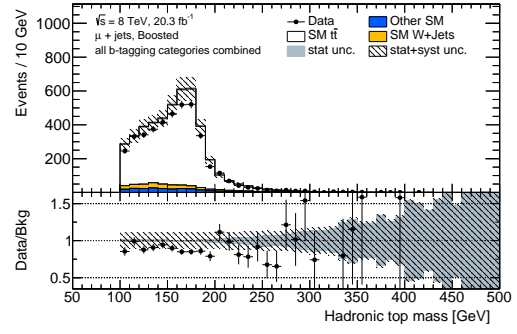
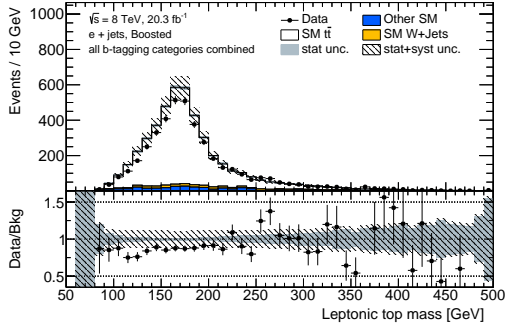
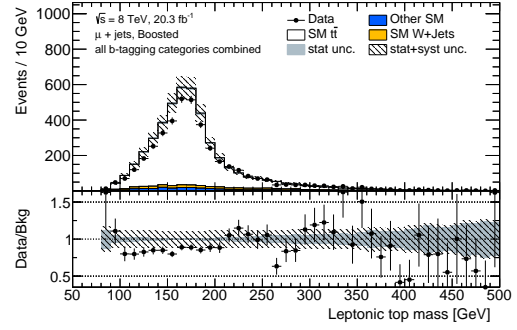
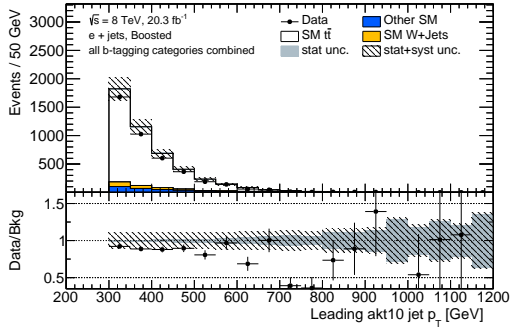
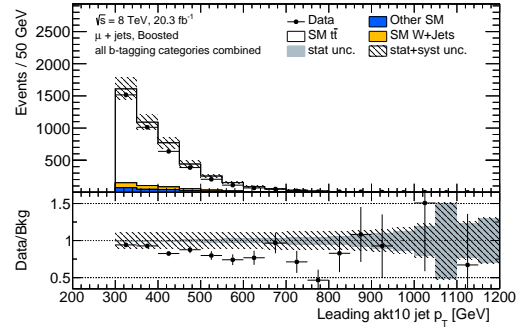
(a) Hadronic top mass, $e+jets$ (b) Hadronic top mass, $\mu+jets$ (c) Leptonic top mass, $e+jets$ (d) Leptonic top mass, $\mu+jets$ (e) Leading jet p_T , $e+jets$ (f) Leading jet p_T , $\mu+jets$

Figure 47: Comparison of data and Standard Model expectation for specific variables of the boosted selection: Reconstructed mass of the (a),(b) hadronically decaying top candidate, the (c),(d) leptonically decaying top candidate and the (e),(f) leading p_T large radius jet in the event in the $e+jets$ and $\mu+jets$ channel separately after the reconstruction in the boosted topology. The Standard Model background is shown in a stacked histogram, including $t\bar{t}$, $W+Jets$ and all remaining (merged) background processes. The bottom panel shows the data/MC agreement with the gray and shaded area indicating the statistical and the total systematic uncertainty respectively.

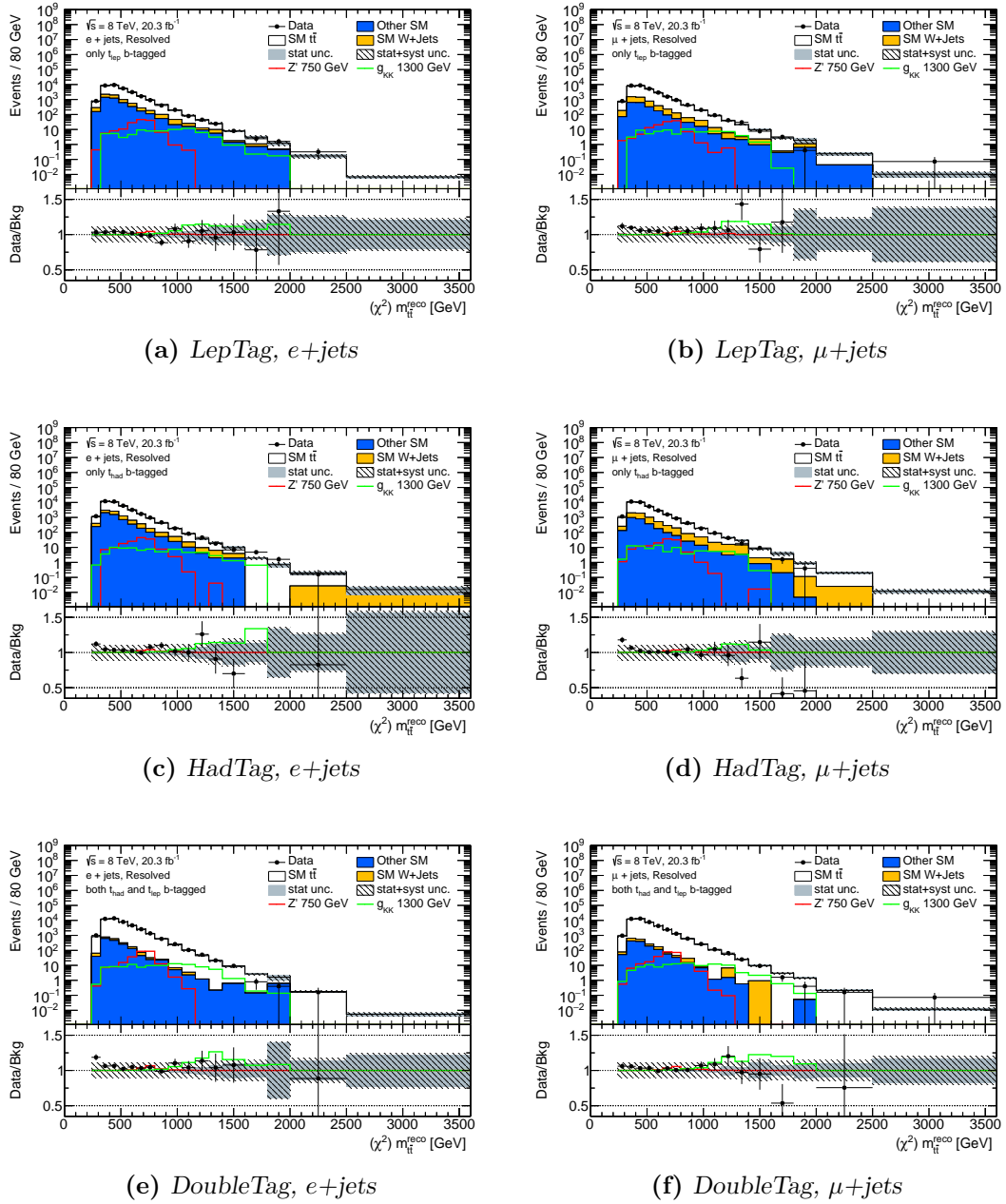


Figure 48: Comparison of data and Standard Model expectation for $m_{t\bar{t}}$ distributions of the resolved selection: Reconstructed mass of the full $t\bar{t}$ system $m_{t\bar{t}}$ for categories with (a),(b) leptonic side only, (c),(d) hadronic side only and (e),(f) both sides with a b -tagged jet association for the e +jets and μ +jets channel separately after the reconstruction in the resolved topology. The Standard Model background is shown in a stacked histogram, including $t\bar{t}$, W +Jets and all remaining (merged) background processes. The bottom panel shows the data/MC agreement with the gray and shaded area indicating the statistical and the total systematic uncertainty respectively. Expected distributions for hypothetical signal leptophobic topcolor Z' (750 GeV) and RS Kaluza-Klein gluon g_{KK} (1300 GeV) resonances are overlaid (non-stacked).

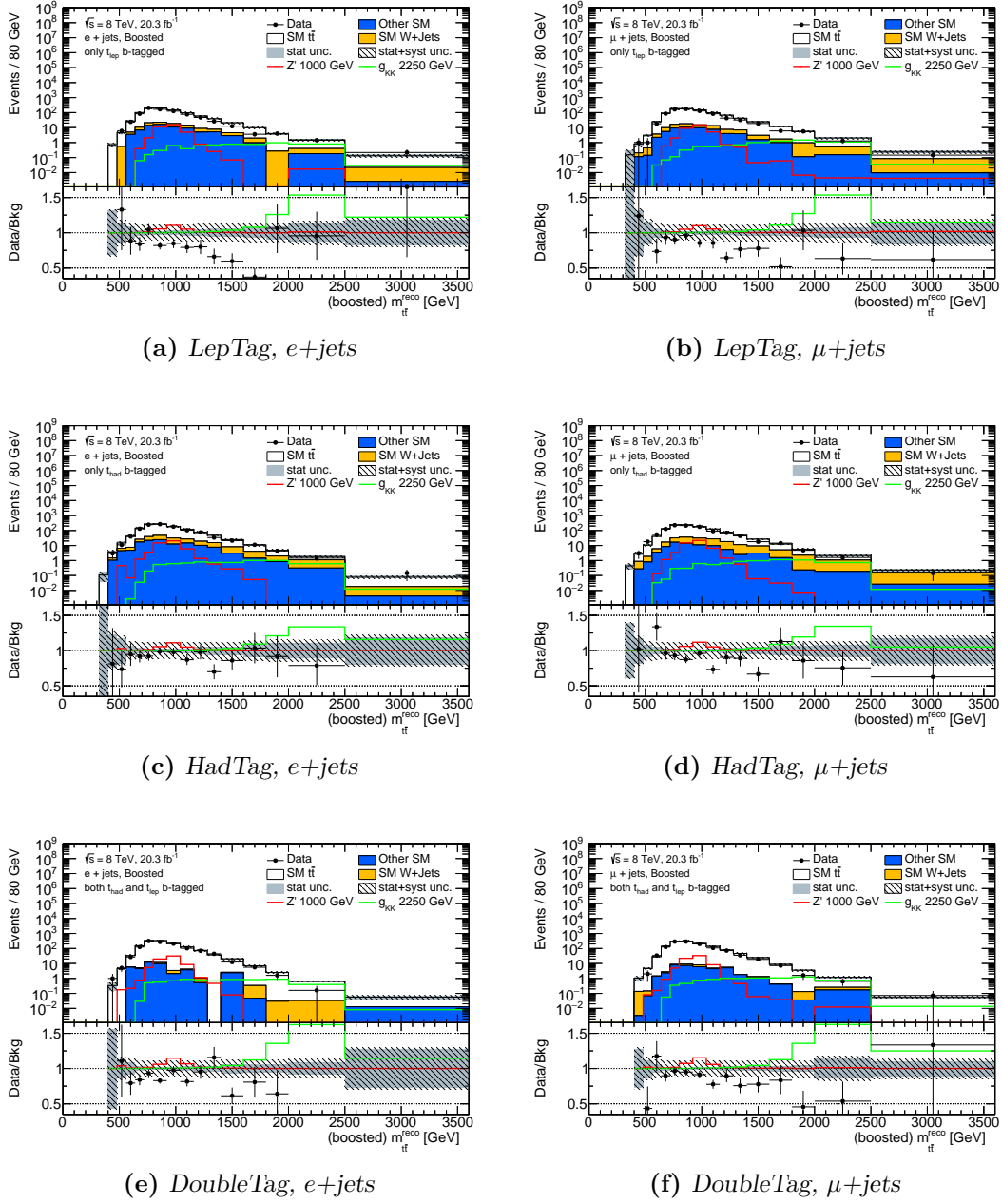


Figure 49: Comparison of data and Standard Model expectation for $m_{t\bar{t}}$ distributions of the boosted selection: Reconstructed mass of the full $t\bar{t}$ system $m_{t\bar{t}}$ for categories with (a),(b) leptonic side only, (c),(d) hadronic side only and (e),(f) both sides with a b -tagged jet association for the e +jets and μ +jets channel separately after the reconstruction in the resolved topology. The Standard Model background is shown in a stacked histogram, including $t\bar{t}$, W +Jets and all remaining (merged) background processes. The bottom panel shows the data/MC agreement with the gray and shaded area indicating the statistical and the total systematic uncertainty respectively. Expected distributions for hypothetical signal leptophobic topcolor Z' (1000 GeV) and RS Kaluza-Klein gluon g_{KK} (2250 GeV) resonances are overlaid (non-stacked).

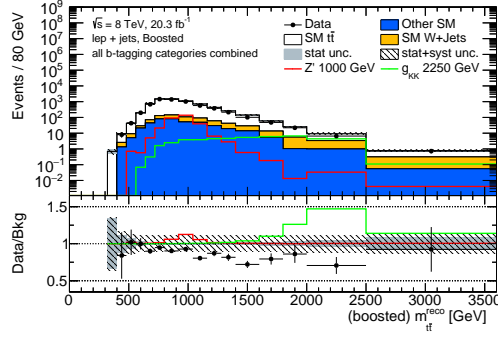
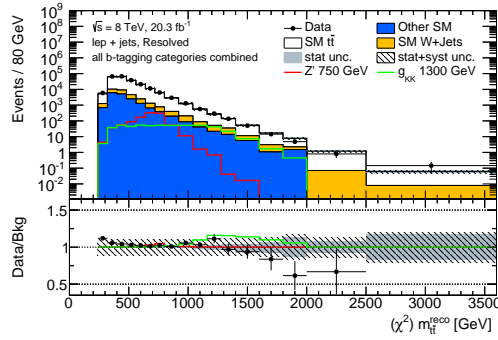
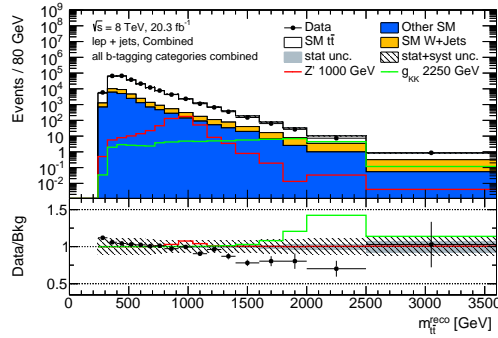
(a) *Boosted topology*(b) *Resolved topology*(c) *All combined*

Figure 50: Comparison of data and Standard Model expectation for combined $m_{t\bar{t}}$ distributions : Reconstructed mass of the full $t\bar{t}$ system $m_{t\bar{t}}$ for (a) boosted selection, (b) resolved selection and (c) both selections combined. All figures show combined e +jets and μ +jets channels and all b-tagging categories combined. The Standard Model background is shown in a stacked histogram, including $t\bar{t}$, W +Jets and all remaining (merged) background processes. The bottom panel shows the data/MC agreement with the gray and shaded area indicating the statistical and the total systematic uncertainty respectively. Expected distributions for hypothetical signal leptophobic topcolor Z' (750 GeV or 1000 GeV) and RS Kaluza-Klein gluon g_{KK} (1300 GeV or 2250 GeV) resonances are overlaid (non-stacked).

10

Analysis results

The twelve invariant mass spectra of the fully reconstructed $t\bar{t}$ system $m_{t\bar{t}}$ presented in chapter 9 are used as final discriminating observables for the analysis. A qualitative comparison of the distributions for data and Standard Model expectations from simulation is performed using the *BumpHunter* [112] tool. This hypothesis-testing tool identifies local excesses or deficits in the distributions of data compared to Standard Model expectations, taking the *look-elsewhere effect*¹ [113] into account over the full range of the mass spectra. A significant deviation is required to appear at the same place in each of the 12 distinct channels.

Taking all statistical and systematic uncertainties into account, no significant deviation of the observed data from the total Standard Model expectations is observed. A hypothesis test for selected theories beyond the Standard Model as discussed in section 2.6 is performed to set upper limits on the cross section times branching ratio for each signal model. Two different techniques are applied for the hypothesis testing, namely *Bayesian* and CL_S , briefly discussed in section 10.1. The final upper limits and exclusions are presented in section 10.2 for the Bayesian and in section 10.3 for the CL_S method, followed by a discussion of the comparison between the two techniques in section 10.4.

¹The look-elsewhere effect (LEE) is a statistical technique to compensate for a potential bias of a statistically significant observation due to limited parameter space or specific region of interest (e.g. testing for a resonance of a specific mass), which usually reduces the significance of the observation. Hence a statistical significant observation taking the LEE into account is a much stronger and more robust statement.

10.1 Hypothesis testing

The final aim of the analysis is to test the results against the hypothesis of the presence of any signal described by given models. In detail this means considering two different hypotheses, one defining the *null hypothesis* H_0 , while the other one defines the alternative hypothesis H_1 . The assignment of the hypothesis types depends on the test intended. For a discovery one tests the background-only hypothesis (H_0) against the signal hypothesis (H_1) and tries to reject H_0 . For an exclusion one tests the signal hypothesis (H_0) against the background-only hypothesis (H_1) and tries to reject H_0 . These tests never allow to completely accept or reject a specific hypothesis, but to favor one hypothesis over another at a certain confidence level. This confidence level (CL) is related to the so-called significance level $\alpha = 1 - \text{CL}$, traditionally set to 1% or 5%. Hence a hypothesis test rejecting the null hypothesis H_0 in favor of an alternative hypothesis H_1 at a confidence level of $\text{CL} = 95\%$ implies a maximum remaining type-I error of 5%, i.e. the probability of falsely rejecting a true null hypothesis.

Two philosophies have been established in high energy physics for hypothesis testing, the *Frequentist* and the *Bayesian* method, which will be summarized briefly in the following based on [114] and [115]. The core of both hypothesis testing procedures is the likelihood function \mathcal{L} , describing a probability density function for the number of observed events in data D , given the background yield B (from Standard Model expectations) with a specific contribution of signal events S scaled with a normalization factor $\mu \geq 0$ (signal strength), as shown in equation (10.1). A normalization of $\mu = 0$ corresponds to the background-only hypothesis (i.e. no signal contribution), while $\mu > 0$ denotes a signal hypothesis with a given signal strength.

$$\mathcal{L}(\mu) = P(D|\lambda(\mu, S, B)) \quad \lambda(\mu, S, B) = \mu \cdot S + B \quad (10.1)$$

Since in high energy physics not only single values, but usually distributions of discriminants are analyzed in form of histograms, the likelihood, which is described as a product of Poisson distributions, can be expressed as shown in equation (10.2) with yield λ_j , including nuisance parameters θ parametrizing systematic uncertainties, in a given bin j with the number of total entries n_j in that bin out of N total bins.

$$\mathcal{L}(\mu, \theta) = \prod_{j=1}^N \frac{(\lambda_j(\mu, S, B, \theta))^{n_j}}{n_j!} \cdot e^{-\lambda_j(\mu, S, B, \theta)} \cdot \prod_y G(\theta_y^0 - \theta_y) \quad (10.2)$$

Systematic uncertainties are taken into account with probability density functions, typically denoted by Gaussian distributions G with unit width for the full set of systematic uncertainties y , varying the parameters θ around the central value θ^0 of auxiliary measurements e.g. during maximization of the Likelihood.

Frequentist

The frequentist method defines a test statistic t_μ via a profile likelihood ratio as denoted in equation (10.3). The numerator represents a setup maximizing the likelihood for a given μ finding the best θ , while the expression in the denominator varies both μ and θ to maximize the likelihood, providing a maximal statistical power (Neyman-Pearson lemma). This allows to test for the null hypothesis $\mu = 0$ and different signal strengths $\mu > 0$.

$$t_\mu = -2 \ln \left(\frac{\mathcal{L}(\mu, \hat{\theta})}{\mathcal{L}(\hat{\mu}, \hat{\theta})} \right) \quad (10.3)$$

The upper limit μ_{CL} for a chosen confidence level CL under a given hypothesis H_μ can then be obtained from a probability distribution function $f(t_\mu|\mu)$ of the test statistic, determined by pseudo-data generated according to an input model as given in equation (10.4).

$$\text{CL} = \int_{t_{\mu\text{CL}}}^{\infty} f(t_\mu|\mu=0) dt_\mu \quad (10.4)$$

In summary the frequentist approach fixes the nuisance parameters θ beforehand, achieving the best agreement between data and Standard Model expectations, trying to add a signal contribution afterwards. Hence this approach excludes theories reproducing the data with small probabilities under given nuisance parameters θ with $\alpha = P_\mu(N_\mu < D|\theta) < 1 - \text{CL}$.

The frequentist approach is problematic for very small values of α or vanishing signal contributions which in case of downward fluctuations can lead to a rejection of a signal hypothesis one is not actually sensitive to. To avoid this risk, one defines the so-called CL_S limit shown in equation (10.5), comparing the CL for a signal plus background hypothesis to the background-only hypothesis. Technically speaking this is not a proper confidence level definition any more but still provides a powerful measure for the compatibility of the data with the signal hypothesis, which was used e.g. for the statement of the Higgs discovery (cf. [6]).

$$\text{CL}_S = \frac{\text{CL}_{S+B}}{\text{CL}_B} = \frac{P(N \leq D|S+B)}{P(N \leq D|B)} \quad (10.5)$$

Bayesian

The Bayesian method uses Bayes' theorem denoted in equation (10.6), describing the likelihood $P(M|D)$ (usually called posterior) for a specific model M under the given data D . This can be expressed as the probability of the data under the given model $P(D|M)$ (which is defined by the Likelihood $\mathcal{L}(\mu)$, cf. equation (10.2)), multiplied with a prior probability of the model $P(M)$, normalized by the sum of the posterior of all theories $P(D) = P(M|D) + P(!M|D)$.

$$P(M|D) = \frac{P(D|M) \cdot P(M)}{P(D)} \quad (10.6)$$

The prior probability $P(M)$ adds a precedent understanding of the model before looking

at the actual data, which is the most critical point of the Bayesian approach, since usually the model is rather unknown. Hence the most common approach is to use a flat prior for the tested model, not adding any specific information, although one can use the posterior of earlier iterations as new prior to add some knowledge about the model.

The confidence level CL can be obtained from these posterior distributions for fixed data with varied nuisance parameters excluding a set of theories such that the posterior probability of the excluded theories is $1 - \text{CL}$ as shown in equation (10.7).

$$1 - \text{CL} = P(\mu \geq \mu_{\text{CL}}|D) = \frac{\int_{\mu_{\text{CL}}}^{\infty} P(D|\mu) P(\mu) d\mu}{\int_0^{\infty} P(D|\mu) P(\mu) d\mu} \quad (10.7)$$

Comparison

Both methods provide a powerful estimator to test specific hypotheses, although they use rather different approaches. While the frequentist method provides a probability for the observed data given a specific hypothesis, the Bayesian method provides a *degree of belief* (since there is no probability for a theory) of a hypothesis, given the observed data.

10.2 Bayesian method results

Limits for the analysis using the Bayesian method are derived exclusively for this thesis. Earlier iterations of this analysis used the Bayesian limit setting method provided by the Mainz group, replaced by the nowadays more common CL_S method in the publication of this analysis. The available software framework for Bayesian limit setting has been adapted and improved to suit the needs for the analysis in this thesis, providing the opportunity for a sanity check of the CL_S limits, comparing between two different techniques for limit setting.

Figure 51 shows the typical design of a figure for limit setting results in high energy physics (often referred to as "brazilian-plots" due to the color design). These plots show the cross section times branching ratio for a resonance of a given model decaying to $t\bar{t}$ as a function of the resonance mass. The black dotted line shows the *expected* upper limit (at a given confidence level) on the cross section times branching ratio for a given resonance mass, obtained from Asimov² toy experiments. The green and yellow bands denote the 1σ and 2σ uncertainty on this expected limit respectively. Considering the real data recorded by the experiment as input, one obtains the straight black line, representing the *observed* upper limits as a real comparison between data and Standard Model expectations. The predicted upper limits from theory calculations are shown as the blue dashed line. The bullets in the observed upper limit curve represent mass points which are calculated explicitly, all intermediate mass regions are interpolated between these points. A hint for a new resonance would show up as an excess of the observed limit above the expected limit. On the other hand, if the curve of the expected/observed upper limit is below the cross section predicted

²Asimov experiments describe a test of an algorithm using the expected simulation only instead of real recorded data to test for a predictable and controllable outcome.

by the theory curve, the given theory can be excluded at these resonance masses at the given confidence level. The plots in figure 51 only include statistical uncertainties, which do not consider any effect due to systematic uncertainties in the analysis. Hence these plots can easily yield a larger deviation between the expected and observed upper limits, taken as a sanity check of the method itself rather than a final result.

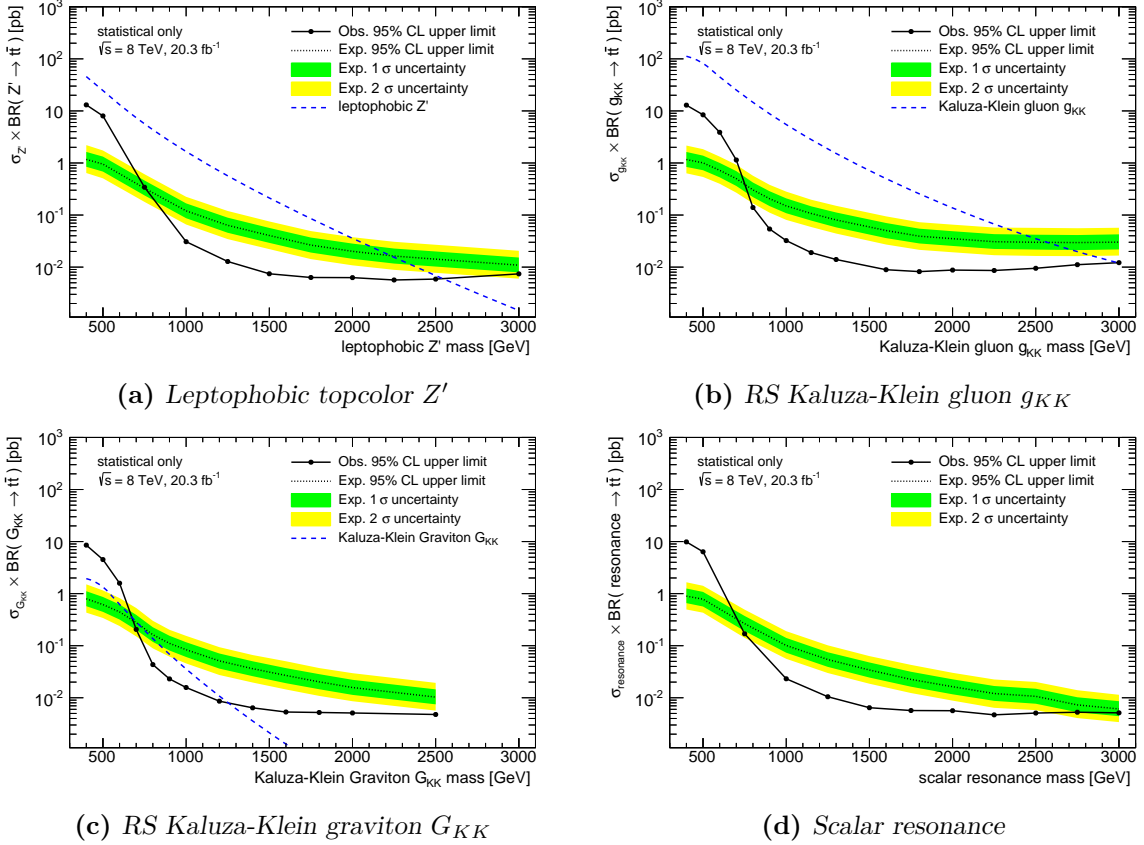


Figure 51: Bayesian (statistical uncertainties only, resolved+boosted selection) observed and expected upper limits on the production cross section times branching ratio to $t\bar{t}$ final states as a function of the mass of a (a) leptophobic topcolor Z' , (b) Randall-Sundrum Kaluza-Klein gluon g_{KK} , (c) Randall-Sundrum Kaluza-Klein graviton G_{KK} and (d) scalar resonances.

The final result is represented by figure 52, considering statistical and systematic uncertainties in the limit setting. Since in this case the systematic uncertainties (represented by the nuisance parameters in the Bayesian method) are varied during the calculation of the upper limits, the uncertainty bands on the expected limits are much broader compared to statistical only limits. These plots confirm the statement of the analysis of the $m_{t\bar{t}}$ spectra, that no significant excess can be seen between simulation and data, since the observed limits are well within the uncertainties of the expected limits. A sanity check for a reasonable treatment of the various systematic uncertainties during the limit setting procedure is provided by figure 53, showing the pulls and uncertainties on the posterior distributions for each systematic uncertainty, using the example of a Z' resonance with a mass of 2 TeV. The shifts of the nuisance parameters are drawn from a unit-width Gaussian distribution and each value is

assigned with a likelihood value. Hence the ideal systematic description results in a centered (pull=0) expectation value (denoted by the black bullet) and a 1σ uncertainty (denoted by the black error bar) in this type of plot, confirming a good understanding of the given systematic. If a systematic uncertainty is likely to be pulled strongly to achieve a better agreement between data and background+signal, its proper description seems disputable. Also a strong (small error bar, $\sigma \ll 1$) or weak (large error bar, $\sigma \gg 1$, underestimated uncertainty) constraint of the systematic needs to be cross checked in detail. Figure 53 shows stronger pulls on systematic uncertainties with a generally large impact, e.g. the b-tag high p_T and large radius jet mass resolution systematic uncertainties. Also the small radius jet vertex fraction is pulled stronger compared to others, although checks of the specific posterior distributions show a reasonable behavior. In general the majority of uncertainties is constrained by the fitting procedure, which results from the fact that they are initially treated as uncorrelated, while these constraints introduce some sort of expectable correlation. A rather strong constraint can only be observed for the initial and final state radiation uncertainty. Also here sanity checks of the posterior distributions and fit convergences confirmed a reasonable result. Additionally the red bullets and error bars show the expected pulls and uncertainties when using toy-data (Asimov test), predicting a trend for the pull and uncertainty, which is also confirmed by the majority of systematic uncertainties.

With this complete picture with all (statistical and systematic) uncertainties taken into account and cross checked, upper limits on the cross section times branching ratio are set for each model for masses from 0.5 up to 3.0 TeV. Based on these results, exclusion limits are set on the signal models as summarized in table 19. A leptophobic topcolor Z' is excluded for masses below 1.9 (2.1) TeV and a Randall-Sundrum Kaluza-Klein gluon g_{KK} for masses below 2.1 (2.4) TeV for observed (expected) upper cross section times branching ratio limits at 95% confidence level. A study of the width-dependence of the upper limits for a Randall-Sundrum Kaluza-Klein gluon g_{KK} resonance shown in figure 52(e) results in an observed upper limit weakened by a factor of 1.7 from 0.40 pb to 0.69 pb over a range of width from 10% to 40% for a resonance mass of 1 TeV. For larger masses of 2 (3) TeV the limits even weaken by a factor of 2.2 (2.8) from 0.09 (0.09) pb to 0.20 (0.26) pb over this range. The amount of data used in this analysis does not provide enough sensitivity to set exclusion limits on the Randall-Sundrum Kaluza-Klein graviton G_{KK} and the Scalar resonance limit is not tested against any specific theory description.

The full list of explicit observed and expected cross section times branching ratio limits for statistical only and statistical+systematic uncertainties for all mass points for the selected BSM models are listed in appendix A.5.

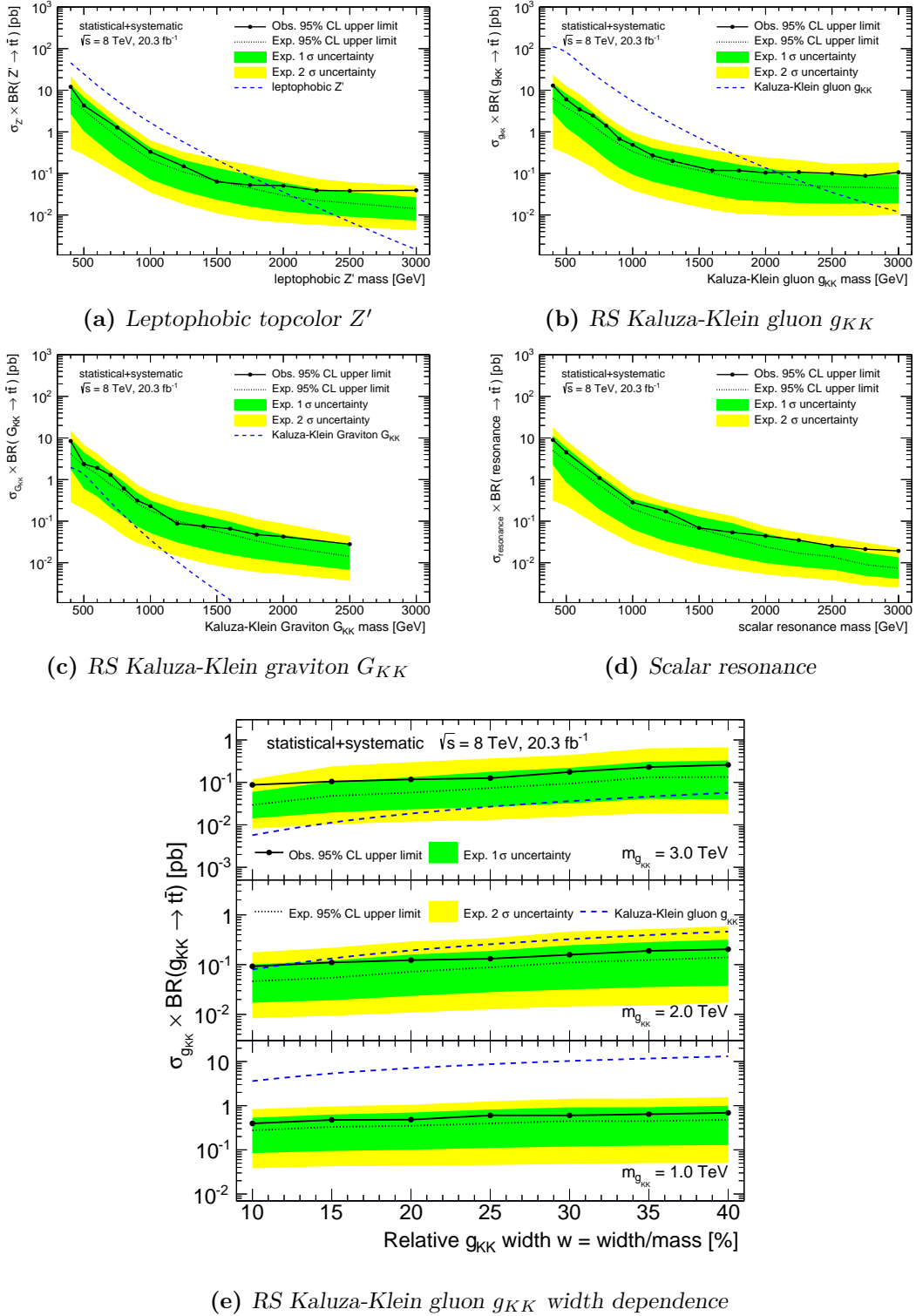


Figure 52: Bayesian (systematic+statistical uncertainties, resolved+boosted selection) observed and expected upper limits at 95% confidence level on the production cross section times branching ratio to $t\bar{t}$ final states as a function of the mass of a (a) leptophobic topcolor Z' , (b) Randall-Sundrum Kaluza-Klein gluon g_{KK} , (c) Randall-Sundrum Kaluza-Klein graviton G_{KK} and (d) scalar resonance, as well as a (e) Randall-Sundrum Kaluza-Klein gluon g_{KK} width dependence study.

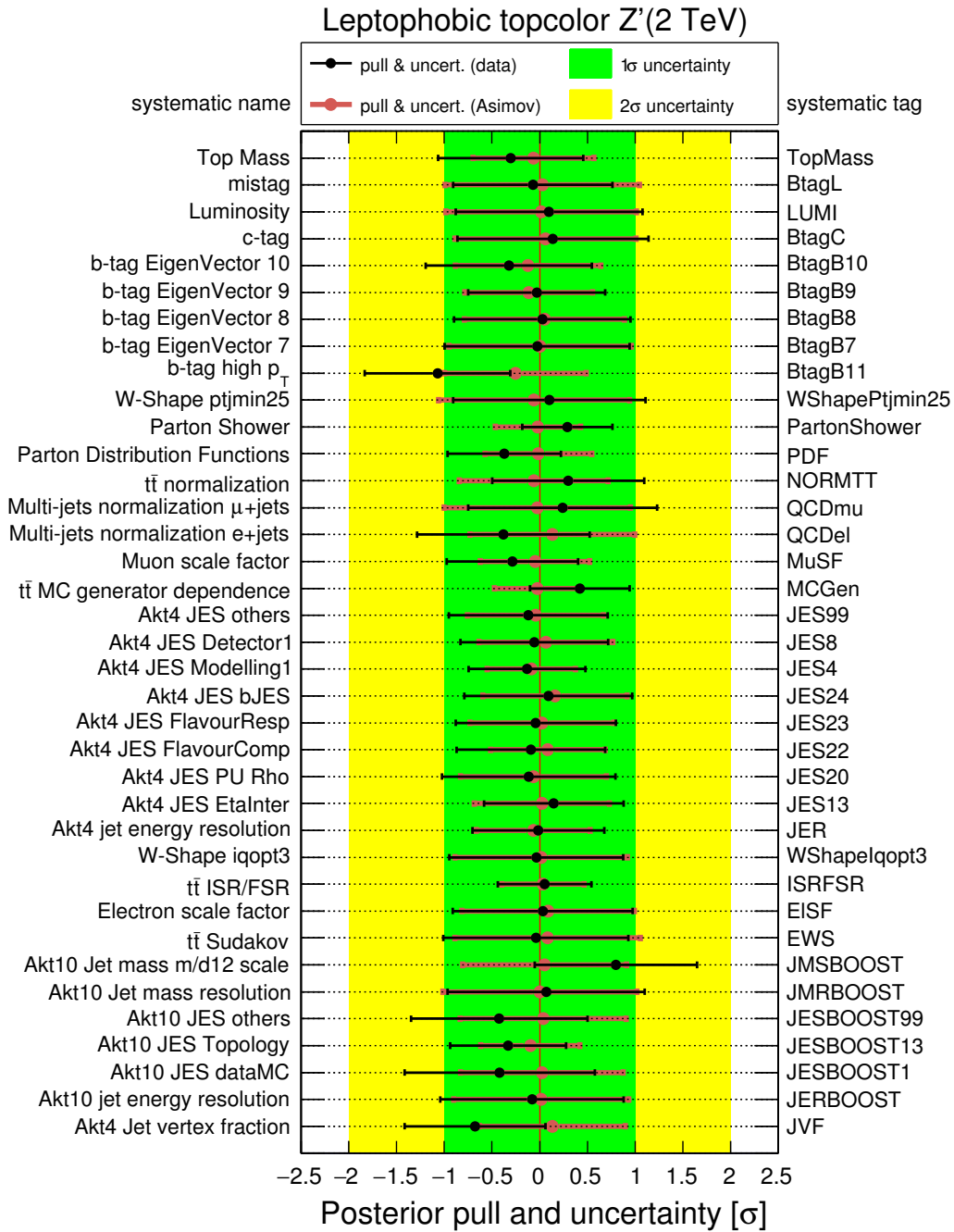


Figure 53: Summary of the posterior pulls and uncertainties for each systematic uncertainty resulting from the Bayesian limit setting procedure considering systematic and statistical uncertainties, using the example of a leptophobic topcolor Z' resonance with a mass of 2 TeV. 1σ and 2σ uncertainty bands are shown along with expected pulls and uncertainties for Asimov tests, overlaid with actual pulls and uncertainties for data with the resolved+boosted selection.

model	mass [TeV]	$\sigma \times \text{BR}$ [pb]	exclusion [TeV]
Leptophobic topcolor Z'	0.4	12.09 (6.37)	m < 1.9 (2.1)
	3.0	0.04 (0.01)	
RS Kaluza-Klein gluon g_{KK}	0.4	12.96 (6.39)	m < 2.1 (2.4)
	3.0	0.11 (0.04)	
RS Kaluza-Klein graviton G_{KK}	0.4	8.45 (4.18)	(no exclusion)
	2.5	0.03 (0.01)	
Scalar resonance	0.4	9.00 (5.01)	(no exclusion)
	3.0	0.02 (0.08)	

Table 19: Bayesian (systematic+statistical uncertainties, resolved+boosted selection) observed and expected upper limits at 95% confidence level on the production cross section times branching ratio for a given mass range and upper mass exclusion limits for selected BSM signal benchmark models.

10.3 CL_s method results

The official publication of the analysis [8] uses the CL_s method to derive limits and exclusions on the models considered in this analysis. The corresponding upper limits are shown in figure 54. Based on these results, exclusion limits are set on the signal models as summarized in table 20. A leptophobic topcolor Z' is excluded for masses below 1.8 (2.0) TeV and a Randall-Sundrum Kaluza-Klein gluon g_{KK} for masses below 2.2 (2.3) TeV for observed (expected) upper cross section times branching ratio limits at 95% confidence level. The observed upper limits for the Randall-Sundrum Kaluza-Klein gluon g_{KK} model weaken by a factor of 2 from 0.4 pb to 0.78 pb over a range of width from 10% to 40% for a resonance mass of 1 TeV. For larger masses of 2 (3) TeV these limits weaken by a factor of 3 from 0.08 (0.06) pb to 0.24 (0.21) pb over this range, as presented in figure 54(e).

Due to a higher acceptance, the limits are stronger for the RS Kaluza-Klein graviton G_{KK} and scalar resonances at same mass points compared to a leptophobic topcolor Z' or RS Kaluza-Klein gluon g_{KK} resonance. Especially for masses greater than 1.8 TeV, all models show a weaker observed upper limit on the cross section times branching ratio than the expected ones, which is a result of the profile likelihood method allowing for a constraint on the systematic uncertainties, shifting the central values of the nuisance parameters and their associated uncertainties.

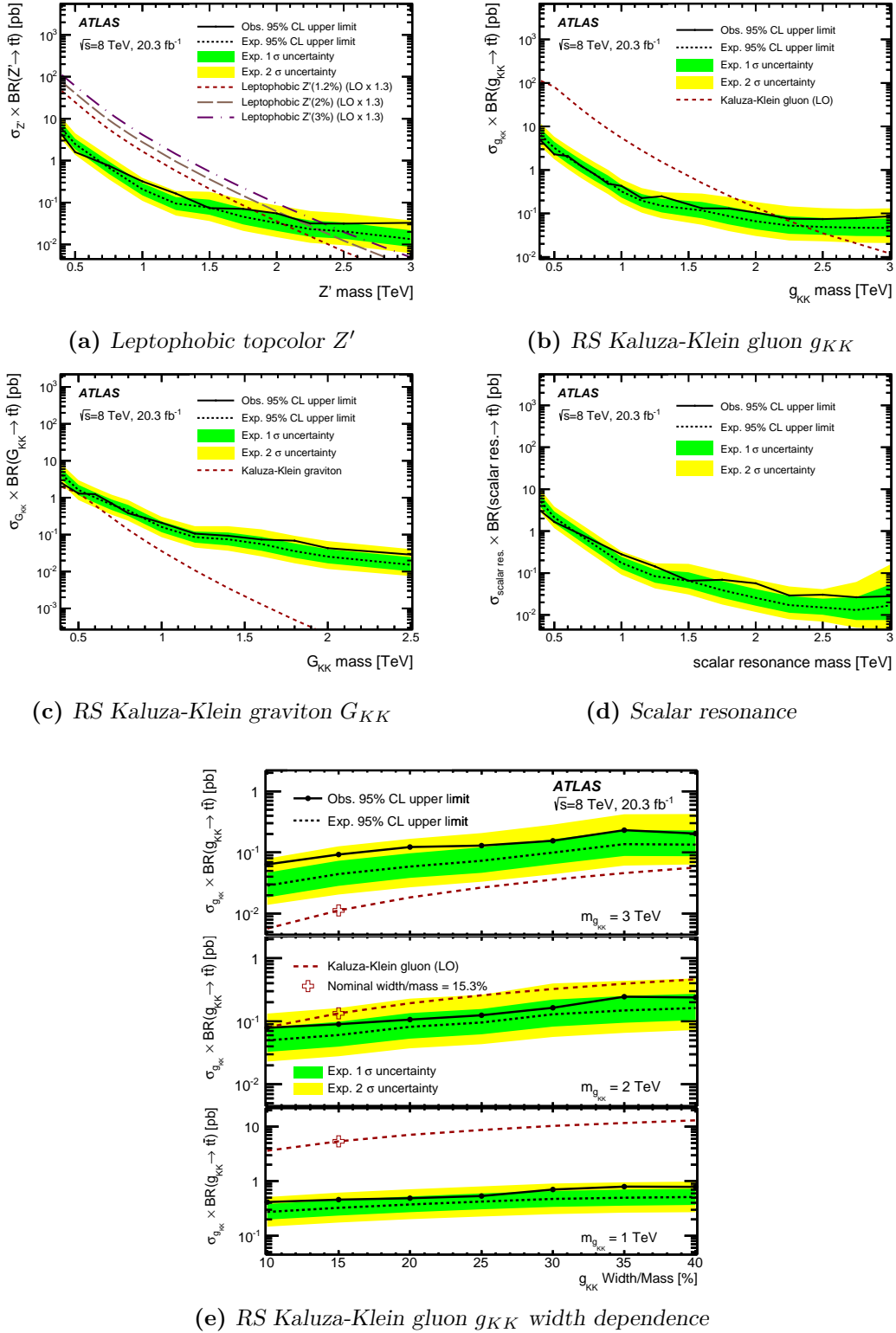


Figure 54: CL_S (systematic+statistical uncertainties, resolved+boosted selection) observed and expected upper limits on the production cross section times branching ratio to $t\bar{t}$ final states as a function of the mass of a (a) leptophobic topcolor Z' , (b) Randall-Sundrum Kaluza-Klein gluon g_{KK} , (c) Randall-Sundrum Kaluza-Klein graviton G_{KK} and (d) scalar resonance, as well as a (e) Randall-Sundrum Kaluza-Klein gluon g_{KK} width dependence study [8].

model	mass [TeV]	$\sigma \times \text{BR}$ [pb]	exclusion [TeV]
Leptophobic topcolor Z'	0.4	4.17 (7.86)	m < 1.8 (2.0)
	3.0	0.02 (0.03)	
RS Kaluza-Klein gluon g_{KK}	0.4	4.75 (8.75)	m < 2.2 (2.3)
	3.0	0.09 (0.08)	
RS Kaluza-Klein graviton G_{KK}	0.4	2.48 (5.91)	(no exclusion)
	2.5	0.03 (0.02)	
Scalar resonance	0.4	7.11 (5.91)	(no exclusion)
	3.0	0.05 (0.02)	

Table 20: CL_S (systematic+statistical uncertainties, resolved+boosted selection) observed and expected upper limits at 95% confidence level on the production cross section times branching ratio for a given mass range and upper mass exclusion limits for selected BSM signal benchmark models [8].

10.4 Comparison of CL_S and Bayesian method

The results for both methods presented in the previous sections show reasonable and comparable limits, while the Bayesian method shows a slightly stronger limit on the leptophobic topcolor Z' and Randall-Sundrum Kaluza-Klein gluon g_{KK} resonances (apart from g_{KK} observed). Since the results of this thesis include some minor updates of calibrations and tool improvements compared to the published analysis, this improvement in limits should not only be understood to be caused by the alternative method itself.

To put the comparison on a more qualitative and reasonable level, the Bayesian limit setting method is also applied to the same (i.e. identical) input used for the CL_S method in the publication. A direct comparison between these two results is shown in figure 55. Apart from the known black-green-yellow design of the limit plots used here for the results obtained from the Bayesian method, this plot contains another red-blue-orange set of observed and expected limits overlaid for the results obtained from the CL_S method. Since this plot uses identical input, it shows the raw differences resulting from the two distinctive limit setting methods.

The most conspicuous disparity in this comparison is the width of the green-yellow and blue-orange colored 1σ and 2σ uncertainty bands of the expected upper limits. While the dashed lines for the raw expected upper limits are comparable, the Bayesian method shows much broader uncertainty bands compared to the CL_S method. For plots considering only statistical uncertainties, these uncertainty bands are comparable, pointing out the diverse treatment of systematic uncertainties of the two methods causing the difference in width of the uncertainty bands. While the CL_S methods fixes the best value for the nuisance parameters before the calculation of the upper limit, the Bayesian method varies them during the hypothesis testing, assigning probabilities to the nuisance parameters themselves and

allowing for a broader range, resulting in a larger uncertainty on the expected upper limit. Larger deviations between the observed upper limits mainly occur in the low mass region below resonance masses of $m < 800$ GeV, where the *HistFitter* software framework used to calculate the CL_S limits is found to be unstable given the final spectra of this analysis due to convergence problems for the lower mass points, leading to shifted upper limits. Also the Bayesian method sees a double-peak behavior in the posterior distributions (hinting for a higher probability for a signal strength $\mu > 0$) for the low mass points resulting in a looser limit. Other mass regions show rather small differences, all well even within the smaller uncertainty bands of the CL_S method.

On the technical side the Bayesian method is often criticized for rather long computing times, due to the multiple toy experiments with variations for each nuisance parameter. A set of limits for all four considered BSM models is produced with a time consumption of about 2 weeks (depending on the capacity of the local cluster) in the context of this thesis, which represents an acceptable time consumption for a CPU-intensive task and therefore is competitive to the CL_S limit setting procedure.

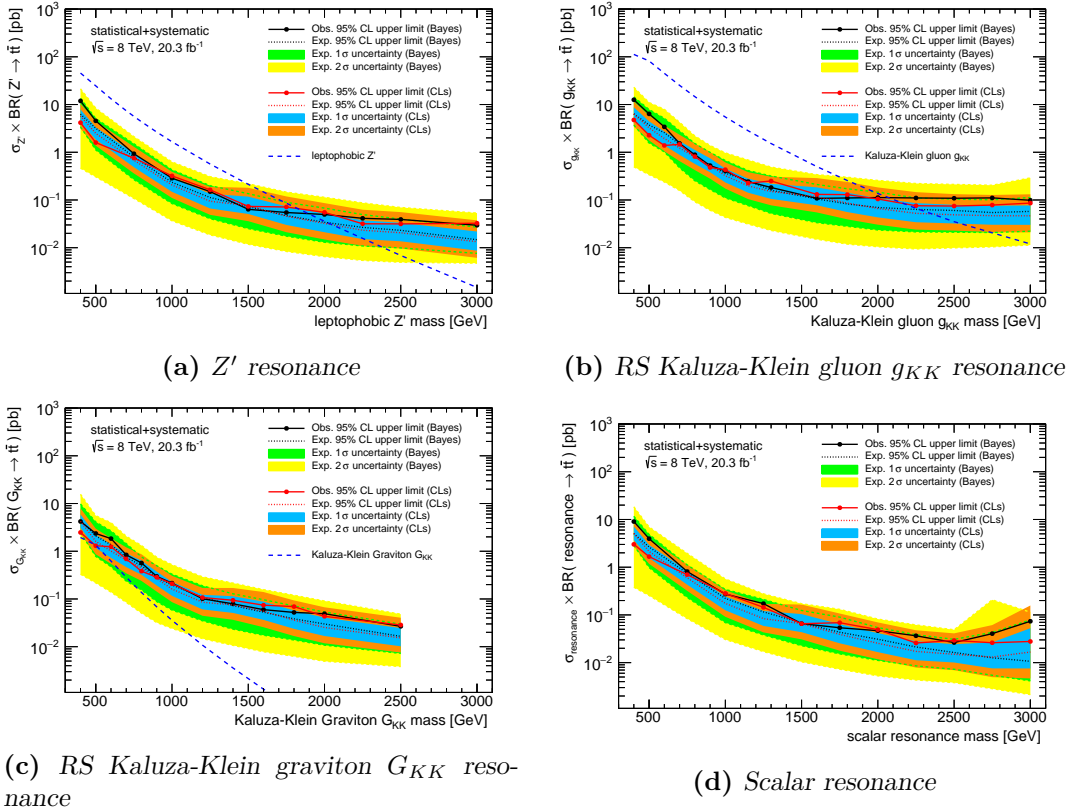


Figure 55: Comparison of (systematic+statistical uncertainties, resolved+boosted selection) observed and expected (including $\pm 1\sigma$ and $\pm 2\sigma$ variations) upper limits on the cross section times branching ratio at 95% confidence level for a (a) leptophobic topcolor Z' , (b) Randall-Sundrum Kaluza-Klein gluon g_{KK} , (c) Randall-Sundrum Kaluza-Klein graviton G_{KK} and (d) scalar resonance. The input $m_{t\bar{t}}$ spectra for this comparison are taken from the spectra used for the publication.

11

Analysis improvements

This section introduces the improvements for the analysis presented in this thesis using alternative top tagging techniques. After a short motivation in section 11.1, an alternative top tagger algorithm is presented in detail in section 11.2 and applied in the lepton+jets $t\bar{t}$ environment in section 11.3, introducing different setups with cut-based optimization as well as a multivariate analysis approach. After discussing the systematic uncertainties introduced by the top tagging algorithm, the final results are compared with the analysis in this thesis in section 11.5.

11.1 Motivation

Identification of top jets containing all decay products of a top decay using top tagging techniques (cf. section 4.5.7) is of major interest at high energy particle colliders at a center of mass energy in the TeV regime. A variety of algorithms are under development to identify a jet as originating from the hadronization shower of a top quark.

The current procedure applied in the analysis presented in this thesis is to apply a b-tagging criterion as a major rejection cut against W+Jets background and to require a large radius jet with a significant boost (cf. section 6.2.2) including a splitting scale of $\sqrt{d_{12}} > 40$ GeV, which represents a very basic substructure requirement on this large radius jet.

Another approach is to use the HEPTOPTAGGER algorithm [87, 88] which was originally developed and optimized in an all-hadronic $t\bar{t}$ environment. The algorithm applies a more detailed substructure analysis and identifies all three decay products of the top quark explicitly. This algorithm is tested in the context of this analysis and optimized for good signal efficiency and selection significance to identify the hadronically decaying top in the

lepton+jets $t\bar{t}$ environment. This procedure provides good separation power against W+Jets signatures and hence allows to drop the b-tagging requirement from the event selection. Since the uncertainty on b-tagging is one of the major systematic uncertainties in this analysis (cf. section 8.5), dropping this uncertainty is a potential improvement which has to be compared to the impact of uncertainties introduced by the HEPTOPTAGGER algorithm.

11.2 HEPTopTagger algorithm

The following subsections discuss the intermediate steps of the HEPTOPTAGGER algorithm in more detail.

The starting point for top tagging is a large radius jet, which in this study is reconstructed from cluster information of each event to build a Cambridge/Aachen (cf. section 4.5) jet with a radius parameter of $R = 1.5$ using the jet clustering tool `Fastjet v3.0.3` [98] and calibrated afterwards [86]. The HEPTOPTAGGER algorithm analyzes the substructure of this large radius jet to identify all decay products of the hadronic top decay ($t \rightarrow W+b \rightarrow q+\bar{q}'+b$) explicitly using the following six subsequent steps.

1. Find hard substituents of the large radius jet [hard subjets]
2. Recluster inclusive filtered subjets [filtered subjets]
3. Recluster three exclusive top subjets [reclustered subjets]
4. Build top candidate
5. Apply W-mass constraint
6. Apply top mass window

An illustration of the top tagging procedure is shown in figure 56.

11.2.1 Find Hard substituents of large radius jet

The clustering of the input large radius jet is reversed to find hard subjets and drop soft radiations. Reverting the last clustering step of a parent jet j_{parent} provides two subjets j_{sub}^i . While subjet $i = 1$ is defined as the subjet with the larger mass $m_{j_{\text{sub}}^1} > m_{j_{\text{sub}}^2}$, it has to fulfill a mass drop criterion of $m_{j_{\text{sub}}^1} < t_{\text{MD}} \cdot m_{j_{\text{parent}}}$ with a fractional threshold t_{MD} , to ensure two subjets sharing a minimum fraction of the parent jet mass representing two hard radiations. If this requirement is not met by a jet pair, j_{sub}^2 is dismissed and j_{sub}^1 is further declustered¹. If the mass drop criterion is fulfilled, each of the two subjets is checked against a mass cut-off. If the subjet satisfies $m_{j_{\text{sub}}^i} < m_C$, it is considered as a hard subjet and otherwise declustered again. In the following steps, all permutations of hard subjet triplets are analyzed.

¹i.e. taken as new input parent jet for the mass drop algorithm

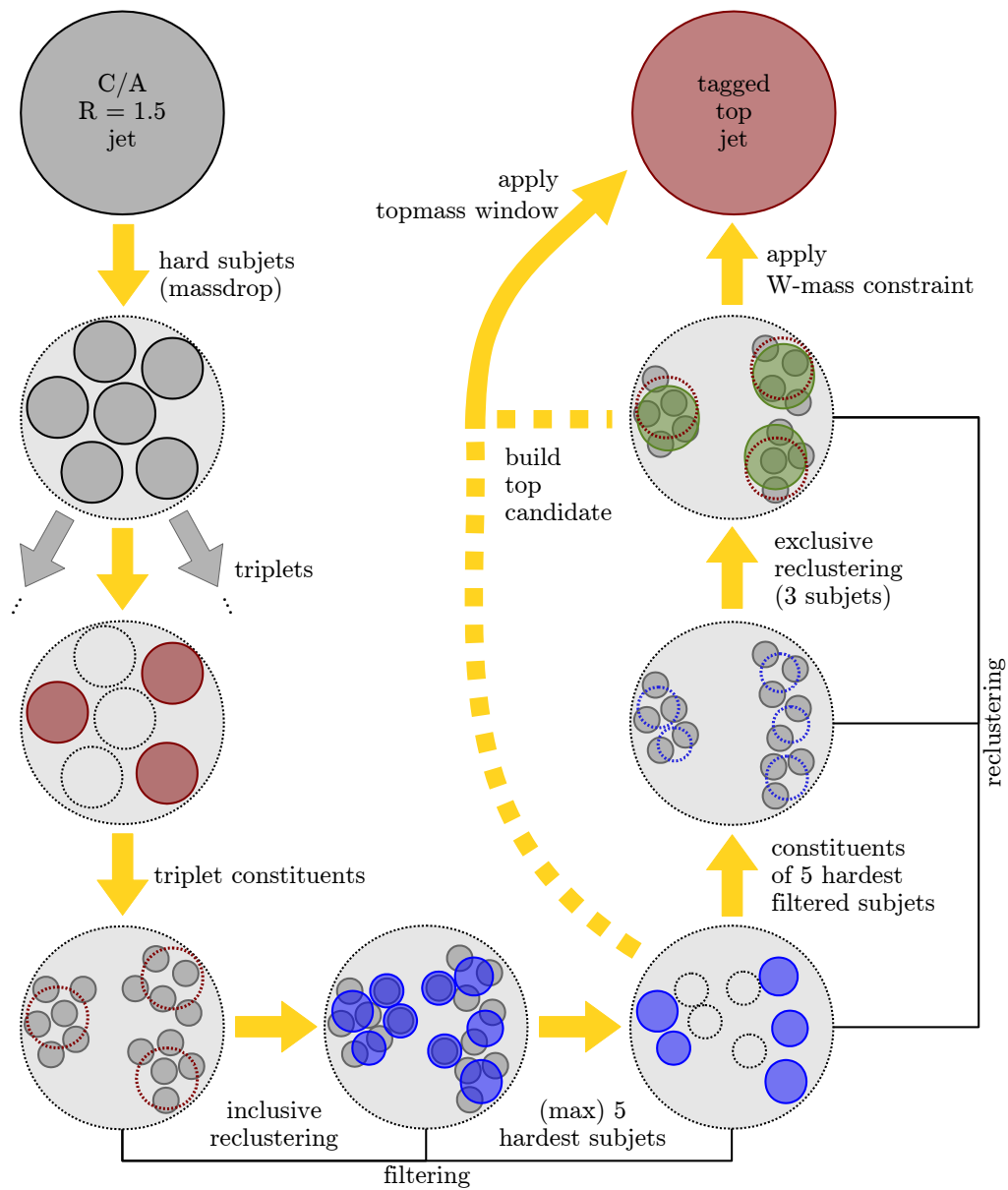


Figure 56: Intermediate steps of the HEPTOPTAGGER algorithm, declustering a large Cambridge/Aachen $R=1.5$ jet into hard subjects, testing all permutations of triplets of hard subjects, applying inclusive filtering and reclustering three exclusive subjects, identified as the decay products of the top candidate. The final objects are tested against W -mass and top-mass constraints.

11.2.2 Recluster inclusive filtered subjects

The constituents of a given triplet of hard subjects are reclustered with a dynamic radius parameter depending on the distance ΔR_{ij} between two hard subjects i, j of the current triplet as given in equation (11.1), while a minimum radius $R_{\text{filter}}^{\text{min}}$ is set.

$$R_{\text{filter}} = \min\left(R_{\text{filter}}^{\text{min}}, 0.5 \cdot \min(\Delta R_{ij})\right) \quad (11.1)$$

These filtered subjects are calibrated and a minimum p_{T} threshold $p_{\text{T,filter}}^{\text{min}}$ is applied afterwards. In the following only a subset N_{filter} of the hardest filtered subjects is considered.

11.2.3 Recluster three exclusive top subjects

The constituents of the filtered subjects are used to recluster exactly three top subjects with a fixed radius parameter $R_{\text{exclusive}}$, while a minimum of 3 filtered subject constituents is required. These top subjects are again calibrated and a minimum p_{T} threshold $p_{\text{T,recluster}}^{\text{min}}$ is applied afterwards. The indices of the reclustered subjects are sorted by the p_{T} of the jet : $p_{\text{T},j_{\text{excl}}^1} > p_{\text{T},j_{\text{excl}}^2} > p_{\text{T},j_{\text{excl}}^3}$. These three exclusive subjects are considered as candidates for the top decay products.

11.2.4 Build top candidate

Depending on the setup of the algorithm, the final top candidate is either build from the constituents of the filtered subjects (as used as input for the exclusive reclustering) or from the three exclusive reclustered subjects. Due to the additional calibration of the reclustered subjects, these two procedures may result in slightly different kinematics for the final top candidate. All triplets passing this step provide a *valid top candidate*, which is tested against specific criteria.

11.2.5 Apply W-mass constraint

While the previous steps provide a good rejection against multijet QCD background, the W-mass constraint improves rejection against W+Jets background. The mass of the dijet combination of two exclusive reclustered subjects m_{ij} has to match the W-mass and the full combination of all three jets m_{ijk} is required to represent the top mass. Both constraints are applied within a pre-defined uncertainty of the reference masses defined in equation (11.2)

$$m_{\text{W}} = 80.4 \text{ GeV} \quad m_{\text{top}} = 172.3 \text{ GeV} \quad (11.2)$$

All permutations of combinations of the three exclusive subjects are tested on a plane of ratios of the masses of the combined objects $\frac{m_{23}}{m_{123}}$ vs. $\arctan\left(\frac{m_{13}}{m_{12}}\right)$.

$$x_{\text{low}} < \arctan\left(\frac{m_{13}}{m_{12}}\right) < x_{\text{up}} \quad (11.3)$$

$$\left(\frac{m_{23}}{m_{123}}\right) > y_{\text{low}} \quad (11.4)$$

Equations (11.3) and (11.4) reject extreme cases of the mass ratios with at least one very low mass subjet by applying simple cuts.

$$\sqrt{1 - R_{\text{max}}^2 \left(1 + \left(\frac{m_{13}}{m_{12}}\right)^2\right)} < \left(\frac{m_{23}}{m_{123}}\right) < \sqrt{1 - R_{\text{min}}^2 \left(1 + \left(\frac{m_{13}}{m_{12}}\right)^2\right)} \quad (11.5)$$

$$\sqrt{1 - R_{\text{max}}^2 \left(1 + \left(\frac{m_{12}}{m_{13}}\right)^2\right)} < \left(\frac{m_{23}}{m_{123}}\right) < \sqrt{1 - R_{\text{min}}^2 \left(1 + \left(\frac{m_{12}}{m_{13}}\right)^2\right)} \quad (11.6)$$

$$R_{\text{min}} < \left(\frac{m_{23}}{m_{123}}\right) < R_{\text{max}} \quad (11.7)$$

The other three equations define an A-Shape cut characteristic for the HEPTOPTAGGER algorithm. Three lines are defined, representing $m_{12} = m_W$ (equation (11.5)), $m_{13} = m_W$ (equation (11.6)) and $m_{23} = m_W$ (equation (11.7)) applied with a relative band of acceptance of σ , hence defining $R_{\text{min}}^{\text{max}} = (1 \pm \sigma) \cdot \frac{m_W}{m_{\text{top}}}$. An illustration of these cuts is shown in figure 57.

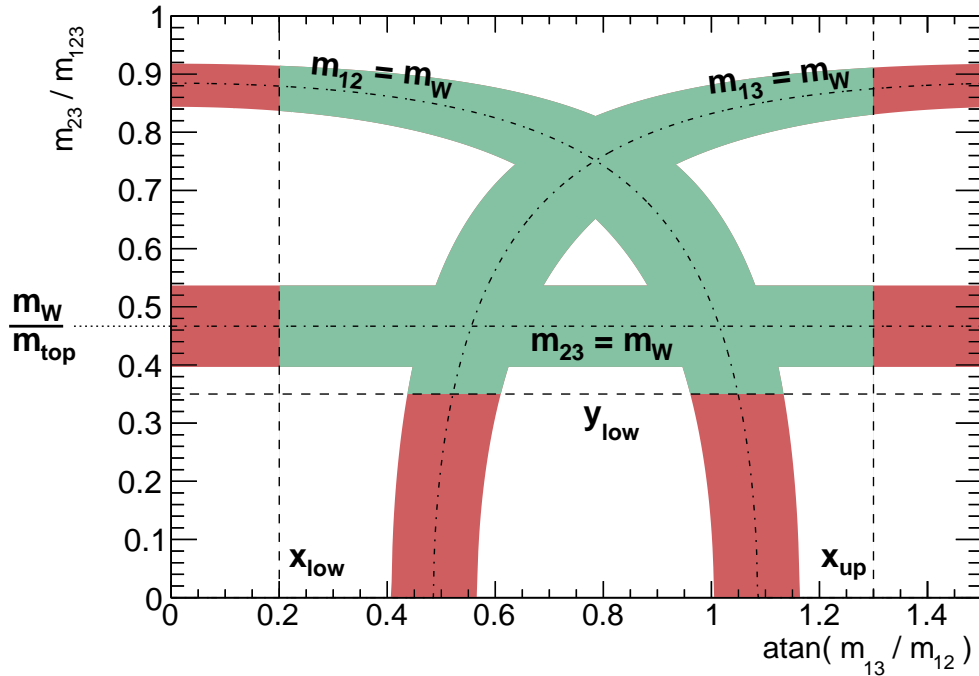


Figure 57: Illustration of the A-Shape cut used in the W -mass constraint of the HEPTOPTAGGER algorithm to reject major background components such as W +Jets and multijet. Cuts applied to the ratios of masses of combined subjets force at least one combination of two subjets to match the reference W -mass within a defined width σ (here $\sigma = 30\%$).

11.2.6 Apply top mass window

The mass of the final reconstructed top candidate $m_{\text{candidate}}^{\text{top}}$ is required to satisfy a defined mass range given in equation (11.8).

$$m_{\text{min}}^{\text{top}} < m_{\text{candidate}}^{\text{top}} < m_{\text{max}}^{\text{top}} \quad (11.8)$$

Since a large radius jet might contain more than one triplet of hard subjet permutations providing a valid top candidate, the triplet with the top candidate mass closest to the reference top mass is selected.

11.3 Analysis with the HEPTopTagger

Similar to the resolved and boosted selection in the analysis in this thesis (cf. section 6.2), a specific *top tagger selection* with the HEPTOPTAGGER algorithm is applied, which is also based on a general pre-selection of events (cf. section 6.2.1).

A small radius jet is associated to the leptonic top decay similarly to the boosted selection (cf. section 6.2.2) via $\Delta R(\ell, j) < 1.5$ and referred to as *leptonic b-jet* or j_{lep} in the following. The jets of the Cambridge/Aachen $R = 1.5$ jet collection have to fulfill specific boosted criteria as of central jets $|\eta| < 2.0$ and a high $p_{\text{T}} > 300$ GeV, as well as a good separation to the leptonic top decay, angular distance to the lepton ℓ of $d\phi(\ell, \text{jet}) > 2.3$ and radial distance to the leptonic b-jet of $dR(j_{\text{lep}}, \text{jet}) > 1.5$. Jets satisfying these criteria are referred to as *taggable* jets. A jet with a valid top candidate satisfying the W-mass constraint and the top mass window is referred to as a *tagged* jet. For rare cases with more than one tagged large radius jet per event, the highest p_{T} jet is selected.

An additional truth matching is applied for $t\bar{t}$ and signal samples for an efficient optimization of the algorithm. An event topology satisfying a significant boost on truth parton-level for the top decay products q_i as of $dR(\text{top}_{\text{truth}}, q_i) < 1.6$ is referred to as *truth taggable* event. If a jet in this event is located close to the truth top parton $dR(\text{top}_{\text{truth}}, \text{jet}) < 0.75 \cdot R$, it is referred to as *truth tagged*² jet.

The same requirements are applied to the anti- k_{t} $R = 1.0$ collection to allow for a consistent comparison between the ATLAS tagger (cf. section 6.2.2) and the HEPTOPTAGGER.

11.3.1 Algorithm configurations

The default working point of the HEPTOPTAGGER (referred to as *HTT0* in the following) as presented in the publication paper of the algorithm was optimized for the all-hadronic $t\bar{t}$ environment with a very pure signal selection and high background rejection at cost of signal efficiency. Since the analysis in the lepton+jets $t\bar{t}$ environment presented in this thesis does not face a background contribution as large as the all-hadronic $t\bar{t}$ environment, alternative

²A truth tag is independent of a tag of the HEPTOPTAGGER algorithm.

configurations of the HEPTOPTAGGER algorithm, optimized for improved signal efficiency and tolerating a lower background rejection, are tested.

Two alternative configurations, modifying some of the internal parameters of the algorithm (referred to as *HTT1* and *HTT2* in the following), are presented. An overview of the parameters of the different configurations is listed in table 21. One of the major changes is the choice of the k_t instead of the C/A clustering algorithm for the subjet reclustering, which has been suggested by one of the authors of the HEPTOPTAGGER algorithm in a private communication.

Since the k_t clustering algorithm combines hardest objects last (cf. section 4.5.2), this algorithm is the most intuitive choice for reversing the clustering of hard objects, since the C/A clustering algorithm does not take the p_T of constituents into account. A known issue with the HEPTOPTAGGER algorithm is the reconstruction of a top candidate with an underestimated mass, peaking around the W-mass of ~ 80 GeV, for a small but perceivable fraction of events. These events miss one decay product of the top quark decay during reconstruction, e.g. rejected by the subjet p_T threshold. A study on this threshold parameter concluded, that lowering this threshold recovers some of these events to a reasonable top mass. Although this also recovers a large fraction of W+Jets events, that look more $t\bar{t}$ -like. Hence a minimum threshold of 15 GeV is tested with the HTT2 configuration as a compromise between an improved top mass resolution and a drop in background rejection, compared to 20 GeV for the HTT0 and HTT1 configurations .

11.3.2 Cut-based optimization

Beside the modified clustering configurations, the W-mass constraint is loosened to a simple box-cut for the HTT1/HTT2 configurations, instead of the characteristic A-Shape as well as applying a broader top mass window for a significant gain in efficiency. The cuts applied to the subjet mass plane as a W-mass constraint for each configuration are shown in figure 58, comparing between signal ($t\bar{t}$) and background (W+Jets). Figure 58(a) and 58(b) illustrate the typical A-shape cut for the default configuration HTT0 as a rather confining cut on the mass ratios. The plots for the HTT1 (58(c), 58(d)) and HTT2 (58(e), 58(f)) configurations denote a generally higher acceptance and the less stringent box-cut setup. These plots show all triplets with a valid top candidate from truth tagged jets for $t\bar{t}$ and taggable jets for W+Jets. Since the top mass window is applied after this cut, they also include triplets with a non-reasonable top mass, mostly located in the outer regions of the plots, while the center region denotes top candidates with reasonable subjet mass ratios, which is selected by each configuration. A conspicuous difference is the effect of the two different jet clustering algorithms (C/A and k_t), which is mainly caused by the additional p_T dependence of the k_t clustering algorithm.

Variable	HTT0	HTT1	HTT2
truth matching			
truth taggable event	$dR(\text{top}_{\text{truth}}, q_i) < 1.6$		
truth tagged jet	$dR(\text{top}_{\text{truth}}, \text{jet}) < 0.75 \cdot R$		
taggable input jets			
clustering algorithm	Cambridge/Aachen (C/A)		
clustering radius	1.5		
kinematics	$p_T > 300 \text{ GeV}, \eta < 2.0$		
separation to leptonic top-decay	$d\phi(\ell, \text{jet}) > 2.3, dR(\text{lepjet}, \text{jet}) > 1.5$		
mass drop (hard subjects)			
mass drop threshold t_{MD}	0.8		
mass drop cutoff m_C	50 GeV		
filtering (filtered subjects)			
clustering algorithm	C/A	k_t	k_t
minimum clustering radius $R_{\text{filter}}^{\text{min}}$	0.25	0.25	0.25
minimum p_T threshold $p_{T,\text{filter}}^{\text{min}}$	20 GeV	20 GeV	15 GeV
reclustering (reclustered subjects)			
clustering algorithm	C/A	k_t	k_t
clustering radius $R_{\text{exclusive}}$	$\pi/2$	$\pi/2$	$\pi/2$
minimum p_T threshold $p_{T,\text{recluster}}^{\text{min}}$	20 GeV	20 GeV	15 GeV
top candidate			
build from subjet collection	filtered	reclustered	reclustered
number of filtered subjects N_{filter}	3-5	3-5	3-5
W-mass constraint			
cut-type	A-Shape	Box	Box
band of acceptance σ	0.3	-	-
lower x-bound x_{low}	0.20	0.35	0.30
upper x-bound x_{up}	1.30	1.15	1.20
lower y-bound y_{low}	0.35	0.28	0.18
top mass window			
range $m_{\text{top}}^{\text{min}} - m_{\text{top}}^{\text{max}}$	140 – 210 GeV	100 – 210 GeV	100 – 210 GeV

Table 21: Input parameters and internal parameters of the HEPTOPTAGGER algorithm for three different configurations.

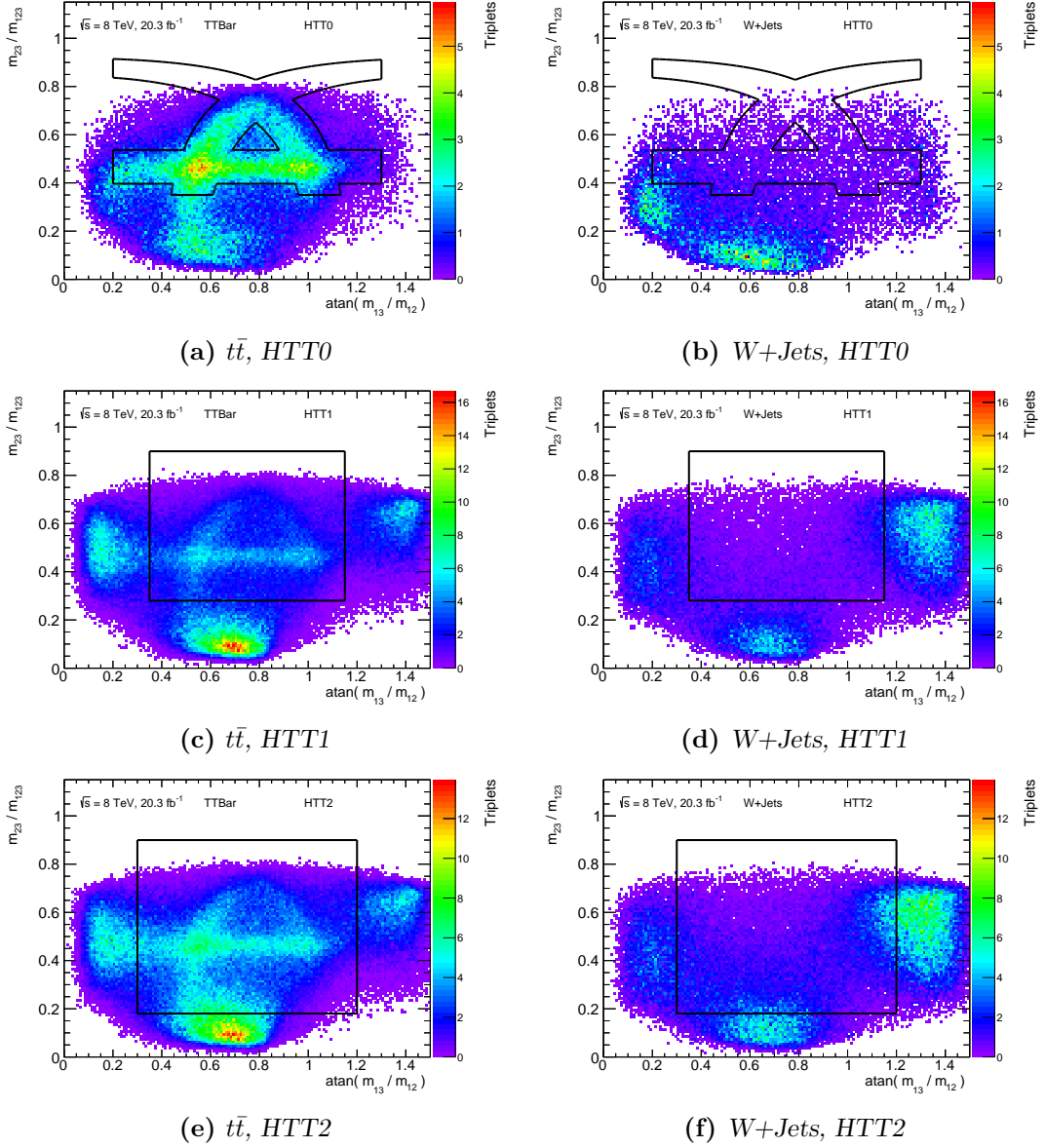


Figure 58: W -mass constraint on the subject $\frac{m_{23}}{m_{123}}$ vs. $\text{atan}(\frac{m_{13}}{m_{12}})$ mass plane applied in the HEPTOPTAGGER algorithm for different configurations for all triplets in (a),(c),(e) truth tagged jets in $t\bar{t}$ events and (b),(d),(f) taggable jets in $W+Jets$ events. The cuts applied are indicated by the area of the black lined shapes.

11.3.3 Multivariate analysis

The classical approach of a cut-based analysis with a consecutive list of cuts on specific variables can be improved using a multivariate analysis, which is studied for the output of the HEPTOPTAGGER algorithm instead of applying the W - and top-mass constraints, as suggested in [116]. The multivariate analysis is applied using a decision tree algorithm implemented in the TMVA framework [117].

A decision tree represents a collection of cuts used to classify given events as signal or background, based on a set of well defined discriminating variables. The information of several input variables is condensed into one single quantity, properly considering their correlations. This procedure has proven high performance in a range of fields like medicine, finance and also particle physics. A tree is trained for a dataset with predefined signal and background contributions. The input (root node) is analyzed for a cut on a specific variable with a maximum separation power between signal and background, classifying the analyzed data into two different nodes. Each new node is analyzed in an iterative procedure until the number of events within a given node drops below a predefined minimal threshold or the maximum depths of the tree is reached. The separation power per node is estimated using the so-called *Gini*-index G , which is a measure for the signal purity.

$$G = p(1 - p) \quad \text{with} \quad p = \frac{N_{\text{signal}}}{N_{\text{all}}} \quad (11.9)$$

This way a complete tree of cut decisions is created to classify each event depending on its specific variable values as illustrated in figure 59, considering a set of variables analyzed in the HEPTOPTAGGER, such as the combined subjet mass m_{12} , the p_T of the top candidate p_T^{top} and the mass of the top candidate m_{top} . A signal event not satisfying the first separation cut can still be recovered for deeper level criteria of the tree, while it would be lost for a simple list of consecutive cuts.

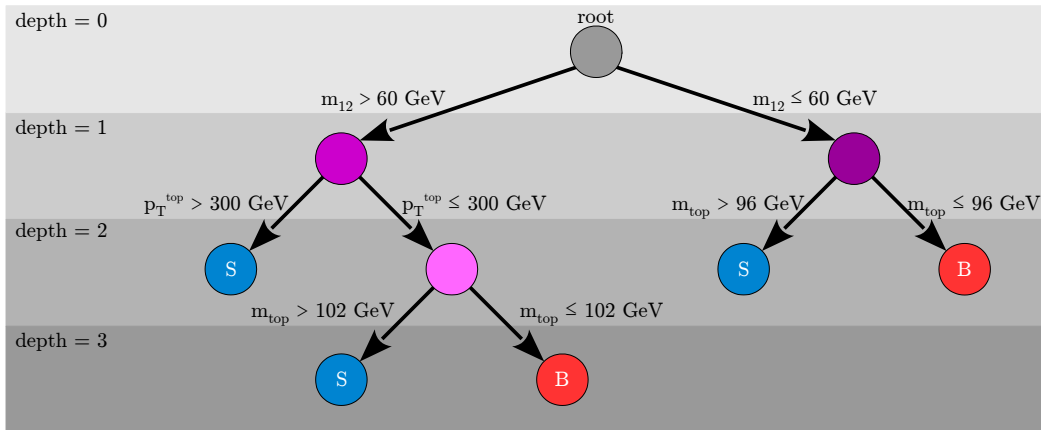


Figure 59: Structure of a decision tree, classifying a given dataset into signal- (S) and background-like (B) events. Starting from a root node, a series of cuts with maximum separation power is applied to separate the different event types. The procedure is aborted by a maximum tree depth (here chosen as 3) or a minimum event yield per node.

The performance of these decision trees can be improved significantly introducing *boosting*, creating a large set of decision trees with a specific weight applied per tree. One of the most common boosting techniques is the adaptive boost (*AdaBoost*), also provided in the TMVA framework. This technique assigns a larger weight to mis-classified events, increasing their impact on the decisions during the creation of the next tree. Thereby the performance is significantly improved, especially analyzing complex systems, including variables with a low separation power. The final discriminant is an overall output weight (response v), which is assigned to each event (with its specific variable values), giving an estimate if this event is more signal- ($v \simeq +1$) or background-like ($v \simeq -1$). The significance $s = S/\sqrt{S+B}$ is optimized for the number of signal (S) and background (B) events passing a chosen cut on the response. A well chosen set of input variables allows for a good separation power with signal events tending towards responses of $v \rightarrow +1$ and background events towards $v \rightarrow -1$.

While a subset of the original input is used for training, the complementary subset is used to test the results against overtraining, applying the outcome of the training to the test dataset. These two distributions should ideally match within a low error rate, while larger discrepancies hint for an overtraining effect, optimizing for small fluctuations as false signal- or background-characteristic features in the training dataset. This so-called *Kolmogorov-Smirnov* test implemented in the TMVA framework represents a measure for the comparison of the training- and test-distributions. *Boosted Decision Trees* (BDT) are much more robust against overtraining compared to standard decision trees. More detailed information on the TMVA framework can be found in [117].

The BDT in this study is trained on hard subjet triplet level. Considering all triplets with a valid top candidate within a distance to the truth top with $dR(t_{\text{truth}}, t_{\text{triplet}}) < 1.125$ in a $t\bar{t}$ sample, one triplet per event with the mass closest to the truth top mass $\min(m_t^{\text{truth}} - m_t^{\text{triplet}})$ is selected as signal input. All triplets with a valid top candidate from all non- $t\bar{t}$ background sources are added as background, defined for each configuration HTTi. Including only variables describing the hadronic top decay as used by the default HEPTOPTAGGER configuration (combined subjet masses m_{ij} , top candidate mass and p_T , large radius jet mass and η) only shows a minor improvement compared to the cut-based optimization, since these variables have a strong separation power covered by the cut-based approach. An optimization tuned for the lepton+jets $t\bar{t}$ environment explicitly, including variables of the leptonic top decay (lepton η and p_T , leptonic top mass and p_T , leptonic b-jet p_T) and also separation variables between the hadronic and leptonic top decay (radial distances $dR(\ell, j_{\text{lep}})$, $dR(j, j_{\text{lep}})$ and angular distance $d\phi(j, \ell)$, [$j = \text{large radius jet}$]) shows a significant improvement in efficiency. These additional variables have a weak separation power on the full distribution, but may differ on an event-by-event basis, depending on their correlation to other variables. Extracting small differences of such variables on a deeper break-down of a subset of events represents the real advantage of multivariate analysis over a classical cut-based approach, while the risk of overtraining has to be kept in mind. An overview of the input variable distributions is shown in figure 60 using the example of the HTT0 configuration.

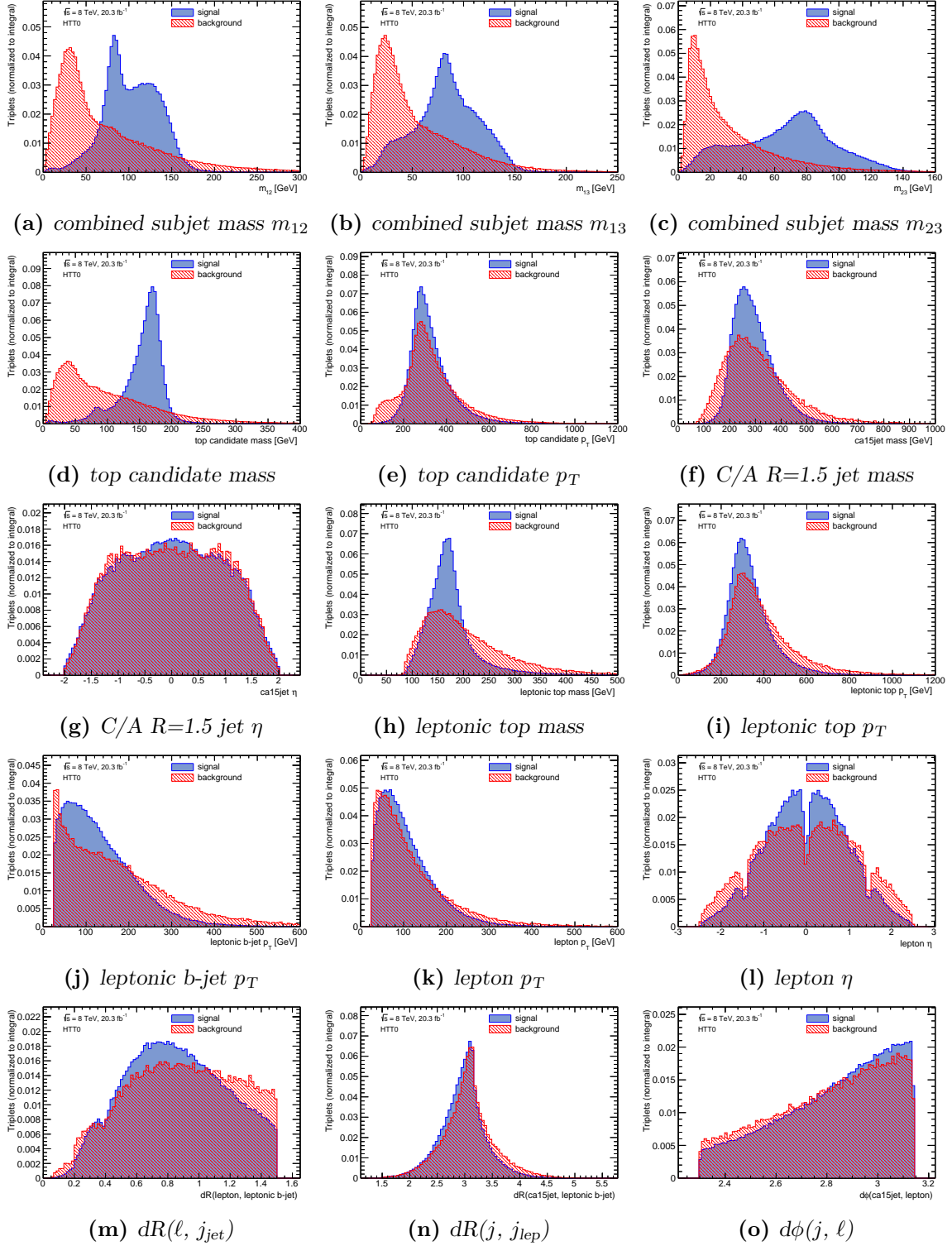


Figure 60: TMVA input variables for the HTT0 configuration. Signal distributions shown in blue are derived from truth-matched $t\bar{t}$ triplets, red background from all non- $t\bar{t}$ triplets with a valid top candidate for taggable large radius jets. Signal and background distributions are normalized to the integral for a direct shape comparison. While variables (a)-(g) are used in the default HEPTOP-TAGGER algorithm, variables (h)-(o) are added for a more specific optimization for the lepton+jets $t\bar{t}$ environment.

Non-trivial correlations between the input variables are considered by the TMVA framework as shown in the input variable correlation matrices for signal and background in figure 61. As expected, a stronger correlation can be observed for the top candidate mass and the subjet combination masses m_{ij} . The variables that show a largely different correlation behavior between signal and background are especially promising to bring an improvement in separation power, hinting for signature specific quantities. Beside the default separation power of the HEPTOPTAGGER algorithm, using the difference in correlation for signal and background of the top candidate mass and the subjet masses m_{ij} , especially variables connected to the leptonic top decay show potential improvements compared to the cut-based approach, such as the η of the lepton and the large radius jet, or the radial separation dR between the lepton and the leptonic b-jet to the p_T of the different objects.

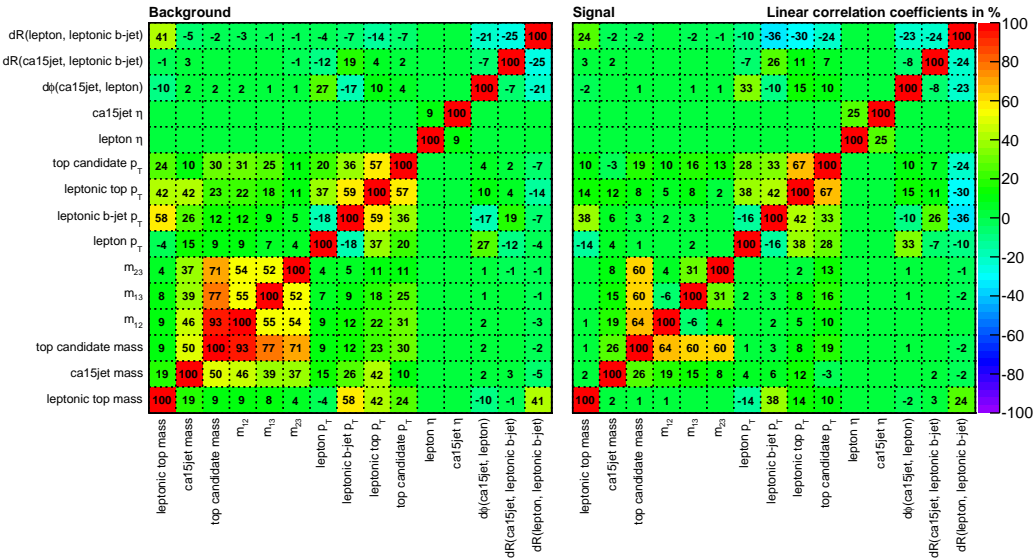


Figure 61: TMVA input variable correlation matrices exemplarily shown for the HTT0 configuration for signal ($t\bar{t}$) and background (non- $t\bar{t}$), while the z-axis ranges from -100 (full anti-correlation) to $+100$ (full correlation). Variable combinations with empty cells (0) or small values do not have any correlation.

11.3.4 Comparison of working points and ATLAS tagger

The trained BDTs are applied to the full analysis for all events with a taggable jet and optimized for maximum significance $s = S/\sqrt{S+B}$ for signal (S) and background (B) yields by scanning the BDT response v for different thresholds. To ensure model independence for the tested benchmark BSM models in this analysis, the significance is optimized using SM $t\bar{t}$ as signal and W+Jets, as major source of background in this analysis, as background. The maximum BDT response per event is chosen among all triplets within all taggable large radius jets. Triplets within a taggable jet with insufficient substructure information may fail during the reconstruction of a valid top candidate. These triplets are assigned with a default response of $v = -1.0$. The maximum BDT response with an optimization of the significance

$s_{S=t\bar{t}}^{B=W+Jets} = N_{t\bar{t}} / \sqrt{N_{t\bar{t}} + N_{W+Jets}}$ and the corresponding cut-value on the BDT response is shown in figure 62 for the HTT0 configuration (cf. appendix A.6 for other configurations).

These results include tuning of some general parameters of the TMVA framework such as the total number of trees, the number of cut intervals scanning for the best separation cut, as well as the abortion criteria with the maximum depth of each tree and the minimum threshold of events per node. These parameters have been tuned for a maximum significance and satisfying overtraining test results, all others are set to default values (cf. [117]).

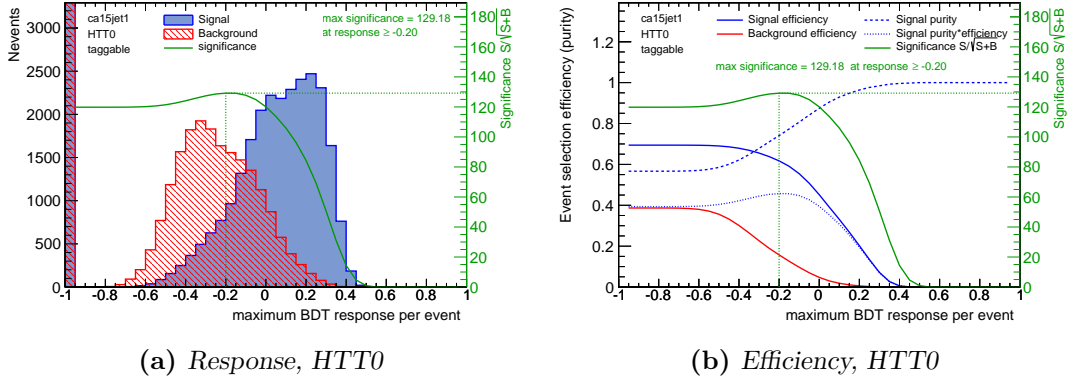


Figure 62: BDT response and efficiency for multivariate analysis optimization for the HTT0 configuration of the HEPTOPTAGGER algorithm. The response on $t\bar{t}$ signal (S) is shown in blue and for $w+Jets$ background (B) in red. The green curve shows the significance $S/\sqrt{S+B}$ at a given cut-value of the BDT response.

Beside the task of choosing the best configuration among the presented setups, the comparison of the HEPTOPTAGGER performance with the ATLAS tagger is of major interest in this study. A contrasting juxtaposition of the studied setups is given in figure 63. These kind of curves³ are a common way to compare the performance of different algorithms, plotting the background rejection⁴ $1/\varepsilon_B$ (for all $W+Jets$ events with a taggable jet) as a function of the signal efficiency ε_S (for all $t\bar{t}$ events with a truth tagged jet). An optimal algorithm reaches the upper right corner with large background rejection and efficient signal identification. For a direct comparison between the ATLAS tagger and the HEPTOPTAGGER, using individual input jet collections, each considered jet is matched to an anti- k_t $R = 1.0$ truth jet and the result is plotted in bins of p_T of these matched jets. The plot shows the ATLAS tagger with a scan of the cut on the $\sqrt{d_{12}}$ variable denoted by the gray line, which is limited by the additional requirement on the jet mass $m_{jet} > 100$ GeV, and the default working point chosen in this analysis of $\sqrt{d_{12}} = 40$ GeV, marked by the black cross. The shifted blue curve and cross includes the b-tagging requirement. The cut based approach for the optimization of the HEPTOPTAGGER algorithm is marked by a colored star each of the three configurations. For the TMVA optimization, a scan of the cut on the BDT response for each configuration is indicated by a colored line as well as the working point of optimal significance marked by a correspondingly colored cross.

³commonly referred to as Receiver Operator Characteristic (ROC) curve.

⁴plotted as $1/\varepsilon_B$ for a better discrimination, since the background efficiency is usually rather small.

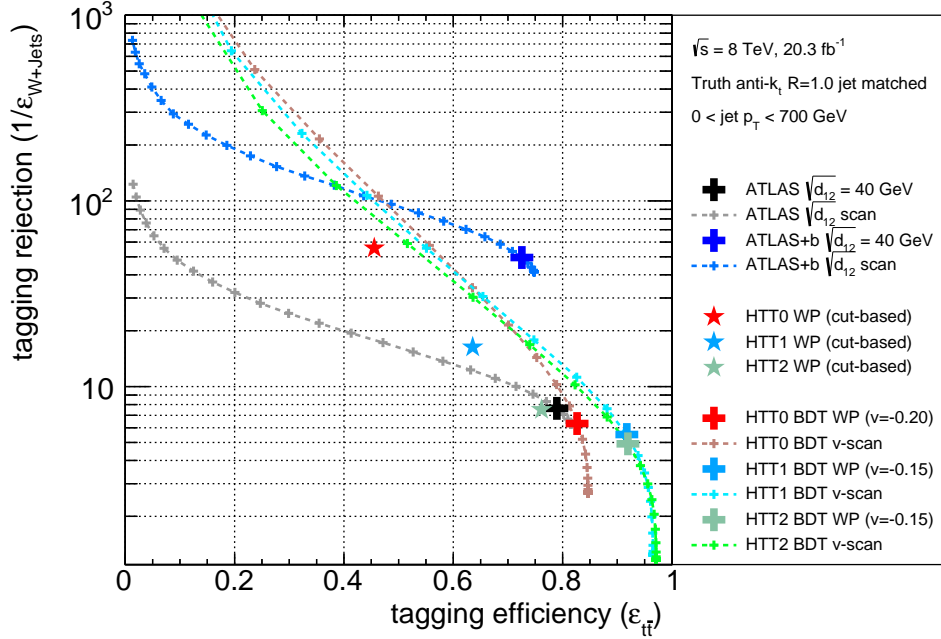
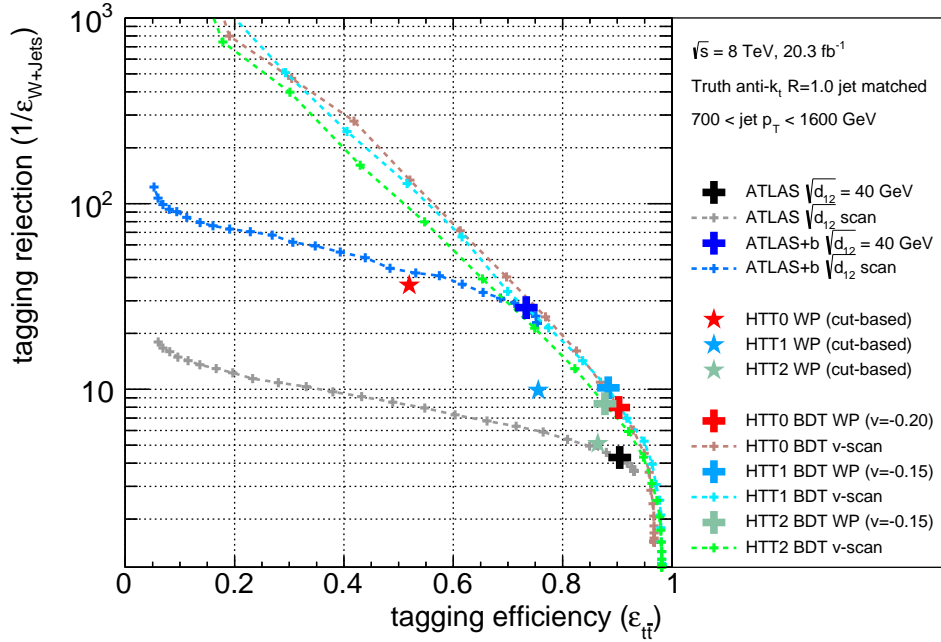
(a) Low p_T region of matched anti- k_t $R = 1.0$ truth jets(b) High p_T region of matched anti- k_t $R = 1.0$ truth jets

Figure 63: Tagging rejection for taggable jets in background ($W+Jets$) $1/\varepsilon_{W+Jets}$ events vs. tagging efficiency for truth tagged jets in signal ($t\bar{t}$) $\varepsilon_{t\bar{t}}$ events for different taggers and configurations in the (a) low jet p_T and (b) high jet p_T region. The ATLAS setup with and without b -tagging is compared with the cut-based and BDT-optimized HEPTOPTAGGER configurations. (The efficiency and rejection for the plotted small crosses are calculated explicitly, intermediate regions are interpolated.)

Including the b-tagging requirement for the ATLAS tagger improves the background rejection significantly, but the signal efficiency is decreased due to the limited b-tagging efficiency of $\sim 70\%$. The cut-based default configuration HTT0 shows good background rejection, but rather small signal efficiency, as stated in the beginning of this chapter due to the optimization in the context of a very clean all-hadronic $t\bar{t}$ environment. The modified configurations HTT1/HTT2 improve the signal efficiency, but do not outperform the ATLAS+b tagger, significantly dropping in background rejection with increasing signal efficiency. Switching to the multivariate analysis optimization allows to reach regions of much higher signal efficiency especially for the low p_T region below 700 GeV. In this region the HTT0 setup shows a significant drop in background rejection for higher signal efficiency compared to the HTT1/HTT2 configurations. This effect vanishes for the high p_T region above 700 GeV, where all three configurations demonstrate a similar performance. This behavior can be expected from the different clustering procedures for the C/A and k_t algorithms, depending on the pure distance and additional p_T dependence respectively, which loses impact in boosted regimes with high p_T objects and merged decay products. The freedom of choice of the working point for the BDT setup also shows an improved setup with a slightly better efficiency at same background rejection compared to the default ATLAS+b tagger in the high p_T region, which is the main kinematic region of interest for boosted top decays, while low p_T events are recovered by the resolved selection. Despite this direct comparison, the working point with optimal significance for the BDT optimization is observed for an increased signal efficiency at cost of reduced background rejection as denoted by the colored crosses.

11.3.5 Multijet for HEPTopTagger

Background from sources of non-prompt leptons due to QCD multijet production is estimated using the QCD event weights provided for the analysis in this thesis (cf. section 5.2.6). The lepton selection is loosened to allow for lepton fakes used in the multijet samples, i.e. dropping the mini-isolation and only requiring medium instead of tight criteria (cf. section 4.3.2). Since the boosted selection and the toptagger selection use the same pre-selection for signal regions with a significant boost, this procedure represents a reasonable estimation.

11.3.6 Uncertainties

Systematic uncertainties taken into account specifically for the HEPTOPTAGGER algorithm are the jet energy scale (JES) uncertainties on the input large radius jets and the subjets. While the uncertainty on the jet energy resolution (JER) is found to be negligible for the large radius jet, it is considered for the subjets. Since no cuts are applied to raw jet masses but only on mass ratios, no explicit uncertainties on jet mass scale (JMS) and resolution (JMR) are applied [86]. A qualitative statement of the impact of these uncertainties on the final discriminant $m_{t\bar{t}}$ in the combined e/μ +jets channel is given in figure 64.

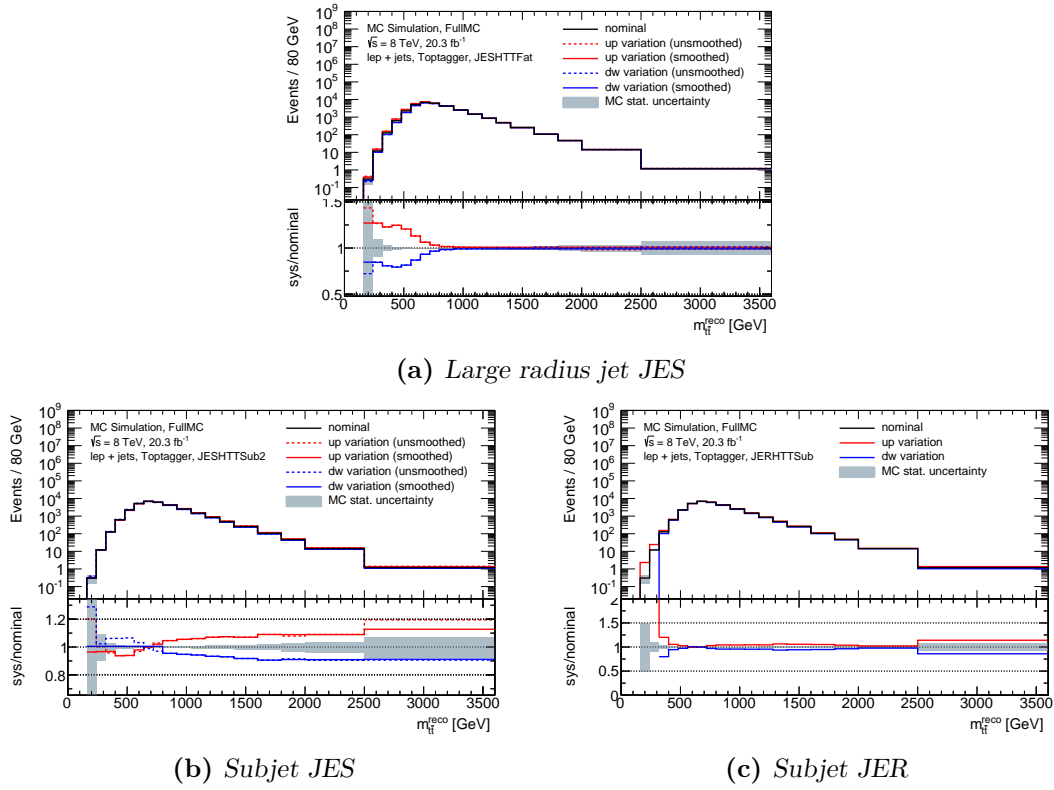


Figure 64: HEPTOPTAGGER specific systematic uncertainties for the (a) large radius input jet energy scale (JES), (b) subjet jet energy scale (JES) and (c) subjet jet energy resolution (JER).

A quantitative summary of all systematic uncertainties in the resolved+toptagger analysis, applying the optimal HTT0 configuration as an example, is given in table 22. Compared to the resolved+boosted analysis in this thesis (cf. table 17), the uncertainties affecting the resolved selection are not changed significantly, since these changes would only be caused indirectly by a different overlap removal with the corresponding selection in the boosted topology. The toptagger selection shows a decreased impact of PDF, ISR/FSR and some $t\bar{t}$ modeling uncertainties compared to the boosted selection, stating a more stable performance of the HEPTOPTAGGER algorithm compared to the ATLAS tagger. The most conspicuous change is the replacement of the large impact b-tagging systematic in the boosted selection by medium impact HEPTOPTAGGER uncertainties, especially for the leptophobic topcolor Z' resonance with a mass of 1.75 TeV. The overall systematic uncertainty in the boosted topology is significantly decreased from 17.6% (20.2%) for the boosted selection down to 12.0% (10.3%) for the toptagger selection for the full background (Z' with mass of 1.75 TeV).

Systematic uncertainties	Resolved		Toptagger	
	impact [%]		impact [%]	
	Bkg.	Z'	Bkg.	Z'
Luminosity	2.5	2.8	2.8	2.8
Parton Distribution Function (PDF)	5.4	9.4	6.3	9.2
Initial (ISR) / Final state radiation (FSR)	4.1	-	2.8	-
$t\bar{t}$ parton shower and fragmentation	6.0	-	3.4	-
$t\bar{t}$ normalization	5.6	-	4.4	-
$t\bar{t}$ electro-weak virtual correction	0.2	-	0.2	-
$t\bar{t}$ generator	2.0	-	0.4	-
$t\bar{t}$ top quark mass	1.0	-	2.9	-
W+Jets generator	< 0.1	-	< 0.1	-
Multi-jet normalization e +jets	0.3	-	0.2	-
Multi-jet normalization μ +jets	0.1	-	0.2	-
HEPTOPTAGGER large-R jet energy scale (JES)	< 0.1	< 0.1	5.6	0.5
HEPTOPTAGGER subjet energy scale (JES)	< 0.1	< 0.1	2.1	0.8
HEPTOPTAGGER subjet energy resolution (JER)	< 0.1	< 0.1	3.3	2.5
Small-R jet energy scale (JES)	5.8	2.8	0.3	1.4
Small-R jet energy resolution (JER)	0.9	7.2	0.6	0.5
Jet vertex fraction	2.7	1.7	0.4	0.1
b-tagging b-jet efficiency	1.1	2.0	-	-
b-tagging c-jet efficiency	0.1	0.8	-	-
b-tagging light-jet efficiency	< 0.1	0.1	-	-
Electron efficiency	0.2	0.6	0.5	1.4
Muon efficiency	0.9	1.0	1.0	1.2
MC statistical uncertainty	0.1	3.7	0.1	0.8
All systematic uncertainties	12.9	13.3	12.0	10.3

Table 22: Average impact of the dominant systematic uncertainties on the total background yield and on the estimated yield for a leptophobic topcolor Z' resonance with a mass of 1.75 TeV for combined e +jets and μ +jets channel in the resolved and toptagger (HTT0 setup) selection. Shifts are given in percent of the nominal yield. Uncertainties not applicable (e.g. uncertainties on $t\bar{t}$ modeling) for a Z' resonance are denoted with a bar (-) in the table.

11.4 Comparison of data and Standard Model expectations

The full analysis is performed for the MVA optimization of the HEPTOPTAGGER applying the HTT0 configuration. The uncertainty provided for the subjects in the HEPTOPTAGGER algorithm has been studied for C/A subjects. Although also a k_t subjet JES calibration is provided, the C/A setup was tested intensively. Hence the choice of the HTT0 configuration takes the best available knowledge into account. The optimized significance with a minimum BDT response of $v \geq -0.2$ (cf. figure 62) shows the best performance in the ROC curve among the configurations and good significance as listed in table 23. This table shows the BSM model independent optimization on the full set of SM $t\bar{t}$ events, with a significantly improved significance compared to the ATLAS setups. Since the cross section of the BSM models is unknown at this point, not the common $s = S/\sqrt{S+B}$ significance definition is chosen for signal, but using the signal efficiency $\varepsilon_{\text{signal}}$, which is independent of the cross section, and using the definition of the signal significance as $s_{\text{signal}} = \varepsilon_{\text{signal}}/\sqrt{N_{\text{MC}}}$.

setup	$t\bar{t}$ (full) [10^{-5}]	$t\bar{t}$ [10^{-6}]	Z' [10^{-3}]	g_{KK} [10^{-4}]	G_{KK} [10^{-3}]	Scalar [10^{-3}]
HTT0(BDT)	1.67	1.71	1.27	7.72	1.69	1.53
HTT1(BDT)	1.83	1.72	1.20	7.37	1.56	1.43
HTT2(BDT)	1.81	1.68	1.10	6.72	1.41	1.30
ATLAS	1.07	1.75	1.23	7.43	1.62	1.50
ATLAS+b	1.04	1.95	1.38	8.40	1.73	1.63

Table 23: Significance for the ATLAS tagger and different MVA optimized HEPTOPTAGGER configurations for the full $t\bar{t}$ selection and for an applied mass window of $1.5 < m_{t\bar{t}} < 2.4$ TeV, comparing with benchmark model resonances with a mass of 2 TeV. Significance s is listed for $s_{t\bar{t}} = \varepsilon_{t\bar{t}}/\sqrt{N_{t\bar{t}} + N_{\text{non-}t\bar{t}}}$ and $s_{\text{resonance}} = \varepsilon_{\text{resonance}}/\sqrt{N_{\text{MC}}}$.

The full $t\bar{t}$ system is reconstructed combining the selected lepton, the reconstructed neutrino, the leptonic b-jet as the leptonic top candidate t_ℓ and the top candidate with the best BDT response per event as the hadronic top candidate t_h . The cut on the optimized response and its separation on all backgrounds and signal is shown in figure 65. Since the W+Jets normalization procedure presented in chapter 7 relies on b-tagging, only the charge asymmetry normalization is applied in the toptagger selection. The heavy flavor scaling factors have been tested to have a negligible effect on the total W+Jets shape. A comparison of data and Standard Model expectations for the masses of the reconstructed top candidates and the fully reconstructed $t\bar{t}$ system $m_{t\bar{t}}$ for this setup are shown in figure 66 and the combined $m_{t\bar{t}}$ distributions in figure 67.

After applying all event selection criteria, a total selected event yield of 217 509 and 38 700 remains in observed data, while a total of 207939 ± 26824 and 36696 ± 4404 are expected from simulation of Standard Model processes for the resolved and toptagger selection respectively. Both yields agree within their uncertainties. The detailed expected yields for each background source are listed in table 24 including associated systematic uncertainties. A comparison with the boosted selection (cf. table 18) shows an improved total acceptance by a factor of 4 in the toptagger selection. A decreased $t\bar{t}$ purity is compensated by the lowered overall systematic uncertainty (cf. table 22).

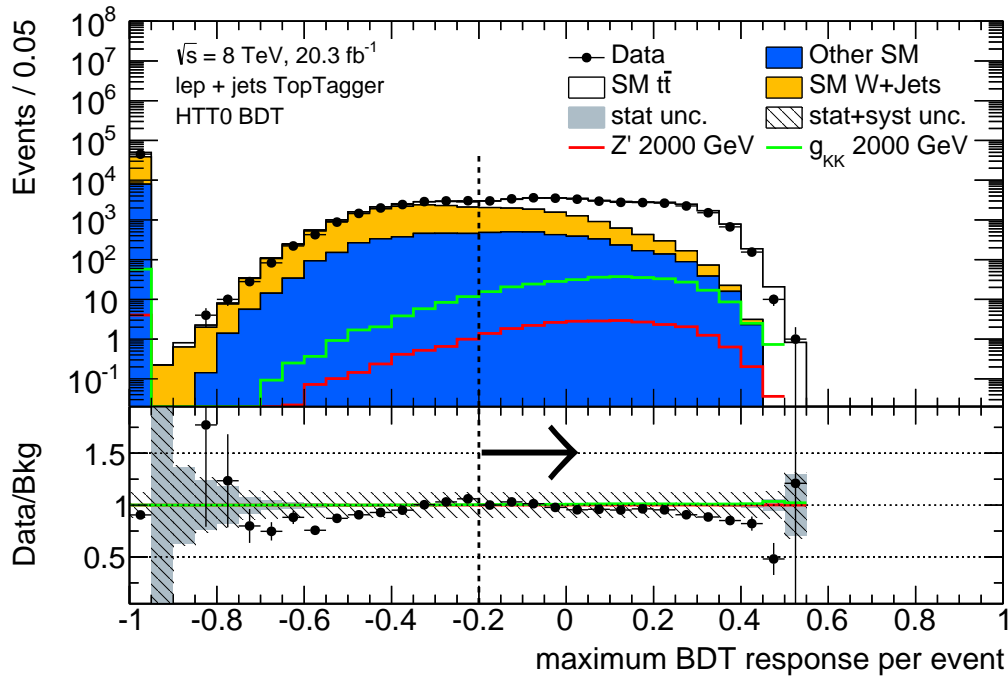


Figure 65: BDT response on analysis level using the MVA optimization for the HTT0 configuration with a comparison of data and Standard Model expectations. The Standard Model background is shown in a stacked histogram, including $t\bar{t}$, W+Jets and all remaining (merged) background processes. The bottom panel shows the data/MC agreement with the gray and shaded area indicating the statistical and the total systematic uncertainty respectively. Expected distributions for hypothetical signal leptophobic topcolor Z' (2000 GeV) and Randall-Sundrum Kaluza-Klein gluon g_{KK} (2000 GeV) resonances are overlaid (non-stacked).

Source	e +jets	μ +jets	total
$t\bar{t}$	$12\,878 \pm 1636$	$13\,247 \pm 1682$	$26\,125 \pm 3\,318$
Singletop	626 ± 56	687 ± 62	1313 ± 118
$t\bar{t}+V$	101 ± 6	103 ± 6	203 ± 12
Multijet	282 ± 96	60 ± 21	342 ± 117
W+Jets	$3\,328 \pm 483$	$3\,365 \pm 488$	$6\,693 \pm 970$
Z+Jets	889 ± 164	481 ± 88	1370 ± 252
Diboson	321 ± 32	329 ± 33	651 ± 65
Total	$18\,424 \pm 2\,211$	$18\,272 \pm 2\,193$	$36\,696 \pm 4\,404$
Data	19 676	19 024	38 700

(a) *Toptagger selection*

Source	e +jets	μ +jets	total
$t\bar{t}$	$89\,184 \pm 11\,861$	$88\,478 \pm 11\,768$	$177\,662 \pm 23\,629$
Singletop	$3\,758 \pm 440$	$3\,714 \pm 435$	$7\,473 \pm 874$
$t\bar{t}+V$	252 ± 13	249 ± 13	500 ± 26
Multijet	$5\,284 \pm 999$	$1\,050 \pm 198$	$6\,334 \pm 1\,197$
W+Jets	$6\,351 \pm 718$	$7\,036 \pm 795$	$13\,388 \pm 1\,513$
Z+Jets	$1\,349 \pm 453$	621 ± 209	$1\,970 \pm 662$
Diboson	311 ± 55	300 ± 53	611 ± 108
Total	$106\,490 \pm 13\,737$	$101\,449 \pm 13\,087$	$207\,939 \pm 26\,824$
Data	111 243	106 266	217 509

(b) *Resolved selection*

Table 24: Event yields for data and Standard Model expectations after applying the full (a) toptagger and (b) resolved selection and reconstruction. including the impact of the sum in quadrature of all systematic uncertainties on the Standard Model expectations as uncertainty.

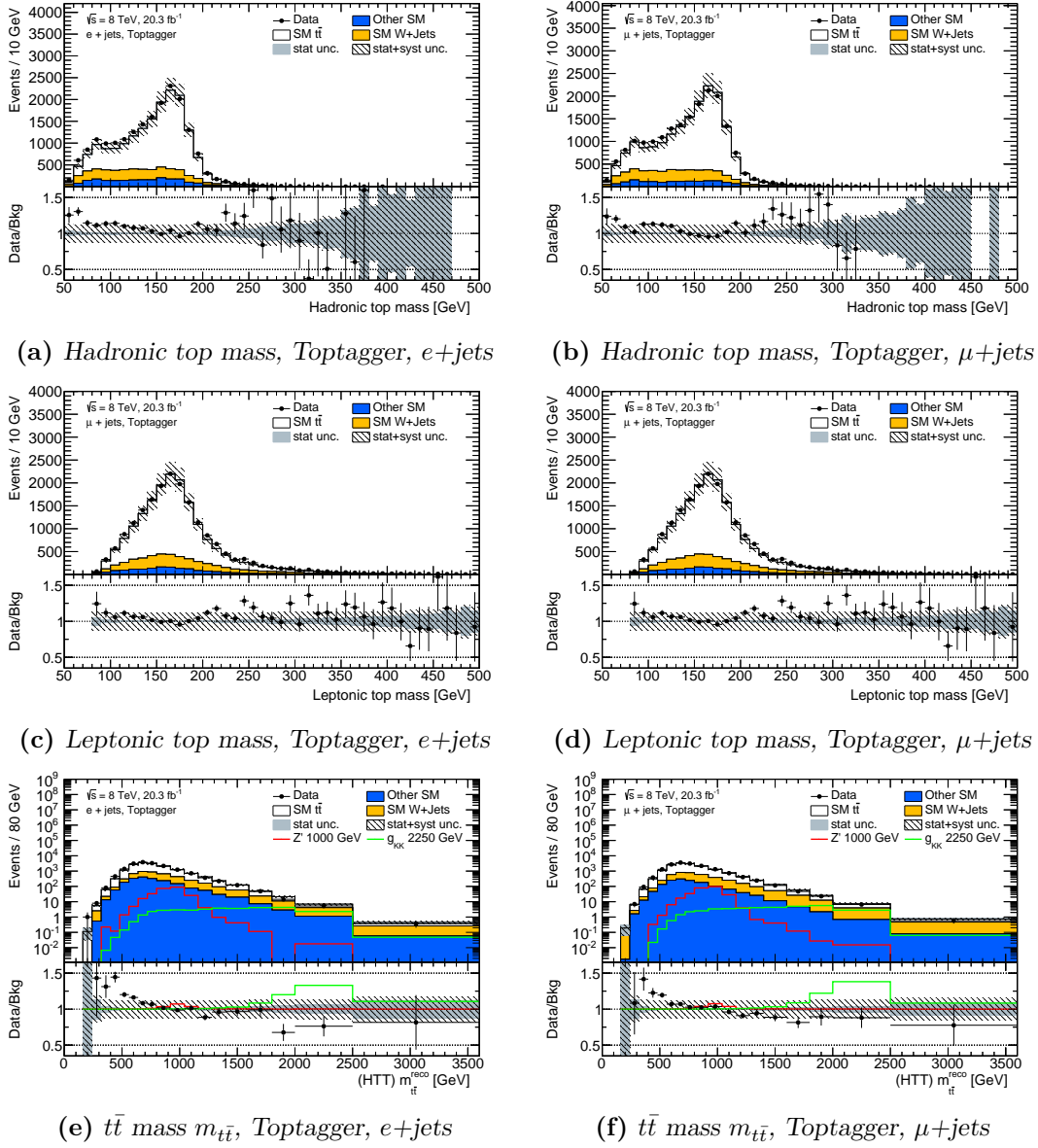


Figure 66: Comparison of data and Standard Model expectations for specific variables of the toptagger (*HTT0* configuration) selection : Reconstructed mass of the (a),(b) hadronically decaying top candidate, the (c),(d) leptonically decaying top candidate and the (e),(f) full $t\bar{t}$ system in the $e+jets$ and $\mu+jets$ channel respectively after the full event reconstruction in the boosted topology. The Standard Model background is shown in a stacked histogram, including $t\bar{t}$, $W+Jets$ and all remaining (merged) background processes. The bottom panel shows the data/MC agreement with the gray and shaded area indicating the statistical and the total systematic uncertainty respectively. Expected distributions for hypothetical signal leptophobic topcolor Z' (750 GeV or 1000 GeV) and Randall-Sundrum Kaluza-Klein gluon g_{KK} (1300 GeV or 2250 GeV) resonances are overlaid (non-stacked) for the $m_{t\bar{t}}$ distributions.

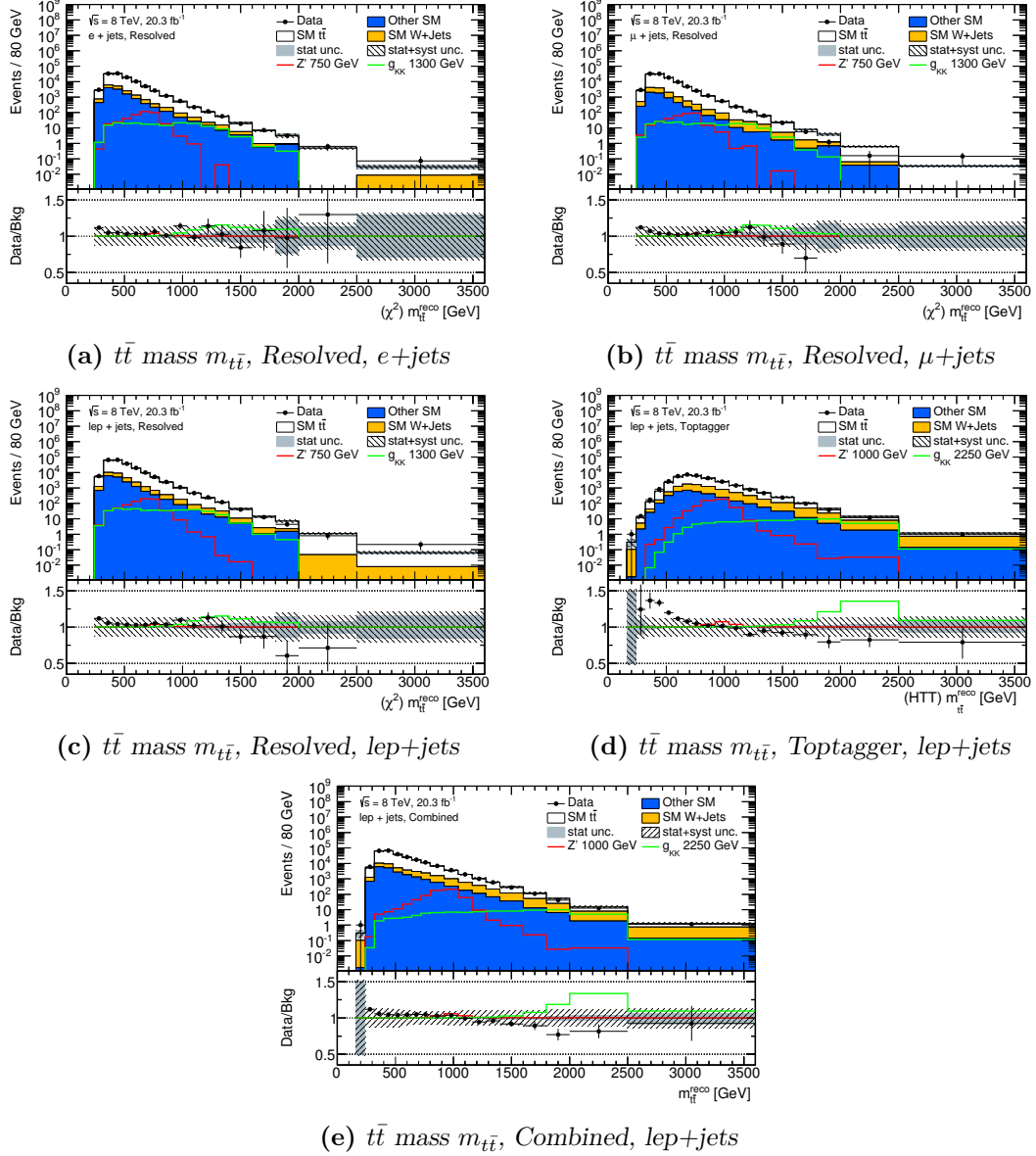


Figure 67: Comparison of data and Standard Model expectations for the reconstructed mass of the full $t\bar{t}$ system $m_{t\bar{t}}$ for the resolved selection in the (a) e +jets and (b) μ +jets channel, in the combined lepton+jets channel for the (c) resolved and (d) toptagger selection, and (e) all channels and selections combined. The Standard Model background is shown in a stacked histogram, including $t\bar{t}$, W +Jets and all remaining (merged) background processes. The bottom panel shows the data/MC agreement with the gray and shaded area indicating the statistical and the total systematic uncertainty respectively. Expected distributions for hypothetical signal leptophobic topcolor Z' (750 GeV or 1000 GeV) and Randall-Sundrum Kaluza-Klein gluon g_{KK} (1300 GeV or 2250 GeV) resonances are overlaid (non-stacked).

11.5 Results

The four invariant mass spectra of the fully reconstructed $m_{t\bar{t}}$ system (e +jets and μ +jets channel, resolved and toptagger selection) presented in section 11.4 are used as final discriminating observables for this study. The Bayesian limit setting procedure (cf. section 10.1) is applied for a leptophobic topcolor Z' and a RS Kaluza-Klein gluon g_{KK} to compare the exclusion power to the analysis presented in this thesis. Upper limits on the cross section times branching ratio are set on a mass range from 0.5 up to 3.0 TeV as shown in figure 68. The pulls and uncertainties on the posterior distributions for each systematic for a Z' resonance with a mass of 2 TeV are shown in figure 69, stating a good sanity for the calculated limits. The Asimov test predicts a stronger constraint on the HEPTOPTAGGER systematic uncertainties, while the constraints in data show a more stable behavior. Based on these results, a leptophobic topcolor Z' is excluded for masses below 2.1 (2.1) TeV and a Randall-Sundrum Kaluza-Klein gluon g_{KK} for masses below 2.3 (2.4) TeV for observed (expected) upper cross section times branching ratio limits at 95% confidence level, summarized in table 25. The expected limit is comparable with the analysis presented in this thesis, while the observed limit is improved from 1.9 (2.1) to 2.1 (2.4) for a Z' (g_{KK}). A direct comparison for resonances with a mass of 2.25 TeV is shown in table 26. While the expected limits are comparable for both analysis, the observed limits are improved with the toptagger selection by a factor 2.

model	mass [TeV]	$\sigma \times \text{BR}$ [pb]	exclusion [TeV]
leptophobic topcolor Z'	0.4	12.44 (9.14)	m < 2.1 (2.1)
	3.0	0.01 (0.01)	
RS Kaluza-Klein gluon g_{KK}	0.4	14.39 (7.76)	m < 2.3 (2.4)
	3.0	0.05 (0.04)	

Table 25: Observed (expected) upper limits on the cross section times branching ratio for a given mass range and upper mass exclusion limits comparing with theory cross sections different models using the Bayesian method.

setup	Z' (2.25 TeV)	g_{KK} (2.25 TeV)
	Obs. (Exp.) [pb]	Obs. (Exp.) [pb]
Bayesian Resolved+Boosted	0.039 (0.022)	0.11 (0.05)
Bayesian Resolved+HTT0 BDT	0.020 (0.022)	0.05 (0.05)

Table 26: Comparison of upper limits on cross section times branching ratio at a 95% confidence level for a Z' and g_{KK} resonance with masses of 2 TeV, derived using the Bayesian method from the Resolved+Boosted analysis and the HTT0 configuration using the HEPTOPTAGGER algorithm with MVA optimization.

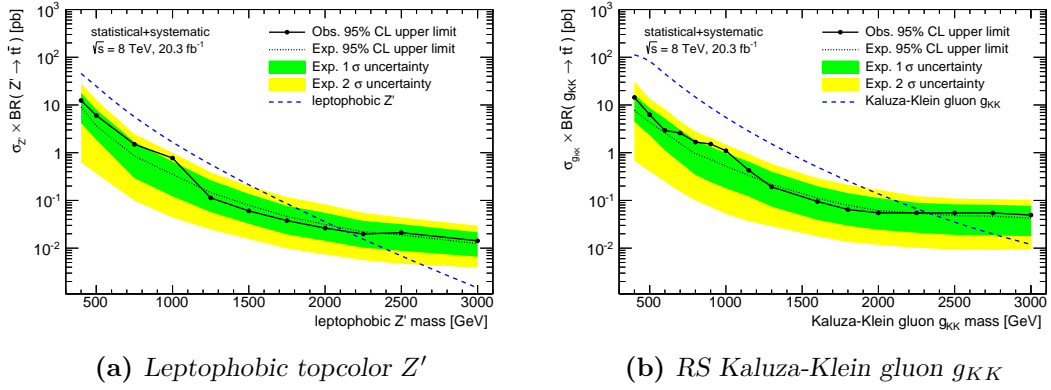


Figure 68: Bayesian (systematic+statistical uncertainties, resolved+toptagger selection) observed and expected upper limits on the production cross section times branching ratio to $t\bar{t}$ final states as a function of the mass of a (a) leptophobic topcolor Z' and (b) RS Kaluza-Klein gluon g_{KK} .

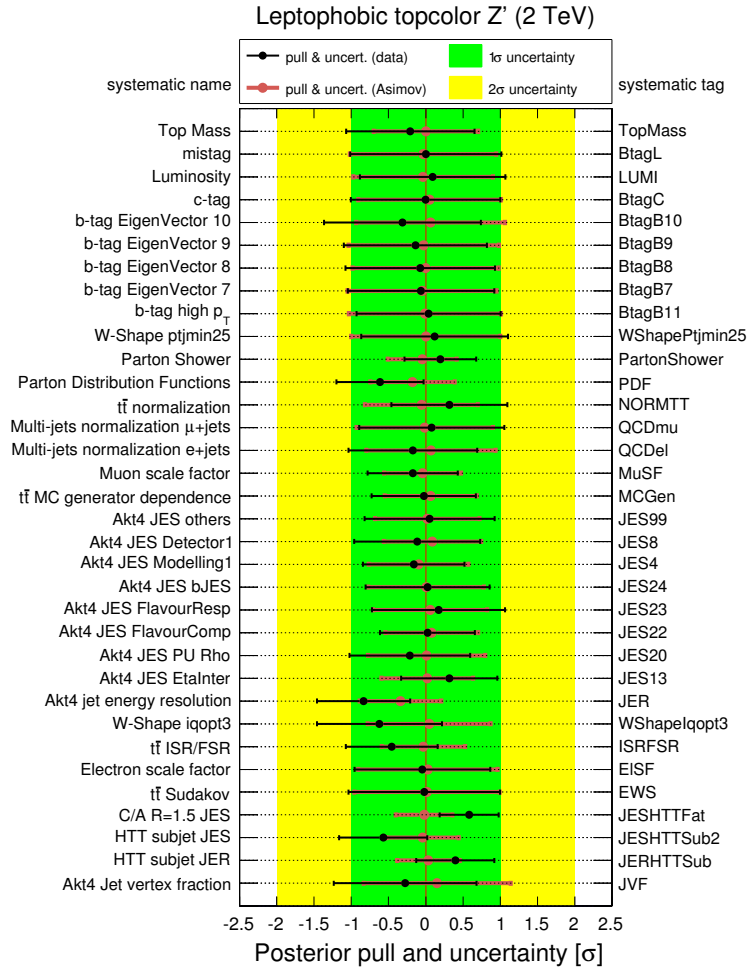


Figure 69: Summary of the posterior pulls and uncertainties for each systematic uncertainty resulting from the Bayesian limit setting procedure considering systematic and statistical uncertainties, using the example of a leptophobic topcolor Z' resonance with a mass of 2 TeV. 1σ and 2σ uncertainty bands are shown along with expected pulls and uncertainties for Asimov tests, overlaid with actual pulls and uncertainties for data with the resolved+toptagger selection.

12

Summary

The present thesis has presented a model independent search for new heavy resonances decaying to $t\bar{t}$ in the lepton+jets channel with the ATLAS detector.

The decay of the top pair is reconstructed in fully resolved and boosted event topologies. Resolved topologies with a signature of three jets as the signature of the hadronically decaying top, and one jet, one lepton and missing transverse energy as signature of the leptonically decaying top, are reconstructed with a χ^2 algorithm to assign the jets to the top decay products. Boosted topologies with all decay products of the hadronically decaying top merged into one large radius jet are reconstructed with a basic top tagging technique. Background contributions from multijet QCD and W+Jets events among other minor backgrounds are suppressed successfully via requirements on the multiplicities and kinematic properties of jets and leptons, as well as during the explicit reconstruction of the top jets. The full dataset recorded during RUN I in the 2012 data-taking period at the Large Hadron Collider (LHC) at a center of mass energy of $\sqrt{s} = 8$ TeV proton-proton collisions by the ATLAS experiment with an integrated luminosity of $\int \mathcal{L} dt = 20.3 \text{ fb}^{-1}$ good for physics is considered in this analysis. The reconstructed mass of the full $t\bar{t}$ system $m_{t\bar{t}}$ as final discriminant is analyzed for deficits or excesses compared to the Standard Model expectations.

Special emphasis in this thesis is set on the estimation of the W+Jets background with a data-driven method, analyzing the heavy flavor composition and normalization of W+Jets events. A software tool has been developed to apply correction factors on the flavor composition and charge asymmetry normalization in W+Jets events for the nominal spectra as well as for each major systematic uncertainty considered in the presented analysis, diminishing the impact of the uncertainties on the final results.

The final $m_{t\bar{t}}$ spectra in all signal regions, the e +jets and μ +jets channel in the resolved and boosted selection and divided into b-tagging categories, are consistent between data and Standard Model expectations within the systematic uncertainties. Therefore upper limits on the cross section times branching ratio are set on a selection of benchmark models, a leptophobic topcolor Z' , Randall-Sundrum Kaluza-Klein gluon g_{KK} and Randall-Sundrum Kaluza-Klein graviton G_{KK} as well as scalar resonances for masses from 0.5 up to 3 TeV. Based on these results, a leptophobic topcolor Z' is excluded for masses below 1.9 (2.1) TeV and a Randall-Sundrum Kaluza-Klein gluon g_{KK} for masses below 2.1 (2.4) TeV for observed (expected) upper cross section times branching ratio limits at 95% confidence level using the Bayesian limit setting procedure. These results improve the limits set by earlier iterations of the analysis. The achieved sensitivity does not allow to set explicit mass exclusions on a Randall-Sundrum Kaluza-Klein graviton G_{KK} or a scalar resonance, which has not been tested in earlier iterations of the analysis before.

An additional study on analysis improvements using the HEPTOPTAGGER algorithm with a more detailed jet substructure analysis to identify the hadronically decaying top jet has been presented.

A set of configurations for the top tagging algorithm has been studied for improved signal efficiency and sensitivity for the reconstruction of $t\bar{t}$ decays in boosted topologies. An optimization applying simple cuts on the substructure of the reconstructed top candidate is out-performed by a multivariate analysis approach, using a boosted decision tree. This BDT is trained with additional kinematic information of the leptonically decaying top compared to the default setup of the tested top tagger algorithm. An optimized significance leads to improved exclusion limits for considered benchmark models.

Current analysis of the dataset recorded during RUN II in the 2015 data-taking period with an integrated luminosity of $\int \mathcal{L} dt = 3.2 \text{ fb}^{-1}$ good for physics at a center of mass energy of $\sqrt{s} = 13 \text{ TeV}$ proton-proton collisions are ongoing and the 2016 data-taking period is about to start. This high center of mass energy opens frontiers to an even higher energy regime, providing an increased production cross section for $t\bar{t}$ pairs and improving the sensitivity for searches for new heavy resonances. The present thesis motivates the usage of advanced top tagging algorithms for analysis in this energy regime with even stronger boosted event topologies for an improved discovery potential of heavy resonances decaying to $t\bar{t}$.



Appendix

A.1 Calculation of the longitudinal momentum component of the neutrino $p_{z,\nu}$

The longitudinal momentum component of the neutrino $p_{z,\nu}$ can be calculated using the information of the lepton from the leptonic W-decay and the missing transverse momentum E_T^{miss} following the procedure presented first in [100].

The sum of the four-momenta of the lepton p_ℓ and the neutrino p_ν in a leptonic decay of a W boson have to add up to the four-momentum of the W-Boson p_W , hence

$$p_W = p_\ell + p_\nu$$

If we square this equation, we get

$$p_W^2 = p_\ell^2 + p_\nu^2 + 2p_\ell p_\nu$$

Neglecting the masses of the lepton and the neutrino compared to the mass of the W-boson $M_\nu \lll M_\ell \ll M_W$ with the relation $p_i^2 = M_i^2$ one can simplify to

$$\begin{aligned} M_W^2 &= 2 p_\ell p_\nu = 2 \cdot [E_\ell E_\nu - \vec{p}_\ell \cdot \vec{p}_\nu] \\ &= 2 \cdot [E_\ell E_\nu - (\vec{p}_{T,\ell} \cdot \vec{p}_{T,\nu} - p_{z,\ell} p_{z,\nu})] \\ &= 2 \cdot [E_\ell E_\nu - (p_{T,\ell} p_{T,\nu} \cos(\Delta\phi_{\ell,\nu}) - p_{z,\ell} p_{z,\nu})] \end{aligned}$$

Using the abbreviation $\xi = \frac{M_W^2}{2} + p_{T,\ell} p_{T,\nu} \cos(\Delta\phi_{\ell,\nu})$ this simplifies to

$$E_\ell E_\nu = \xi + p_{z,\ell} p_{z,\nu}$$

Expressing the energy of the massless neutrino E_ν by its momentum components via $E_\nu = p_\nu^2$, one can write

$$E_\ell \sqrt{p_{T,\nu}^2 + p_{z,\nu}^2} = \xi + p_{z,\ell} p_{z,\nu}$$

Squaring this equation and rearranging the terms, one can obtain a quadratic equation in $p_{z,\nu}$

$$0 = p_{z,\nu}^2 - 2 \cdot \frac{\xi p_{z,\ell}}{E_\ell^2 - p_{z,\ell}^2} \cdot p_{z,\nu} + \frac{E_\ell^2 p_{T,\ell}^2 - \xi^2}{E_\ell^2 - p_{z,\ell}^2}$$

Using the identity $p_{T,\ell}^2 = E_\ell^2 - p_{z,\ell}^2$ one can get the two solutions of this quadratic equation via

$$(p_{z,\nu})_{1,2} = \frac{\xi p_{z,\ell}}{p_{T,\ell}^2} \pm \sqrt{\left(\frac{\xi p_{z,\ell}}{p_{T,\ell}^2}\right)^2 - \frac{E_\ell^2 p_{T,\ell}^2 - \xi^2}{p_{T,\ell}^2}}$$

The transversal $p_{x,y}$ components of the neutrino can be obtained from the E_T^{miss} vector

$$\begin{aligned} p_T &= E_T^{\text{miss}} \\ p_{x,\nu} &= E_T^{\text{miss}} \cdot \cos(\phi_{E_T^{\text{miss}}}) \\ p_{y,\nu} &= E_T^{\text{miss}} \cdot \sin(\phi_{E_T^{\text{miss}}}) \end{aligned}$$

A.2 Monte Carlo samples

This section lists the Monte Carlo simulation samples used for the analysis for each Standard Model background expectation and signal benchmark BSM model and the standard generator used for simulation. Some backgrounds are analyzed for different generators for systematic uncertainty studies.

TTBar (Powheg+Pythia) [+systematic samples]

```
*Standard Analysis*
mc12_8TeV.110404.PowhegPythia_P2011C_ttbar_hdamp172p5_nonallhad.merge.NTUP_COMMON.e3151_s1773_s1776_r4485_r4540_p1575/

*MC Generator 1.1 AF2 Pythia/Herwig comparison*
mc12_8TeV.110404.PowhegPythia_P2011C_ttbar_hdamp172p5_nonallhad.merge.NTUP_COMMON.e3151_a220_a205_r4540_p1575/
mc12_8TeV.105860.PowhegJimmy_AUET2CT10_ttbar_LeptonFilter.merge.NTUP_COMMON.e1576_a159_a171_r3549_p1575

*MC Generator 1.2 Pythia/MC@NLO comparison and PDF uncertainty study*
mc12_8TeV.105200.McAtNloJimmy_CT10_ttbar_LeptonFilter.merge.NTUP_COMMON.e1513_s1499_s1504_r3945_r3549_p1562/

*Initial/Final state radiation study*
mc12_8TeV.1172[09,10].AcerMCPythia_AUET2BCTEQ6L1_[More,Less]PS_ttbar_noallhad.merge.NTUP_COMMON.e1378_a159_a171_r3549_p1575/

*top mass uncertainty*
mc12_8TeV.11784[0,2].TTbar_MT17[0,5]0_nonallhad_PowHeg_Pythia_P2011C.merge.NTUP_COMMON.e2051_s1581_s1586_r3658_r3549_p1562/
```

TTBar+V (MadGraph+Pythia)

```
mc12_8TeV.11935[3,4,5,6].MadGraphPythia_AUET2BCTEQ6L1_ttbar[W,Wj,Z,Zj].merge.NTUP_COMMON.e1352_s1499_s1504_r3658_r3549_p1575/
```

W+Jets (AlpGen+Pythia)

```
mc12_8TeV.14702[5-9].AlpGenPythia_Auto_P2011C_WenuNp[0-4].merge.NTUP_COMMON.e1879_s1581_s1586_r3658_r3549_p1575/
mc12_8TeV.147030.AlpGenPythia_Auto_P2011C_WenuNp5incl.merge.NTUP_COMMON.e1879_s1581_s1586_r3658_r3549_p1575/
mc12_8TeV.14703[3-7].AlpGenPythia_Auto_P2011C_WmunuNp[0-4].merge.NTUP_COMMON.e1880_s1581_s1586_r3658_r3549_p1575/
mc12_8TeV.147038.AlpGenPythia_Auto_P2011C_WmunuNp5incl.merge.NTUP_COMMON.e1880_s1581_s1586_r3658_r3549_p1575/
mc12_8TeV.14704[1-5].AlpGenPythia_Auto_P2011C_WtaunuNp[0-4].merge.NTUP_COMMON.e1881_s1581_s1586_r3658_r3549_p1575/
mc12_8TeV.147046.AlpGenPythia_Auto_P2011C_WtaunuNp5incl.merge.NTUP_COMMON.e1881_s1581_s1586_r3658_r3549_p1575/

mc12_8TeV.20005[6-9].AlpGenPythia_Auto_P2011C_WcNp[0-3].merge.NTUP_COMMON.e2384_s1581_s1586_r3658_r3549_p1575/
mc12_8TeV.200060.AlpGenPythia_Auto_P2011C_WcNp4incl.merge.NTUP_COMMON.e2384_s1581_s1586_r3658_r3549_p1575/
mc12_8TeV.20015[6-8].AlpGenPythia_Auto_P2011C_WccNp[0-2].merge.NTUP_COMMON.e2384_s1581_s1586_r3658_r3549_p1575/
mc12_8TeV.200159.AlpGenPythia_Auto_P2011C_WccNp3incl.merge.NTUP_COMMON.e2384_s1581_s1586_r3658_r3549_p1575/
mc12_8TeV.20025[6-8].AlpGenPythia_Auto_P2011C_WbbNp[0-2].merge.NTUP_COMMON.e2384_s1581_s1586_r3658_r3549_p1575/
mc12_8TeV.200259.AlpGenPythia_Auto_P2011C_WbbNp3incl.merge.NTUP_COMMON.e2384_s1581_s1586_r3658_r3549_p1575/
```

W+Jets Akt10 filtered (AlpGen+Pythia)

```
mc12_8TeV.19000[1-5].AlpGenPythia_Auto_P2011C_WenuNp [1-5]_Akt10Pt250.merge.NTUP_COMMON.e2327_s1581_s1586_r4485_r4540_p1606/
mc12_8TeV.19001[1-5].AlpGenPythia_Auto_P2011C_WmunuNp [1-5]_Akt10Pt250.merge.NTUP_COMMON.e2328_s1581_s1586_r4485_r4540_p1606/
mc12_8TeV.19002[1-5].AlpGenPythia_Auto_P2011C_WtaunuNp[1-5]_Akt10Pt250.merge.NTUP_COMMON.e2329_s1581_s1586_r4485_r4540_p1606/

mc12_8TeV.19005[0-3].AlpGenPythia_Auto_P2011C_WbbNp[0-3]_Akt10Pt250.merge.NTUP_COMMON.e2327_s1581_s1586_r4485_r4540_p1606/
mc12_8TeV.19004[0-3].AlpGenPythia_Auto_P2011C_WccNp[0-3]_Akt10Pt250.merge.NTUP_COMMON.e2327_s1581_s1586_r4485_r4540_p1606/
mc12_8TeV.19003[0-4].AlpGenPythia_Auto_P2011C_WcNp [0-4]_Akt10Pt250.merge.NTUP_COMMON.e2327_s1581_s1586_r4485_r4540_p1606/
```

Z+Jets (AlpGen+Pythia)

```
mc12_8TeV.14710[5-9].AlpGenPythia_Auto_P2011C_ZeeNp[0-4].merge.NTUP_COMMON.e1879_s1581_s1586_r3658_r3549_p1575/
mc12_8TeV.147110.AlpGenPythia_Auto_P2011C_ZeeNp5incl.merge.NTUP_COMMON.e1879_s1581_s1586_r3658_r3549_p1575/
mc12_8TeV.14711[5-7].AlpGenPythia_Auto_P2011C_ZmunuNp[0-4].merge.NTUP_COMMON.e1880_s1581_s1586_r3658_r3549_p1575/
mc12_8TeV.147118.AlpGenPythia_Auto_P2011C_ZmunuNp5incl.merge.NTUP_COMMON.e1880_s1581_s1586_r3658_r3549_p1575/
```

```

mc12_8TeV.14712[1-5].AlpGenPythia_Auto_P2011C_ZtautauNp[0-4].merge.NTUP_COMMON.e1881_s1581_s1586_r3658_r3549_p1575/
mc12_8TeV.147126. AlpGenPythia_Auto_P2011C_ZtautauNp5incl.merge.NTUP_COMMON.e1881_s1581_s1586_r3658_r3549_p1575/

mc12_8TeV.20033[2-4]. AlpGenPythia_Auto_P2011C_ZeebbNp[0-2]. merge.NTUP_COMMON.e2384_s1581_s1586_r3658_r3549_p1575/
mc12_8TeV.200335. AlpGenPythia_Auto_P2011C_ZeebbNp3incl. merge.NTUP_COMMON.e2384_s1581_s1586_r3658_r3549_p1575/
mc12_8TeV.20034[0-2]. AlpGenPythia_Auto_P2011C_ZmumubbNp[0-2]. merge.NTUP_COMMON.e2385_s1581_s1586_r3658_r3549_p1575/
mc12_8TeV.200343. AlpGenPythia_Auto_P2011C_ZmumubbNp3incl. merge.NTUP_COMMON.e2385_s1581_s1586_r3658_r3549_p1575/
mc12_8TeV.2003[48-50].AlpGenPythia_Auto_P2011C_ZtautauNp[0-2].merge.NTUP_COMMON.e2386_s1581_s1586_r3658_r3549_p1575/
mc12_8TeV.200351. AlpGenPythia_Auto_P2011C_ZtautauNp3incl.merge.NTUP_COMMON.e2386_s1581_s1586_r3658_r3549_p1575/
mc12_8TeV.20043[2-4]. AlpGenPythia_Auto_P2011C_ZeeccNp[0-2]. merge.NTUP_COMMON.e2384_s1581_s1586_r3658_r3549_p1575/
mc12_8TeV.200435. AlpGenPythia_Auto_P2011C_ZeeccNp3incl. merge.NTUP_COMMON.e2384_s1581_s1586_r3658_r3549_p1575/
mc12_8TeV.20044[0-2]. AlpGenPythia_Auto_P2011C_ZmumuccNp[0-2]. merge.NTUP_COMMON.e2385_s1581_s1586_r3658_r3549_p1575/
mc12_8TeV.200443. AlpGenPythia_Auto_P2011C_ZmumuccNp3incl. merge.NTUP_COMMON.e2385_s1581_s1586_r3658_r3549_p1575/
mc12_8TeV.2004[48-50].AlpGenPythia_Auto_P2011C_ZtautauNp[0-2].merge.NTUP_COMMON.e2386_s1581_s1586_r3658_r3549_p1575/
mc12_8TeV.200451. AlpGenPythia_Auto_P2011C_ZtautauNp3incl.merge.NTUP_COMMON.e2386_s1581_s1586_r3658_r3549_p1575/

```

SingleTop (Powheg+Pythia) [+systematic samples]

Standard Analysis

```

mc12_8TeV.11009[0,1]. PowhegPythia_P2011C_singletop_tchan_lept_[top,antitop].merge.NTUP_COMMON.e2575_s1773_s1776_r4485_r4540_p1575/
mc12_8TeV.1101[19,40].PowhegPythia_P2011C_st_[schan_lep,Wtchan_incl_DR]. merge.NTUP_COMMON.e1743_s1581_s1586_r3658_r3549_p1575/

```

PDF uncertainty study

```

mc12_8TeV.10834[3-5].McAtNloJimmy_AUET2CT10_SingleTopSChanW[e,mu,tau]nu.merge.NTUP_COMMON.e1525_s1499_s1504_r3658_r3549_p1575/
mc12_8TeV.110101. AcerMCPythia_P2011CCTEQ6L1_singletop_tchan_l. merge.NTUP_COMMON.e1731_s1581_s1586_r3658_r3549_p1575/
mc12_8TeV.108346. McAtNloJimmy_AUET2CT10_SingleTopWtChanIncl. merge.NTUP_COMMON.e1525_s1499_s1504_r3658_r3549_p1575/

```

Diboson (Sherpa)

```

mc12_8TeV.18358[5,6]. Sherpa_CT10_Z[W,Z]toeeqq_MassiveCB. merge.NTUP_COMMON.e2370_s1581_s1586_r4485_r4540_p1575/
mc12_8TeV.18358[7,8]. Sherpa_CT10_Z[W,Z]tomumuqq_MassiveCB. merge.NTUP_COMMON.e2370_s1581_s1586_r4485_r4540_p1575/
mc12_8TeV.1835[89,90].Sherpa_CT10_Z[W,Z]totautauqq_MassiveCB.merge.NTUP_COMMON.e2370_s1581_s1586_r4485_r4540_p1575/
mc12_8TeV.18373[4,5]. Sherpa_CT10_W[W,Z]toenuqq_MassiveCB. merge.NTUP_COMMON.e2347_s1581_s1586_r4485_r4540_p1575/
mc12_8TeV.18373[6,7]. Sherpa_CT10_W[W,Z]tomunuqq_MassiveCB. merge.NTUP_COMMON.e2347_s1581_s1586_r4485_r4540_p1575/
mc12_8TeV.18373[8,9]. Sherpa_CT10_W[W,Z]totanuqq_MassiveCB. merge.NTUP_COMMON.e2347_s1581_s1586_r4485_r4540_p1575/

```

Zprime (Pythia8)

```

mc12_8TeV.110899.Pythia8_AU2MSTW2008LO_zprime400_tt.merge.NTUP_COMMON.e2512_s1499_s1504_r3658_r3549_p1575
mc12_8TeV.110901.Pythia8_AU2MSTW2008LO_zprime500_tt.merge.NTUP_COMMON.e1345_s1499_s1504_r3658_r3549_p1562/
mc12_8TeV.110902.Pythia8_AU2MSTW2008LO_zprime750_tt.merge.NTUP_COMMON.e1345_s1499_s1504_r3658_r3549_p1562/
mc12_8TeV.110903.Pythia8_AU2MSTW2008LO_zprime1000_tt.merge.NTUP_COMMON.e1345_s1499_s1504_r3658_r3549_p1562/
mc12_8TeV.110904.Pythia8_AU2MSTW2008LO_zprime1250_tt.merge.NTUP_COMMON.e1345_s1499_s1504_r3658_r3549_p1562/
mc12_8TeV.110905.Pythia8_AU2MSTW2008LO_zprime1500_tt.merge.NTUP_COMMON.e1345_s1499_s1504_r3658_r3549_p1562/
mc12_8TeV.110906.Pythia8_AU2MSTW2008LO_zprime1750_tt.merge.NTUP_COMMON.e1345_s1499_s1504_r3658_r3549_p1575/
mc12_8TeV.110907.Pythia8_AU2MSTW2008LO_zprime2000_tt.merge.NTUP_COMMON.e1345_s1499_s1504_r3658_r3549_p1562/
mc12_8TeV.110908.Pythia8_AU2MSTW2008LO_zprime2250_tt.merge.NTUP_COMMON.e1345_s1499_s1504_r3658_r3549_p1562/
mc12_8TeV.110909.Pythia8_AU2MSTW2008LO_zprime2500_tt.merge.NTUP_COMMON.e1345_s1499_s1504_r3658_r3549_p1575/
mc12_8TeV.110910.Pythia8_AU2MSTW2008LO_zprime3000_tt.merge.NTUP_COMMON.e1345_s1499_s1504_r3658_r3549_p1562/

```

KKGluon (MadGraph + Pythia8)

constant width

```

mc12_8TeV.182764.MadGraphPythia8_AU2MSTW2008LO_KKGluon400.merge.NTUP_COMMON.e2450_s1499_s1504_r3658_r3549_p1575/
mc12_8TeV.115550.MadGraphPythia8_AU2MSTW2008LO_KKGluon500.merge.NTUP_COMMON.e1606_s1499_s1504_r3658_r3549_p1562/
mc12_8TeV.115551.MadGraphPythia8_AU2MSTW2008LO_KKGluon600.merge.NTUP_COMMON.e1606_s1499_s1504_r3658_r3549_p1562/
mc12_8TeV.115552.MadGraphPythia8_AU2MSTW2008LO_KKGluon700.merge.NTUP_COMMON.e1606_s1499_s1504_r3658_r3549_p1562/
mc12_8TeV.115553.MadGraphPythia8_AU2MSTW2008LO_KKGluon800.merge.NTUP_COMMON.e1606_s1499_s1504_r3658_r3549_p1575/
mc12_8TeV.119318.MadGraphPythia8_AU2MSTW2008LO_KKGluon900.merge.NTUP_COMMON.e1606_s1499_s1504_r3658_r3549_p1562/
mc12_8TeV.115554.MadGraphPythia8_AU2MSTW2008LO_KKGluon1000.merge.NTUP_COMMON.e1606_s1499_s1504_r3658_r3549_p1562/
mc12_8TeV.119319.MadGraphPythia8_AU2MSTW2008LO_KKGluon1150.merge.NTUP_COMMON.e1606_s1499_s1504_r3658_r3549_p1562/
mc12_8TeV.115555.MadGraphPythia8_AU2MSTW2008LO_KKGluon1300.merge.NTUP_COMMON.e1606_s1499_s1504_r3658_r3549_p1575/
mc12_8TeV.115556.MadGraphPythia8_AU2MSTW2008LO_KKGluon1600.merge.NTUP_COMMON.e1606_s1499_s1504_r3658_r3549_p1562/
mc12_8TeV.115799.MadGraphPythia8_AU2MSTW2008LO_KKGluon1800.merge.NTUP_COMMON.e1606_s1499_s1504_r3658_r3549_p1575/
mc12_8TeV.119582.MadGraphPythia8_AU2MSTW2008LO_KKGluon2000.merge.NTUP_COMMON.e1606_s1499_s1504_r3658_r3549_p1562/
mc12_8TeV.158768.MadGraphPythia8_AU2MSTW2008LO_KKGluon2250.merge.NTUP_COMMON.e1606_s1499_s1504_r3658_r3549_p1562/
mc12_8TeV.158769.MadGraphPythia8_AU2MSTW2008LO_KKGluon2500.merge.NTUP_COMMON.e1606_s1499_s1504_r3658_r3549_p1575/

```


A.3 Distributions of systematic uncertainty shifts

This appendix shows the impact of systematic uncertainties on the final $m_{t\bar{t}}$ discriminant of the total Standard Model expectation and all b-tagging categories combined. The effect on the resolved and boosted selections are displayed in section A.3.1 and A.3.2 respectively. Each plot shows the nominal spectrum and the up/down variation for the given systematic uncertainty, while its effect is illustrated in a ratio of the systematic variation divided by the nominal spectrum. The grey band shows the statistical uncertainty on the total background. If a smoothing (cf. section 8.4) is applied to the given systematic, this is indicated by a comparison of the systematic effect with and without smoothing.

A.3.1 Resolved selection

The systematic shift for each uncertainty in the resolved selection listed in table 27 is shown in figures 70 and 71

name	description
BtagB7	B-tagging b-jet efficiency (component 7)
BtagB8	B-tagging b-jet efficiency (component 8)
BtagB9	B-tagging b-jet efficiency (component 9)
BtagB10	B-tagging b-jet efficiency (component 10)
BtagB(hp_T)	B-tagging b-jet efficiency (high p_T extrapolation)
BtagC	B-tagging c-jet efficiency
BtagL	B-tagging light-jet efficiency
EISF	Electron scale factor
MuSF	Muon scale factor
JES4	Small jet energy scale (component 4, Modelling1)
JES8	Small jet energy scale (component 8, Detector1)
JES13	Small jet energy scale (component 13, EtaInter.Model)
JES20	Small jet energy scale (component 20, PileupRhoTop)
JES22	Small jet energy scale (component 22, FlavComp)
JES23	Small jet energy scale (component 23, FlavResp)
JES24	Small jet energy scale (component 24, BJES)
JES99	Small jet energy scale (sum of all other components)
JER	Small jet energy resolution
Lumi	Luminosity
$t\bar{t}$ norm	$t\bar{t}$ normalization
ISR/FSR	Initial- and final state radiation
PS	Parton Showering and Fragmentation
MCGen	MC Generator
EWS	Electro-weak correction
PDF	Parton Distribution Functions
TopMass	Top mass
WShapePtjmin10	W-Shape ptjmin10
WShapeIqopt3	W-Shape iqopt3

Table 27: Names of systematic uncertainties considered in the resolved selection.

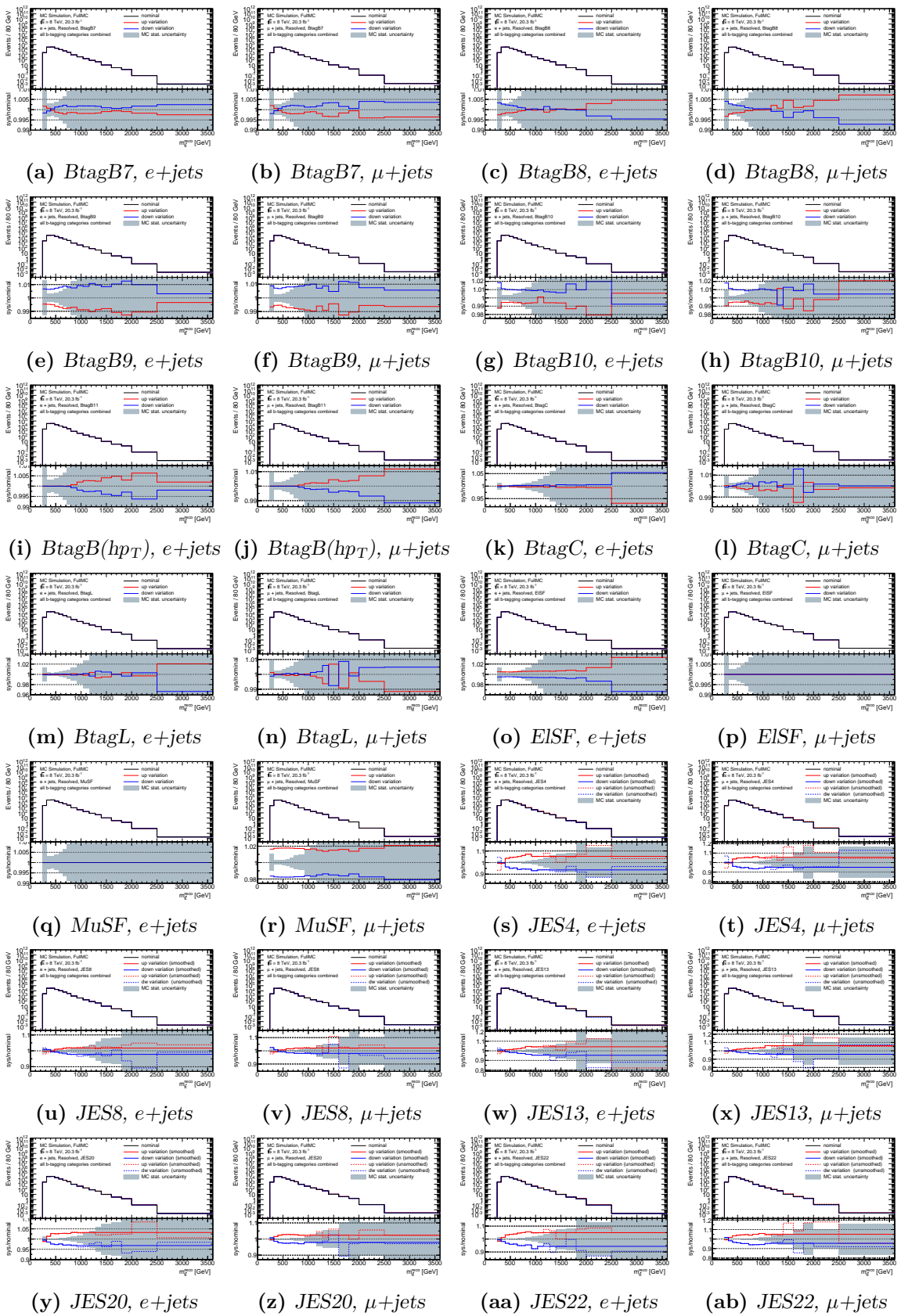


Figure 70: Impact of various systematic uncertainties in the resolved selection (A)

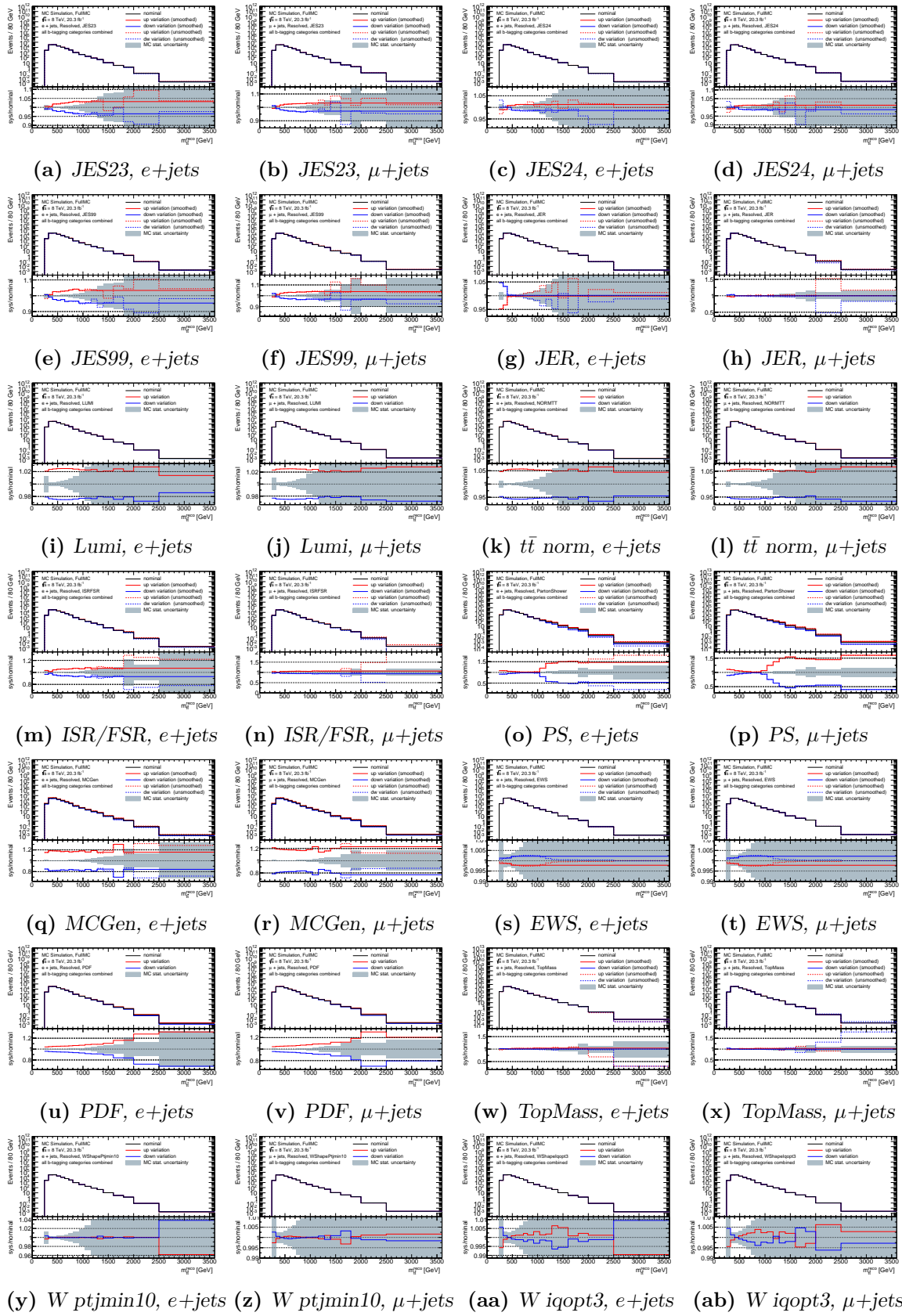


Figure 71: Impact of various systematic uncertainties in the resolved selection (B)

A.3.2 Boosted selection

Figures 72 - 74 show the systematic shifts in the boosted selection. Apart from the systematic descriptions listed in table 27, the boosted selection uses some additional systematics explained in table 28.

name	description
JMRB	Large jet mass resolution
JMSB	Large jet mass scale
JERB	Large jet energy resolution
JESB1	Large jet energy scale (component 1, Data/MC)
JESB13	Large jet energy scale (component 13, topology)
JESB99	Large jet energy scale (sum of all other components)

Table 28: Names of systematic uncertainties considered in the boosted selection.

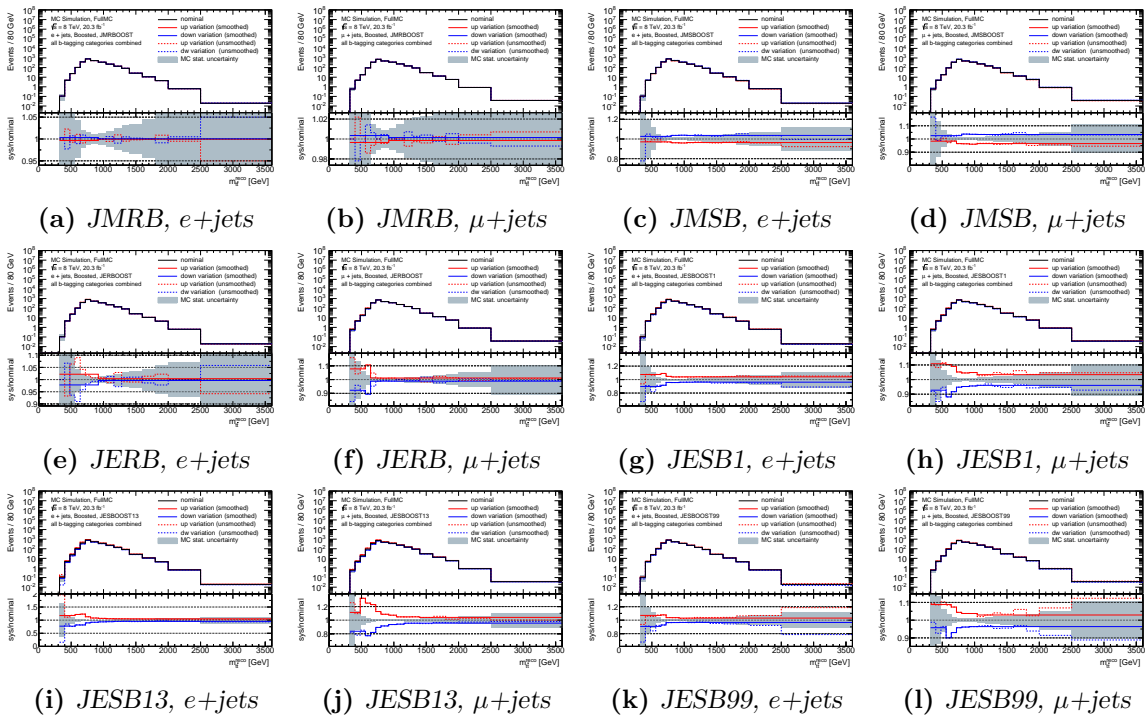


Figure 72: Impact of various systematic uncertainties in the boosted selection (A)

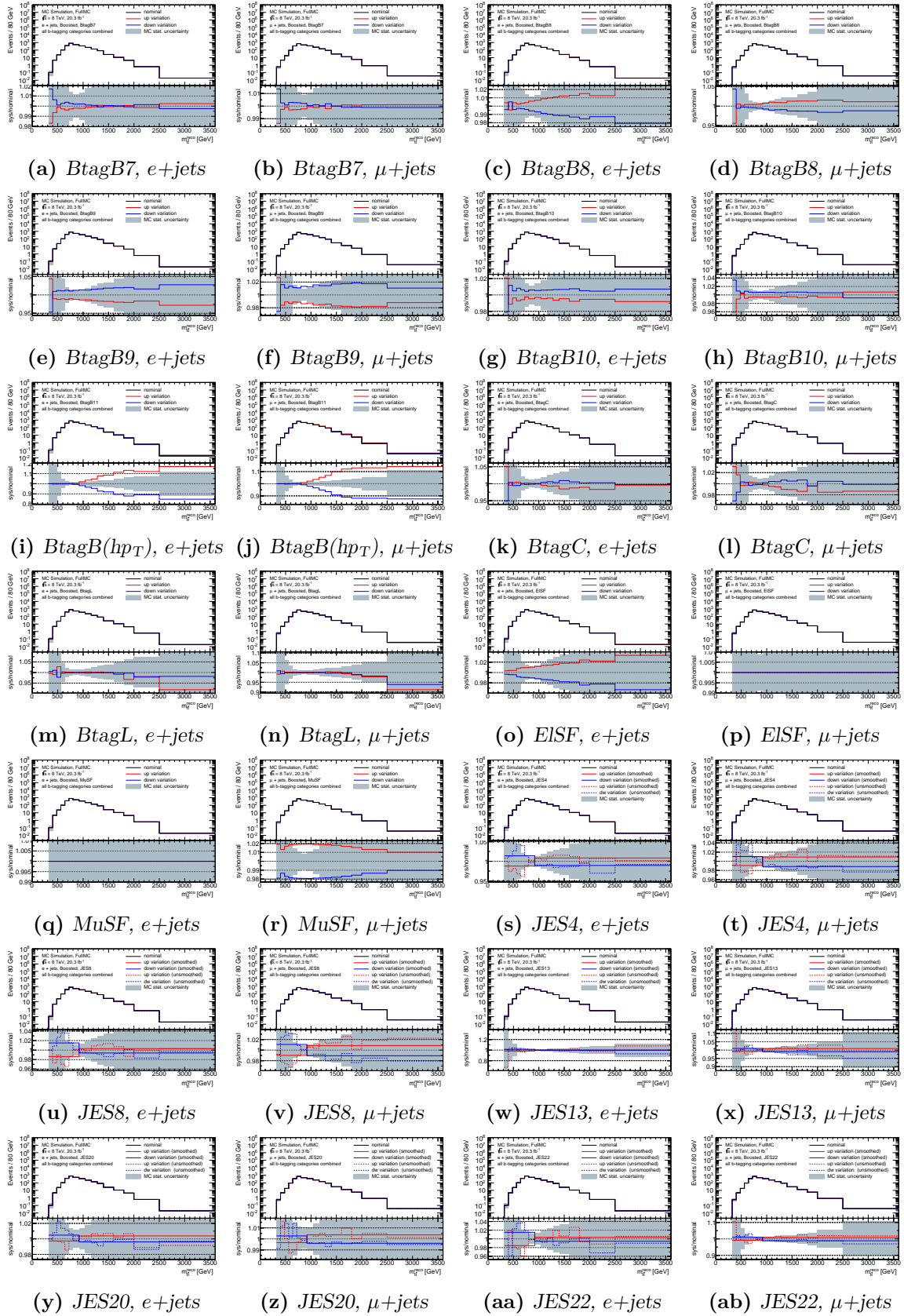


Figure 73: Impact of various systematic uncertainties in the boosted selection (B)

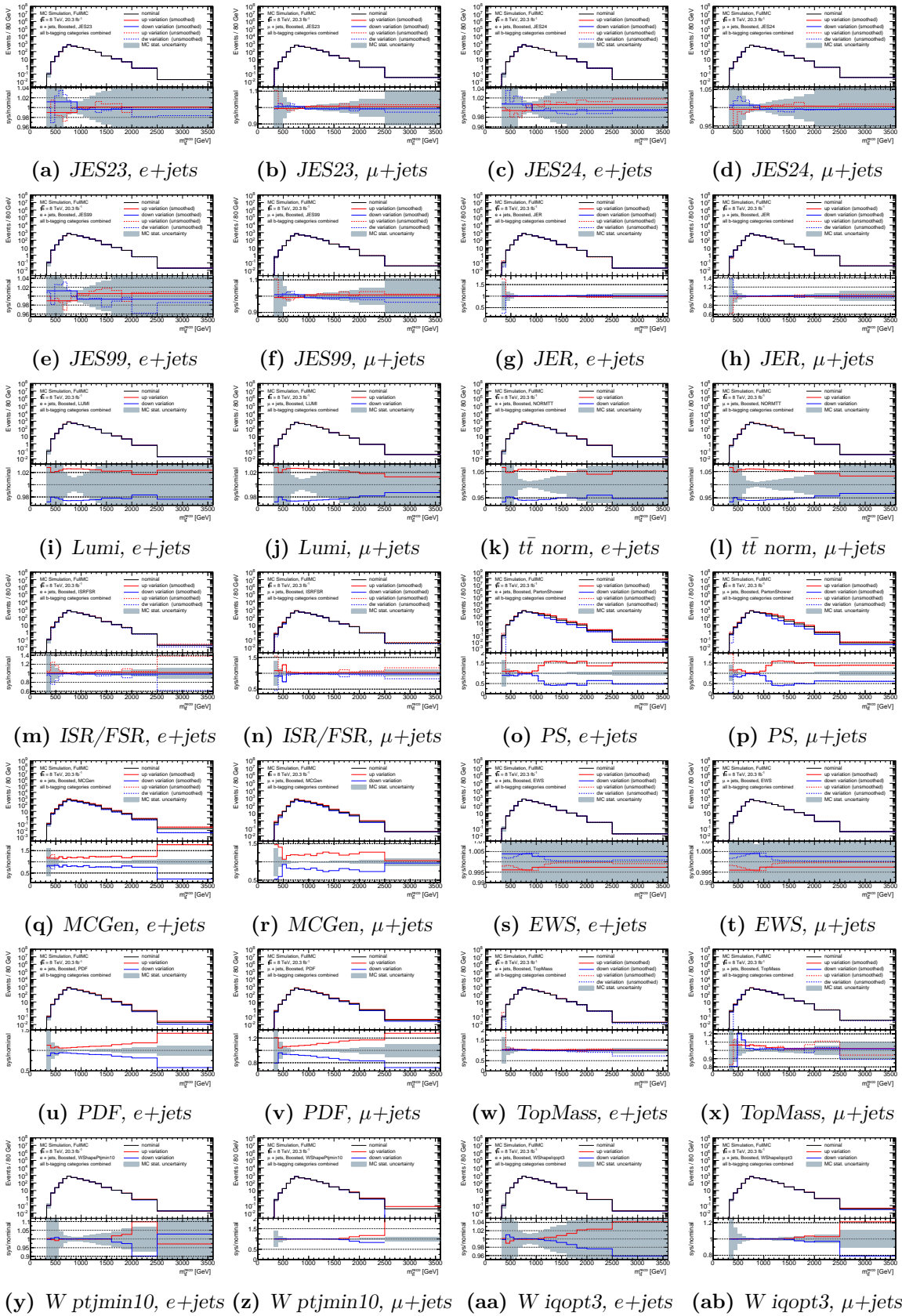


Figure 74: Impact of various systematic uncertainties in the boosted selection (C)

A.4 Distributions of PDF uncertainty shifts

This appendix shows the IntraPDF combination for a given PDF set and the final InterPDF combination to the MEAN variation (cf. section 8.3.5) in figures 75 - 78 , comparing the effects on the $m_{t\bar{t}}$ spectra in all b-tagging categories combined. Each plot shows the variation band resulting from the specific combination scheme for the given PDF set, providing ratios relative to the central variation and also compared to the nominal spectrum.

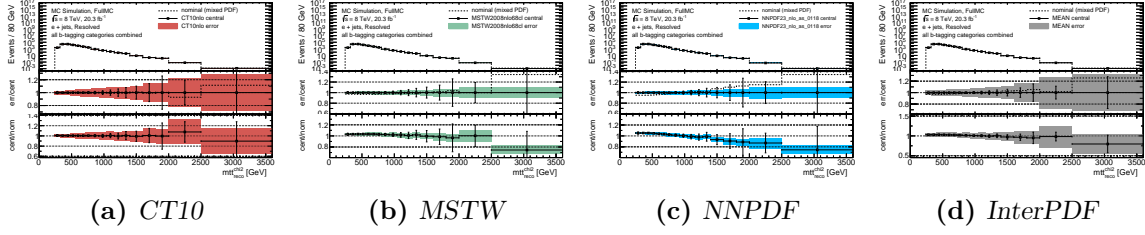


Figure 75: Intra- and InterPDF uncertainties for, resolved selection, $e+jets$ channel.

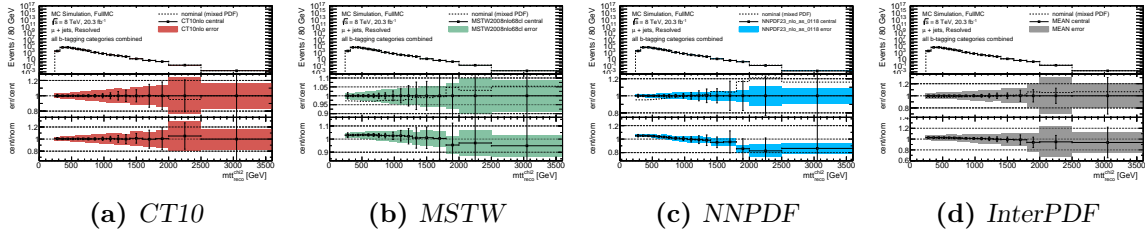


Figure 76: Intra- and InterPDF uncertainties, resolved selection, $\mu+jets$ channel.

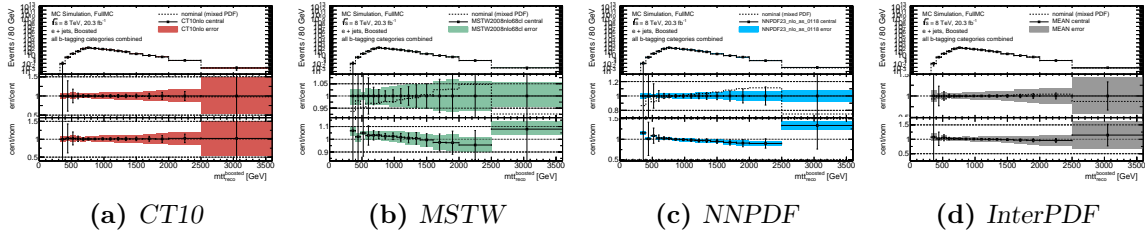


Figure 77: Intra- and InterPDF uncertainties, boosted selection, $e+jets$ channel.

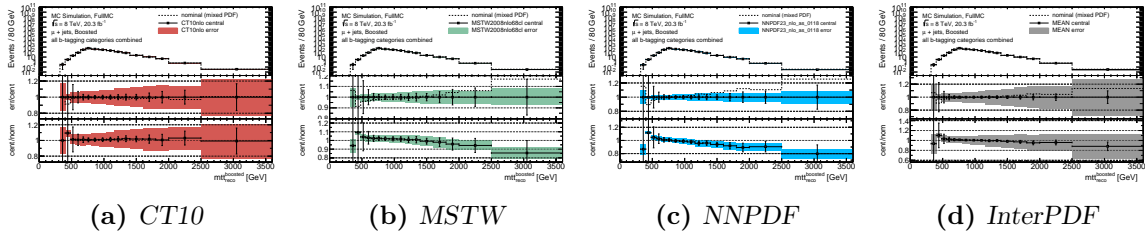


Figure 78: Intra- and InterPDF uncertainties, boosted selection, $\mu+jets$ channel.

A.5 Limits on cross section times branching ratio

mass [GeV]	Obs. [pb]	Exp. [pb]				
		-2σ	-1σ	central	$+1\sigma$	$+2\sigma$
400	12.08852	0.39313	2.69714	6.36800	13.69250	21.96667
500	4.28307	0.28097	1.02826	3.30153	6.68125	9.36562
750	1.26946	0.09889	0.23100	0.76183	1.50500	2.20875
1000	0.33042	0.03467	0.07123	0.21555	0.41754	0.62588
1250	0.14845	0.01822	0.03741	0.10724	0.21048	0.32949
1500	0.06328	0.01095	0.02322	0.06738	0.13564	0.22167
1750	0.05251	0.00781	0.01602	0.04450	0.09189	0.16126
2000	0.05083	0.00654	0.01219	0.02946	0.06030	0.10772
2250	0.03897	0.00584	0.01041	0.02249	0.04289	0.07477
2500	0.03816	0.00518	0.00912	0.01934	0.03595	0.06157
3000	0.03928	0.00432	0.00735	0.01420	0.02677	0.05081

(a) *Leptophobic topcolor Z'*

mass [GeV]	Obs. [pb]	Exp. [pb]				
		-2σ	-1σ	central	$+1\sigma$	$+2\sigma$
400	8.45488	0.28731	1.77692	4.17825	9.52650	15.34500
500	2.35674	0.19436	0.60444	2.12868	4.53682	6.83250
600	1.90554	0.12642	0.39341	1.35162	2.72738	4.21400
700	1.29487	0.07701	0.20768	0.75625	1.52389	2.27125
800	0.61042	0.04517	0.12822	0.49762	0.88360	1.39300
900	0.31354	0.03003	0.07462	0.26456	0.49114	0.75260
1000	0.23001	0.02320	0.05214	0.17778	0.31721	0.51238
1200	0.08729	0.01450	0.03093	0.10151	0.19143	0.30394
1400	0.07574	0.00984	0.02143	0.06948	0.13814	0.22314
1600	0.06564	0.00736	0.01556	0.04805	0.09723	0.16910
1800	0.04755	0.00597	0.01232	0.03341	0.06527	0.11231
2000	0.04252	0.00536	0.01014	0.02470	0.04691	0.08744
2500	0.02791	0.00375	0.00671	0.01420	0.02717	0.04402

(b) *RS Kaluza-Klein graviton G_{KK}*

mass [GeV]	Obs. [pb]	Exp. [pb]				
		-2σ	-1σ	central	$+1\sigma$	$+2\sigma$
400	8.99692	0.31228	2.27088	5.00646	11.41603	18.32688
500	4.53717	0.23121	0.85615	2.80000	5.97125	8.65000
750	1.09049	0.07523	0.18954	0.73200	1.28700	2.06220
1000	0.28287	0.02853	0.06324	0.19760	0.34071	0.54350
1250	0.17096	0.01573	0.03278	0.10309	0.21418	0.28900
1500	0.06888	0.00948	0.02163	0.06574	0.12737	0.19212
1750	0.05380	0.00688	0.01397	0.03936	0.08986	0.13239
2000	0.04423	0.00525	0.00985	0.02431	0.05040	0.07480
2250	0.03484	0.00444	0.00803	0.01692	0.03393	0.05321
2500	0.02550	0.00380	0.00684	0.01399	0.02679	0.04123
2750	0.02125	0.00287	0.00486	0.00903	0.01755	0.03074
3000	0.01924	0.00256	0.00410	0.00737	0.01353	0.02278

(c) *Scalar resonance*

Table 29: Bayesian (systematic+statistical uncertainties, resolved+boosted selection) observed and expected (including $\pm 1(2)\sigma$ variations) upper limits at 95% confidence level on the production cross section times branching ratio to $t\bar{t}$ final states for selected BSM signal benchmark models: (a) *Leptophobic topcolor Z'* , (b) *RS Kaluza-Klein graviton G_{KK}* and (c) *scalar resonance*.

mass [GeV]	Obs. [pb]	Exp. [pb]				
		-2σ	-1σ	central	$+1\sigma$	$+2\sigma$
400	12.96264	0.40185	2.83235	6.38735	14.65342	23.42812
500	6.03584	0.30184	1.25000	3.83068	8.25588	12.57917
600	3.47846	0.20477	0.73857	2.52188	5.15000	8.11750
700	2.46434	0.14012	0.41344	1.43323	2.94044	4.44933
800	1.40673	0.08234	0.22383	0.80674	1.61583	2.43938
900	0.67550	0.05587	0.13537	0.50050	0.98774	1.45731
1000	0.48641	0.03924	0.09425	0.33576	0.62750	0.96813
1150	0.26955	0.02856	0.06312	0.22442	0.40953	0.68487
1300	0.19971	0.02134	0.04919	0.16060	0.33279	0.51775
1600	0.11842	0.01329	0.02971	0.10189	0.21510	0.35228
1800	0.11728	0.01069	0.02285	0.07308	0.16333	0.29137
2000	0.10385	0.01021	0.02125	0.05946	0.13274	0.24272
2250	0.10816	0.00952	0.01944	0.05329	0.10627	0.20872
2500	0.10003	0.00954	0.01882	0.04753	0.09420	0.16975
2750	0.08768	0.00979	0.01881	0.04583	0.09264	0.17550
3000	0.10684	0.01020	0.01908	0.04451	0.09453	0.18455

(a) RS Kaluza-Klein gluon g_{KK} , constant width ($\Gamma = 15.3\%$)

width Γ [%]	Obs. [pb]	Exp. [pb]				
		-2σ	-1σ	central	$+1\sigma$	$+2\sigma$
10	0.39623	0.03811	0.08424	0.27680	0.53286	0.83050
15	0.47550	0.04276	0.09455	0.33078	0.63133	0.96375
20	0.48221	0.04358	0.10015	0.35025	0.69950	1.04875
25	0.60396	0.04538	0.11071	0.39750	0.81682	1.25563
30	0.60223	0.04774	0.11856	0.44804	0.91795	1.43437
35	0.64132	0.05022	0.12477	0.44700	0.92350	1.45208
40	0.68884	0.05049	0.12854	0.47816	0.99500	1.56042

(b) RS Kaluza-Klein gluon g_{KK} (1 TeV), variable width

width Γ [%]	Obs. [pb]	Exp. [pb]				
		-2σ	-1σ	central	$+1\sigma$	$+2\sigma$
10	0.09262	0.00840	0.01723	0.04635	0.10060	0.17632
15	0.11056	0.00940	0.01927	0.05445	0.12040	0.21787
20	0.12305	0.01090	0.02347	0.07190	0.15965	0.29237
25	0.13157	0.01265	0.02802	0.08826	0.18860	0.33851
30	0.15800	0.01447	0.03160	0.11053	0.24487	0.46180
35	0.18932	0.01507	0.03541	0.12369	0.28395	0.51795
40	0.20346	0.01738	0.03781	0.13970	0.31733	0.58970

(c) RS Kaluza-Klein gluon g_{KK} (2 TeV), variable width

width Γ [%]	Obs. [pb]	Exp. [pb]				
		-2σ	-1σ	central	$+1\sigma$	$+2\sigma$
10	0.08750	0.00814	0.01418	0.02944	0.05983	0.11805
15	0.10470	0.01027	0.01957	0.04807	0.10373	0.23767
20	0.11766	0.01191	0.02315	0.05737	0.13220	0.29990
25	0.12607	0.01304	0.02647	0.07376	0.17790	0.36475
30	0.17594	0.01581	0.03205	0.09366	0.22110	0.44252
35	0.22956	0.01870	0.04100	0.13161	0.30667	0.63650
40	0.25904	0.01803	0.03953	0.13426	0.32838	0.66750

(d) RS Kaluza-Klein gluon g_{KK} (3 TeV), variable width

Table 30: Bayesian (systematic+statistical uncertainties, resolved+boosted selection) observed and expected (including $\pm 1(2)\sigma$ variations) upper limits at 95% confidence level on the production cross section times branching ratio to $t\bar{t}$ final states for selected BSM signal benchmark models: RS Kaluza-Klein gluon g_{KK} resonance with (a) fixed width and variable width for a mass of (b) 1 TeV, (c) 2 TeV and (d) 3 TeV.

mass [GeV]	Obs. [pb]	Exp. [pb]				
		-2σ	-1σ	central	$+1\sigma$	$+2\sigma$
Leptophobic topcolor Z'						
400	13.06149	0.64119	0.84627	1.17131	1.63157	2.20400
500	8.01591	0.50728	0.68369	0.95160	1.32603	1.73798
750	0.34176	0.17883	0.23827	0.32706	0.46074	0.60818
1000	0.03078	0.06579	0.08695	0.12038	0.16749	0.22410
1250	0.01281	0.03450	0.04567	0.06347	0.08905	0.11965
1500	0.00744	0.02216	0.02923	0.04047	0.05656	0.07532
1750	0.00632	0.01425	0.01904	0.02646	0.03696	0.04920
2000	0.00628	0.01081	0.01444	0.02011	0.02829	0.03754
2250	0.00566	0.00886	0.01170	0.01632	0.02273	0.03063
2500	0.00589	0.00776	0.01024	0.01422	0.01996	0.02685
3000	0.00742	0.00600	0.00791	0.01089	0.01527	0.02057
RS Kaluza-Klein gluon g_{KK}						
400	12.90657	0.63339	0.83962	1.16542	1.62805	2.16150
500	8.42266	0.53875	0.72581	1.00483	1.38414	1.84167
600	3.88269	0.39895	0.53029	0.72242	1.00278	1.32500
700	1.14176	0.26883	0.36193	0.50012	0.69728	0.92255
800	0.13942	0.16752	0.22094	0.30415	0.42111	0.56914
900	0.05391	0.11116	0.14870	0.20593	0.28678	0.38060
1000	0.03232	0.08073	0.10847	0.14983	0.20897	0.28185
1150	0.01900	0.05888	0.07826	0.10728	0.14709	0.19696
1300	0.01400	0.04410	0.05799	0.08052	0.11201	0.15043
1600	0.00891	0.02716	0.03607	0.05051	0.07032	0.09434
1800	0.00820	0.02145	0.02847	0.03927	0.05472	0.07285
2000	0.00877	0.01927	0.02550	0.03515	0.04891	0.06540
2250	0.00861	0.01693	0.02232	0.03076	0.04295	0.05751
2500	0.00949	0.01637	0.02172	0.02996	0.04189	0.05675
2750	0.01113	0.01623	0.02120	0.02959	0.04129	0.05580
3000	0.01217	0.01666	0.02187	0.03018	0.04257	0.05700
RS Kaluza-Klein graviton G_{KK}						
400	8.54343	0.43125	0.57440	0.79681	1.11208	1.50900
500	4.51501	0.34094	0.44682	0.61657	0.86287	1.15325
600	1.58595	0.23874	0.31829	0.44563	0.61862	0.82178
700	0.20555	0.15111	0.20118	0.27768	0.39100	0.52980
800	0.04337	0.08883	0.11826	0.16247	0.22619	0.30067
900	0.02303	0.06168	0.08087	0.11100	0.15509	0.20233
1000	0.01574	0.04566	0.06072	0.08379	0.11651	0.15450
1200	0.00860	0.02735	0.03631	0.05105	0.07083	0.09370
1400	0.00641	0.01962	0.02599	0.03617	0.05019	0.06615
1600	0.00532	0.01443	0.01905	0.02683	0.03709	0.05025
1800	0.00522	0.01086	0.01458	0.02019	0.02840	0.03720
2000	0.00510	0.00857	0.01136	0.01573	0.02212	0.02967
2500	0.00477	0.00567	0.00748	0.01029	0.01449	0.01933
Scalar resonance						
400	9.86301	0.49643	0.65745	0.89709	1.25459	1.65346
500	6.37229	0.43064	0.56615	0.78215	1.07970	1.41500
750	0.16929	0.14184	0.19120	0.26472	0.37253	0.49260
1000	0.02316	0.05600	0.07340	0.10105	0.14096	0.19013
1250	0.01047	0.02986	0.03919	0.05424	0.07478	0.10162
1500	0.00644	0.01861	0.02446	0.03412	0.04763	0.06316
1750	0.00569	0.01232	0.01631	0.02251	0.03156	0.04280
2000	0.00564	0.00881	0.01165	0.01630	0.02260	0.03015
2250	0.00470	0.00641	0.00872	0.01206	0.01682	0.02245
2500	0.00508	0.00578	0.00768	0.01065	0.01492	0.02011
2750	0.00527	0.00407	0.00527	0.00729	0.01022	0.01397
3000	0.00513	0.00340	0.00443	0.00610	0.00859	0.01141

Table 31: Bayesian (statistical uncertainties only, resolved+boosted selection) observed and expected (including $\pm 1(2)\sigma$ variations) upper limits at 95% confidence level on the production cross section times branching ratio to $t\bar{t}$ final states for selected BSM signal benchmark models.

mass [GeV]	Obs. [pb]	Exp. [pb]				
		-2σ	-1σ	central	$+1\sigma$	$+2\sigma$
400	12.44081	0.62697	4.20174	9.14182	17.93714	28.72600
500	6.03090	0.36649	1.86000	3.65552	8.04706	12.65000
750	1.49797	0.09909	0.29318	0.85333	1.67217	2.45458
1000	0.77085	0.04379	0.12230	0.35129	0.65319	0.99675
1250	0.11292	0.02464	0.05708	0.14642	0.26542	0.38893
1500	0.06030	0.01549	0.03253	0.07917	0.13735	0.20137
1750	0.03776	0.00982	0.01944	0.04629	0.07693	0.11770
2000	0.02626	0.00739	0.01423	0.03137	0.05495	0.08266
2250	0.01976	0.00559	0.01025	0.02199	0.03726	0.05520
2500	0.02110	0.00470	0.00879	0.01896	0.03191	0.04396
3000	0.01424	0.00391	0.00662	0.01238	0.02154	0.02959

(a) *Leptophobic topcolor Z'*

mass [GeV]	Obs. [pb]	Exp. [pb]				
		-2σ	-1σ	central	$+1\sigma$	$+2\sigma$
400	14.39334	0.67324	4.44960	7.75875	16.58250	30.64661
500	6.25227	0.40769	2.32857	4.36452	8.66250	13.58056
600	2.92771	0.24799	1.11457	2.63032	5.27797	8.25525
700	2.58299	0.15243	0.62436	1.56150	3.00760	4.52233
800	1.67079	0.10012	0.34234	0.94756	1.82042	2.77286
900	1.51966	0.07259	0.24306	0.71776	1.33983	2.06062
1000	1.09887	0.05209	0.18095	0.52339	0.98145	1.48438
1150	0.42922	0.03660	0.12119	0.33564	0.64983	0.93587
1300	0.19197	0.02879	0.07417	0.21615	0.40025	0.58462
1600	0.09512	0.01767	0.03919	0.11160	0.19847	0.29245
1800	0.06452	0.01344	0.02963	0.07897	0.14220	0.21331
2000	0.05487	0.01178	0.02433	0.06136	0.11227	0.16775
2250	0.05485	0.01010	0.02106	0.05427	0.08966	0.12318
2500	0.05470	0.00940	0.01896	0.04804	0.08266	0.10937
2750	0.05457	0.00916	0.01857	0.04681	0.08111	0.10637
3000	0.04943	0.00942	0.01782	0.04249	0.07679	0.10245

(b) *RS Kaluza-Klein gluon g_{KK}*

Table 32: Bayesian (systematic+statistical uncertainties, resolved+toptagger selection) observed and expected (including $\pm 1(2)\sigma$ variations) upper limits at 95% confidence level on the production cross section times branching ratio to $t\bar{t}$ final states for selected BSM signal benchmark models: (a) *Leptophobic topcolor Z'* and (b) *Randall-Sundrum Kaluza-Klein gluon g_{KK}* .

A.6 Response and Efficiency of BDT configurations

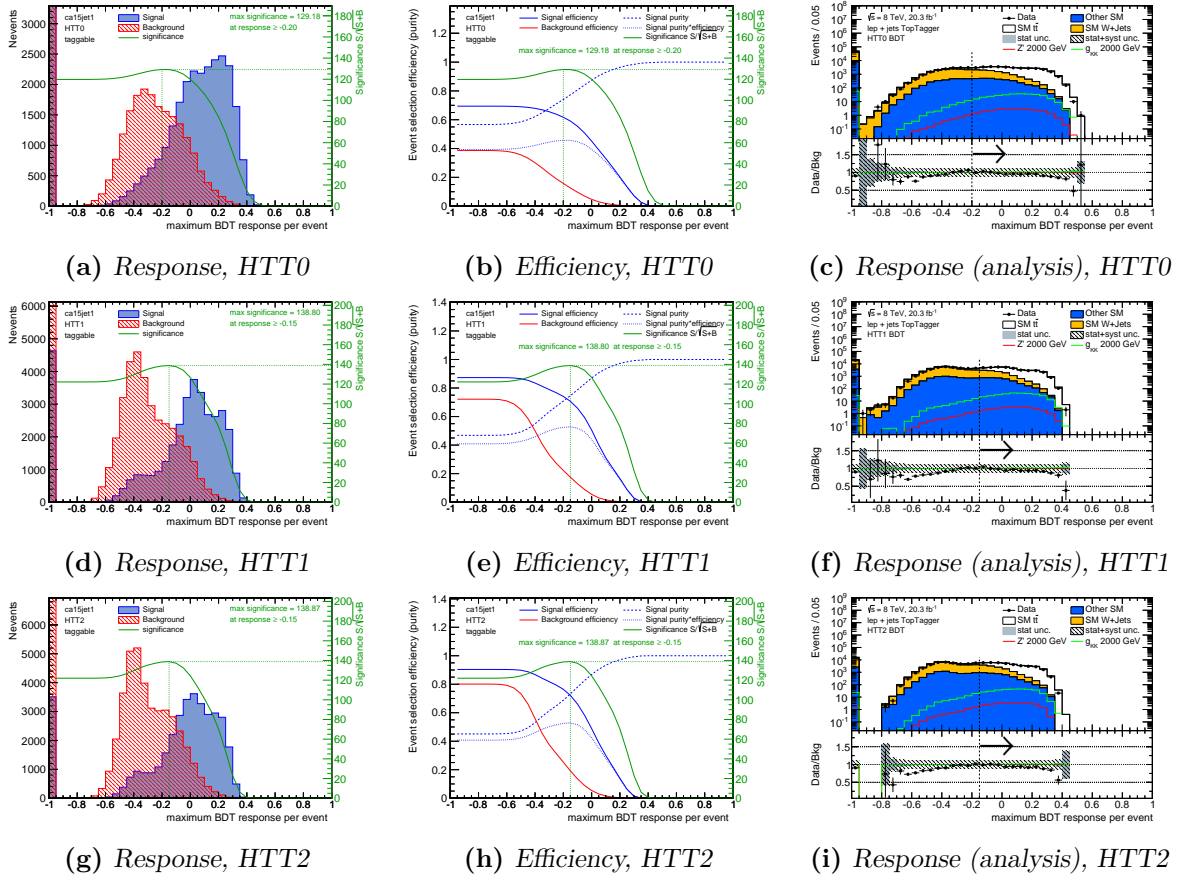


Figure 79: BDT response and efficiency for multivariate analysis optimization for different configurations of the HEPTOPTAGGER algorithm. The response for $t\bar{t}$ signal (S) is shown in blue and for W +Jets background (B) in red. The green curve shows the significance $S/\sqrt{S+B}$ at a given cut-value of the BDT response. Additionally a comparison of data and Standard Model expectations on analysis level is shown. The Standard Model background is shown in a stacked histogram, including $t\bar{t}$, W +Jets and all remaining (merged) background processes. The bottom panel shows the data/MC agreement with the gray and shaded area indicating the statistical and the total systematic uncertainty respectively. Expected distributions for hypothetical signal leptophobic topcolor Z' (2000 GeV) and RS Kaluza-Klein gluon g_{KK} (2000 GeV) resonances are overlaid (non-stacked).

B

List of Figures

1	Feynman diagrams of leading order $t\bar{t}$ production channels	11
2	Parton Distribution Functions	11
3	Top pair decay modes branching fractions	13
4	Feynman diagram of Lepton+jets $t\bar{t}$ pair decay	14
5	Recent results for top mass and $t\bar{t}$ cross section measurements	16
6	Current reach of ATLAS searches for new phenomena	18
7	Overview of the CERN collider complex	21
8	Overview of the ATLAS detector	23
9	Geometry of the ATLAS detector	24
10	Definition of the pseudorapidity η at the ATLAS detector	25
11	The ATLAS Inner Detector	27
12	The ATLAS calorimeter systems	28
13	The ATLAS muon spectrometer	29
14	The ATLAS trigger and Data Acquisition system	31
15	ATLAS performance in RUN I in 2012 data taking period	34
16	Inner Detector tracking efficiency	36
17	Number of vertices vs. average number of interactions	36
18	Electron reconstruction efficiency	38
19	Combined electron identification and reconstruction efficiency	38
20	Muon reconstruction efficiency	40
21	Comparison of the jet-shape of different jet reconstruction algorithms	43

22	Jet Vertex Fraction discrimination and efficiency	45
23	Tagging efficiencies for the MV1 tagger	46
24	E_x^{miss} and E_y^{miss} resolution	47
25	Good for physics 2012 ATLAS dataset integrated luminosity	50
26	Muon trigger efficiency	51
27	Selection efficiency gain for the Delayed stream	51
28	Feynman diagrams for V+Jets background processes	53
29	Feynman diagrams for $t\bar{t}$ +V background processes	53
30	Feynman diagrams for diboson background processes	53
31	Feynman diagrams for single top background processes	54
32	Selection efficiency for selected benchmark signal models	69
33	Reconstructed invariant resonance mass in the boosted selection	71
34	Reconstructed invariant resonance mass in the resolved selection	73
35	Event display of a boosted $t\bar{t}$ decay	74
36	Input event yields for W+Jets normalization scale factors	77
37	Charge asymmetry for background samples	78
38	Jet multiplicities for W+Jets normalization	83
39	Detector acceptance of r_{MC} and truth lepton η	85
40	Effect of the W+Jets SFs on the $m_{t\bar{t}}$ spectrum w/ and w/o CA normalization	85
41	Derivation of ptjmin25 W+Jets uncertainty weights	91
42	Comparison of ptjmin10 and ptjmin25 systematic impact	91
43	Effect of W+Jets scale factors on systematic impact	92
44	Combined InterPDF uncertainties	95
45	Effect of systematic smoothing	97
46	Data/MC comparison for specific variables of the resolved selection	101
47	Data/MC comparison for specific variables of the boosted selection	102
48	Data/MC comparison for $m_{t\bar{t}}$ distributions of the resolved selection	103
49	Data/MC comparison for $m_{t\bar{t}}$ distributions of the boosted selection	104
50	Data/MC comparison for combined $m_{t\bar{t}}$ distributions	105
51	Bayesian limits (statistical uncertainties only, resolved+boosted selection)	111
52	Bayesian limits (systematic+statistical uncertainties, resolved+boosted)	113
53	Bayesian limit posterior pull and uncertainty summary ($Z' \ 2 \text{ TeV}$)	114
54	CL _S limits (systematic+statistical uncertainties, resolved+boosted selection)	116
55	Comparison of Bayesian and CL _S limits	118
56	Intermediate steps of the HEPTOPTAGGER algorithm	121
57	Illustration of the HEPTOPTAGGER algorithm A-Shape cut	123
58	HEPTOPTAGGER W-mass constraint for different working points	127

59	Structure of a decision tree	128
60	TMVA input variables	130
61	TMVA input variable correlations	131
62	BDT response and efficiency	132
63	Tagger comparison for efficiency and background rejection	133
64	HEPTOPTAGGER specific systematic uncertainties	135
65	BDT response on analysis level	138
66	Data/MC comparison for specific variables of the boosted selection	140
67	Data/MC comparison for combined $m_{t\bar{t}}$ distributions	141
68	Bayesian exclusion limits (systematic+statistical uncertainties, toptagger) . .	143
69	Bayesian exclusion limits posterior pull and uncertainty summary (toptagger)	143
70	Impact of various systematic uncertainties in the resolved selection (A)	153
71	Impact of various systematic uncertainties in the resolved selection (B)	154
72	Impact of various systematic uncertainties in the boosted selection (A)	155
73	Impact of various systematic uncertainties in the boosted selection (B)	156
74	Impact of various systematic uncertainties in the boosted selection (C)	157
75	Intra- and InterPDF uncertainties, resolved selection, e +jets channel	158
76	Intra- and InterPDF uncertainties, resolved selection, μ +jets channel	158
77	Intra- and InterPDF uncertainties, boosted selection, e +jets channel	158
78	Intra- and InterPDF uncertainties, boosted selection, μ +jets channel	158
79	BDT response and efficiency for different working points	163

C

List of Tables

1	Recent mass measurements for the six quarks of the Standard Model	6
2	Recent mass measurements for the six leptons of the Standard Model	7
3	Quantum numbers in the Standard Model	8
4	Attributes of the twelve gauge bosons of the Standard Model	8
5	Leptonic decay channels of a W-boson	13
6	LHC run parameters	33
7	Definition of electron identification variables	39
8	Z' resonance signal cross sections and widths for given mass points	56
9	RS Kaluza-Klein gluon g_{KK} cross sections and widths for given mass points .	56
10	RS Kaluza-Klein gluon g_{KK} cross sections and widths for given mass points .	58
11	Electron quality requirements	61
12	Muon quality requirements	62
13	Jet quality requirements	64
14	Parameters for the resolved χ^2 algorithm	72
15	W+Jets flavor and charge asymmetry normalization scale factors	82
16	Charge asymmetry normalization (Boosted topology)	82
17	Average impact of systematic shifts in resolved and boosted selection	98
18	Event yields in the boosted and resolved selection	100

19	Bayesian (systematic+statistical uncertainties, resolved+boosted) upper limits	115
20	CL_S (systematic+statistical uncertainties, resolved+boosted) upper limits . . .	117
21	HEPTOPTAGGER parameter configurations	126
22	Average impact of systematic shifts in resolved and toptagger selection	136
23	Significance for HEPTOPTAGGER and ATLAS configurations	137
24	Event yields in the toptagger and resolved selection	139
25	Bayesian upper limits for benchmark models	142
26	Limit comparison between different procedures	142
27	Names of systematic uncertainties considered in the resolved selection	152
28	Names of systematic uncertainties considered in the boosted selection	155
29	Bayesian upper limits (systematic+statistical, resolved+boosted)(1)	159
30	Bayesian upper limits (systematic+statistical, resolved+boosted)(2)	160
31	Bayesian upper limits (statistical only, resolved+boosted)	161
32	Bayesian upper limits (systematic+statistical, resolved+toptagger)	162

D

Bibliography

- [1] The UA1 Collaboration
Experimental observation of isolated large transverse energy electrons with associated missing energy at $\sqrt{s} = 540\text{GeV}$
Physics Letters B, Volume 122, Issue 1, Pages 103-116 (1983)
[DOI:10.5170/CERN-1983-004.123](https://doi.org/10.5170/CERN-1983-004.123)

- [2] The UA1 Collaboration
Further evidence for charged intermediate vector bosons at the SPS collider
Physics Letters B, Volume 129, Issues 3-4, Pages 273-282 (1985)
[DOI:10.1016/0370-2693\(83\)90860-2](https://doi.org/10.1016/0370-2693(83)90860-2)

- [3] The UA2 Collaboration
Observation of single isolated electrons of high transverse momentum in events with missing transverse energy at the CERN $p\bar{p}$ collider
Physics Letters B, Volume 122, Issues 5-6, Pages 476-485 (1983)
[DOI:10.1016/0370-2693\(83\)91605-2](https://doi.org/10.1016/0370-2693(83)91605-2)

- [4] The CDF Collaboration
Observation of Top Quark Production in $p\bar{p}$ Collisions
Physical Review Letter, Volume 74, Issue 14 (1995)
[DOI:10.1103/PhysRevLett.74.2626](https://doi.org/10.1103/PhysRevLett.74.2626)

- [5] The DØ Collaboration
Observation of the Top quark
Physical Review Letter, Volume 74, Issue 14 (1995)
[DOI:10.1103/PhysRevLett.74.2632](https://doi.org/10.1103/PhysRevLett.74.2632)
- [6] The ATLAS Collaboration
Observation of a new particle in the search for the Standard Model Higgs boson with the ATLAS detector at the LHC
Physics Letters B, Volume 716, Issue 1, Pages 1-29 (2012)
[DOI:10.1016/j.physletb.2012.08.020](https://doi.org/10.1016/j.physletb.2012.08.020)
- [7] The CMS Collaboration
Observation of a new boson at a mass of 125 GeV with the CMS experiment at the LHC
Physics Letters B, Volume 716, Issue 1, Pages 30-61 (2012)
[DOI:10.1016/j.physletb.2012.08.021](https://doi.org/10.1016/j.physletb.2012.08.021)
- [8] The ATLAS Collaboration
A search for $t\bar{t}$ resonances using lepton-plus-jets events in proton-proton collisions at $\sqrt{s} = 8$ TeV with the ATLAS detector
Journal of High Energy Physics (JHEP), Volume 2015, Issue 8, Article 148 (2015)
[DOI:10.1007/JHEP08\(2015\)148](https://doi.org/10.1007/JHEP08(2015)148)
- [9] M. V. G. 't Hooft
Regularization and Renormalization of Gauge Fields
Nuclear Physics B, Volume 44, Issue 1, Pages 189-213 (1972)
[DOI:10.1016/0550-3213\(72\)90279-9](https://doi.org/10.1016/0550-3213(72)90279-9)
- [10] N. Cabibbo
Unitary Symmetry and Leptonic Decays
Physical Review Letter, Volume 10, Issue 12 (1963)
[DOI:10.1103/PhysRevLett.10.531](https://doi.org/10.1103/PhysRevLett.10.531)
- [11] M. Kobayashi and T. Maskawa
CP-Violation in the Renormalizable Theory of Weak Interaction
Progress of Theoretical Physics, Volume 49, Issue 2, Pages 652-657 (1973)
[DOI:10.1143/PTP.49.652](https://doi.org/10.1143/PTP.49.652)
- [12] K.A. Olive et al. (Particle Data Group)
Review of Particle Physics - The CKM Quark-mixing matrix
Chinese Physics C, Volume 38, Number 9 (2014)
[DOI:10.1088/1674-1137/38/9/090001](https://doi.org/10.1088/1674-1137/38/9/090001)

- [13] The LHCb Collaboration
Observation of $J/\psi p$ resonances consistent with pentaquark states in $\Lambda_b^0 \rightarrow J/\psi K^- p$ decays
Physical Review Letter, Volume 115, Issue 7 (2015)
[DOI:10.1103/PhysRevLett.115.072001](https://doi.org/10.1103/PhysRevLett.115.072001)
- [14] K.A. Olive et al. (Particle Data Group)
Review of Particle Physics - Quark masses review
Chinese Physics C, Volume 38, Number 9 (2014)
[DOI:10.1088/1674-1137/38/9/090001](https://doi.org/10.1088/1674-1137/38/9/090001)
- [15] K.A. Olive et al. (Particle Data Group)
Review of Particle Physics - The top quark
Chinese Physics C, Volume 38, Number 9 (2014)
[DOI:10.1088/1674-1137/38/9/090001](https://doi.org/10.1088/1674-1137/38/9/090001)
- [16] The SNO Collaboration
Direct Evidence for Neutrino Flavor Transformation from Neutral-Current Interactions in the Sudbury Neutrino Observatory
Physical Review Letter, Volume 89, Issue 1 (2002)
[DOI:10.1103/PhysRevLett.89.011301](https://doi.org/10.1103/PhysRevLett.89.011301)
- [17] W. Rodejohann
Neutrino-less Double Beta Decay and Particle Physics
International Journal of Modern Physics E, Volume 20, Issue 9 (2011)
[DOI:10.1142/S0218301311020186](https://doi.org/10.1142/S0218301311020186)
- [18] K.A. Olive et al. (Particle Data Group)
Review of Particle Physics - Electron summary listing
Chinese Physics C, Volume 38, Number 9 (2014)
[DOI:10.1088/1674-1137/38/9/090001](https://doi.org/10.1088/1674-1137/38/9/090001)
- [19] K.A. Olive et al. (Particle Data Group)
Review of Particle Physics - Muon summary listing
Chinese Physics C, Volume 38, Number 9 (2014)
[DOI:10.1088/1674-1137/38/9/090001](https://doi.org/10.1088/1674-1137/38/9/090001)
- [20] K.A. Olive et al. (Particle Data Group)
Review of Particle Physics - Tau summary listing
Chinese Physics C, Volume 38, Number 9 (2014)
[DOI:10.1088/1674-1137/38/9/090001](https://doi.org/10.1088/1674-1137/38/9/090001)

- [21] K.A. Olive et al. (Particle Data Group)
Review of Particle Physics - Neutrino properties listing
Chinese Physics C, Volume 38, Number 9 (2014)
[DOI:10.1088/1674-1137/38/9/090001](https://doi.org/10.1088/1674-1137/38/9/090001)
- [22] K.A. Olive et al. (Particle Data Group)
Review of Particle Physics - W-Boson summary listing
Chinese Physics C, Volume 38, Number 9 (2014)
[DOI:10.1088/1674-1137/38/9/090001](https://doi.org/10.1088/1674-1137/38/9/090001)
- [23] K.A. Olive et al. (Particle Data Group)
Review of Particle Physics - Z-Boson summary listing
Chinese Physics C, Volume 38, Number 9 (2014)
[DOI:10.1088/1674-1137/38/9/090001](https://doi.org/10.1088/1674-1137/38/9/090001)
- [24] K.A. Olive et al. (Particle Data Group)
Review of Particle Physics - Photon summary listing
Chinese Physics C, Volume 38, Number 9 (2014)
[DOI:10.1088/1674-1137/38/9/090001](https://doi.org/10.1088/1674-1137/38/9/090001)
- [25] S. L. Glashow
Partial-symmetries of weak interactions
Nuclear Physics Volume 22, Issue 4 (1961)
[DOI:10.1016/0029-5582\(61\)90469-2](https://doi.org/10.1016/0029-5582(61)90469-2)
- [26] S. Weinberg
A model of leptons
Physical Review Letter, Volume 19, Issue 21 (1967)
[DOI:10.1103/PhysRevLett.19.1264](https://doi.org/10.1103/PhysRevLett.19.1264)
- [27] A. Salam
Elementary Particle Physics: Relativistic Groups and Analyticity
Eighth Nobel Symposium (1968)
- [28] P. W. Higgs
Broken Symmetries and the Masses of Gauge Bosons
Physical Review Letter, Volume 13, Issue 16 (1964)
[DOI:10.1103/PhysRevLett.13.508](https://doi.org/10.1103/PhysRevLett.13.508)
- [29] F. Englert and R. Brout
Broken Symmetry and the Mass of Gauge Vector Mesons
Physical Review Letter, Volume 13, Issue 9 (1964)
[DOI:10.1103/PhysRevLett.13.321](https://doi.org/10.1103/PhysRevLett.13.321)

- [30] The ATLAS Collaboration
Measurement of the top pair production cross-section in 8 TeV proton-proton collisions using kinematic information in the lepton+jets final state with ATLAS
Physical Review D, Volume 91, Issue 11 (2015)
[DOI:10.1103/PhysRevD.91.112013](https://doi.org/10.1103/PhysRevD.91.112013)
- [31] A. D. Martin, W. J. Stirling, R. S. Thorne, *et al.*
Parton distributions for the LHC
European Physics Journal C, Volume 63, Issue 2, Pages 189-285 (2009)
[DOI:10.1140/epjc/s10052-009-1072-5](https://doi.org/10.1140/epjc/s10052-009-1072-5)
- [32] The ATLAS Collaboration
Top Public Results
ATLAS (2015)
<https://twiki.cern.ch/twiki/bin/view/AtlasPublic/TopPublicResults>
- [33] R. Harris, C. Hill, and S. Parke
Cross Section for Topcolor Z' decaying to top-antitop
Fermilab-FN-687 (1999)
[arXiv:hep-ph/9911288](https://arxiv.org/abs/hep-ph/9911288)
- [34] R. Harris and S. Jain
Cross Sections for Leptophobic Topcolor Z' decaying to top-antitop
European Physics Journal C, Volume 72, Issue 7, Article 2072 (2012)
[DOI:10.1140/epjc/s10052-012-2072-4](https://doi.org/10.1140/epjc/s10052-012-2072-4)
- [35] The DØ Collaboration
Search for $t\bar{t}$ resonances in the lepton plus jets final state in $p\bar{p}$ collisions at $\sqrt{s} = 1.96$ TeV
Physics Letters B, Volume 668, Issue 2, Pages 98-104 (2008)
[DOI:10.1016/j.physletb.2008.08.027](https://doi.org/10.1016/j.physletb.2008.08.027)
- [36] The CDF Collaboration
Search for resonant $t\bar{t}$ production in $p\bar{p}$ collisions at $\sqrt{s} = 1.96$ TeV
Physical Review Letter, Volume 100, Issue 23 (2007)
[DOI:10.1103/PhysRevLett.100.231801](https://doi.org/10.1103/PhysRevLett.100.231801)
- [37] The ATLAS Collaboration
A search for $t\bar{t}$ resonances in the lepton plus jets final state with ATLAS using 4.7fb^{-1} of pp collisions at $\sqrt{s} = 7$ TeV
Physical Review D, Volume 88, Issue 1 (2013)
[DOI:10.1103/PhysRevD.88.012004](https://doi.org/10.1103/PhysRevD.88.012004)

- [38] B. Lillie, L. Randall, and L.-T. Wang
The Bulk RS KK-gluon at the LHC
Journal of High Energy Physics (JHEP), Volume 2007, Issue 9, Article 74 (2007)
[DOI:10.1088/1126-6708/2007/09/074](https://doi.org/10.1088/1126-6708/2007/09/074)
- [39] K. Agashe, H. Davoudiasl, G. Perez, *et al.*
Warped Gravitons at the LHC and Beyond
Physical Review D, Volume 76, Issue 3 (2007)
[DOI:10.1103/PhysRevD.76.036006](https://doi.org/10.1103/PhysRevD.76.036006)
- [40] The ATLAS Collaboration
Exotic Public Results
ATLAS (2015)
<https://twiki.cern.ch/twiki/bin/view/AtlasPublic/ExoticsPublicResults>
- [41] O. S. Bruening, P. Collier, P. Lebrun, *et al.*
LHC Design Report
CERN (2004)
[CERN-2004-003-V-1](https://cds.cern.ch/record/550780/files/CERN-2004-003-V-1.pdf)
- [42] C. Lefèvre
The CERN accelerator complex, Complexe des accélérateurs du CERN
CERN (2008)
[CERN-DI-0812015](https://cds.cern.ch/record/1170787/files/CERN-DI-0812015.pdf)
- [43] The ALICE Collaboration
The ALICE experiment at the CERN LHC
Journal of Instrumentation (JINST), Volume 3, Issue 8, Article 2 (2008)
[DOI:10.1088/1748-0221/3/08/S08002](https://doi.org/10.1088/1748-0221/3/08/S08002)
- [44] The LHCb Collaboration
The LHCb Detector at the CERN LHC
Journal of Instrumentation (JINST), Volume 3, Issue 8, Article 5 (2008)
[DOI:10.1088/1748-0221/3/08/S08005](https://doi.org/10.1088/1748-0221/3/08/S08005)
- [45] The CMS Collaboration
The CMS experiment at the CERN LHC
Journal of Instrumentation (JINST), Volume 3, Issue 8, Article 4 (2008)
[DOI:10.1088/1748-0221/3/08/S08004](https://doi.org/10.1088/1748-0221/3/08/S08004)
- [46] The ATLAS Collaboration
ATLAS detector and physics performance: Technical Design Report, 1
CERN (1999)
[ATLAS-TDR-14; CERN-LHCC-99-014](https://cds.cern.ch/record/176426/files/ATLAS-TDR-14;CERN-LHCC-99-014.pdf)

- [47] The ATLAS Collaboration
ATLAS detector and physics performance: Technical Design Report, 2
CERN (1999)
[ATLAS-TDR-15; CERN-LHCC-99-015](#)
- [48] J. Pequenao
Computer generated image of the whole ATLAS detector
ATLAS (2008)
[CERN-GE-0803012](#)
- [49] J. Pequenao
Computer generated image of the ATLAS inner detector
ATLAS (2008)
[CERN-GE-0803014](#)
- [50] J. Pequenao
Computer generated image of the ATLAS inner detector endcap
ATLAS (2008)
[ATLAS-CONF-2014-047](#)
- [51] J. Pequenao
Computer generated image of the ATLAS calorimeter
ATLAS (2008)
[CERN-GE-0803015](#)
- [52] J. Pequenao
Computer generated image of the ATLAS Muons subsystem
ATLAS (2008)
[CERN-GE-0803017](#)
- [53] S. van der Meer
Calibration of the effective beam height in the ISR
CERN (1968)
[CERN-ISR-PO-68-31](#)
- [54] The ATLAS Collaboration
The Luminosity Monitor of the ATLAS Experiment
ATLAS (2009)
[ATL-LUM-PROC-2009-004](#)
- [55] V. Cindro, D. Dobos, I. Dolenc, *et al.*
The ATLAS Beam Conditions Monitor
Journal of Instrumentation (JINST), Volume 3, Issue 2, Article 4 (2008)
[DOI:10.1088/1748-0221/3/02/P02004](#)

- [56] K. Kordas, M. Abolins, I. Alexandrov, *et al.*
The ATLAS Data Acquisition and Trigger: concept, design and status
Nuclear Physics B, Volume 172, Pages 178-182 (2006)
[DOI:10.1016/j.nuclphysbps.2007.08.004](https://doi.org/10.1016/j.nuclphysbps.2007.08.004)
- [57] The ATLAS Collaboration
The ATLAS Data Acquisition System: from Run 1 to Run 2
37th International Conference on High Energy Physics Proceedings (2014)
[ATL-DAQ-PROC-2014-035](https://arxiv.org/abs/1405.3061)
- [58] The ATLAS Collaboration
ATLAS Computing: technical design report
CERN (2005)
[CERN-LHCC-2005-022](https://arxiv.org/abs/1405.3061)
- [59] C. Eck, J. Knobloch, L. Robertson, *et al.*
LHC computing Grid: Technical Design Report
CERN (2005)
[CERN-LHCC-2005-024](https://arxiv.org/abs/1405.3061)
- [60] M. Bajko, F. Bertinelli, N. Catalan-Lasheras, *et al.*
Report of the Task Force on the Incident of 19th September 2008 at the LHC
CERN (2009)
[CERN-LHC-PROJECT-Report-1168](https://arxiv.org/abs/1405.3061)
- [61] F. Formenti, Z. Charifoulline, G. J. Coelingh, *et al.*
Upgrade of the Quench Protection Systems for the Superconducting Circuits of the LHC Machine at CERN: From Concept and Design to the First Operational Experience
1st International Particle Accelerator Conference Proceedings (2010)
[CERN-ATS-2010-129](https://arxiv.org/abs/1405.3061)
- [62] K. Foraz
LS1 general planning and strategy for the LHC, LHC injectors
Chamonix 2012 Workshop on LHC Performance Proceedings (2012)
[DOI:10.5170/CERN-2012-006.212](https://doi.org/10.5170/CERN-2012-006.212)
- [63] CERN Press
LHC experiments are back in business at a new record energy
CERN (2015)
<http://press.web.cern.ch/press-releases/2015/06/lhc-experiments-are-back-business-new-record-energy>

- [64] R. Bruce, G. Arduini, S. Fartoukh, *et al.*
Baseline LHC machine parameters and configuration of the 2015 proton run
Chamonix 2014: LHC Performance Workshop Proceedings (2014)
[DOI:10.5170/CERN-2015-002.100](https://doi.org/10.5170/CERN-2015-002.100)
- [65] C. Buttar and D. della Volpe
Letter of Intent for the Phase-II Upgrade of the ATLAS Experiment
CERN (2012)
[ATL-COM-UPGRADE-2012-040](https://arxiv.org/abs/1207.4044)
- [66] The ATLAS Collaboration
Physics at a High-Luminosity LHC with ATLAS (Update)
CERN (2012)
[ATL-PHYS-PUB-2012-004](https://arxiv.org/abs/1207.4044)
- [67] M. Lamont
The LHC from commissioning to operation
CERN (2011)
[CERN-ATS-2011-186](https://arxiv.org/abs/1107.3542)
- [68] The ATLAS Collaboration
Total Integrated Luminosity in 2012
ATLAS (2012)
<https://twiki.cern.ch/twiki/bin/view/AtlasPublic/LuminosityPublicResults>
- [69] The ATLAS Collaboration
Total Integrated Luminosity in 2015
ATLAS (2015)
<https://twiki.cern.ch/twiki/bin/view/AtlasPublic/LuminosityPublicResultsRun2>
- [70] The ATLAS Collaboration
Full 2012 pp collisions dataset ATLAS performance
ATLAS (2012)
<https://twiki.cern.ch/twiki/bin/view/AtlasPublic/RunStatsPublicResults2010>
- [71] The ATLAS Collaboration
Expected Performance of the ATLAS Experiment - Detector, Trigger and Physics
CERN (2009)
[arXiv:0901.0512](https://arxiv.org/abs/0901.0512)
- [72] K. Hamano, A. Morley, and A. Salzburger
Track Reconstruction Performance and Efficiency Estimation using different ID geometry samples
CERN (2012)
[ATL-COM-PHYS-2012-1541 \(internal\)](https://arxiv.org/abs/1207.4044)

- [73] F. Meloni, S. Pagan Griso, and A. Morley
Nvertices vs average number of interactions for different beamspot profiles: Collision performance plots for approval
CERN (2013)
[ATL-COM-PHYS-2013-1511 \(internal\)](#)
- [74] The ATLAS Collaboration
Electron efficiency measurements with the ATLAS detector using the 2012 LHC proton-proton collision data
CERN (2014)
[ATLAS-CONF-2014-032](#)
- [75] W. Lampl, S. Laplace, D. Lelas, *et al.*
Calorimeter Clustering Algorithms: Description and Performance
CERN (2008)
[ATL-LARG-PUB-2008-002](#)
- [76] The ATLAS Collaboration
Measurement of the muon reconstruction performance of the ATLAS detector using 2011 and 2012 LHC proton-proton collision data
European Physics Journal C, Volume 74, Issue 11, Article 3130 (2014)
[DOI:10.1140/epjc/s10052-014-3130-x](#)
- [77] S. Catani, Y. Dokshitzer, M. Seymour, *et al.*
Longitudinally invariant $K(t)$ clustering algorithms for hadron hadron collisions
Nuclear Physics B, Volume 406, Issues 1-2, Pages 187-224 (1993)
[DOI:10.1016/0550-3213\(93\)90166-M](#)
- [78] S. D. Ellis and D. E. Soper
Successive Combination Jet Algorithm For Hadron Collisions
Physical Review D, Volume 48, Issue 7 (1993)
[DOI:10.1103/PhysRevD.48.3160](#)
- [79] M. Cacciari, G. P. Salam and G. Soyez
The anti- k_t jet clustering algorithm
Journal of High Energy Physics (JHEP), Volume 2008, Issue 4, Article 63 (2008)
[DOI:10.1088/1126-6708/2008/04/063](#)
- [80] Y. L. Dokshitzer, G. D. Leder, S. Moretti and B. R. Webber
Better Jet Clustering Algorithms
Journal of High Energy Physics (JHEP), Volume 1997, Issue 8, Article 1 (1997)
[DOI:10.1088/1126-6708/1997/08/001](#)

- [81] M. Wobisch and T. Wengler
Hadronization Corrections to Jet Cross Sections in Deep-Inelastic Scattering
Workshop on Monte Carlo Generators for HERA Physics (Plenary Starting Meeting)
Proceedings (PITHA-99-16) (1998)
[arXiv:hep-ph/9907280](#)
- [82] The ATLAS Collaboration
Jet energy measurement and its systematic uncertainty in proton-proton collisions at $\sqrt{s} = 7$ TeV with the ATLAS detector
European Physics Journal C, Volume 75, Issue 1, Article 17 (2015)
[DOI:10.1140/epjc/s10052-014-3190-y](#)
- [83] D. Krohn, J. Thaler, and W. L.-T.
Jet Trimming
Journal of High Energy Physics (JHEP), Volume 2010, Issue 2, Article 84 (2010)
[DOI:10.1007/JHEP02\(2010\)084](#)
- [84] The ATLAS Collaboration
Pile-up subtraction and suppression for jets in ATLAS
CERN (2013)
[ATLAS-CONF-2013-083](#)
- [85] The ATLAS Collaboration
Calibration of the performance of b-tagging for c and light-flavour jets in the 2012 ATLAS data
CERN (2014)
[ATLAS-CONF-2014-046](#)
- [86] C. F. Andersen, E. Bergeaas Kuutmann, J. Caudron, *et al.*
Boosted top quark identification in pp collisions at $\sqrt{s} = 8$ TeV with the ATLAS detector
CERN (2014)
[ATL-COM-PHYS-2014-1492](#)
- [87] T. Plehn, M. Spannowsky, M. Takeuchi, *et al.*
Stop Reconstruction with Tagged Tops
Journal of High Energy Physics (JHEP), Volume 2010, Issue 10, Article 78 (2010)
[DOI:10.1007/JHEP10\(2010\)078](#)
- [88] G. P. S. T. Plehn and M. Spannowsky
Fat Jets for a Light Higgs
Physical Review Letter, Volume 104, Issue 11 (2010)
[DOI:10.1103/PhysRevLett.104.111801](#)

- [89] The ATLAS Collaboration
Performance of Missing Transverse Momentum Reconstruction in ATLAS studied in Proton-Proton Collisions recorded in 2012 at $\sqrt{s} = 8$ TeV
CERN (2013)
[ATLAS-CONF-2013-082](#)
- [90] The ATLAS Collaboration
The ATLAS Simulation Infrastructure
European Physics Journal C, Volume 70, Issue 3, Pages 823-874 (2010)
[DOI:10.1140/epjc/s10052-010-1429-9](#)
- [91] The GEANT4 Collaboration
GEANT4: A Simulation toolkit
Nuclear Instruments and Methods in Physics Research Section A, Volume 605, Issue 3, Pages 250-303 (2002)
[DOI:10.1016/S0168-9002\(03\)01368-8](#)
- [92] . The ATLAS Collaboration, M. Beckingham, M. Duehrssen, *et al.*
The simulation principle and performance of the ATLAS fast calorimeter simulation FastCaloSim
Conference on Computing in High Energy and Nuclear Physics 2010, Proceedings (2010)
[ATL-PHYS-PUB-2010-013](#)
- [93] T. Sjostrand, S. Mrenna, P. Skands, *et al.*
A Brief Introduction to PYTHIA 8.1
Computer Physics Communications, Volume 178, Issue 11 (2008)
[DOI:10.1016/j.cpc.2008.01.036](#)
- [94] The ATLAS Collaboration
Performance of the ATLAS muon trigger in pp collisions at $\sqrt{s} = 8$ TeV
European Physics Journal C, Volume 75, Issue 3, Article 120 (2015)
[DOI:10.1140/epjc/s10052-015-3325-9](#)
- [95] A. Altheimer, K. Behr, E. Bergeaas Kuutmann, *et al.*
A search for $t\bar{t}$ resonances using lepton-plus-jets events in proton-proton collisions at $\sqrt{s} = 8$ TeV with the ATLAS detector
CERN (2015)
[ATL-COM-PHYS-2014-003](#)
- [96] J. Gao, C. S. Li, B. H. Li, *et al.*
Next-to-leading order QCD corrections to the heavy resonance production and decay into top quark pair at the LHC
Physical Review D, Volume 82, Issue 1, Article 20 (2010)
[DOI:10.1103/PhysRevD.82.014020](#)

- [97] ATLAS TopReconstructionGroup
TopCommonObjects
ATLAS TopCommonObjects TWiki (internal) (2015)
<https://twiki.cern.ch/twiki/bin/viewauth/AtlasProtected/TopCommonObjects>
- [98] M. Cacciari, G. Salam, and G. Soyez
FastJet user manual
European Physics Journal C, Volume 72, Issue 3, Article 1896 (2012)
[DOI:10.1140/epjc/s10052-012-1896-2](https://doi.org/10.1140/epjc/s10052-012-1896-2)
- [99] S. Calvet, C. Pollard, and J. Zhong
Electron-Jet Overlap Removal for the $l + jets t\bar{t}$ Resonances Search
CERN (2014)
[ATL-COM-PHYS-2014-343](#)
- [100] T. Chwalek
Messung der W-Boson-Helizitätsanteile in Top-Quark-Zerfällen mit dem CDF II Experiment und Studien zu einer frühen Messung des $t\bar{t}$ -Wirkungsquerschnitts mit dem CMS Experiment
CERN (2010)
[CERN-THESIS-2010-255](#)
- [101] The ATLAS Collaboration
A search for $t\bar{t}$ resonances in the lepton plus jets final state with ATLAS using 14 fb^{-1} of pp collisions at $\sqrt{s} = 8 \text{ TeV}$
CERN (2013)
[ATLAS-CONF-2013-052](#)
- [102] B. Acharya, J. Adelman, S. Adomeit, *et al.*
Object selection and calibration, background estimations and MC samples for the Winter 2013 Top Quark analyses with 2012 data
CERN (2013)
[ATL-COM-PHYS-2013-088](#)
- [103] The ATLAS Collaboration
Measurement of the differential cross-section of highly boosted top quarks as a function of their transverse momentum in $\sqrt{s} = 8 \text{ TeV}$ proton-proton collisions using the ATLAS detector
Physical Review D, Volume 93, Issue 3 (2016)
[DOI:10.1103/PhysRevD.93.032009](https://doi.org/10.1103/PhysRevD.93.032009)
- [104] A. Cooper-Sarkar, J. Ferrando, C. Issever, *et al.*
Measurement of the W-production Charge Asymmetry with ATLAS
CERN (2010)
[ATL-PHYS-INT-2010-019 \(internal\)](#)

- [105] The ATLAS Collaboration
Improved luminosity determination in pp collisions at $\sqrt{s} = 7$ TeV using the ATLAS detector at the LHC
European Physics Journal C, Volume 73, Issue 8, Article 2518 (2013)
[DOI:10.1140/epjc/s10052-013-2518-3](https://doi.org/10.1140/epjc/s10052-013-2518-3)
- [106] ATLAS TopReconstructionGroup
TopPdfUncertainty
ATLAS TopPDF TWiki (internal) (2015)
<https://twiki.cern.ch/twiki/bin/view/AtlasProtected/TopPdfUncertainty>
- [107] A. Buckley, J. Ferrando, S. Lloyd, *et al.*
LHAPDF6: parton density access in the LHC precision era
European Physics Journal C, Volume 75, Issue 3, Article 132 (2015)
[DOI:10.1140/epjc/s10052-015-3318-8](https://doi.org/10.1140/epjc/s10052-015-3318-8)
- [108] H.-L. Lai, M. Guzzi, J. Huston, *et al.*
New parton distributions for collider physics
Physical Review D, Volume 82, Issue 7 (2010)
[DOI:10.1103/PhysRevD.82.074024](https://doi.org/10.1103/PhysRevD.82.074024)
- [109] J. Gao, M. Guzzi, J. Huston, *et al.*
The CT10 NNLO Global Analysis of QCD
Physical Review D, Volume 89, Issue 3 (2014)
[DOI:10.1103/PhysRevD.89.033009](https://doi.org/10.1103/PhysRevD.89.033009)
- [110] A. D. Martin, W. J. Stirling, R. S. Thorne, *et al.*
Uncertainties on alpha S in global PDF analyses
European Physics Journal C, Volume 64, Issue 4, Pages 653-680 (2009)
[DOI:10.1140/epjc/s10052-009-1164-2](https://doi.org/10.1140/epjc/s10052-009-1164-2)
- [111] R. D. Ball, V. Bertone, S. Carrazza, *et al.*
Parton distributions with LHC data
Nuclear Physics B, Volume 867, Issue 2, Pages 244-289 (2013)
[DOI:10.1016/j.nuclphysb.2012.10.003](https://doi.org/10.1016/j.nuclphysb.2012.10.003)
- [112] G. Choudalakis
On hypothesis testing, trials factor, hypertests and the BumpHunter
Proceedings, PHYSTAT 2011 Workshop on Statistical Issues Related to Discovery Claims in Search Experiments and Unfolding, CERN, Geneva, Switzerland 17-20 January 2011 (2011)
[arXiv:1101.0390](https://arxiv.org/abs/1101.0390)

- [113] L. Lyons
Open statistical issues in particle physics
Annals of Applied Statistics 2008, Vol. 2, No. 3, 887-915 (2008)
[DOI:10.1214/08-AOAS163](https://doi.org/10.1214/08-AOAS163)
- [114] E. Gross
Practical Statistics Lecture
2015 European School of High Energy Physics (2015)
<https://indico.cern.ch/event/381289>
- [115] M. Baak, G. J. Besjes, D. Cañete, *et al.*
HistFitter software framework for statistical data analysis
European Physics Journal C, Volume 75, Issue 4, Article 153 (2015)
[DOI:10.1140/epjc/s10052-015-3327-7](https://doi.org/10.1140/epjc/s10052-015-3327-7)
- [116] G. Kasieczka, T. Plehn, T. Schell, *et al.*
Resonance Searches with an Updated Top Tagger
Journal of High Energy Physics (JHEP), Volume 2015, Issue 6, Article 203 (2015)
[DOI:10.1007/JHEP06\(2015\)203](https://doi.org/10.1007/JHEP06(2015)203)
- [117] A. Hoecker, P. Speckmayer, J. Stelzer, *et al.*
TMVA - Toolkit for Multivariate Data Analysis
11th International Workshop on Advanced Computing and Analysis Techniques in Physics Research (ACAT) (C07-04-23.1) (2007)
[arXiv:physics/0703039](https://arxiv.org/abs/physics/0703039)

Curriculum Vitae

[In der elektronischen Fassung aus Datenschutzgründen entfernt]

Ausgewählte Veröffentlichungen

- [1] The ATLAS Collaboration
A search for $t\bar{t}$ resonances using lepton-plus-jets events in proton-proton collisions at $\sqrt{s} = 8$ TeV with the ATLAS detector
Journal of High Energy Physics (JHEP), Volume 2015, Issue 8, Article 148 (2015)
DOI : [10.1007/JHEP08\(2015\)148](https://doi.org/10.1007/JHEP08(2015)148)

- [2] The ATLAS Collaboration
Identification of high transverse momentum top quarks in pp collisions at $\sqrt{s} = 8$ TeV with the ATLAS detector
CERN (2016) (submitted to JHEP)
arXiv : [1603.03127](https://arxiv.org/abs/1603.03127)

- [3] The ATLAS Collaboration
Measurement of the differential cross-section of highly boosted top quarks as a function of their transverse momentum in $\sqrt{s} = 8$ TeV proton-proton collisions using the ATLAS detector
Physical Review D, Volume 93, Issue 3 (2016)
DOI : [10.1103/PhysRevD.93.032009](https://doi.org/10.1103/PhysRevD.93.032009)

- [4] The ATLAS Collaboration
Measurement of the top quark pair production cross section in the single-lepton channel with ATLAS in proton-proton collisions at 8 TeV using kinematic fits with b-tagging
CERN (2012)
CDS : [ATLAS-CONF-2012-149](https://cds.cern.ch/record/1490000/files/ATLAS-CONF-2012-149)

- [5] The ATLAS Collaboration
A search for $t\bar{t}$ resonances in the lepton plus jets final state with ATLAS using 14 fb^{-1} of pp collisions at $\sqrt{s} = 8$ TeV
CERN (ATLAS CONF Note) (2013)
CDS : [ATLAS-CONF-2013-052](https://cds.cern.ch/record/1490000/files/ATLAS-CONF-2013-052)

- [6] The ATLAS Collaboration
A search for $t\bar{t}$ resonances in the lepton plus jets final state with ATLAS using 4.7 fb^{-1} of pp collisions at $\sqrt{s} = 7$ TeV
Physics Review D, Volume 88, Issue 1 (2013)
DOI : [10.1103/PhysRevD.88.012004](https://doi.org/10.1103/PhysRevD.88.012004)

- [7] The ATLAS Collaboration
A search for $t\bar{t}$ resonances with the ATLAS detector in 2.05 fb^{-1} of proton-proton collisions at $\sqrt{s} = 7$ TeV
The European Physics Journal C, Volume 72, Issue 7 (2012)
DOI : [10.1140/epjc/s10052-012-2083-1](https://doi.org/10.1140/epjc/s10052-012-2083-1)